UNIVERSITÀ
DEGLI STUDI
FIRENZE

Dipartimento di Fisica
e Astronomia

International Doctorate in
Atomic and Molecular Photonics
Ciclo XXXVI

Exploring Novel Quantum Phases in Ultracold Magnetic Gases

Dipolar supersolids and ferromagnetic phases in spinor condensates

Candidate
Nicolò Antolini (DT30959)

Thesis Advisor
Prof. Giovanni Modugno

Director
Prof. Diederik S. Wiersma

University of Florence. October 2023

This thesis has been submitted on October 30, 2023 and defended on April 15, 2024 in front of a Board of Examiners composed by:
Prof. Hanns-Christoph Nägerl (Innsbruck University),
Dott.ssa Irene Costantini (Università di Firenze),
Prof. Colm Delaney (Trinity College Dublin).

An online updated version of the thesis will be available at:
quantumgases.lens.unifi

Exploring Novel Quantum Phases in Ultracold Magnetic Gases
PhD Thesis. University of Florence

This thesis has been typeset by LATEXusing the code developed by Niccolò Preti (niccolo.preti@unifi.it)

Last modified May 13, 2024

Author's email: nantolini@unifi.it

Summary

Novel magnetic phases arising from quantum phase transitions are at the frontier in ultracold quantum gases experiments. In this thesis, I focus on two different phases: the dipolar supersolid found in quantum gases with dipolar interactions, and the easy-plane ferromagnetic phase realized in a spin-1 spinor condensate.

Dipolar supersolids are a counterintuitive phase of matter, mixing properties of crystals and superfluids, which have been discovered only recently in experiments employing strongly dipolar atoms like dysprosium or erbium. This novel quantum phase still needs to be explored in its complexity. In this thesis, I explore its defining properties, like the onset of the crystallization process leading to supersolids from superfluids, and the superfluid response of the system. The latter is described by the so-called superfluid fraction, which is reduced in supersolids with respect to standard superfluids, due to presence of a periodic modulation of the wavefunction that breaks the continuous translational symmetry of the system. To address the crystallization phase transition, I use an approach based on the Landau theory of phase transitions, developing a model describing the dipolar supersolid confined in harmonic traps. Although the theory of quantum phase transition is typically applied at the thermodynamic limit, we find that discontinuous phase transitions, reminiscent of first-order phase transitions in infinite systems, occur also in our finite-sized system composed by $3-4$ clusters with thousands of atoms each. Increasing the transverse harmonic confinement we find that the character of the transition changes smoothly from discontinuous to continuous, and we interpret this behavior as a dimensional crossover in the supersolid lattice structure dimensionality.

The continuous quantum phase transition is employed to adiabatically prepare supersolids near their absolute ground state, a key step for probing their superfluid response. Here, I focus on the experimental assessment of the superfluid fraction, a fundamental quantity for dipolar supersolids. The measurement of the superfluid fraction is based on the study of a peculiar collective excitation of the supersolid, the Josephson dynamics. Indeed, the very nature of supersolids, which are composed by a series of superfluid clusters interconnected by low density regions, realizes a Josephson junctions array where the barriers are not imposed externally, but comes only from the interaction within the system. The Josephson oscillation can be selectively excited using a phase imprinting technique, and observed in the experiment as coherent oscillations of both population imbalance and phase difference between neighboring clusters. Theoretically, I discuss how the prediction of Leggett's theory of the superfluid fraction, originally developed for rotating supersolid in annular geometry, can be mapped in the case of linear systems in presence of an imprinted phase twist. This way, I establish a connection between the superfluid fraction and the Josephson coupling energy of a single junction, which can be measured in the experiment. Our results agree with Leggett's predictions, demonstrating a new general method to measure the superfluid fraction of supersolid-like systems, which may be applicable also in other materials.

In the context of spinor condensates, I contributed to a preliminary investigation of novel topological excitations resulting from a quench across a phase transition connecting the polar phase to the easy-plane ferromagnetic phase in a spin-1 system. From numerical simulations there are strong evidences that during the out-of-equilibrium dynamics triggered by the quench, the chaotic evolution of the spinor phase would produce a peculiar topological excitation, the so-called instanton, which is characterized by a cusp divergence of the transverse magnetization in a precise spatio-temporal point of the system dynamics. These spacetime vortices, may be described as the consequence of the evolution of the spinor phase in an effective periodic potential which I contributed to characterize experimentally.

Ringraziamenti

Pensare alla strada percorsa in questi anni mi fa sentire principalmente molto fortunato. Si potrebbe dire che le persone di scienza non *credano* alla fortuna, ma la verità è che il più delle volte le circostanze fortuite, propiziate certo dall'esperienza e dalla logica, diventano una risorsa indispensabile tanto per la vita, quanto per la buona riuscita di un esperimento. Negli ultimi quattro anni, la mia fortuna è stata quella di incontrare persone eccezionali. Con alcune ci ho lavorato, altre mi hanno coltivato e fatto crescere, altre ancora sostenuto e curato.

Ringrazio per primo tutto il gruppo *disprosio*, che mi ha accolto e guidato, dandomi la possibilità di confrontarmi con bellissime sfide. Grazie a Giulio, compagno indubitabile, per aver alimentato ogni giorno la mia curiosità e avermi dimostrato il valore della tenacia. Grazie a Carlo, Luca e Andrea, i miei lab-guru, per avermi trasmesso quell'inestimabile sapere pratico che non si può né leggere né spiegare. Grazie a Niccolò, per averci messo tutto se stesso, sempre, dal primo giorno. Grazie a Luca, Charles, Giovanni e Pietro, per le belle discussioni degli ultimi mesi. Un ringraziamento speciale, infine, lo devo a Giovanni, per la cura e l'attenzione che ha verso il mondo e gli altri. La tua guida in questi anni è stata fondamentale.

I want to thank also the group which hosted me in Heidelberg. I would have never predicted that such a strong connection, both personal and scientific, could grow in so little time. Thanks to all the *matterwavers* and, in particular to Yannick, Stefan, David and Felix for dedicating so much time to me, inside and outside the lab. Thanks Helmut, for your friendship and the stimulating discussions. Thanks Markus, for giving me the possibility to join such a beautiful team and to challenge myself on a completely new project.

Grazie alla mia famiglia per avermi sempre sostenuto.

Grazie a Francesca, per camminare con me al nostro ritmo.

Al netto di tutti gli effetti, voi tuttə avete fatto la differenza.

Contents

List of publications

- Biagioni, G.*, **Antolini, N.***, Alaña, A., Modugno, M., Fioretti, A., Gabbanini, C., Tanzi, L. and Modugno, G. (2022). Dimensional crossover in the superfluid-supersolid quantum phase transition. Physical Review X, 12(2), 021019. `https://doi.org/10.1103/PhysRevX.12.021019`

- Alaña, A., **Antolini, N.**, Biagioni, G., Egusquiza, I. L., and Modugno, M. (2022). Crossing the superfluid-supersolid transition of an elongated dipolar condensate. Physical Review A, 106(4), 043313. `https://doi.org/10.1103/PhysRevA.106.043313`

- **Antolini, N.** (2022). Controlling the character of the superfluid-supersolid quantum phase transition. Il nuovo cimento C, 45(6), 1-4. `http://dx.doi.org/10.1393/ncc/i2022-22159-7`
  Best Communication award at SIF National Congress 2021

- Biagioni, G.*, **Antolini, N.***, Donelli, B., Pezzè, L., Smerzi, A., Fattori, M., Fioretti, A., Gabbanini, C., Inguscio, M., Tanzi, L. and Modugno, G. (2023). Measurement of the superfluid fraction of a supersolid by Josephson effect. Nature *in press.*

- Preti, N., **Antolini, N.**, Biagioni, G., Fioretti, A., Modugno, G., Tanzi, L., and Gabbanini, C. (2024). A blue repulsive potential for dysprosium Bose-Einstein condensates. arXiv preprint `https://doi.org/10.48550/arXiv.2403.18677`.

* *These authors contributed equally.*

Chapter 1
Introduction

Phase transitions are ubiquitous in nature and they play a fundamental role in the behavior of matter, as we experience it. These transformations, whether from solid to liquid, liquid to gas, or various other forms, are encountered in a myriad of natural phenomena. From the freezing and melting of water in the Earth's hydrological cycle to the transition of metals from solid to liquid in the heart of a star, phase transitions are central to understand the physical and chemical properties of our universe. They influence everything from the formation of crystals in minerals to the behavior of biological macromolecules in living organisms. In our daily lives, we experience typically classical phase transitions, which are driven primarily by thermal fluctuations and occur at well-defined temperatures. They can be described using classical thermodynamics and statistical mechanics [74]. This thesis primarily delves into a different type of phase transitions, dealing with the quantum behavior of matter, that takes place at very low temperatures, where the usual thermal effects aren't a significant factor. Quantum phase transitions [160, 97] are dominated by the quantum mechanical behavior of particles and, instead of temperature, they are driven by variations in other parameters entering the system Hamiltonian, thus modifying the ground state energy of the system. When the energy of the system changes, the ground state configuration changes, giving rise to a variety of different new quantum phases.

In the context of quantum phase transitions, ultracold quantum gases [47] are of great importance as they offer an ideal experimental platform for investigating these transitions at extremely low temperatures. These ultracold gases, typically achieved through techniques like laser cooling and evaporative cooling, allow the manipulation of the quantum behavior of particles to an unprecedented degree. By tuning parameters such as particle density and interaction strength, it is possible to explore and control the emergence of various quantum phases connected to the physics of superfluids and superconductors. In this perspective, extensive research has been done in the last twenty years on the quantum phases arising in ultracold gases in optical lattices [60, 127], which can be captured by the Bose-Hubbard model [79]. Here, the paradigmatic example is the quantum phase transition between the superfluid phase and insulating phases driven by interactions [59] or disorder [154]. The physics governing electrons in solids can instead be studied using fermions in the framework of the Fermi-Hubbard model [52, 11], which predicts many novel superconductive phases, such as pair-density wave phases [1], that may be connected to high-temperature superconductivity.

The topic of this thesis is the study of novel quantum phases associated to the symmetry breaking of continuous symmetries [58] in quantum gases experiments. Mainly, I investigated a new state of matter arising from the crystallization of a superfluid of magnetic atoms, the so-called *dipolar supersolid* [153], a counterintuitive state of matter that combines the properties of solids and superfluids. In the three years of my Ph.D. time, I worked in the group of Prof. Giovanni Modugno in Firenze and Pisa, on a dysprosium experiment which allow to observe the supersolid, studying the phase transition leading to this fascinating state of matter [15, 10, 3] and its superfluid response [16]. During my Ph.D. time, I also had the opportunity to join the group of Prof. Markus K. Oberthaler at the Kirchhoff Institut für Physik in Heidelberg, for a three month internship, where I worked ferromagnetic phases in spinor condensates [84]. Scratching the surface of this fascinating topic, I contributed to a preliminary study of topological excitations which can be observed during the out-of-equilibrium dynamics towards this magnetic quantum phase.

Until recently, the quantum many-body physics accessible in ultracold gases systems has been limited by the fact that atoms typically interact via short-range forces, changing their momentum or internal state during the collision. Indeed, a new item in the quantum gases toolbox was added a few years ago with the demonstration of strongly dipolar gases [114] based on magnetic atoms, where long-range dipole-dipole interactions compete with short-range physics. Other possible platforms to observe the effects of long-range interactions are based on polar molecules [188, 99], which develop a finite electric dipole in the ground state, and atoms confined in optical resonators [98], where infinite-range interactions are mediated by the cavity photons. Long-range interactions are predicted to lead to a variety of fundamentally new phenomena [43] such as exotic insulating phases in optical lattices [29, 12] or quantum state of matter stabilized by quantum fluctuations [137], like quantum droplets [167, 82, 28] and dipolar supersolids [181, 22, 42].

The mixed properties of supersolids come from the spontaneous breaking of two U(1) symmetries: the continuous translational symmetry [32] and the global phase symmetry [142]. Indeed, supersolids exhibit both a crystal-like order manifested as a periodic modulation of the wavefunction, and the phase order typical of superfluids, where particles share coherently the same macroscopic wavefunction. Originally proposed more than 50 years ago [61, 9, 38, 103], in the last decades supersolids have been the topic of strenuous search in a variety of quantum systems, ranging from solid helium [34] to superconducting Josephson junctions [6]. Historically, the first approach to supersolidity was to prove the presence of off-diagonal long-range order, associated to a superfluid behavior, in solids. In solid ^{4}He, the supersolid was proposed to emerge [9, 38] from the zero-point motion of defects in the crystalline structure that, at very low temperatures, should be able to condense (as actual bosonic particles). Changing the perspective, the opposite approach is to search for crystallization transitions in superfluid systems. Following this idea, supersolidity has been finally discovered in various cold atoms systems: atoms in optical cavities [106], spin-orbit coupled Bose-Einstein condensates [110, 151], and dipolar gases [181, 22, 42]. Differently from the case of solid helium, these are known as *cluster supersolids*, more similar to the idea of Gross [61], where not a single atom, but many particles sit in each lattice site of the supersolid, giving to the system a strong superfluid response.

Dipolar supersolids result from the crystallization of a Bose-Einstein condensate of strongly magnetic atoms, typically lanthanides, that feature long-range anisotropic dipole-dipole interactions. Similarly to ^{4}He, dipolar gases have an excitation spectrum which can host a maxon-roton structure [162], where a minimum at finite k gives rise to excitations of the superfluid wavefunction showing a spatial modulation. The energy of these excitations, called *rotons*, can be tuned in experiments [41], and eventually decreased until the point where a quantum phase transition occurs, and the density modulated phase becomes the new ground state of the system. This spontaneous breaking of the translational symmetry arise from the attractive part of dipole-dipole interactions, competing with the repulsive contact interactions and the kinetic energy to balance the total mean-field energy around zero. In this scenario, quantum fluctuations play an important role in stabilizing the supersolid phase, as their zero-point energy gives an additional repulsive contribution (the so-called *Lee-Huang-Yang correction*) [112] which prevents the system collapse [95, 27]. The resulting supersolid can be described as an ensemble of atomic clusters arranged in a lattice, connected by weak density links. The latter ensure a finite coupling between the clusters, leading to the global phase coherence of the supersolid. The peculiarity of dipolar supersolids is that the strength of the weak links can be tuned in experiments, going from systems with only a small density modulation to ones with very depleted links. When the clusters become totally disconnected we cross a second quantum phase transition, realizing a *droplets crystal*, an incoherent system where each cluster is *per se* a superfluid with fixed phase. The typical lattice spacing of dipolar supersolids (which is also connected to the roton wavelength) is fixed in practice by the harmonic oscillator length in the direction of the dipoles, associated to the harmonic confinement typically employed in experiments.

The character of the crystallization quantum phase transition leading to trapped dipolar supersolids was, until recently, a rather open question. Although this type of phase transition share some similarities with classical ones connected with other density modulated materials, such as the Rosensweig phase in ferrofluids [159] or the smectic phase in liquid crystals [32], an experimental study of trapped supersolids was lacking. In Chapter 2 I address this problem, discussing the character of the transition and its dependence on the supersolid lattice dimensionality [15, 10]. Remarkably, the behavior of the transition is related to the supersolid finite compressibility, which allow the deformation of the lattice structure in presence of an external confinement. Indeed, the dipolar supersolid is quite soft with respect to the other systems explored so far [106, 110]. As a function of the external confinement, the lattice dimensionality changes smoothly from 1D towards 2D, and the character of the transition follow this dimensional crossover, changing from continuous to discontinuous.

To describe the extraordinary properties of supersolids, Leggett introduced in the 1970s the concept of *superfluid fraction* f_s as a fundamental quantity which measures the superfluid response of the system. In his seminal paper [103], he linked the periodic modulation of the superfluid density in supersolids to a reduction of their superfluidity ($f_s < 1$), manifested by an increased moment of inertia experienced under rotation. A reduced superfluid fraction does not qualify a system as a supersolid [36, 184], but quantify its deviation from standard superfluids. So far, the experimental observations of supersolidity have been focused on other phenomena, such as the presence of Goldstone modes associated to the spontaneous breaking of two symmetries [192, 182, 63] or the non-classical rotational inertia [183], which demonstrated the superfluidity of dipolar supersolids. Nevertheless, a direct measurement of the superfluid fraction would be of fundamental importance, since f_s may be a key quantity also for other quantum phases showing a periodic modulated density. In Chapter 3, I discuss a new experimental method, based on the Josephson effect [80], to measure the superfluid fraction of a dipolar supersolid. Starting from Leggett's idea of superfluid fraction, we demonstrate that it is possible to extract f_s of a single lattice cell of a trapped supersolid, from the Josephson oscillations between adjacent clusters. Remarkably, this type of coherent dynamics peculiar to superconductors or superfluids separated by a barrier, is naturally present in a supersolid. Indeed, the couplings across the weak links of a supersolid are given only by the interactions, without any external potential, and they are naturally connected to the superfluid fraction.

In this perspective, the single cell of a dipolar supersolid also realizes a bosonic Josephson junction of a new type, where the position of the barrier is free to move. A theoretical description of such complex object is still lacking, and an experimental characterization of the fluctuations of the system would be an interesting direction to explore for both practical and fundamental reasons. Indeed, from the study of fluctuations in a finite temperature system, we may be able to establish a novel method for the system thermometry, based on the already existing models for standard *double-well* bosonic junctions [57]. Moreover, in the language of the Josephson effect we can also try to study the effects of quantum fluctuations beyond the mean-field corrections, like squeezing and entanglement creation [140].

The recent advancements in experimental techniques pushes the imagination also in new directions. In particular, the possibility to produce tailored optical potentials gives the opportunity to explore interesting geometries with dipolar atoms. For supersolids, probably the most fascinating geometry would be the annulus, which was in the focus of the original theories by Leggett [103]. Its natural connection with rotations, would make the annulus the perfect platform to study superfluid phenomena, like partially quantized supercurrents [185], in the supersolid. Moreover, the supersolid confined in a ring, sufficiently thin, realizes an ideal 1D system with boundary conditions, where it would be possible to study the excitations spectrum, for example, without perturbations and inhomogeneities induced by the finite size. I discuss the experimental steps towards the realization of such a system in Chapter 4, together with other techniques employed in our experiment.

While the physics of dipolar supersolids does not involve the spin degree of freedom of the particles composing the system, the rich internal structure of lanthanides can be used to realize synthetic dimensions [33, 199] or explore entanglement [163]. In general, spin physics can be studied in the context of quantum gases with spinor Bose-Einstein condensates, where bosonic particles are in a mixture of different spin states, and interact by standard and spin-changing collisions [84]. Detaching from the large spin case of lanthanides, the additional degree of freedom arising from spin interactions, has been explored typically with alkali atoms realizing spin-1 [177] and spin-2 [35] systems, or even with weakly dipolar atoms, like chromium [135], which lead to a spin-3 system. Besides the numerous magnetic quantum phases arising in such systems, spin-changing collisions also give rise to spin dynamics, when the system is brought out-of-equilibrium [176]. From the study of the time evolution of such systems towards a new equilibrium state, we can get intuition about general phenomena associated with universal scaling, even connected to cosmological models or nuclear collisions [148]. Moreover, during the dynamics many topological excitations, like exotic solitons [101, 55], emerge from spin interactions.

Focusing on spin-1 systems, a rather rich phase diagram can be explored as a function of the standard and spin-changing collisions strength. In ^{87}Rb, where collisions are repulsive and the spin coupling is ferromagnetic, we can study the quantum phase transition arising from the breaking of the full rotational symmetry of the spin orientation, given by spin-changing collisions [150]. The result of this transition is the so called *easy-plane ferromagnetic phase*, which is characterized from a finite magnetization in the x-y plane of the spin space, pointing in equally probable directions. In experiments, this quantum phase is typically reached by quenching the system interactions and follow the resulting out-of-equilibrium dynamics until the system settles in the new ground state. In Chapter 5, I focus on this particular topic, discussing preliminary results connected to the possible observation of exotic topological excitations emerging from the spin dynamics after such quench [172].

Chapter 2

The superfluid-supersolid quantum phase transition

In this chapter, I will focus on the quantum phase transition between a superfluid made of relatively strong magnetic atoms and the so-called dipolar supersolid. Besides the phenomenological description of the supersolid phase, which usually stems from the discussion of the competing mechanisms between short- and along-range interactions in dipolar quantum gases, here I will present a more general approach using the language of quantum phase transitions. Remarkably, the physics of dipolar supersolids is well captured by the Landau theory of phase transitions [97], even in the case of experimental systems with finite size and temperature. Many properties of both the ground state and excitations of the supersolid can be understood by looking at the character of the phase transition itself. Probably, the most intriguing question about the crystallization process leading to the supersolidity in quantum gases experiments is whether this quantum phase transition happens continuously or with a jump in the order parameter, since these two different characters would strongly affect the properties of the system, especially in experiments, where the transition from the superfluid to the supersolid is crossed in a finite time. On one hand, a continuous phase transition would be of interest for the possibility of smoothly tuning the order parameter in the supersolid phase, controlling the relative importance of the superfluid behavior over the crystal one. Moreover, almost excitations-free supersolids can be produced by adiabatically crossing a continuous phase transition in experiments, enabling the possibility to observe delicate phenomena, such as the quantum entanglement expected to rise from the interactions [119] or the formation of topological defects due to Kibble-Zurek mechanism [200, 46, 13]. On the other hand, discontinuous transitions are linked to more exotic crystal structures [131], usually in two dimensions, realizing an interesting platform to observe partially quantized vortices and their competition with the density modulation of the supersolid [56, 7]. The fast dynamics typically associated with discontinuous transitions also allow for engineering the supersolid formation process in experiments, for example exploiting *bang-bang* protocols [2].

Despite the rich literature regarding the superfluid-supersolid quantum phase transition, both theoretical models [144, 121, 168, 197, 198, 155, 18] and experimental observations [181, 22, 42], have not been conclusive in establishing the character of the transition, especially for confined systems. Here I address this problem, discussing the results of a recent experiment by our group [15, 10], where we found that the continuous or discontinuous character of the phase transition can be tuned in experiments, controlling the dimensionality of the crystal structure [1] .

A fundamental link between the supersolid lattice dimensionality and the behavior of the transition emerges clearly for infinite systems. The simplest theoretical models predicting the supersolidity employ bosons with *soft-core* interactions [44, 67, 111], and give important insights on the character of the transition. In analogy to classical [2] crystallization transition, these models predict either first-order transitions in two dimensions [144, 121], or second-order transitions in one dimension [168]. When dipolar interactions are taken into account, the landscape is far richer. The transition is predicted to be of first-order in two dimensions for both triangular and honeycomb lattices [197, 198] and, only for a critical value of the atomic density, we can have a second-order phase transition. This single point extends into a density interval when one-dimensional systems are considered [155, 18]. As I will discuss later in this chapter, the effect of the atomic density is understood as a competition between the kinetic energy and the zero-point energy of the quantum fluctuations [197], which have a crucial role in the stability of the supersolid [112].

---

[1] Note that, typically, the dimensionality of the supersolid structure is lower than the actual system dimensionality. For a three-dimensional system, the translational symmetry is spontaneously broken either along one or two directions.

[2] Here I use *classical*, referring to phase transition where the temperature is changed instead of a parameter of the system Hamiltonian.

This broad scenario gains another layer of complexity when actual experimental systems are considered. The precise control of the trapping confinement, typical of quantum gases experiments, gives the opportunity to change continuously from 1D to 2D the dimensionality of the supersolid lattice [143], which is ultimately not easy to define in the intermediate regimes. Besides the direct effect of the trapping potential which gives the system a finite size, the shape of the atomic cloud is modified by the interactions [178], favoring configurations elongated along the dipoles for stronger dipolar interactions. Moreover, the harmonic confinement also leads to an inhomogeneous density in experimental systems, producing the coexistence of the supersolid in the bulk of the cloud, where the density is high enough to allow for the phase transition to happen [181], with superfluid tails in lower density regions. Despite all these challenges, this quantum phase transition has been explored in experiments realizing quasi-one-dimensional supersolids, where the lattice structure consists of a single row of density clusters arranged along the weak axis of the harmonic trap. In the following chapter, I will refer to this kind of supersolid structure as *single-row* supersolid, to avoid misunderstandings with the actual dimensionality of the system. Experimentally, supersolids with a two-dimensional lattice structure have been so far realized only by crossing a classical phase transition, namely by reducing the temperature of the gas and passing from a thermal cloud directly to a supersolid. The so-called *evaporation* of the supersolid [174], would not be the object of this chapter.

Coming back to the quantum phase transition, numerical simulations for trapped 2D supersolids predict a discontinuous character [70, 19]. On the other hand, single-row supersolids have been the object of intensive experimental studies reporting only partial insights about the character of the transition. By looking at the behavior of experimental observables when the transition is crossed, it can be argued that in some cases it has to be either discontinuous [181, 22, 182], or continuous [139], while in some other observations, the character of the transition remained not assessed [69]. In the work by our group [15, 10], we solve this complex puzzle, demonstrating that is possible to observe both types of quantum phase transitions, leading to supersolids with different dynamical properties. By controlling the external harmonic confinement, the character of the transition changes smoothly from continuous to discontinuous as the dimensionality of the supersolid lattice changes from strictly 1D towards the 2D configuration. This behavior is reminiscent of the second- and first-order phase transition taking place in 1D and 2D respectively in the thermodynamic limit.

The most important novelty, with respect to other crystallized phases, is that the supersolid is not infinitely rigid, but its structure can be deformed across this dimensional crossover, to adjust the crystalline structure to the external confinement. Indeed, the discontinuous transition typical of 2D materials exists in the supersolid even in the single-row regime, where the two-dimensional behavior is maintained by the superfluid density background. The different effective dimensionality of the single-row supersolids featuring continuous or discontinuous phase transitions is even clearer if we look at their dynamics [3]. Indeed, when the translational symmetry is broken along a certain direction, we can assume that the lack of adiabaticity would trigger an oscillation in the harmonic trap. In the case of discontinuous transitions, we observe excitations along two directions, perpendicular to the dipoles, meaning that the system responds as a material with a 2D structure. On the other hand, for continuous transitions, we observe dynamics only along the direction of the clusters, as expected for a one-dimensional system.

2.1 The crystallization of a superfluid

Let's start considering Fig. 2.1, depicting both the superfluid and supersolid density distributions, obtained by numerical simulations, for our experimental conditions. We can think of each atom as a magnetic dipole aligned in the $\hat{z}$ direction by a magnetic field $\boldsymbol{B}$, and confined in the three spatial directions by an anisotropic harmonic potential, elongated in the $\hat{x}$ direction. For clarity, I will refer to this direction as *longitudinal.* Once the superfluid-supersolid transition is crossed, a density modulation grows within the system: the clusters develop thanks to the attractive part of dipole-dipole interaction, and extend in the magnetic field direction, maintaining from one another a fixed distance λ along the longitudinal direction, forming a crystalline structure. The lattice spacing λ of the supersolid is connected to the harmonic length in the $\boldsymbol{B}$ field direction, approximated by $\ell_z = \sqrt{\hbar/2\pi m\nu_z}$. This

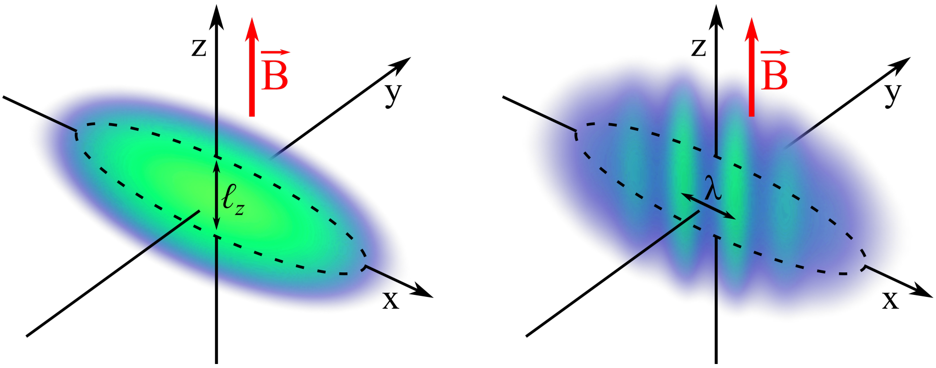

Figure 2.1: Density distributions of a trapped superfluid (left) and a supersolid in a single-row arrangement (right) for typical experimental parameters. The atomic magnetic dipoles align along the z direction due to the presence of the magnetic field B. The significant length scales are the vertical harmonic confinement length ℓ_z and the lattice spacing of the supersolid λ.

spacing is in close proximity to the wavelength of the roton excitation mode of the superfluid [162, 41].

The system is formally described in terms of the extended Gross-Pitaevskii Equation (eGPE) [137], which includes in the standard Hamiltonian the Lee-Huang-Yang correction [112], namely the zero-point energy of quantum fluctuations arising from both contact interactions (collisions) [3] and dipole-dipole interactions. Considering a fully condensate system with superfluid density $\rho(\boldsymbol{r}) = |\psi(\boldsymbol{r})|^2$, the energy functional is

$$E = E_{kin} + E_{trap} + E_{cont} + E_{dd} + E_{LHY}, \tag{2.1}$$

with

$$\begin{aligned}
E_{kin} &= \int \frac{\hbar^2}{2m} |\nabla\psi(\boldsymbol{r})|^2 \mathrm{d}\boldsymbol{r}\,, \\
E_{trap} &= \int V_{trap}(\boldsymbol{r})\rho(\boldsymbol{r})\mathrm{d}\boldsymbol{r}\,, \\
E_{cont} &= \int \frac{g}{2}\rho^2(\boldsymbol{r})\mathrm{d}\boldsymbol{r}\,, \\
E_{dd} &= \frac{C_{dd}}{2} \iint \rho(\boldsymbol{r})V_{dd}(\boldsymbol{r}-\boldsymbol{r}')\rho(\boldsymbol{r}')\mathrm{d}\boldsymbol{r}\mathrm{d}\boldsymbol{r}'\,, \\
E_{LHY} &= g_{lhy} \int \rho^{5/2}(\boldsymbol{r})\mathrm{d}\boldsymbol{r}\,.
\end{aligned} \tag{2.2}$$

---

[3] The short-range *van der Waals* interactions among atoms are treated using a zero-range pseudopotential and described as contact interactions.

The first terms take into account the local mean-field contributions: the kinetic energy, the harmonic confinement $V_{trap}(\boldsymbol{r}) = \frac{m}{2}\sum_{j=x,y,z}\omega_j^2 r_j^2$, the contact interactions, with strength $g = 4\pi\hbar^2 a_s/m$, where a_s is the scattering length describing the collision among dysprosium atoms. Unlike such collisions, the dipolar term is non-local given the long-range nature of the dipole-dipole potential $V_{dd}(\boldsymbol{r}) = (1 - 3\cos^2\theta)/(4\pi r^3)$ describing the interaction of two dipoles at a distance r, with an angle θ between the vector $\boldsymbol{r}$ and the dipole axis[4] [158]. Indeed, E_{dd} depends on the integral of the atomic density, and it's proportional to the dipolar strength $C_{dd} \equiv \mu_0\mu^2$, with μ the modulus of the magnetic dipole moment $\boldsymbol{\mu}$. The beyond-mean-field correction E_{LHY} in the local-density approximation [112] has the same dependence on the atomic density for both contact and dipolar interactions, with a coefficient $g_{LHY} = \frac{256\sqrt{\pi}}{15}\frac{\hbar^2 a_s^{5/2}}{m}\left(1 + \frac{3}{2}\epsilon_{dd}^2\right)$ [190], representing the sum of the two contributions. The control parameter of the phase transition is

$$\epsilon_{dd} = \mu_0\mu^2 N/(3g) = a_{dd}/a_s \tag{2.3}$$

describing the strength of dipolar interactions relative to the contact ones. This quantity is changed during the experimental sequence to pass from the superfluid phase to the supersolid by controlling a_s exploiting a Feshbach resonance [39]. The right-hand side of Eq. 2.3 also defines the so-called *dipolar length* a_{dd}, which plays the role of an effective scattering length for dipolar interactions[5].

The transition from a superfluid to a supersolid state occurs as we decrease the repulsive scattering length a_s, thus increasing ϵ_{dd}. Within the supersolid phase, the dipolar energy diminishes as a result of a more pronounced head-to-tail alignment of dipoles within each cluster. However, this phase is characterized by an increase in both contact energy (stemming from the increasing peak density) and kinetic energy (given by the density modulation). When the dipolar energetic gain outweighs the costs associated with contact and kinetic terms, the transition takes place. Without beyond-mean-field contributions, the supersolid state exhibits instability as the dipolar energy decreases with increasing density. Indeed, when the repulsive part of the interactions

---

[4] Here we define $\cos\theta = \boldsymbol{\mu}\cdot r/(\mu r)$.

[5] Note that the long-ranged nature of dipole-dipole interactions makes impossible to expand the potential in a finite number of partial waves [96], therefore we cannot define a pseudopotential with a simple form [75] as in the case of standard collisions.

is too low, the attractive part of dipolar interaction leads to the collapse of the system [95]. This is averted by the repulsive Lee-Huang-Yang (LHY) energy term, which prevents the density from increasing indefinitely. Remarkably, this stabilization mechanism is based on the sole contribution of quantum fluctuations, which is tiny if compared to the other terms in Eq. 2.1, but still plays a huge role when the sum of the mean-field energies is close to zero. As we decrease the scattering length further, the system undergoes a subsequent phase transition towards a droplet crystal state [181]. In this phase, the superfluid background vanishes with the coherence between clusters [181, 22, 42], and the system is no longer superfluid[6]. In this chapter, I won't discuss this incoherent phase and I will focus only on the supersolid.

2.1.1 Formation of infinite dipolar supersolids

To gain a deeper understanding of the physics underlying the supersolid phase transition, I will start by considering the infinite scenario, where confinement in the $x - y$ plane is removed, focusing on a dipolar quantum gas at zero temperature ($T = 0$). Typically, the fundamental characteristics of a phase transition are described by Landau theory [97]. This theory links the the system's ground state features on how the free energy behaves as a function of the order parameter. In the context of crystallization phase transitions, the order parameter is often denoted as the contrast C of the density modulation. This parameter is zero in phases resembling liquids and takes a non-zero value in phases resembling crystals. To extract the behavior of the free energy, we have to know its dependence on the contrast, and then expand in powers of C as

$$E \simeq E_0 + \ a\, C + b\, C^2 + c\, C^3 + d\, C^4 + \dots, \tag{2.4}$$

where E_0 is the energy for a homogeneous state with $C = 0$. Note that even in the presence of a trap, where the density is given by a Thomas-Fermi profile, we can still define a contrast, by looking at the amplitude of the modulation in the inhomogeneous atomic density. However, I will refer to the $C = 0$ state sill as *homogeneous*, since a finite contrast can only arise from interactions and does not depend

---

[6] As I will discuss in Chapter 3, the energy cost of phase fluctuations between neighbouring cluster vanishes for vanishing density overlaps, destroying the overall phase-coherence of the system. The same does not happen inside the bulk of each cluster, which remains fully superfluid even in the droplets crystal phase.

on the cloud shape, mainly affected by the trapping potential. From the values of the coefficients a, b, c, d we can determine the character of the phase transition by looking at the structure of the free energy $E\left(C\right)$. For infinite systems, the a coefficient is zero and the linear term is neglected. However, this is not the case for trapped systems, as I will discuss in the next section, where the confining potential introduces an energy cost to accumulate density away from the trap center.

To find $E\left(C\right)$ we use the following ansatz for the supersolids density $\rho\left(\boldsymbol{r}\right)$. Near the transition point ($C \ll 1$) the spatial dependence of $\rho\left(\boldsymbol{r}\right)$ can be approximated by a sinusoidal modulation on top of the average density ρ_0 [144, 197, 18]:

$$\rho(\boldsymbol{r}) = \rho_0\Big[1 + C\sum_i \cos(\boldsymbol{k}_i\cdot\boldsymbol{r})\Big], \tag{2.5}$$

where $\boldsymbol{k}_i$ are the lattice vectors defining the supersolid structure. To get an intuitive explanation of why 1D and 2D systems feature continuous and discontinuous transition respectively, we can have a look at the symmetry of the different ground states. In particular, I want to discuss the symmetry associated with the change of sign of the contrast C.

One-dimensional supersolids

When the transformation $C \to -C$ is applied to one-dimensional supersolids, we are basically shifting by one lattice constant the density modulation along the direction of the single $\boldsymbol{k}$ vector describing the supersolid structure. This overall displacement doesn't cost any energy, therefore the 1D supersolid is symmetric under this transformation, and the free energy in Eq. 2.4 must be an even function of C, meaning that the odd coefficients in the expansion must vanish. The character of the transition is then mainly affected by even coefficients. Taking the ansatz $\rho(x) = \rho_0\Big[1 + C\cos(kx)\Big]$ to calculate the energy in Eq. 2.1, and then expanding in powers of C, we find

$$\begin{aligned} d_{1D} &= \frac{\hbar^2\pi}{32m}k\rho_0 - \frac{15\pi g_{lhy}}{512k}\rho_0^{5/2}, \\ f_{1D} &= \frac{\hbar^2\pi}{64m}k\rho_0 - \frac{25\pi g_{lhy}}{8192k}\rho_0^{5/2}, \end{aligned} \tag{2.6}$$

being respectively the fourth- and sixth-order coefficients. Depending on the square of the density, the interactions contribute only to the quadratic term, which changes sign from positive to negative when the scattering length a_s is decreased to cross the transition. The fourth- and sixth-order coefficients are instead given by the interplay between the kinetic and the LHY energy terms, which at the typical experimental densities gives a positive contribution. When the scattering length is lowered to cross the phase transition, the negative contribution from the quadratic term starts to dig a minimum in the free energy at $C \neq 0$. Therefore, the system smoothly develops a finite contrast and the transition is of the second order, as depicted in Fig. 2.2a. In this case, we neglect the effect of the sixth-order term, since the continuous character of the transition is captured just by the quadratic and quartic terms.

Two-dimensional supersolids

Supersolids with a two-dimensional structure [144] show instead a triangular lattice with wave-vectors of equal length satisfying $\boldsymbol{k}_1 + \boldsymbol{k}_2 + \boldsymbol{k}_3 = 0$. Just looking at the insets of Fig. 2.2b, it is clear that in this scenario the $C \to -C$ symmetry is broken: indeed when the sign of the contrast is negative we end up with a honeycomb lattice (where density minima form now a triangular structure) which is not equivalent to starting one. The energy of these two configurations must then be different, meaning that the free energy is an odd function of C. The full calculation of the Landau energy with a sinusoidal ansatz of the form Eq. (2.5) was reported in [197]. In particular, the most important term in the expansion 2.4 is the cubic one. This is again affected by the interplay between kinetic and LHY energies, and at relatively low densities gives a negative contribution. The result is that the free energy develops a barrier at finite C, with a minimum at large positive contrasts which starts to form lowering the scattering lengths a_s. When this minimum touches zero, we have two degenerate ground states, but the systems need to overcome the barrier energy in order to jump to the modulated state. This scenario is typical of second-order phase transitions, resulting in a finite jump of the contrast at the transition point.

High densities: quantum fluctuations effects

In general, at high densities (very far from the experimental possibilities), the contribution of the LHY energy which scales as $\rho^{5/2}$, dominates

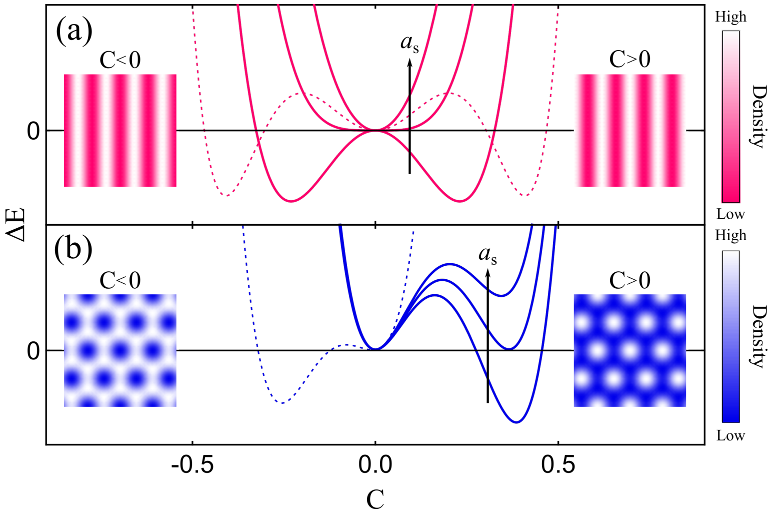

Figure 2.2: Landau theory of the superfluid-supersolid quantum phase transition in the thermodynamic limit. Scenarios for second-order phase transitions in 1D (a) and first-order phase transitions in 2D (b). Solid lines are the typical behavior of the free energy as a function of the order parameter C for varying scattering lengths. Dashed lines are examples of the free energy in the LHY-dominated regime. Insets show the lattice structure.

on the kinetic term, which is linear in ρ. This obviously has an impact on the previous analysis for both 1D and 2D cases. Curiously, in the 2D case, the sign of the cubic term is reversed and the ground state is now at negative contrast, where the honeycomb structure is favored. In [197], they also show the possibility of tuning exactly the density of the system to have a continuous phase transition in 2D. This comes again from the relative importance of the different terms in the expansion, but it's not relevant for the experiments, where finite density fluctuations due to technical noise produce always discontinuous transitions in 2D. To complete the picture, it is also shown in Fig. 2.2a a possible discontinuous phase transition in 1D. Indeed, when the density is high enough the fourth order term in the expansion change sign, becoming negative. To find a minimum in the free energy, we then need to reach the sixth order of the expansion which gives a positive contribution. Lowering the scattering length, we then have a double minimum shape of the free energy, with a barrier given by the quartic term. The latter is dominated by LHY energy, so the resulting discontinuous transition can be placed in the class of fluctuation-induced first-order phase transitions governed by quantum fluctuations, as the ones in superconductors and liquid crystals [65]. The presence of a discontinuous transition in quasi-1D systems at high densities was also revealed by numerical simulations in [18].

2.1.2 Landau model for a trapped system

The effects of the trap on the character of the transition can be appreciated by analyzing the case of one-dimensional systems. Adjusting our density assumption to

$$\rho(x) = \rho_0 g(x) \left[1 + C\cos(kx)\right], \tag{2.7}$$

the simple 1D model previously discussed can be indeed expanded to account for the trap's influence. Here, $g(x)$ represents a normalized Gaussian envelope with width σ, which breaks the symmetry in the contrast's sign, causing slight differences between the density distributions with C and $-C$ respectively. Indeed, the main maximum and the central minimum shift within the trap introduce odd terms into the Landau energy. [7] Specifically, since the trap energy scales linearly with the density, it introduces a linear term in the energy, meaning that a state with a positive contrast ($C > 0$) is energetically favored in terms of trap energy, with respect to a fully superfluid state ($C = 0$). This is due to the fact that by increasing the density at the trap center and establishing lateral minima where the trap potential is most pronounced, the system actually reduces its energy. Recognizing the presence of a trap-induced linear term in the Landau energy provides a plausible explanation for some of the effects we observe in numerical simulations, such as the mixing of continuous and discontinuous behaviors across the phase transition. Particularly, in configurations where the transition is discontinuous, the linear term tends to drive a continuous transition towards states with minimal contrast, subsequently jumping towards the second minimum at a higher contrast.

To capture the change of dimensionality of the lattice structure, as a function of the transverse confinement, the model assumes a 2D geometry with triangular structure, giving the opportunity to evaluate the effect of the trapping potential on the shape of the free energy. A

---

[7] The relative importance of odd terms with respect to even ones, grows for decreasing $k\sigma$, remaining below 10% in the regime relevant for the experiment. At large $k\sigma$ odd terms vanish.

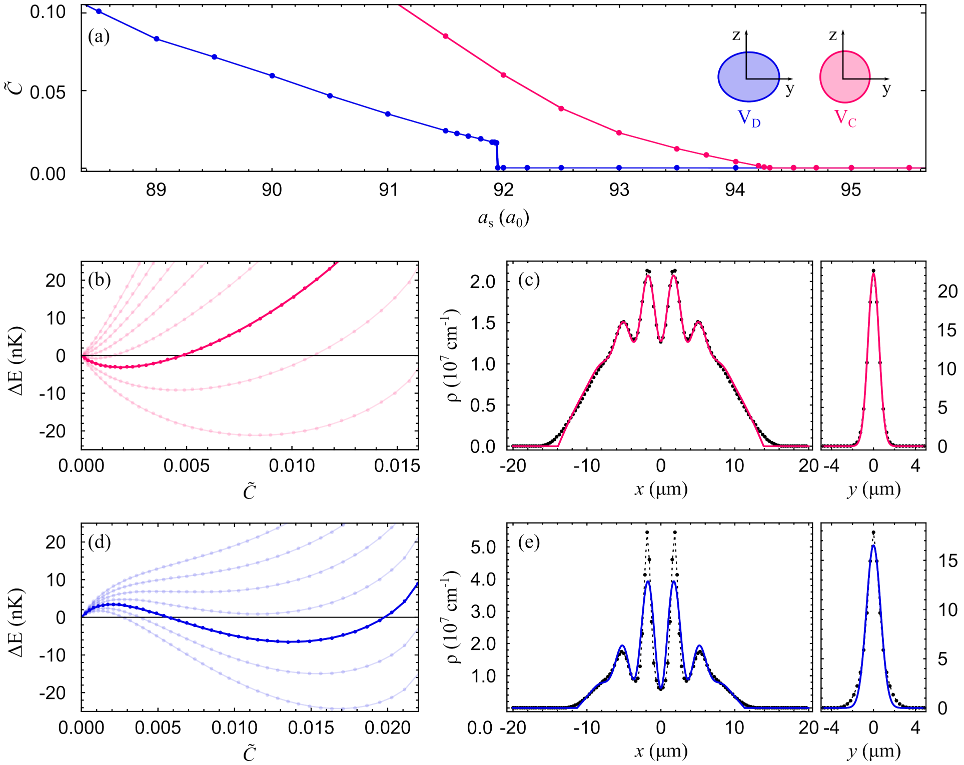

Figure 2.3: Landau free energy calculated with the ansatz 2.8 adjusted to two different trapping configuration featuring continuous or discontinuous transitions. (a) Contrast as a function of the scattering length, for two elongated traps with different transverse confinement. These results are extracted from eGPE numerical simulations of $N = 30 \times 10^3$ ^{162}Dy atoms, employing harmonic traps with frequencies $(15, 100, 94)$ Hz for V_C and $(20, 67, 102)$ Hz for V_D. (c,d) show the Landau free energy from 2.1, for different scattering lengths. Colored lines highlight the single- or double-minima shape of the free energy once the transition is crossed. The contrast is measured by $\tilde{C}$, analogous to C, but measured after a time of flight expansion (substituted in the theory by a Fourier transform). (d,e) are the ground state density profiles along $\hat{x}$ and $\hat{y}$. Black dots are the results of numerical simulations. Colored lines show the trapped model. All the parameters are set to realistic values, minimizing the differences from the simulated densities: (d) $R_x = 8.1\lambda_x$, $\sigma_y = 0.64\lambda_y$, $R_z = 4.9\lambda_z$, $w_x = 2.1\lambda_x$, $\lambda = 1.6\lambda_x$; (e) $R_x = 5.6\lambda_x$, $\sigma_y = 0.46\lambda_y$, $R_z = 5.1\lambda_z$, $w_x = 1.9\lambda_x$.

better resemblance with the experimental configuration can be obtained, instead of using simple Gaussian envelopes in the transverse directions, by modifying the ansatz 2.5 into

$$\rho(\mathbf{r}) = A\left[1 + Ce^{-x^2/2w_x^2}\sum_i \cos(\mathbf{k}_i \cdot \mathbf{r}_0)\left(1 - \frac{x^2}{R_x^2}\right)e^{-y^2/2\sigma_y^2}\left(1 - \frac{z^2}{R_z^2}\right)\right], \tag{2.8}$$

adding a Thomas-Fermi envelope of radius R_x (R_z) in the x (z) direction. The k vectors describing the triangular lattice are

$$\begin{aligned} \mathbf{k}_1 &= 2\pi/\lambda(0,1,0), \\ \mathbf{k}_2 &= -2\pi/\lambda(\sqrt{3}/2,1/2,0), \\ \mathbf{k}_3 &= 2\pi/\lambda(\sqrt{3}/2,-1/2,0), \end{aligned} \tag{2.9}$$

with $\sqrt{3}\lambda$ being the lattice period, $\mathbf{r}_0 = (x - \sqrt{3}\lambda/2, y, 0)$, and A a normalization constant. Another difference from the ansatz 2.5, is that here the sinusoidal modulation has a Gaussian weight with width w_x, such that the superfluid tails of the system are taken into account. The free energy is calculated by integrating the energy functional in Eq. 2.1 with this ansatz, keeping C a free parameter. The other parameters are set by direct comparison of the model 2.8 with numerical simulation of the ground state density. The latter are carried out with direct inputs from the experiment. The results are shown in Fig. 2.3 for two different experimental configurations featuring continuous or discontinuous transitions. This behavior is connected to a single- or double-minima structure of the free energy, Fig. 2.3b,d, when the scattering length is decreased. Note that both the associated supersolid density distributions don't show an evident structure in the transverse direction, demonstrating that the two types of phase transitions can occur for single-row supersolids, for different transverse trapping configurations.

2.1.3 Dimensional crossover

In the previous section, we've seen that even if the concepts of first- and second-order phase transitions must be abandoned in the context of finite-sized systems, the underlying physics governing the crystallization in the thermodynamic limit survives in this regime. Although the transverse confinement is strong enough to suppress almost completely the 2D structure of the supersolid lattice, a discontinuous phase transition persists in single-row systems [181, 22, 182]. The reason why this happens is not straightforward if we think about standard crystals and crystallization processes. Let's consider the formation of an ideal crystal with infinite rigidity and, starting from a 2D system featuring a first-order phase transition, imagine reducing its size in one direction. Once we reach a width comparable to the lattice constant of the crystal, the system can no longer sustain a two-dimensional structure, and the crystallization transition becomes second-order. The fact that in supersolids a regime of discontinuous transitions exists in single-row systems, must be then linked to a finite rigidity. Indeed, the supersolid structure is deformable. Macroscopic distortions of the supersolid lattice without loss of coherence can be observed in experiments [182], arising from excitations described as collective modes of the *solid* part of the system. The idea is that the supersolid ground state can adapt its lattice structure to match external confinements in order to minimize its energy. When the transverse width of the system approaches the lattice constant, the competition between continuous and discontinuous transitions leads to a dimensional crossover, with the supersolid structure changing continuously from 2D to 1D, over a broad region of experimental parameters.

Although the model discussed above give precious insights into the origin of this dimensional crossover, it cannot be used to draw quantitative prediction about the character of the transition for different experimental parameters. Indeed, the Landau model for trapped systems, developed to understand the effects of the trap with respect to the infinite case, assumes the supersolid structure to be fixed, namely keeping the wave-vectors fixed in the Eq. 2.8. As a matter of fact, the deformation of the lattice across the crossover can be studied with the help of numerical simulations of the ground state density. In particular, we explore the dimensional crossover by monitoring the character of the transition for changing atom number and transverse confinement. To compare similar systems, the vertical confinement, which eventually determines the length scale of the supersolid structure, and the longitudinal one are kept fixed. For similarities with the harmonic confinement used in experiments, (ν_x, ν_z) are set to $(20, 80)\,\mathrm{Hz}$ respectively. The number of atoms spans a broad region: at the lower bound $N < 5 \times 10^3$, the average density is low enough in the trap that the supersolid phase consists of a single cluster with long superfluid lateral tails; in the opposite boundary $N > 10 \times 10^4$, well above the possibilities of current experiments employing ^{162}Dy[8], we enter the regime of high densities discussed in the previous section. I will focus on the region between these two boundaries, where the crossover takes place.

Analysis of the supersolid ground state

Numerically, we minimize the energy functional $E[\psi]$ in Eq. 2.1 using a conjugate algorithm [145, 126, 158], leading to the ground state of the system. After being mapped in the Fourier space, the contribute of dipolar interaction E_{dd} in Eqs. 2.2 is calculated using fast Fourier transform algorithms. The numerical code has been provided by Prof. Michele Modugno and coworkers, and I used it to simulate most of the data in this chapter. Varying the system parameters, we extract from each simulation the contrast $\tilde{C}$ of the density modulation, as the height of the Fourier peak at $k_{SS} = 2\pi/\lambda$ associated to the supersolid spacing. As we will see in the next section, this choice is motivated by the presence of a related experimental observable. To obtain $\tilde{C}$ from the ground state density distributions, we start integrating the column density distribution along $\hat{y}$, in order to obtain a one-dimensional profile

$$\rho(x) = \int \mathrm{d}y \, \rho(x, y) = \int \mathrm{d}y \int \mathrm{d}z \, \sqrt{|\psi(x, y, z)|^2}, \qquad (2.10)$$

as shown in Fig. 2.3c,e; then the Fourier transform $|\mathcal{F}[\sqrt{\rho(x)}]|^2$ is calculated. The order parameter $\tilde{C}$ is simply given by the relative height of the first lateral peak with respect to the central one. In the 1D infinite case discussed in Sec. 2.1.2, $\tilde{C} = C^2/16$ in the limit of small contrasts $C \ll 1$. This relation can be proved by Fourier transforming the ansatz 2.7, and looking at the coefficient multiplying the Dirac delta $\delta(k - k_{SS})$.

As I will discuss later in this section, another important parameter to understand the nature of the crossover is the transverse width of the system σ_y. In general, this width changes with the interactions, rapidly decreasing when we cross the phase transition from the superfluid to

---

[8] Note that the atom number in the supersolid phase drops from the typical number, around 5×10^4, in the superfluid phase due to the effect of inelastic collisions enhanced by the increased density in the clusters. In our experiment, we usually realize supersolids with $N = 3 \times 10^4$.

the supersolid. This happens because when the supersolid lattice forms, the density in the atomic cloud gets concentrated in the clusters, thus increasing the width along $\hat{z}$. In the longitudinal direction, instead, the system size depends strongly on the number of clusters in the supersolid lattice, which is clearly dependent on the atom number. An analogous argument is applied for other interesting parameters that describe the supersolid structure at the transition, such as the peak density and the shape of the clusters. To define a quantitative parameter for the transverse size, we choose to analyze the atomic density at the transition point, where $\tilde{C}$ is still very small[9], and the transverse profile $\rho(y)$ (defined similarly to Eq. 2.10) is well described by a Gaussian envelope, therefore we define σ_y as its Gaussian width. The peak density, which gives important information about the role of LHY energy term, is simply extracted from the linear density in Eq. 2.10. Instead, to study the deformation of the clusters, we need to analyze the two-dimensional density $\rho(x, y, 0)$ (which is different from the integrated one, defined in the right-hand side of Eq. 2.10. First, the position of one of the central clusters is found, looking for the maximum density. Then, we define the deformation parameter

$$\beta_{ss} = \langle x^2 - y^2 \rangle / \langle x^2 + y^2 \rangle \tag{2.11}$$

in a smaller spatial window including only the chosen cluster, canceling the contribution of the background density with a threshold filter. Circular clusters have $\beta_{ss} = 0$, while clusters elongated along $\hat{x}$ ($\hat{y}$) have positive (negative) deformations.

Visualizing the dimensional crossover

For each set of parameters, we vary the scattering length a_s, finding the ground state of the system minimizing the energy in Eq. 2.1, and observing the behavior of the transition. The results are reported in Fig. 2.4, which can be considered as a map of the different types of superfluid-supersolid quantum phase transitions. In particular, this study is focused on the blue and magenta regions in Fig. 2.4a, where we find single-row supersolids showing discontinuous and continuous transitions respectively. Being a map, the interesting feature is obviously the *border* between these two regions. In Fig. 2.4b, the evolution of

---

[9] This analysis is performed for the transition at the boundary between the continuous and discontinuous regime, therefore they exhibit a very small jump in $\tilde{C}$.

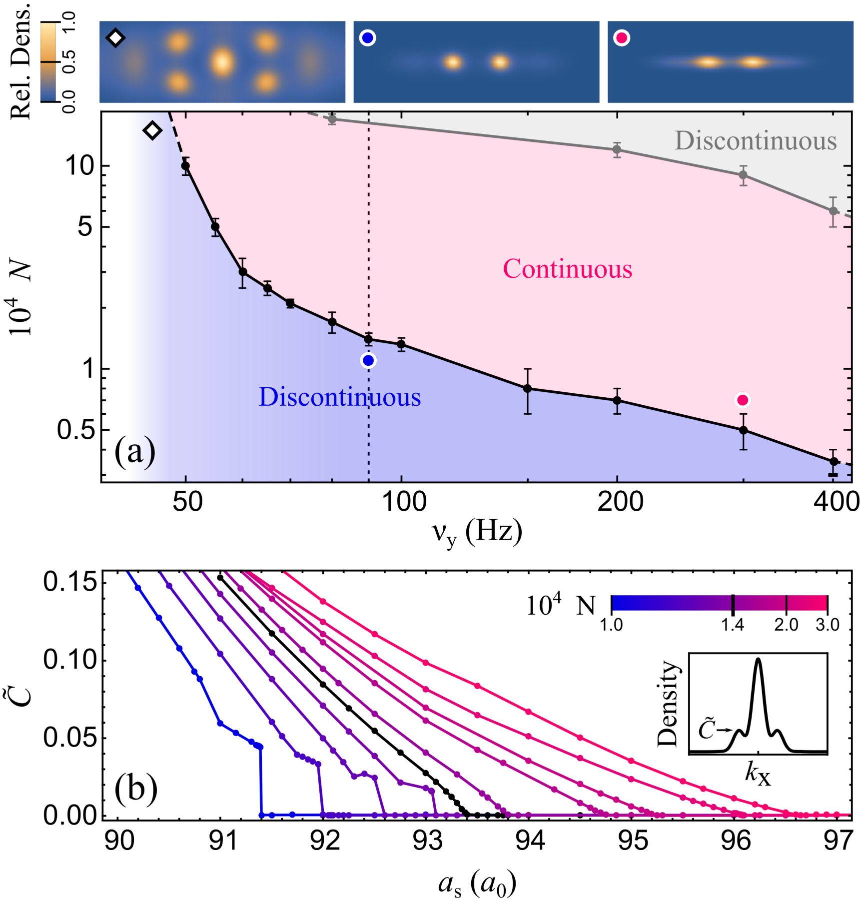

Figure 2.4: Character of the superfluid-supersolid quantum phase transition, extracted from numerical simulations of our system. (a) Map of the different phase transitions as a function of the atom number N and the transverse trap frequency ν_y. The black boundary between the continuous and the discontinuous regions is traced by finely sampling N for each investigated ν_y. The black dots at the boundary represents the *critical* N separating the two regimes. A second crossover from continuous to discontinuous at large ν_y and N is marked by the gray dots. The gray shaded region represents the LHY-dominated regime, where, as an effect of the density inhomogeneity, the supersolid forms initially in a continuous manner in the low density regions (typically the tails of the distribution) and only afterwords the contrast jump at high values in the high density regions (center of the distribution). The white region at very low ν_y marks true two-dimensional regime, where the supersolid shows more than one row of density maxima. In the upper panels are shown three different samples of the column density in the supersolid phase. From right to left: one-row continuous (magenta circle), one-row discontinuous (blue circle), and two-rows (white diamond). (b) Behavior of the order parameter as a function of the scattering length a_s across the dimensional crossover. Each color corresponds to a different N, with $\nu_y = 90\,\text{Hz}$. The center of the crossover is plotted in black. The inset shows the typical momentum distribution of the supersolid, and the definition of the contrast $\tilde{C}$.

the contrast in the system ground state as a function of a_s is shown for a set of different atom numbers at fixed transverse confinement $\nu_y = 90\,\mathrm{Hz}$. Starting from low N, where the transition is strongly discontinuous, the decreasing jump in the contrast at the transition point for increasing N is mapped in shades of color, going toward the continuous side of the crossover. The black points represent the first transition which is almost continuous, i.e the jump in the contrast is not visible (it's smaller than 0.001) with the resolution in a_s steps employed for numerical simulations. This boundary depends in a curious way on the atom number and transverse confinement. Indeed, the region of discontinuous transitions at low atom numbers is more pronounced for weaker confinements, up to the point where ν_y is so small to actually enter the regime of supersolids with more than one row of clusters. For larger confinements, the discontinuous region is more and more suppressed, until basically the phase transition is always continuous and we reach the 1D regime. As shown in the insets of Fig. 2.4a, the inhomogeneity of the density given by the trap leads to a coexistence of a supersolid phase, which is formed in the central region of the harmonic potential, where the density is high enough for the transition to take place, and a superfluid phase in the outer regions. The properties of the system are however dominated by the supersolid part.

Origin of the crossover

While the majority of the phase diagram suggests the development of supersolidity characterized by a single row of density maxima, a Fourier analysis uncovers a density background with a two-dimensional structure. In particular, assuming the lattice structure to be triangular in real space, we expect the Fourier space to show a hexagonal pattern. To reveal such a pattern, we analyzed the Fourier transform of the ground state densities looking along the transverse direction, slightly off from the $k_x = 0$ line, as presented in Fig. 2.5. Formally we evaluate the quantity

$$T(k_y) = \mathcal{F}[\rho(x,y)](k_x = k_x', k_y), \tag{2.12}$$

where k_x' is chosen to maximize the amplitude of the signal A_y. This amplitude clearly decreases the more the lateral clusters along the transverse direction are suppressed. Nevertheless, $T(k_y)$ presents a non-vanishing structure even in the case of single-row supersolids.

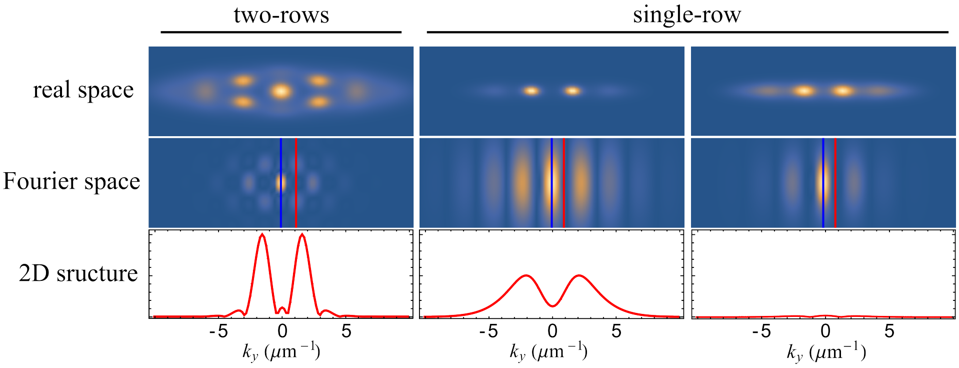

Figure 2.5: Detection of the triangular structure of trapped supersolids, via Fourier analysis. The upper panels show the real space density distribution for three different supersolid ground states showing an actual 2D structure (left) and a single-row of clusters (right). The panels in the center show the same density distributions in the Fourier space. Vertical lines mark $k_x = 0$ (blue) and k_x' (red) along which we expect to find transverse peaks in the Fourier signal. The lower panels show such a signal, normalized to the two-rows case.

We performed the same analysis to probe the role of the triangular structure in the crossover, finding that it has a direct connection with the change of nature of the phase transition. Indeed, when the structure is strongly suppressed, the character of the transition changes from discontinuous to continuous. The results are presented in Fig. 2.6. Notably, Fourier peaks are observed not only along the k_x, Fig. 2.6c, direction but also along the k_y direction, Fig. 2.6d, albeit with a significantly smaller amplitude. Moreover, these peaks are characterized by a large momentum spacing. This can be linked to the fact that, when the natural triangular structure is strongly deformed by the trap, the length scales in the transverse direction are small (compared to the longitudinal ones). We then expect broader and larger features in the Fourier signal along k_y with respect to k_x. Both the effects of the suppression of the 2D structure and change in the k-space length scale, are r eported in Fig. 2.6e-f, where we explore the crossover by varying the atom number N at fixed nu_y.

In the Landau picture, this crossover implies that, as the atom number increases, the 2D triangular structure is gradually suppressed and deformed. This can be described as a gradual decrease of the cubic term in the energy expansion, in particular the one associated with the kinetic energy. Ultimately, this process diminishes the discontinuity

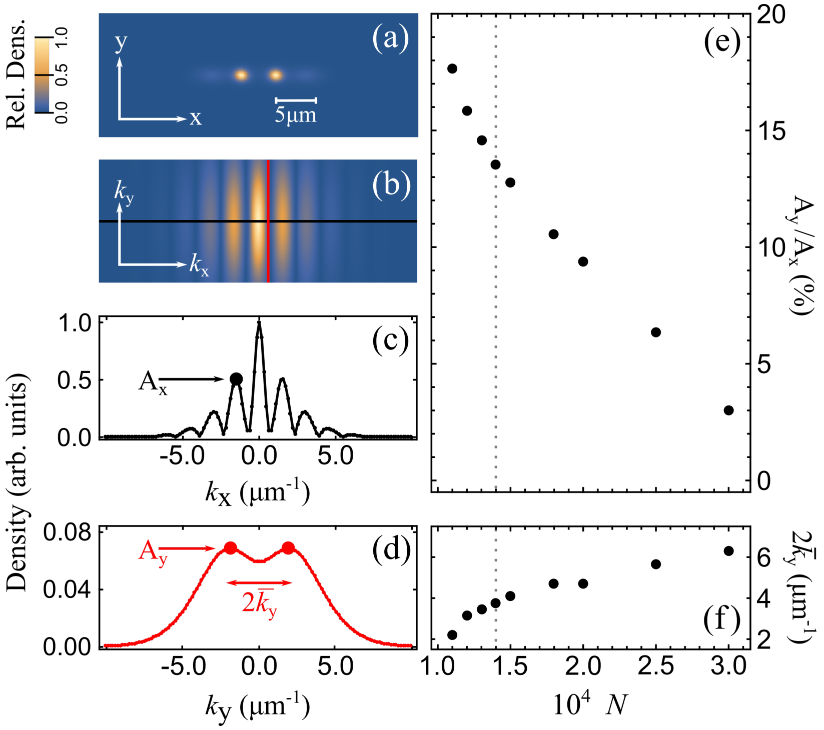

Figure 2.6: Suppression and deformation of the triangular 2D structure of the density background of supersolids in the dimensional crossover. Density profiles in real-space (a) and Fourier-space (b) of a single-row supersolid. The solid lines indicates the cuts in Fourier density along which we evaluate $T(k_y)$ (red) and the its counterpart along k_x (black), plotted in (d) and (c) respectively. The ratio between the amplitudes of Fourier signals A_y/A_x (e) and the Fourier spacing of $T(k_y)$ (f) is plotted as a function of N for supersolid at fixed contrast $\tilde{C} \simeq 0.04\%$. The vertical dotted lines in (e-f) marks the boundary between continuous and discontinuous transitions.

until the transition becomes smooth and continuous. The same effect is noticed when ν_y is increased while maintaining a constant N. This behavior can be explained in terms of a change in the supersolid compressibility for changing atom numbers. The triangular structure is deformed more easily by the trap when N is small, making it possible for the discontinuous transition to persist even for tight transverse confinements. To support this argument, we can have a look at the transverse size of the system. In particular, we analyzed the transverse width of the density distributions just before the critical point, where $\tilde{C} \sim 0$, for the transitions at the center of the crossover (boundary in Fig. 2.4). The results are shown in Fig. 2.7a. Remarkably, for a large part of the investigated confinements, $\nu_y > 70\,\text{Hz}$, the transverse size σ_y at the center of the crossover is close to the characteristic width of a non-interacting system, which is proportional to the natural harmonic oscillator length ℓ_y. Smaller widths result in discontinuous transitions, supporting the idea that this happens when *enough space* is available for the system to develop a deformed 2D structure. Introducing ℓ_y, is then required in order to define the *available space* for the system in the harmonic confinement.

For $\nu_y < 70\,\text{Hz}$, instead, σ_y become larger than $\ell_y/\sqrt{2}$ with a very rapid increase of the peak density, which is plotted in Fig. 2.7c. We interpret these deviations as the onset of an LHY-dominated regime, where quantum fluctuations increase the transverse width σ_y to limit a further increase in the peak density. The growing importance of the LHY energy term at high N and low ν_y affects also the shape of the supersolid clusters, which is connected again to the compressibility of the system. In Fig. 2.7b, the deformation parameter β_{ss} (defined in Eq. 2.11) indeed becomes negative in the region of high densities, meaning that the supersolid clusters start to be elongated along $\hat{y}$. In this regime, continuous transitions (still possible for high enough atom numbers in the upper left part of the map in Fig. 2.4) lead to a 1D structure of *stripes*, as reported in previous numerical simulations [198, 71]. In the opposite region of strong transverse confinements, the clusters are elongated along $\hat{x}$, with $\beta_{ss} > 0$.

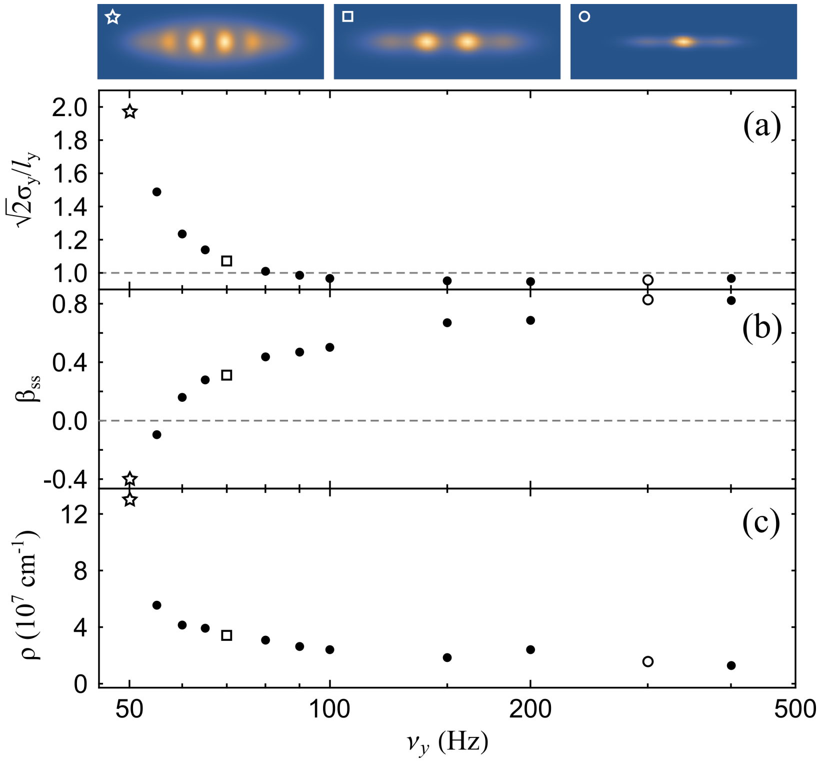

Figure 2.7: Interesting features of supersolids at the boundary between the continuous and discontinuous regimes. Each point corresponds to the transitions marked with black dots in Fig. 2.4. (a) Transverse width σ_y, (b) deformation parameter β_{ss} extracted from the central clusters of the supersolid, and (c) maximum of the linear density $\rho(x)$. Examples of x-y density distributions are shown as insets.

2.2 Dimensional crossover in experiments

To validate the theoretical predictions based on the numerical simulations and the analysis discussed in the previous section, we carried out an experimental investigation of the crossover in the superfluid-supersolid phase transition. We employ a quantum gas of magnetic atoms of ^{162}Dy with a dipolar length of $a_{dd} = 130\ a_0$ (see Eq. 2.3), confined within optical potentials in the same conditions of the numerical simulations already presented. Shifting from continuous to discontinuous transitions simply requires adjusting the aspect ratio of the harmonic potential in the $y-z$ plane while keeping the atom number constant. To do so, we specifically selected two distinct potentials

$$\begin{aligned} V_C: \quad & (\nu_x, \nu_y, \nu_z) = (15.0\ (0.7), 101.0\ (0.3), 93.9\ (0.6))\,\mathrm{Hz}\,, \\ V_D: \quad & (\nu_x, \nu_y, \nu_z) = (21.8(1.0), 67.0\ (0.8), 102.0\ (0.7))\,\mathrm{Hz}\,, \end{aligned} \tag{2.13}$$

featuring a continuous and a discontinuous phase transition respectively. Numerical results for the quantum phase transition associated with these harmonic traps have been already shown in Fig. 2.3a. In both scenarios, a single-row of supersolid clusters forms, with thousands of atoms per site, keeping the mean atom count at the transition approximately around $N = 3 \times 10^4$.

The starting point of the experiments is a Bose-Einstein condensate of about 6×10^4 ^{162}Dy atoms in a crossed optical trap at a magnetic field $B \simeq 5.5\,\mathrm{G}$. Further details about the experimental techniques employed to produce such our dipolar condensate can be found in the introduction to Chapter 4. At this magnetic field value, we sit far enough from any Feshbach resonance, to have the scattering length, which is our experimental control parameter, around its background value of $\approx 140\,\mathrm{a}_0$ [179, 180]. The transition is crossed by lowering a_s exploiting a series of Feshbach resonances around 5.3 G [181, 23], by adiabatically changing the magnetic field towards the critical value of the scattering length. Our resolution in controlling the magnetic field is 1 mG, while the field stability is about 0.5 mG, which gives us a stability in a_s of about $0.3\,\mathrm{a}_0$. More details about the magnetic field calibration are given in Sec. 4.1. Once the quantum phase transition is crossed, we promptly turn off the optical potential and allow the system to expand for 90 ms, employing a magnetic-field gradient to counteract gravity. Roughly 200 µs prior to the releasing of the atoms, we boost the contact interaction strength by setting $a_s \simeq 140\ a_0$. This minimizes the influence of dipolar interaction during the first stage of the expansions. Ultimately, we image the atomic density, which we interpret as the momentum distribution $\rho(k_x, k_y)$, using standard absorption imaging techniques, exploiting the strong optical transition at 421 nm. The same sequence can be used to probe also the dynamics of the system once we bring it back into the superfluid phase, after having crossed the phase transition.

2.2.1 Crossing the superfluid-supersolid transition and back

Very differently from the theoretical model and the numerical results discussed in the previous section, in the experiment, the system is brought out of equilibrium. Indeed, the experiment focuses on the dynamic evolution of the system while varying a_s, starting from the superfluid side of the transition. Since we are not talking anymore about the ground state of the system, being it either in the superfluid or in the supersolid phase, we need to introduce new considerations. Specifically, the dynamic nature of the problem brings in concepts like adiabaticity, dissipation, and, in cases of discontinuous phase transitions, hysteresis. Since during the whole experimental sequence the system is maintained at temperatures well below the condensation critical temperature (about 60 nK for our system [116]), I will neglect finite temperature effects, like the presence of a finite condensed fraction or thermal effects on the system dynamics.

To reduce the effect of non-adiabaticity introduced by the finite time scales of magnetic field ramps employed in the experiments, we choose the ramp speed to balance between adiabaticity and the impact of unavoidable three-body losses [181]. Indeed, even if the slowest possible ramp would be ideally the best choice, spending a finite time near a scattering length divergence, while crossing a Feshbach resonance, has a dramatic effect on the final atom number. The chosen rate (see Sec. 4.1.1) allows a nearly adiabatic transition across the potential V_C. Besides effects arising from the interactions, the density has also a huge role in the losses. It's important to note that the three-body loss rate, scaling as ρ^2, reaches its maximum at the density peaks within the supersolid phase. These losses have a dual effect on the study of the phase transition. On one hand, they decrease the density ρ over time,

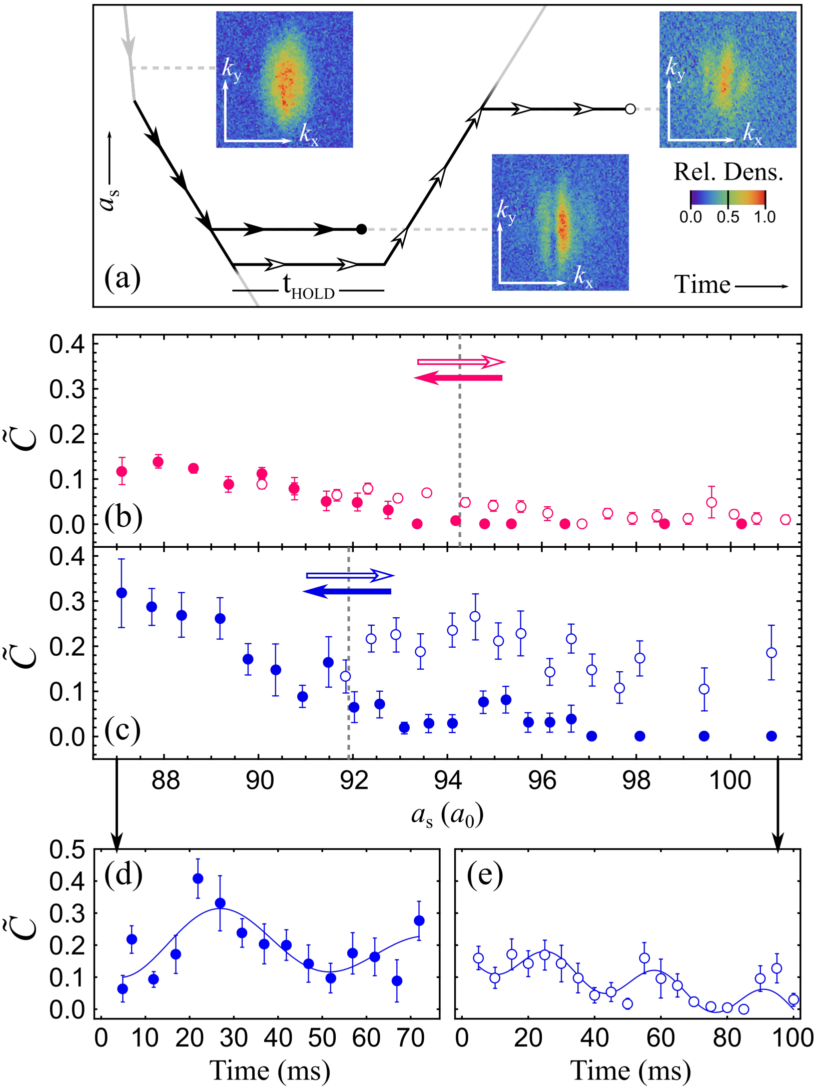

Figure 2.8: Observation of both continuous and discontinuous quantum phase transitions in experiments. (a) Sketch of the trajectories of a_s as a function of time for the in-going (filled symbols) and the out-going (empty symbols) ramps. The three sample distributions are the experimental single-shot images of the momentum distribution of the system at the different experimental steps. (b-c) Experimental order parameter $\tilde{C}$ as a function of the scattering length a_s, during the in-going (dots) and the out-going (circles) ramps for potentials V_C (b) and V_D (c). The vertical dashed lines represents the numerical predictions for the critical point of the phase transitions. (d-e) Dynamics of $\tilde{C}$ for potential V_D in the in-going ramp at $a_s = 87.3\ a_0$ (d) and in the out-going ramp at $a_s = 100.3\ a_0$ (e). Error bars on experimental points are the standard error of the mean, associated to 10-20 measurements. The solid lines are fits with a damped oscillation model.

reducing the visibility of the contrast in time-of-flight images; on the other hand, they introduce a damping of the excitations associated with a local increase in density.

Evolution of the contrast

In Fig. 2.8 are reported the primary experimental observations when crossing the superfluid-supersolid transition in potentials V_C and V_D. Specifically, we examine the evolution of $\tilde{C}$ for an in-going ramp from the superfluid to the supersolid (filled circles) and for a subsequent out-going ramp from the supersolid to the superfluid (open circles). The experimental trajectories in the $a_s - t$ plane are shown in Fig.2.8a. The characteristic time for forming the supersolid is determined to be 20 ms, defining the holding time before imaging.

The distinctive density modulation associated with the supersolid shows the characteristic side peaks in the momentum distribution, as illustrated in the insets of Fig. 2.8a representing typical measured distributions. Those can be related to the theoretical momentum distribution, $\rho(k_x, k_y)$, albeit with minor modifications due to interactions during the expansion. The primary observable is the contrast $\tilde{C}$, which we can define experimentally by the relative height of the peak at the characteristic momentum of the supersolid, as outlined in the theory. To extract $\tilde{C}$ we carry out a systematic analysis of each experimental image. Firstly, we perform a rotation of the momentum distribution in the plane to align the interference peaks along the k_x direction and we integrate over k_y to obtain the 1D momentum distribution $\rho(k_x)$. Finally, we fit $\rho(k_x)$ utilizing a double-slit model

$$\rho(k_x) = A_0 \exp\left[-\frac{(k_x - k_0)^2}{2\sigma^2}\right]\{1 + A_1 \sin\left[\pi(k_x - k_0)/k_r + \phi\right]\} \quad (2.14)$$

where A_0, k_0 and σ are, respectively, the amplitude, center, and width of the envelope, while A_1, k_r and ϕ are the amplitude, period (in the momentum space) and phase of the modulation. In a typical experimental image, the phase is approximately $\pi/2$, resulting in a central peak sided by two symmetrical lateral peaks. In order to detangle the contrast $\tilde{C}$ from phase fluctuations around $\pi/2$, we *rephase* the fitted function by enforcing $\phi = \pi/2$. We define

$$\tilde{C} = \max{}^L/\max{}^C\,, \quad (2.15)$$

where $\max^C$ and $\max^L$ represent the values of the central and first lateral maxima.

Phase transitions in potentials V_C and V_D exhibit markedly distinct behaviors, as illustrated in Fig. 2.8b-c. In potential V_C (panel b), the in-going ramp demonstrates a smooth increase of $\tilde{C}$, marked by minor shot-to-shot fluctuations. During the out-going ramp, $\tilde{C}$ gradually returns to zero, meaning that the phase transition can be crossed sequentially in both directions without inducing significant excitations. In contrast, potential V_D (panel c) displays strong fluctuations of $\tilde{C}$ even before the phase transition followed by a sharp increase around $93\,\mathrm{a}_0$. Notably, during the out-going ramp, $\tilde{C}$ remains significantly high, extending up to at least $10\,\mathrm{a}_0$ in the superfluid regime. This hysteresis-like effect is given by the intrinsic lack of adiabaticity peculiar to discontinuous transitions. Indeed, as I will discuss below, it is possible to associate the finite contrast we observe in the superfluid region after the out-going ramp, to the excitation of a collective mode with the same spatial structure of the supersolid. While transition V_C can be traversed back and forth in an almost adiabatic manner given our ramp speed, crossing transition V_D is intrinsically non-adiabatic, as expected for continuous and discontinuous phase transitions, respectively.

Hysteresis

Besides the effects of the non-adiabaticity, having a discontinuous transition raises questions about the possibility of observing an actual hysteresis, as predicted for first-order phase transitions. Indeed, from the numerical simulation of the system dynamics, a small hysteresis can be detected by changing the direction in which we cross the transition in potential V_D, starting from the absolute ground state. The width of the hysteresis cycle is about $0.5\,\mathrm{a}_0$ much smaller than the experimental resolution on the scattering length, which is $2\,\mathrm{a}_0$. Moreover, trying to emulate the experimental sequence, by entering in the supersolid phase and ramping back to the superfluid, this effect tends to vanish. From a formal point of view, it has to be specified that the very concept of hysteresis cannot be applied to our experimental system which is not at the equilibrium. However, this intriguing phenomenon could, in theory, be studied if the dissipation were sufficiently high to allow the system to dissipate all the energy acquired during the crossing of the phase transition.

Dynamics and excitations

The dynamic nature of the experiment gives also another perspective to look at these two different behaviors. Indeed, to have a complete picture, we must observe the dynamic of the system triggered by the crossing of the transition in both directions. Substantial excitations of various collective modes can be observed in the case of potential V_D. I will first focus on the oscillation of the order parameter $\tilde{C}$, mainly affecting the dynamics triggered by the discontinuous transition. Such oscillations are also present for potential V_C, albeit with significantly smaller amplitude, and are given by a non-perfect adiabaticity of the magnetic field ramps. In a broader context, I will discuss the effect of the excitations in the two scenarios in the next section 2.2.2.

Turning back to the contrast, Fig. 2.8d-e illustrate the dynamics of $\tilde{C}$ in trap V_D after the in- and out-going ramps. Data points in panel (c) have to be considered as the first maximum in the time evolution after the in-going ramp, occurring about 20 ms after the end of the ramp. This gives also a measure of the formation time of the supersolid structure. We fit the time evolution of the contrast with damped sinusoidal oscillation of the form

$$\tilde{C}(t) = A \sin\left(\sqrt{(2\pi\nu)^2 - \tau^2}\, t + \phi\right) \mathrm{e}^{-t/\tau} + Bt + \mathrm{off} \tag{2.16}$$

extracting the oscillation frequency ν and the damping time τ. After the in-going ramp (panel d), the oscillation amplitude A is smaller than its offset off, resulting in a finite contrast throughout the observed time evolution. The oscillation frequency, $\nu = 21(3)\,\mathrm{Hz}$, agrees with the so-called amplitude mode of the supersolid, as previously studied in [182]. Upon crossing back the transition (panel e), we observe again a sinusoidal oscillation. This time, however, its amplitude is comparable to its mean value, and the contrast touches zero in the minima of the oscillation. Intuitively, we describe the two kinds of collective motion as perturbations around the equilibrium configuration, which is the supersolid (where $\langle\tilde{C}\rangle_t \neq 0$) after the in-going ramp, and the superfluid (where instead $\langle\tilde{C}\rangle_t = 0$) after the out-going ramp. To complete the picture, we also note that the damping time decreases by an order of magnitude going from the BEC to the supersolid. For V_D we get $\tau = 100 \pm 41$ ms at 94.3 a_0 and $\tau = 15 \pm 5$ ms at 87.4 a_0.

To theoretically support our observations, we can compare these results with a dynamical numerical simulation of the time evolution of the ground state experiencing a magnetic field ramp analog to the experimental one. The numerical simulation of the dynamics, carried out by Prof. Michele Modugno and coworkers, are based on the solution of the Gross-Pitaevskii equation $i\hbar\partial_t\psi = \delta E/\delta\psi^*$, by using the FFT split-step method discussed in [78]. It's very important to note that this method does not take into account thermal or quantum fluctuations (except the LHY correction), and neglects any energy dissipation mechanism, such as losses, which are unavoidable in the experiment. Given the lack of dissipation, the simulations utilized scattering-length ramps slower by one order of magnitude compared to the experiment. As a matter of fact, the ramp speed employed in the experiment, $0.5\,\mathrm{a}_0/\mathrm{ms}$, in the simulations is not distinguishable from a sudden quench of the scattering length. In practice, the slowdown is chosen by investigating the effect of different ramp speeds in the case of continuous transitions, employing trap V_C, for example. With $\dot{a}_s = 0.05\,\mathrm{a}_0/\mathrm{ms}$, we obtain a quasi-adiabatic crossing of the continuous transition, similar to what we observe in the experiment, afflicted by the dissipation. As shown in Fig. 2.9, the contrast grows after the in-going ramp on a timescale similar to the experimental formation time, then oscillates around a relatively high value. On the other hand, the out-going ramp induces an oscillation in $\tilde{C}$ with a smaller amplitude and minima at zero. Both the dynamics can be visualized in real space by looking at the 1D density profiles reported in Fig. 2.9f-h, where clearly the equilibrium phases are modulated (c) or unmodulated (g) respectively for the in- and out-going dynamics. This fact agrees with the idea that the latter dynamics is in fact a collective mode of the superfluid, akin to the so-called roton mode [138], but in the high amplitude regime, where a rigorous Bogoliubov analysis is not possible. Remarkably, the same collective mode can be excited starting with a superfluid at a fixed scattering larger than the critical one, by sudden removal of a static periodic potential with the same structure of the supersolid [17], or simply by initialize the density of the starting point of a numerical simulation, shaped like a supersolid. The relation between this collective oscillation and the roton mode, peculiar to dipolar systems, is also supported by the fact

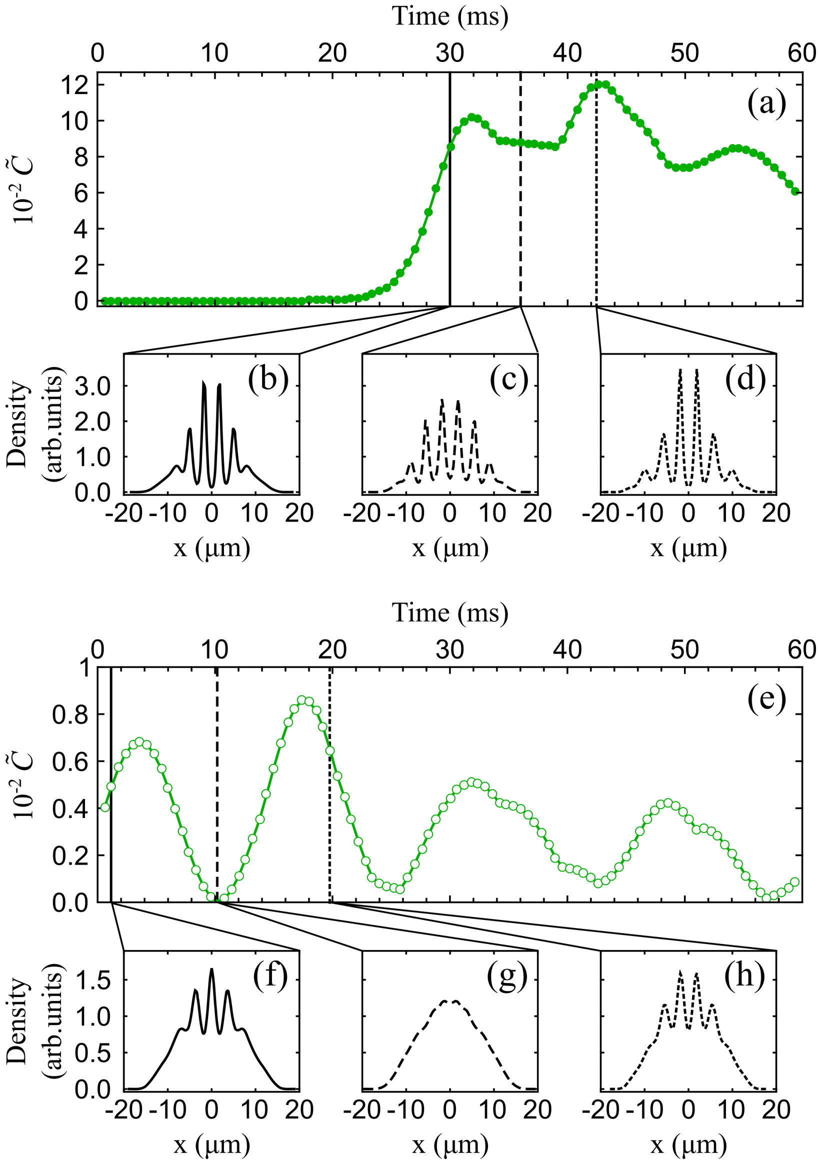

Figure 2.9: Numerical simulations of the dynamics of $\tilde{C}$ in the potential V_C. (a) Dynamics after the in-going ramp from 95 a_0 to 93 a_0 showing the growth of $\tilde{C}$ after the supersolid formation time and its oscillations around a non-zero value. (e) Dynamics after the out-going ramp from 90 a_0 to 95 a_0, showing that the oscillations touch zero. Panels (b-d) and (f-h) show the snapshots of the density distribution along x at selected times indicated by vertical lines in (a) and (e).

that the oscillation amplitude diminishes significantly if the dipolar energy term is removed from Eq. 2.1.

Another type of excitation triggered by the crossing of the phase transition, is the so-called breathing mode, namely the oscillation of the width of the cloud. The longitudinal and transverse breathing modes for the traps used in the experiment have been investigated numerically in [3]. The results are reported in Fig. 2.10, showing the behavior of longitudinal width of the supersolid w_{SS} as a function of time, for a sudden quench and the ramp speed replicating the experimental observations. Note that the amplitude of w_{SS} oscillations is smaller in the ramp case, but remains somewhat finite for both traps. Indeed, to form the clusters the system has to *move* density along the longitudinal direction, drastically changing its width, which starts to oscillate, once the supersolid is formed. Even if not studied in detail in the present case, those oscillations feature two frequencies, that can be related to the spontaneous symmetry breaking of both global phase and translational symmetries, distinctive of the supersolid state [182]. Remarkably, from the insets in Fig. 2.10, the transverse dynamics are very different between the two traps. Indeed, the large oscillation of the transverse width for V_D is strongly suppressed for the potential V_C. This qualitative analysis supports the idea that, in tighter traps featuring continuous transitions the transverse degree of freedom is frozen, realizing in practice a quasi-1D system. The effect of the dynamics of the transverse width can also be checked by eye, looking at the snapshots of the time evolution in Fig. 2.10. Indeed, while for V_C the system develops only in the longitudinal degree of freedom, for V_D case the density background extends also in the transverse direction, with secondary density maxima that form a deformed triangular structure. This observation demonstrates that the large oscillations in the transverse width for V_D are given by a 2D response of the superfluid background of the system. On the other hand, for potential V_C, the small oscillations at very high frequencies observed for the transverse width may be explained by a compressional mode of the clusters themselves, which involves much higher energies.

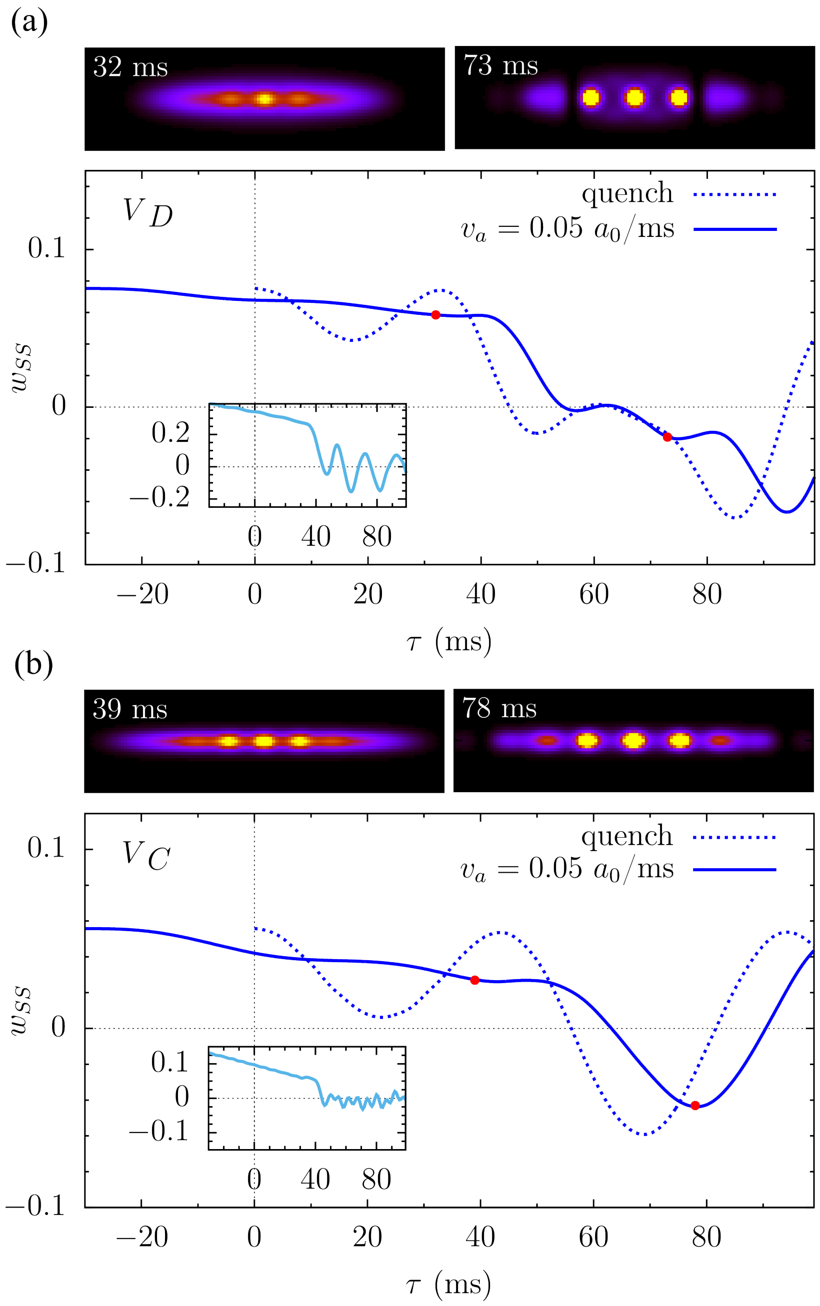

Figure 2.10: Breathing mode excited by crossing the superfluid-supersolid transition in trap V_D (a) and V_C (b). In the main plot, the longitudinal width of the system w_{SS} (normalized to the associated equilibrium width) is plotted as a function of time, after a sudden quench of the scattering length (dotted blue line) or a ramp with speed 0.05 a_0/ms (solid blue line). In the insets of the main plot, the time evolution of the transverse width of the system is plotted in light blue. The top panels show the snapshots of typical 2D densities during the time evolution. The associated time steps are marked with red dots in the main plot.

2.2.2 Measurement of the expansion energy

To analyze the general effects of the excitations in the experiment, besides the amplitude and breathing modes already discussed, we extract the total energy of the system from the momentum distribution measured experimentally. Indeed, during the expansion all the energy contributions are converted into kinetic energy, therefore by comparing the momentum distributions of a generic phase to the one of the superfluid ground state, we obtain a relative measure of the energy gained by the system during its dynamics across the transition. This quantity obviously depends also on the number of atoms in the system, which suffer from shot-to-shot fluctuations, and, as already mentioned for the dissipation mechanisms, decrease sensibly in the supersolid phase. In Fig. 2.11 both the relative total energy and the atom number are presented for the same data of Fig. 2.8. Formally, the total energy of the system after the expansion is given by

$$E_{exp} = \hbar^2 \langle k_x^2 + k_y^2 \rangle / (2m) \,, \tag{2.17}$$

and it is plotted in Fig. 2.11a as the deviation ΔE from the same quantity extracted from the superfluid ground state (namely we adjust the energy offset so that the point at largest a_s value is set to zero). Clearly, V_D shows stronger excitations in both directions with respect to V_C, nevertheless, a quantitative comparison between the two traps for the in-going ramp is difficult, since the supersolid resulting from the discontinuous transition has a larger contrast, hence a larger kinetic energy contribution. On the other hand, a direct comparison can be done on the superfluid side, where the temporal average of $\tilde{C}$ is zero for both potentials. On this side, we see that the energy excess for trap V_C is about 0.5 nK, while it's much larger for V_D, around 4 nK. These numbers can be checked with numerical simulations of the dynamics, which give 0.5 nK and 2.5 nK respectively. It's important to note that E_{exp} overestimates the total energy of the system since we boost the contact interaction just after the release of the system from the optical potentials. Therefore the deviations of the measured energy excess in potential V_D from the numerical results, are at least reasonable.

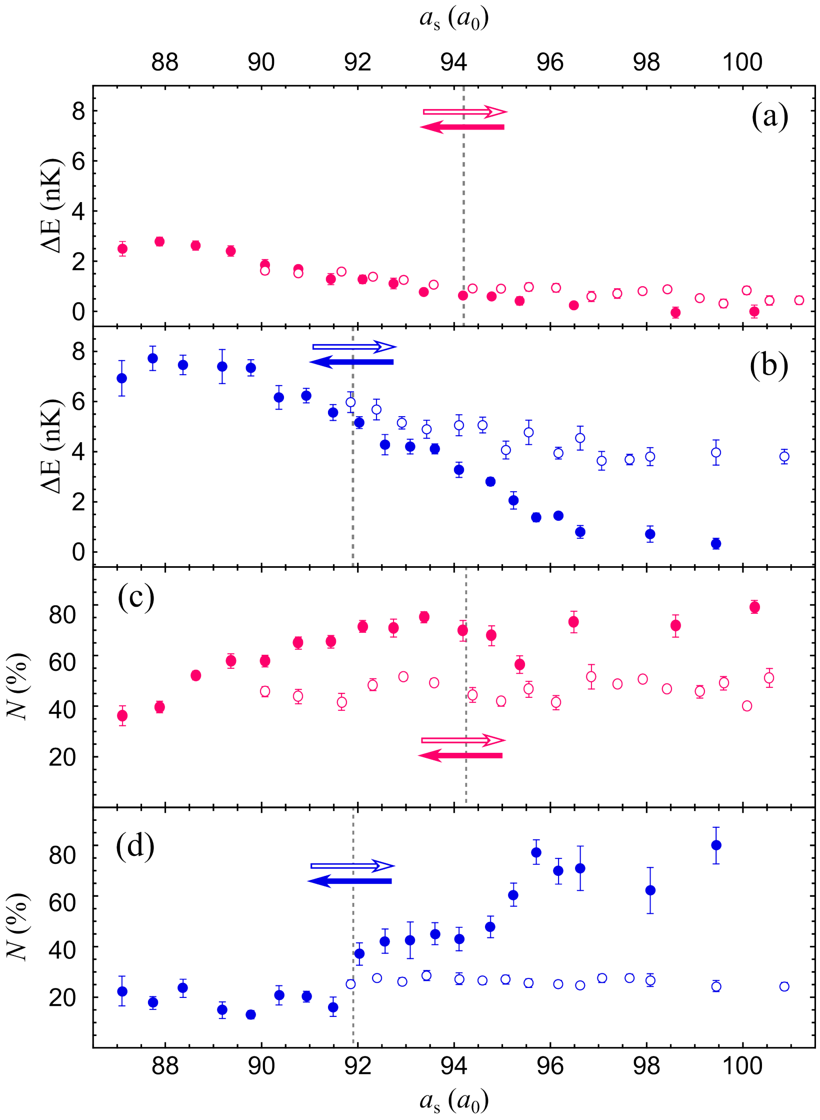

Figure 2.11: Variation of the total energy of the system and atom number across the phase transition. (a-b) Expansion energy extracted from experimental data for potentials V_C and V_D. (c-d) Change in the mean atom number (normalized to its maximum value in the superfluid side) due to losses across the transition for potentials V_C and V_D. In all panels dots and circles represent the energy variation after the in-going and out-going ramps respectively.

Atom losses

The atom number relative to its maximum value for a pure superfluid system, i.e. point at the largest a_S, is shown in Fig. 2.11b. Atom losses, which increase when we enter in the supersolid phase, are mainly due to three-body collisions, that can be modeled as $dN/dt = -K_3\rho^2$. While K_3 is approximately constant across the rather small region of the explored magnetic field, losses are enhanced by the increase in the peak density at the position of the clusters. For the in-going ramp, we observe a reduction of the atom number up to 40% of the initial value for both potential V_D and V_C. Coming back to the superfluid no significant losses are observed, supporting the idea that having already reduced the system density, losses are less effective. Since losses are linked with the formation of the supersolid, looking at the atom number is also interesting from the perspective of determining the character of the transition. Indeed, even if N is not the order parameter of that phase transition, we observe a very similar behavior to $\tilde{C}$. In particular, for V_D a clear jump to lower atom numbers (or a spike in the losses) can be detected at the transition point, helping to establish the experimental value of the critical scattering length for discontinuous transitions.

Energy-Atom number correlations

To extract E_{exp}, taking into account the changing atom number across the transition, we performed the following analysis. Starting from the measured momentum distributions $\rho(k_x, k_y)$, we compute $\delta\rho = \rho - \langle\rho\rangle$ for each experimental shot. The average density $\langle\rho\rangle$ is calculated on the entire dataset, over 800 (500) images for potential V_D (V_C). The energy difference $E - \langle E\rangle$ is then given by

$$\Delta E_{raw} = \left(\frac{\hbar^2}{2m}\right) \int \delta\rho(k_x, k_y) k^2 \mathrm{d}k_x \mathrm{d}k_y \,, \tag{2.18}$$

which gives the energy excess per particle, since the distributions are normalized to $\int \rho(k_x, k_y) d^2k = 1$. To cancel out the effect of atom losses, we correct ΔE_{raw} taking into account the correlations between energy and atom number. The correlations are the effect of repulsive contact interactions that act in the first instants of the otherwise free evolution. Subtler effects, given by the dipole-dipole interactions are not taken into account. Note that there are still no theoretical models to describe the

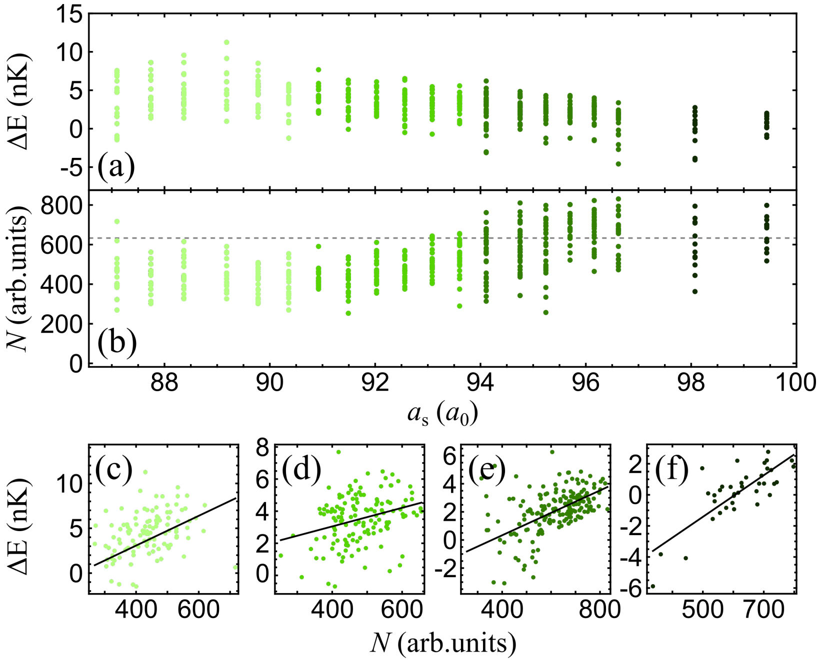

Figure 2.12: Analysis of the expansion energy presented in Fig. 2.11. As an example we show the experimental data for the in-going ramp in the potential V_D. Panels (a-b) show excess energy (raw data) and atom number as a function of the scattering length. The horizontal dashed line marks the average atom number $\bar{N}$ in the superfluid side. Different colours correspond to the subsets in panels (c-f) where the solid lines are the linear regressions used to rescale raw data in panel (a) using Eq. (2.19).

effect of these long-ranged interactions over the expansion of a dipolar gas. Since contact interactions are linear in density, we expect linear correlations in the energy-N plane. The correlation analysis is presented in Fig. 2.12. We first divide our data sets into groups, gathering the realizations at different scattering lengths with common average atom numbers $\bar{N}$. The different groups are highlighted in shades of color in panels Fig. 2.12a-b, showing respectively the raw energies defined in Eq. 2.18 and the raw atom numbers as a function of the scattering length. In panels (c-f) we use a linear regression $\Delta E_{\text{raw}} = \gamma N + \Delta E_0$ to capture the correlations of each group. Raw data are then corrected using the following relation

$$\Delta E = \Delta E_{\text{raw}} - \gamma_i \left(N - \bar{N}\right). \tag{2.19}$$

With this rescaling, ΔE is increased if $N < \bar{N}$ and decreased in the opposite case, by an amount proportional to γ_i for each group. The data obtained are then averaged to extract ΔE plotted in Fig. 2.11.

2.2.3 Fluctuations of the order parameter

Until this point, I have discussed many different experimental observations, pointing in the direction of demonstrating the two different natures of the phase transition for the two studied trapping configurations. In particular, I highlighted evidence showing that, also in our finite system, discontinuous transitions may be observed, arguing that are reminiscent of first-order phase transitions well studied theoretically in the thermodynamic limit. In this section, I will show that indeed this link can be traced, by demonstrating that is possible to infer the *shape* of the Landau free energy, directly from the experimental fluctuations of the order parameter $\tilde{C}$. Studying the histograms of $\tilde{C}$ occurrences at different regions of scattering length, and looking at the accumulation points, it is possible to detect the presence of one, or multiple minima in the Landau free energy of the system. The shot-to-shot fluctuations of the order parameter can have different origins. Since we do not observe finite temperature effects in our experiments[10], we estimate thermal fluctuations small enough to be neglected. On the other hand, we should expect a sensible contribution from quantum fluctuations, which we know play a huge role in the physics of supersolids. As I discussed in Sec. 2.1, they are essential for the stability of

---

[10] No thermal fraction can be detected either in the supersolid or in the superfluid phases

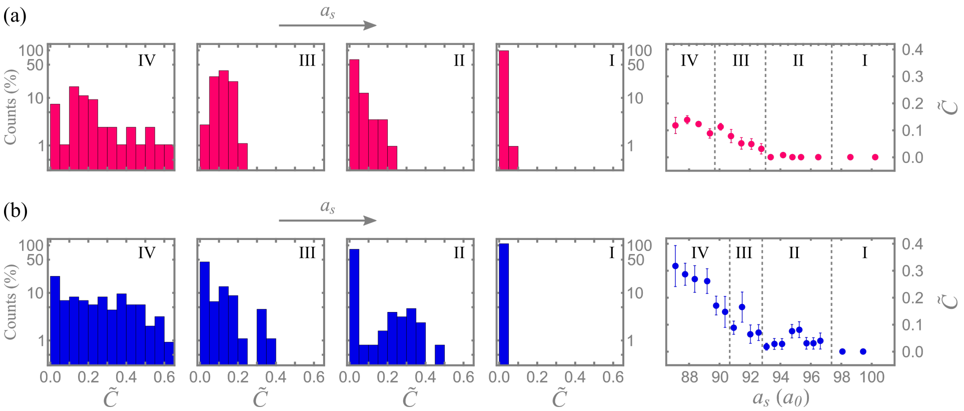

Figure 2.13: Distributions of the order parameter $\tilde{C}$ in different scattering length regions, revealing the different character of the phase transition. (a) Experimental data for the potential V_C. The histograms show the contrast relative to the regions (I-IV) specified in the right-hand plot, showing $\tilde{C}$ after crossing the transition with the in-going ramp. (b) Same analysis for potential V_D. Each region contains 100-150 experimental points. The single- and double-peak feature in region II, demonstrate the single and double-minima structure of the free energy in potential V_C and V_D respectively.

the supersolid ground state and contribute to many interesting properties of their structure. However, technical noise such as the variable atom number from shot to shot (visible in the raw data plotted in Fig. 2.12), dominates in our experiment, making it impossible to detect quantum fluctuations. Luckily, technical fluctuations can be used as a tool to probe the energy landscape of our system, since they have different distributions depending on the shape of the Landau free energy.

The distributions of $\tilde{C}$ for the two different potentials V_C and V_D are reported in Fig. 2.13, together with the data of the in-going ramp already shown in Fig. 2.8b-c. The histograms group together the $\tilde{C}$ data for the two different traps, binned in four regions of scattering length. We first analyze what happens for potential V_C. The first region (I) lays well before the transition, where the system is fully superfluid, hence $\tilde{C} = 0$ in each experimental realization, giving a spike in the corresponding histogram at this value. In the second region (II), at smaller a_s, the density modulation starts to form and we observe a small signal in the histograms at finite $\tilde{C}$. This small population grows further when we cross the phase transition, entering the third region (III). Here the peak at $\tilde{C} = 0$ is strongly depleted and the signal spreads along a broad region of contrast. When the scattering length a_s is further decreased (IV), the average contrast increases and the histograms become noisier. This reflects the increasing noise in the atom number for decreasing scattering lengths, where losses modify the density distribution affecting also the position of the transition point. The main difference in the case of V_D, is that, just before the transition (II) the peak at zero contrast in the histograms splits, and we observe a sensible population at large $\tilde{C}$. This is indeed direct proof of the presence of a secondary minimum at finite contrast in the Landau energy, which can be populated also before crossing the phase transitions thanks to quantum and technical fluctuations [20]. This double-peak feature is still present, even if less evidently, in the third region (III) and then vanishes once we come closer to the droplet crystal regime at small a_s.

The single or double-minima structure in the free energy can be also investigated using our Landau model discussed in Sec. 2.1.2. Indeed, in Fig. 2.3b,d, we already showed the results for the calculated energy as a function of $\tilde{C}$ for both V_C and V_D. As we verified experimentally, they show respectively a single and a double-minima, around the same value of contrast of the fluctuations peaks. However, the model is not exact because it only accounts for the variation of $\tilde{C}$, while in the experiment the whole density distribution changes with the interactions, and during the dynamics. At a qualitative level, we can compare the height of the energy barrier for the discontinuous case with the of energy gained by the system, measured experimentally through the expansion energy. In Fig. 2.3d, the calculated barrier is indeed 5 nK, which is very close to the energy excess reported in Fig. 2.11a and of same order of magnitude of the system temperature.

2.2.4 Supersolid phase coherence

In this chapter, I focused on one of the main properties of supersolids, which is their crystal structure and how it is related to the character of the transition. The other essential ingredient for a supersolid is phase coherence, which will be more at the center in the next chapter. Leaving aside the details of the experimental measure of the superfluid phase, here I just want to show how the coherence properties of the supersolid change for the different types of transitions. This

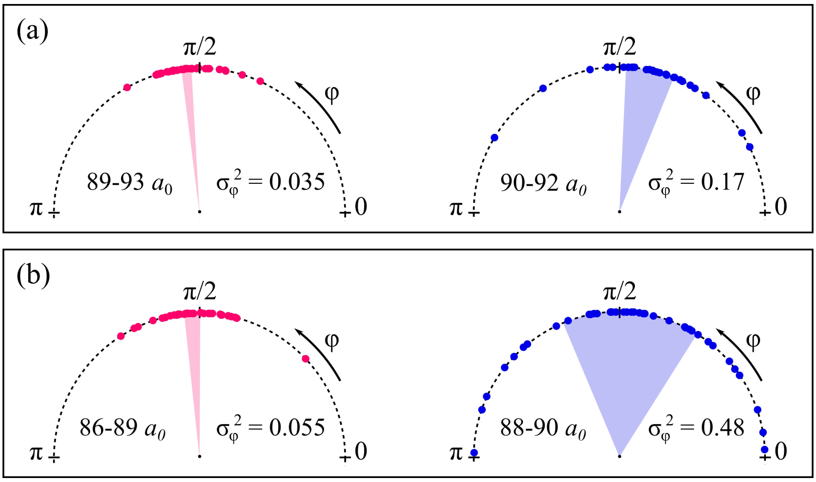

Figure 2.14: Coherence of the supersolid after crossing the continuous (magenta) or the discontinuous (blue) phase transitions, in trap V_C or V_D respectively. (a) Distribution of the phase of the interference pattern just after the transition point. (b) Same distribution in the region of scattering length corresponding to higher density contrasts. The shaded areas represents $\bar{\phi} \pm \sigma^2_{\phi}$, with average phase $\bar{\phi}$ and variance σ^2_{ϕ}.

has an important impact on choosing the best experimental configuration to measure delicate effects related to phase coherence such as the superfluid fraction of the supersolid, as I will discuss in the next chapter.

The phase extracted from the momentum distribution after crossing the phase transition is reported in Fig. 2.14. For both types of transition, we group data into two different regions of scattering length. Similar to what has been done for the fluctuations of the order parameter, we have a first region just after the transition point (intervals [89 : 93] a_0 for V_C and [90 : 92] a_0 for V_D); and a second region extending deeper in the supersolid phase (intervals [86 : 89] a_0 for V_C and [88 : 90] a_0 for V_D). At larger scattering lengths the supersolid is not formed and the phase cannot be measured from the interference pattern recorded after the expansion. For a continuous uniform distribution between 0 and π, we expect the variance of the phase to be $\sigma^2_\phi = \frac{\pi^2}{12} \approx 0.8$ [11]. For both types of transition and in each region of scattering length, we observe a phase variance that is lower than this value, meaning that our system is indeed phase-locked, as we expect for a supersolid. However, the variance is

---

[11] For such distributions ranging from a to b, the variance is $(b-a)^2/12$.

very different between the two types of transitions. Although they both show that the variance increases for decreasing a_s, as an effect of the losses that disrupt the coherence of the system, the distribution for the potential V_D, featuring a variance $\sigma_\phi^2 = 0.17$ in the first region, is rather broad if compared to the very narrow phase variance of $\sigma_\phi^2 = 0.035$ for V_C. In the second region, the variances become $\sigma_\phi^2 = 0.48$ for V_C, in agreement with previous results reported in [181], and $\sigma_\phi^2 = 0.055$ for V_C. This rather large difference in phase coherence demonstrates that by crossing a continuous transition, the supersolid phase is not scrambled by fluctuations, and indeed the system shows a remarkably high coherence, even if the transition is crossed in a finite time.

Chapter 3

The dipolar supersolid as a Josephson junction

In the previous chapter, I introduced the supersolid phase using the language of quantum phase transitions, focusing on understanding the character of the transition and its connection to the supersolid structure. Although it plays a huge role in the system phenomenology, it's important to stress that the density modulation of the supersolid is not the right quantity to describe the supersolid phase. The extraordinary properties of supersolids are indeed more complex than the simple existence of a modulated density in a superfluid, which can be easily created in quantum gases experiments by employing external periodic or quasi-periodic potentials produced from optical lattices and superlattices [60]. In supersolids, the modulation of the superfluid density must be spontaneous, and the supersolid lattice has to share the same possibility, as an actual crystal, to host excitations typical of solids, such as phonons [182], and, as I already discussed in Chapter 2, to have a finite rigidity that allows deformations. The concept of rigidity is indeed very general [8] and does not apply only to the *solid* part of a supersolid. Also the *superfluid* part of this counterintuitive quantum phase, has a finite rigidity, which is captured by the phase stiffness Λ, describing the superfluid response of the system [53]. Akin to how rigidity measures resistance to deformation in classical mechanics, the phase stiffness indicates how difficult it is to change the phase of the order parameter locally. Defined as the energy cost for locally perturbing the phase of the macroscopic wavefunction, a finite phase stiffness describes all fundamental phenomena appearing in a superfluid [105]. Differently from fully superfluid systems, the crystal and phase rigidities are coupled in supersolids, resulting in a reduction of the phase stiffness due to the appearance of a crystal structure. In this chapter, I will focus on a novel method, reported in a very recent work [16] by our group, to quantitatively measure and provide an intuitive description of this reduction. This has been achieved through an experimental assessment of a key quantity for supersolids, the so-called superfluid fraction f_s, based on the Josephson effect [80]. Indeed, we demonstrated the possibility of inducing Josephson oscillations, namely coherent oscillations of the number of atoms and the phase difference, between two adjacent clusters of the dipolar supersolid, showing that the superfluid fraction is linked to the Josephson frequencies.

Originally, the supersolid phase of matter was defined as a quantum state described by a macroscopic wavefunction with a spatial modulation originating from the simultaneous, spontaneous breaking of the global phase and translational symmetries [61, 9, 38, 103]. In the spirit of looking for a finite superfluid response in a solid system, the promising candidate to host a supersolid phase was, at the time, solid helium. In this context, A. J. Leggett proposed in the 1970s that a finite superfluid response could be quantified by the superfluid fraction f_s, which he connected with the nonclassical rotational inertia (NCRI) of a standard superfluid, such as liquid helium at low T, under rotation [103]. In particular, the moment of inertia I for a cylindrical system is

$$I = (1 - f_s) I_C \,, \tag{3.1}$$

which is zero for a fully superfluid system with unitary superfluid fraction, and increases towards the classical value I_C for $f_s < 1$, reaching I_C for a classical system with $f_s = 0$. Leggett's argument is that, in the presence of a periodic modulation of the wavefunction, the superfluid fraction would be reduced, deviating from the unitary value, hence reducing I. In this sense, a sub-unity superfluid fraction would measure the reduction of the superfluid response given by the density modulation. The search for a sub-unity superfluid fraction in solid helium was at the center of many experimental efforts [86, 87], based on global measurements of the NCRI using torsional oscillators to put solid ^{4}He under rotation while reducing the system temperature. However, the preliminary results of a supersolid behavior failed to be confirmed due to difficulties in detangling the NCRI from other temperature-dependent properties, such as the ^{4}He shear modulus [48, 34], and eventually the presence of a supersolid was ruled out [85]. The idea of measuring the superfluid response from rotations has been picked up in the context of dipolar supersolids where many properties connected to the supersolidity have been already tested experimentally. The first observations

[181, 22, 42] demonstrated the presence of a density modulation coexisting in a phase coherent system; then the presence of Goldstone modes, associated with the spontaneous double symmetry breaking were experimentally assessed [63, 182], demonstrating the finite rigidity of the emerging crystal structure. A definitive proof of the superfluidity of the supersolid, besides the observation of long coherence times, was indeed the measurement of the rotational inertia of a dipolar supersolid [183]. The main result of the experiment is reported in Fig. 3.1. Inspired by Leggett's argument, a single-row dipolar supersolid (similar to the one analyzed in the previous chapter) was rotated, exciting the so-called *scissors mode* of the system [123, 124], by triggering a sudden rotation of the atomic cloud around its vertical axis (inset in Fig. 3.1a), and studying the resulting dynamics. From the oscillatory motion of the supersolid, the NCRI can be extracted and, using Eq. 3.1 (modified to take into account the trap geometry), converted in a qualitative estimation of f_s. In Fig. 3.1a, is reported the behavior of superfluid fraction across the phase transition: below the critical point we have a fully superfluid system, while in the supersolid, numerical simulations (black dots) show a decrease of f_s. The experimental point in blue, lying in the supersolid region, is slightly below $f_s = 1$, demonstrating a large superfluid fraction of the dipolar supersolid. This measurement, however, is largely dominated by the contribution of the single clusters (black diamonds) rather by a Leggett-like mechanism. Looking at a snapshot of the scissors dynamics taken from numerical simulations (Fig. 3.1b), we can see that, even if the two main clusters rotates around the center giving a finite contribution to the moment of inertia, the velocity field inside each cluster is more or less constant, as the one of the superfluid halo around the clusters. Although the moment of inertia increases to approach I_C, the superfluid fraction remains very high. This overestimation of the global superfluid fraction makes it practically impossible to detect a deviation from unitarity. The same technique, applied to larger supersolids with 1D or 2D lattice structure, appears to be even worse since the scissors excitation triggers a more complex response [132]. In particular, it has been shown in [156], that in such systems the scissors oscillations have multiple frequencies, all connected to the NCRI, which are difficult to measure experimentally, especially if their period approaches the system lifetime.

The method discussed in this chapter comes from a different ap-

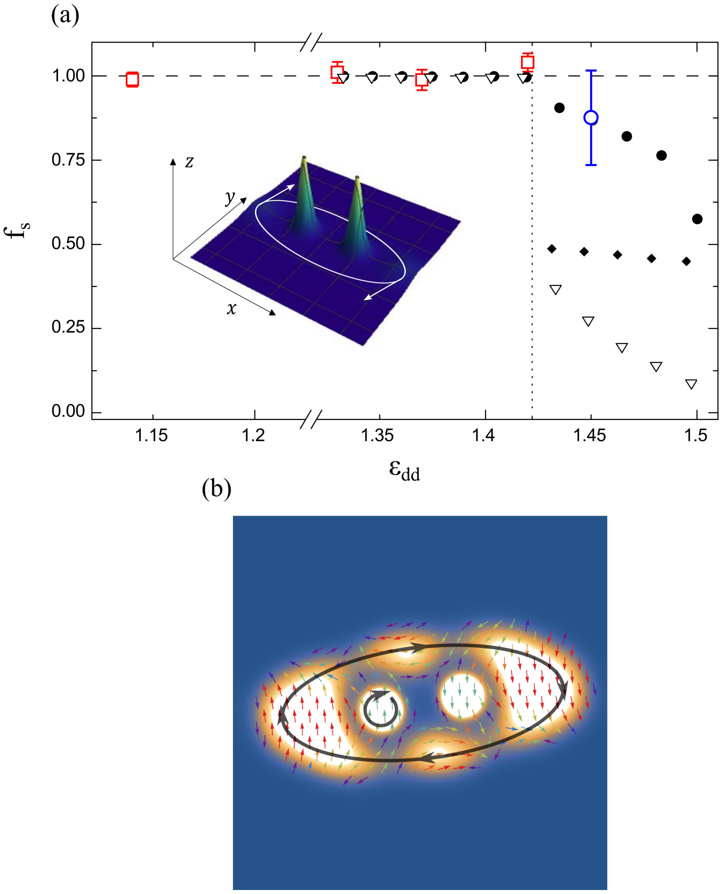

Figure 3.1: Estimation of the superfluid fraction f_s of a dipolar supersolid under rotation via scissors mode dynamics. (a) Superfluid fraction as a function of the interaction parameter ϵ_{dd} adapted from [183]. Black dots are the results extracted from numerical simulations of the experimental system. The vertical dashed line marks the critical point of the superfluid-supersolid quantum phase transition. The red squares are experimental data on the superfluid side, while the blue circle is the result for the supersolid. Open triangles represent the superfluid fraction calculated from the simulated system ground-state, by Leggett's theory. Black diamonds are the contribution to f_s given by the superfluid bulk of the clusters. The protocol used to excite the scissors mode is sketched in the inset. (b) Typical snapshot of the scissors dynamics, from numerical simulations. Higher density regions correspond to brighter colors. The velocity field calculated as the gradient of the phase of the wavefunction, is represented with colored arrows. Two kinds of motions are marked with black arrows: the transport of mass along the external superfluid halo, and the rotation of the central clusters.

proach, shifting from the measurement of global quantities, such as the NCRI, to local ones. We employ the Josephson effect, to probe the local coupling between two adjacent clusters of a dipolar supersolid, which is intimately connected with the superfluid fraction. The Josephson effect, namely the presence of a supercurrent between two superfluid (or superconductor) reservoirs separated by a weak link, has been tested in a number of experiments involving quantum gases of both bosonic [173, 30, 5, 108] and fermionic nature [187], where the weak link is externally imposed using optical potentials. Differently, in the supersolid, the barriers between the supersolid clusters are only given by interactions, without any external potential. This suggests the idea of describing the supersolid as an array of self-induced Josephson junctions. Indeed, in our work [16] we demonstrate such behavior, and we derive the superfluid fraction from the Josephson oscillations in a single lattice cell of the supersolid. Remarkably, by using the generality of the superfluid stiffness, we draw a connection between the superfluid fraction and the coupling energy of the junction. The latter measures the tunneling across the barrier, so it is not interesting in standard bosonic Josephson junctions, where this is usually an external parameter (typically the depth of the optical potential used to create the weak link). In the case of the supersolid, this is instead a key quantity, which quantifies the superfluidity of a supersolid. Depending on the interactions only, we explored a broad range of values of f_s, demonstrating its tunability in dipolar supersolids, from 0.1 towards unity.

Although dipolar supersolids are maybe the most striking example of a supersolid state of matter, with strong superfluidity effects, by following the original definition, a very broad class of materials should be related to the phenomenon of supersolidity, even if in some cases a clear demonstration of the supersolid character of such materials is still to be proven. Indeed, many quantum phases with a spontaneous modulation of the superfluid density have been recently observed. In strongly confined ^{3}He, pair density wave (PDW) order has been observed experimentally [107, 170], arising from the scattering of Copper pairs on the system boundaries. Other PDW phases have been observed in different kinds of superconductive systems, such as iron-based superconductors [113] and cuprates [66, 1], where the superfluid density is connected to the critical temperature T_c [73]. Potential phases associated with a supersolid state might be present within the neutron star's crust [136], as well as in excitons found in semiconductor heterostructures [45]. Instead, a direct connection with supersolidity has been traced in ^{4}He films on graphite substrates and in various ultracold atoms systems. In ^{4}He films, the second layer of helium shows a periodic density modulation induced by the graphite crystal lattice [133, 40], with a decreasing superfluid density as a function of the coverage. The spontaneous breaking of translational symmetry has been observed in ultracold quantum gases in optical cavities [106], where atoms spontaneously arrange in an ordered structure arising from the infinite range of interactions mediated by the cavity photons. A supersolid phase is also under investigation in spin-orbit coupled condensates [110, 151], where the mixing of different spin states coupled by Raman beams, gives rise to a striped modulated density in the condensate.

In this rich but rather complex scenario, emerges the need for a unifying property able to quantify the deviations of supersolids from ordinary systems. The sub-superfluid fraction proposed by Leggett fits perfectly in this context. Not only it is the key property for supersolids, but its measure may be also experimentally accessible in a variety of systems thanks to the connection with the Josephson dynamics. In particular, this possibility is extremely interesting for the superconductor materials showing PDW order [1], where Leggett's idea of a reduced superfluid fraction has never been considered, in favor of the standard superfluid stiffness Λ which is usually assessed from penetration depth measurements [186]. There is indeed evidence that Λ is lower in superconductors hosting PDW phases [133, 40, 24], than in ordinary superconductors.

3.1 Phase stiffness of a dipolar supersolid

Considering a macroscopic wavefunction $\psi e^{i\phi}$, the general definition of the superfluid fraction [103, 53] is the deviation of the kinetic energy cost E_{kin} associated with a local perturbation of the phase, from the case of homogeneous superfluid E_{kin}^{hom}

$$f_s = \frac{E_{kin}\left(\delta\phi\right)}{E_{kin}^{hom}\left(\delta\phi\right)}\,, \tag{3.2}$$

where $\delta\phi \to 0$ is a phase twist on a distance d. A reduced superfluid fraction is then associated with a reduction of the energy cost to locally twist the phase of the system. This concept is pictured in Fig. 3.2. In his seminal paper [103], Leggett considers N bosonic helium atoms confined in a cylindrical annulus with radius R and thickness d, which is rotating at a constant angular velocity Ω. For such a system the kinetic energy[1] is $I\Omega^2/2$, where the moment of inertia depends on the superfluid fraction through Eq. 3.1 and $I_C = N mR^2$. For ordinary superfluids, the moment of inertia, thus the kinetic energy associated with the motion, vanishes for $\Omega \to 0$, due to the quantization of angular momentum [72]. In this context, a reduced superfluid fraction gives rise to a finite I, meaning that the system starts to rotate in the annulus. To calculate the free energy of the system, we must pass in the co-rotating frame [77], where the effect of the rotation at velocity $v = \Omega R$ is to add a phase factor to the wavefunction in the laboratory frame ψ. Indeed, considering the transformation $x' \to x - vt$, $p' \to p - mv$, where primed variables are in the co-rotating frame, the phase of the wavefunction in the two references ϕ' and ϕ must verify

$$\phi'(x', t') = \phi(x, t) + \frac{1}{\hbar}\left(\frac{mv^2}{2}t - mvx\right). \tag{3.3}$$

This additional phase factor in the co-rotating frame depended linearly on the position, meaning that the effect of the rotation in this reference is a change in the phase along the annulus. Calculating the phase difference accumulated over the total length of the annulus, we have

$$\phi'(2\pi R) - \phi'(0) = \phi(2\pi R) - \phi(0) - \frac{1}{\hbar}mv2\pi R. \tag{3.4}$$

This last term can be understood as a phase twist $\delta\phi$ over a distance $d = 2\pi R$

$$\delta\phi = \frac{2\pi m}{\hbar}\Omega R^2, \tag{3.5}$$

which depends on the angular velocity of the rotation. If we now come back to the general definition of f_s in Eq. 3.2, we must calculate E_{kin} as

$$E_{kin} = \frac{\hbar}{2m}\int \mathrm{d}x n(x) \left|\nabla\phi(x)\right|^2 \tag{3.6}$$

by assuming the form of the density $n(x)$ along the annulus[2]. Instead,

---

[1] This accounts for the free energy of the system, connected to the rotation.

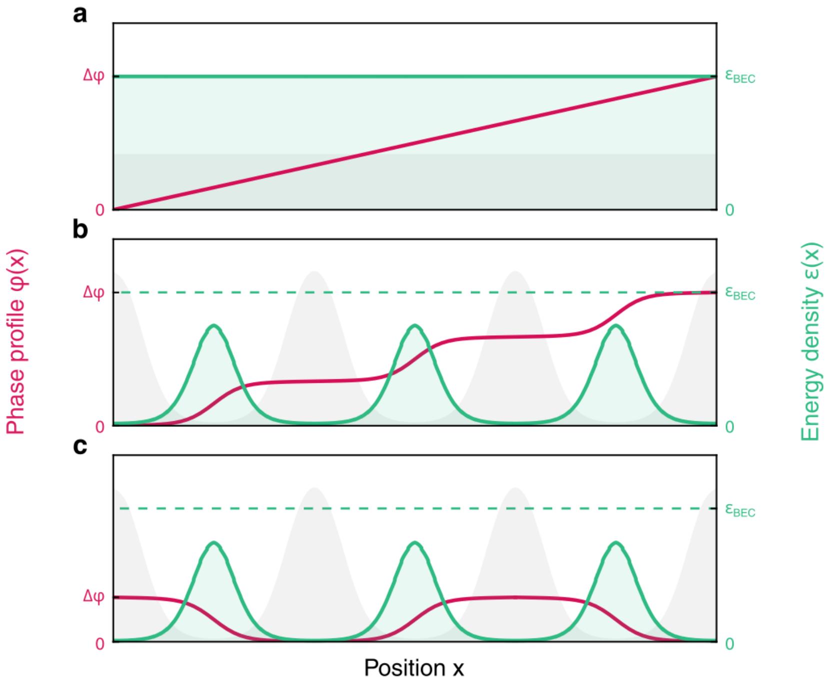

Figure 3.2: Reduction of the superfluid stiffness for density modulated superfluids perturbed by a local phase twist. Shaded gray regions represent the profiles of the superfluid density for a homogeneous system (a) and for a supersolid (b-c). The red curve shows the spatial dependence of the phase of the macroscopic wavefunction in the case of a linear phase twist (a), a rotating supersolid (b), and the Josephson excitation (c) employed in our experiment. The green shaded area represents the kinetic energy density associated with the phase variation for the three cases (integrand of Eq. 3.6). The integral of the green areas is proportional to the superfluid stiffness. The superfluid fraction of of Eq. 3.2 is such integral, normalized to the one of the homogeneous case (a). Note that the reduction of f_s is the same for (b-c), which have the same kinetic energy density.

the form of $\phi(x)$ must be searched in order to minimize E_{kin}. For a homogeneous superfluid (Fig. 3.2a), with $n(x) = consts$, we know that $\phi(x)$ is simply a linear gradient, corresponding to a superfluid velocity $v_s = \hbar\delta\phi/(md)$. The denominator in Eq. 3.2 is then $E_{kin}^{hom} = Nmv_s^2/2$. In the case of periodic modulated density $n(x+\lambda) = n(x)$, Leggett derived $\phi(x)$ employing a variational approach [103, 104] to minimize the energy in Eq. 3.6, finding

$$\phi(x) = \delta\phi \int_0^x \frac{\mathrm{d}x'}{n(x')} \left(\int_0^d \frac{\mathrm{d}x'}{n(x')} \right)^{-1} . \tag{3.7}$$

As shown in Fig. 3.2b, this phase profile has also a modulation, as the density, with the phase gradient increasing in the low-density region while being almost zero in the high-density regions. The accommodation of most of the phase variation in weak links, results in an overall reduction of the kinetic energy, which reads

$$E_{kin}(\delta\phi) = \frac{\hbar^2 N}{2md^2}\delta\phi^2 f_s^{up} \tag{3.8}$$

with the superfluid fraction defined as the following integral over the unit cell

$$f_s^{up} = \left(\frac{1}{\lambda} \int_0^\lambda \frac{\mathrm{d}x}{\bar{n}(x)} \right)^{-1} \tag{3.9}$$

where $\bar{n}$ denotes the normalized 1D superfluid density of the system. It's important to note that this expression of the superfluid fraction corresponds to an upper bound since we have reduced the full three-dimensional problem of the annulus to one dimension. Taking into account the dependence of the density along the vertical and transverse directions, if any, would result in a further reduced superfluid fraction which eventually hit the lower bound f_s^{lo}, obtained by integrating over the other directions f_s^{up}, where now $\bar{n} = \bar{n}(x, y, z)$. Focusing on the upper limit, for homogeneous superfluids we have $\bar{n} = 1$, hence $f_s^{up} = 1$. For the supersolid, where the density is modulated we have instead $f_s^{up} < 1$, and approaches zero if, at least in one point in the unit cell, $\bar{n} \to 0$. The latter case occurs in dipolar systems when dipole-dipole interactions are strong enough to localize all the atoms in the clusters, with no overlaps between adjacent sites, realizing an

---

[2] We consider densities depending only on the position along the annulus, and constant over the width of the annulus, reducing the problem to a 1D model.

incoherent array of droplets, known as *droplet crystal* [181]. I stress that a reduced superfluid fraction in supersolids is not linked to thermal effects. Indeed, from Leggett's theory is clear that the reduction of f_s comes only from the shape of the superfluid density, even if the thermal fraction of the system is zero (namely at $T = 0$). The mapping between rotating supersolids and static systems with a phase twist becomes clear if we now write Eq. 3.8 making $\delta\phi$ explicit

$$E_{kin} = \frac{\hbar^2 N}{2md^2} f_s \left(\frac{2\pi m}{\hbar}\Omega R^2\right)^2 = \frac{1}{2} I_C \Omega^2 f_s \, , \tag{3.10}$$

which is precisely the kinetic energy for the rotating system with $f_s^{lo} \leq f_s \leq f_s^{up}$. This mapping allows us to bring Leggett's theory to a wider field of application, since the superfluid fraction in Eq. 3.9 derived for rotating supersolids, is not peculiar to rotations, but is generalized to all kinds of phase twists.

In [16] we follow this line of thought, associating the superfluid fraction to the Josephson effect. As sketched in Fig. 3.2c, we consider a phase twist similar to the one in Eq. 3.7, but with changing sign every lattice cell of the supersolid. In this context, the mapping with rotations is lost, since the resulting motion of the system is rather an oscillation of the peak density between adjacent clusters without a global flow of density, i.e. the average global phase gradient is zero. However, if we focus on a single supersolid cell, we can still define a phase twist[3] $\Delta\phi$ over a distance $d = \lambda$, and all the previous results, derived in the annulus, remain valid. In particular, since E_{kin} in Eq. 3.8 depends on the square of the phase twist, we find exactly the same kinetic energy density in both cases (Fig. 3.2b-c). The important difference between the two approaches comes instead when we attempt to measure f_s experimentally. As discussed in the introduction of this chapter, in the case of rotation we basically need to measure the moment of inertia I to extract the superfluid fraction of the system. Modeling the supersolid as an array of Josephson junctions, we have direct access to E_{kin} measuring the local coupling between a single junction, instead of a global measure as in the rotation case. Indeed, as I will discuss in more detail in the next section, when a small $\Delta\phi$ is imposed on the single junction the kinetic energy is given by $E_{kin} = NK\Delta\phi^2$ [173],

---

[3] Here I use a different notation, since $\Delta\phi$ is now externally imposed, and doesn't have anything to do with the phase factor $\delta\phi$ in Eq. 3.5, which was given by the rotation.

where K is the coupling energy (or tunneling) of the junction, which can be measured by studying the Josephson oscillations. Inserting this into Eq. 3.2, we can derive an alternative expression for the superfluid fraction

$$f_s = \frac{K}{\hbar^2/(2md^2)}\,, \tag{3.11}$$

which has to be compared with Eq. 3.9. Indeed, Leggett derived an expression analogous to the upper bound of the superfluid fraction in Eq. 3.9 for the coupling energy of a single Josephson junction [196]. However, a connection between f_s and K, has never been considered. This could sound surprising since the two concepts seem to be intimately linked in the supersolid phase, where a sub-unity superfluid fraction directly means a finite Josephson coupling between adjacent clusters and vice versa.

3.2 Josephson model of a supersolid

Let's now discuss how a supersolid can be described as an array of Josephson junctions. I will start with an overview of the well known model which describes a single bosonic Josephson junction [173], which is commonly used to describe the dynamics of a Bose-Einstein condensate trapped in a double-well potential. In this context, it's typical to build a *two-mode* model, where the system wavefunction is decomposed in two mutually orthogonal modes: the symmetric ground state ψ_S and the first anti-symmetric excited state ψ_A of the double well potential. The coupling energy of the system is then defined as the energy difference between these two modes

$$K = \frac{\varepsilon_A - \varepsilon_S}{2}\,. \tag{3.12}$$

To write the Josephson Hamiltonian, we use a change of basis to combine ψ_A and ψ_S into two new modes, localized either on the left, ψ_L, or the right well, ψ_R. We can then associate to the localized modes the populations N_L, N_R, and the phases ϕ_L, and ϕ_R. The Josephson variables are defined as the relative difference of phase and populations

$$\begin{aligned} Z &= \frac{N_L - N_R}{N}\,, \\ \Delta_\phi &= \phi_L - \phi_R\,. \end{aligned} \tag{3.13}$$

The Josephson Hamiltonian with these variables is

$$\mathcal{H}_J = -KN\sqrt{1-Z^2}\cos\left(\Delta\phi\right) + \frac{1}{4}UN^2Z^2\,, \tag{3.14}$$

where U is the interaction energy for the mode ψ_{L}, R. Here we consider a symmetric double well, with $U_L = U_R = U$. Noting that the Josephson variables Z and $\Delta\phi$ are canonically conjugate, namely $\dot{Z} = 2/\left(\hbar N\right)\partial_Z\mathcal{H}$ and $\dot{\Delta\phi} = -2/\left(\hbar N\right)\partial_{\Delta\phi}\mathcal{H}$, we can write two coupled differential equations for the evolution of Z and $\Delta\phi$

$$\begin{aligned}
\hbar\dot{Z} &= -2K\sqrt{1-Z^2}\sin\left(\Delta\phi\right) \xrightarrow{Z,\Delta\phi\ll 1} -2K\sin\left(\Delta\phi\right) \\
\hbar\dot{\Delta}_\phi &= 2K\frac{Z}{\sqrt{1-Z^2}}\cos\left(\Delta\phi\right) - NUZ \xrightarrow{Z,\Delta\phi\ll 1} -\left(2K+NU\right)Z\,,
\end{aligned} \tag{3.15}$$

with a rather simple form in the limit of small oscillations $Z\,,\Delta\phi \ll 1$. Typically, $\dot{\Delta\phi}$ in this limit is rescaled by $2K$, and rewritten simply as $\dot{\Delta\phi} = -\left(1+\Lambda\right)Z$, introducing the dimensionless interaction parameter $\Lambda = NU/2K$.

To get the equation of motion of the Josephson dynamics, hence the Josephson frequency, we compute $\ddot{Z}$ starting from the Eqs. 3.15, obtaining

$$\hbar^2\ddot{Z} = -4K^2\left[1+\Lambda\sqrt{1+Z^2}\cos\left(\Delta\phi\right)\right]Z \xrightarrow{Z,\Delta\phi\ll 1} -4K^2\left(1+\Lambda\right)Z\,, \tag{3.16}$$

which, in the strongly interacting regime $\Lambda \gg 1$, gives $\ddot{Z} = -2KNUZ$, which is the equation of motion of a harmonic oscillator with frequency

$$\omega_J^{(2)} = \sqrt{2KNU}\,, \tag{3.17}$$

where the label (2) specifies that this expression only holds for the *two-mode* model. This has been experimentally verified over a broad range of interaction strengths Λ in [175], also probing the Josephson dynamics in the limit of large amplitudes. Remarkably, for a large enough initial imbalance Z_0, the onset of macroscopic quantum self-trapping (MQST) has been observed, as predicted by the model [173]. In this regime, the initial kinetic energy given to the system by the large imbalance, produces fast oscillations of Z with a non-zero average value. The phase difference $\Delta\phi$, instead, increase linearly time, changing by 2π over the period of Z oscillations. The MQST dynamics triggers at a critical value $Z_0^* = 2\sqrt{\Lambda - 1}/\Lambda$. It's important to note that this phenomenon cannot be produced by large initial phase imprints, i.e. there is no critical value of $\Delta\phi_0$. Indeed, the *two-mode* model here presented can be mapped in the oscillatory dynamics of a nonrigid pendulum [173], where Z is the velocity and $\Delta\phi$ is the angle of the bob. It is then immediate to understand what happens if we increase the initial velocity over the critical value: the bob to rotate, with angular velocity oscillations around a non-zero value, while the position increases linearly. The same effect cannot happen if, instead of starting with an initial velocity, we trigger the dynamics by changing the initial angle. Large phase (angle) excitations can only produce anharmonicity in the oscillations manifested as deviations from a sinusoidal form. This is captured by the general solution of Eq. 3.16 which can be integrated numerically in the limit of large oscillations.

To take a conceptual step closer to the supersolid, I will try to extend this model, intuitively, to the case of a Josephson junctions array (JJA). For example, we can think of an ideal system of junctions identical to the one already introduced, therefore, if we now consider a single junction of the array, all the previous results may apply. The only difference, with respect to the isolated junction, is that now the inflow (or outflow) of atoms in a given reservoir has an additional contribution due to another coupled well. Indeed, in the case of a JJA, each reservoir has two neighbors. From this argument is not surprising that the Eqs. 3.15 must be modified to take into account the additional currents, by substituting $K \to 2K$ in $\dot{Z}$. Note that $\dot{\Delta\phi}$ is unchanged since depends only on the instantaneous difference between the modes populations, weighted by the interaction energy (i.e. does not depend on the currents). The additional factor of two in $\dot{Z}$ transfers then to the frequency as a factor $\sqrt{2}$ with respect to the result in Eq. 3.17 of the *two-mode* model.

The case of the supersolid is even more complex since the system inhomogeneity makes the couplings and the interaction energies different for each junction. However, as I will discuss in the next section, we find that under the right conditions among the energy scales which are fixed

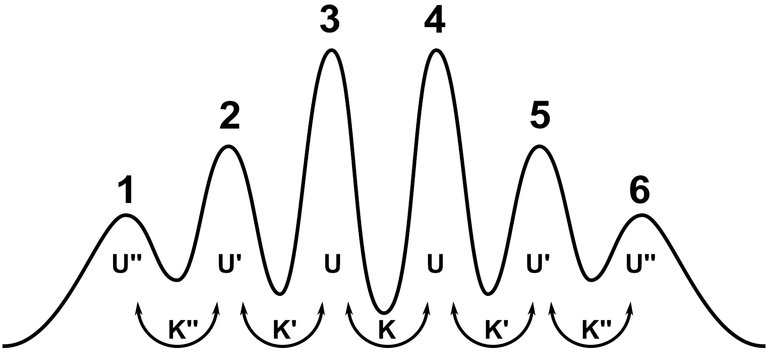

Figure 3.3: Sketch of the inhomogeneous system. Starting from the center clusters we define the interaction energies U, U', and U'', and the coupling energies between clusters K, K', and K''. Note that this sketch is not to scale, and the real lateral modes are indeed very small (see Fig. 3.5a for reference).

by the equilibrium density profile, we can derive an effective model for the supersolid, similar to the one presented here. The idea of a simple description of the Josephson dynamics in a complicated system, as the supersolid, is also supported by the experimental observation discussed below. The main result, from the point of view of the Josephson effect, is that not only the supersolid can sustain Josephson oscillations, but these constitute a normal mode of the system, characterized by a single frequency. Previous theoretical models of the Josephson dynamics in supersolids have instead focused only on a phenomenological model of the relaxation dynamics towards the system ground state [76], associating the measured phase fluctuations with the Josephson couplings.

3.2.1 Six-mode Josephson Model

The Josephson model we developed for describing the supersolid is mainly inspired by the typical experimental configuration sketched in Fig. 3.5. We consider six inhomogeneous clusters labeled by the index $j = 1 \ldots 6$, characterized by a population N_j and a phase ϕ_j, with different couplings and interaction energies. Given the symmetry of the wavefunction with respect to the trap center, we choose $K_{34} = K$, $K_{23} = K_{45} = K'$, and $K_{12} = K_{56} = K''$, and similarly $U_3 = U_4 = U$, $U_2 = U_5 = U'$, and $U_1 = U_6 = U''$. For small perturbations of the equilibrium, the equations for the currents in each mode are given by

$$\begin{aligned}
\dot{N}_1 &= -2K''\sqrt{N_2N_1}\sin\left(\phi_{21}\right),\\
\dot{N}_2 &= 2K''\sqrt{N_2N_1}\sin\left(\phi_{21}\right) - 2K'\sqrt{N_3N_2}\sin\left(\phi_{32}\right),\\
\dot{N}_3 &= 2K'\sqrt{N_3N_2}\sin\left(\phi_{32}\right) - 2K\sqrt{N_4N_3}\sin\left(\phi_{43}\right),\\
\dot{N}_4 &= 2K\sqrt{N_4N_3}\sin\left(\phi_{43}\right) - 2K'\sqrt{N_5N_4}\sin\left(\phi_{54}\right),\\
\dot{N}_5 &= 2K'\sqrt{N_5N_4}\sin\left(\phi_{54}\right) - 2K''\sqrt{N_6N_5}\sin\left(\phi_{65}\right),\\
\dot{N}_6 &= 2K''\sqrt{N_6N_5}\sin\left(\phi_{65}\right)
\end{aligned} \tag{3.18}$$

while the time evolution of phase differences $\phi_{j,j-1} = \phi_j - \phi_{j-1}$ are instead

$$\begin{aligned}
\dot{\phi}_{21} &= E_1 + U''N_1 - U'N_2,\\
\dot{\phi}_{23} &= E_0 + U'N_2 - UN_3,\\
\dot{\phi}_{34} &= U\left(N_3 - N_4\right),\\
\dot{\phi}_{45} &= -E_0 + UN_4 - U'N_5,\\
\dot{\phi}_{56} &= -E_1 + U'N_5 - U''N_6,
\end{aligned} \tag{3.19}$$

where the energy offsets E_0 and E_1 are calculated as the energy of the harmonic traps at the positions $x_{2,5} = \pm 3\lambda/2$, and $x_{1,6} = \pm 5\lambda/2$ for the inner and outer lateral peaks respectively. Note that to derive the Eqs. 3.19 we have considered the limit $\left(N_4 + N_3\right)U/\left(2K\right) \gg 1$ (analogous to the strongly interacting limit $Uplambda \gg 1$ in the *two-mode* model)[4], thus neglecting the tunneling terms in the evolution of the phases. Moreover, considering small oscillations, we can substitute the time-dependent populations N_j with their associated equilibrium values $\bar{N}_j$ in Eqs. 3.18 and Eqs. 3.19.

Let's now focus on a single unit cell of the supersolid. In particular, we want to address the dynamics of the population imbalance $\Delta N = N_3 - N_4$ and phase difference $\phi_{34} = \phi_3 - \phi_4$, between the two central clusters. For an infinite and homogeneous supersolid, the results of the previous section apply, and we recover Josephson oscillations at frequency $\sqrt{4KN_{34}U}$, where N_{34} is now the total number of atoms in the central clusters. In inhomogeneous supersolids, for arbitrary values

---

[4] We checked from numerical simulations that in the whole range investigated our system has $\left(N_4 + N_3\right)U/\left(2K\right) > 25$

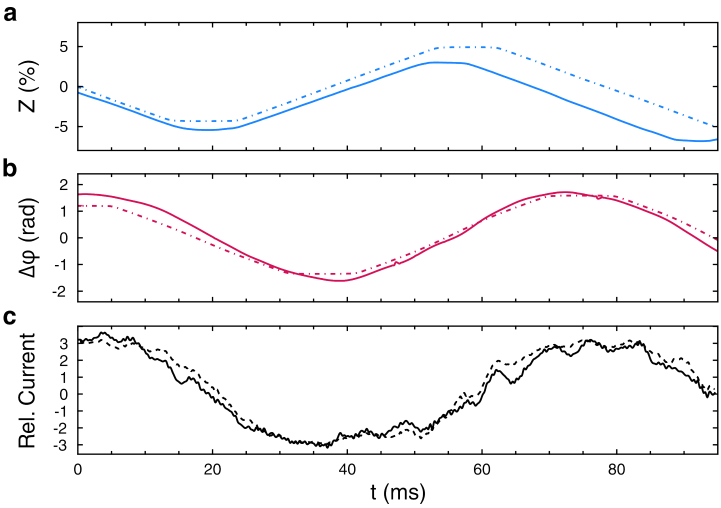

Figure 3.4: Results of the 6-mode model compared to numerical simulations. Time evolution of Z (a) and $\Delta\phi$ (b). Thick lines are numerical eGPE simulations, while dot-dashed lines are the calculations from the 6-mode model. (d) Relative currents between the central and lateral clusters appearing in Eq. 3.21. The solid line is $(N_3 - N_4)/2$, while the dashed line is $(N_6 + N_5 - N_2 - N_1)$. Both quantities are extracted from numerical eGPE simulations, showing that the condition on the currents is satisfied for our system, with $\alpha = 2$.

of the coupling and the interaction energies, the dynamics resulting from the Eqs. 3.18 and Eqs. 3.19 can be integrated numerically showing multiple frequencies given by all the contributions of the different clusters. In the real case, however, the parameters of the model are not arbitrary since the supersolid adjusts its density in the harmonic potential realizing a particular configuration. The dynamics observed in numerical simulations and predicted by the *six-mode* Josephson model, presented in Fig. 3.4, shows indeed clear oscillations at a single frequency. Analytically, this can be derived from the Eqs. 3.18 and Eqs. 3.19, assuming

$$\begin{aligned} \frac{U''}{U'} &= 1 + \frac{K'}{K''}\sqrt{\frac{\bar{N}_3}{\bar{N}_1}}, \\ \frac{U'}{U} &= \left(1 + \frac{K}{K'}\sqrt{\frac{\bar{N}_3}{\bar{N}_2}}\right)\left(1 + \frac{K''}{K'}\sqrt{\frac{\bar{N}_1}{\bar{N}_3}}\right)^{-1}. \end{aligned} \tag{3.20}$$

This condition on the energy scales translates into the currents as

$$\dot{N}_3 - \dot{N}_4 = \alpha\left(\dot{N}_6 - \dot{N}_1 + \dot{N}_5 - \dot{N}_2\right), \tag{3.21}$$

where $\alpha = (U/U' - U/U'')^{-1}$ takes into account the system inhomogeneity. The conditions in Eqs. 3.20, can be verified by extracting all the involved parameters from numerical simulations. A more direct approach is instead to look at the two sides of Eq. 3.21, which is verified in our system for $\alpha = 2$.

The resulting Josephson oscillations are described by the two coupled equations

$$\begin{aligned} \dot{\Delta N} &= -4KN_{34}\sin(\Delta\phi)\,, \\ \dot{\phi}_{34} &= U\Delta N\,, \end{aligned} \tag{3.22}$$

where we keep only linear terms in $\Delta N/N$. Remarkably, these equations are formally identical to the low amplitude limit of Eq. 3.15, with the only modification of the additional factor of two in the current, due to the presence of neighboring clusters. In order to compare these results with the experimental observation, we need to define our observables. Indeed, in the experiment, we cannot resolve directly the population of the individual clusters, since the optical resolution of our imaging system is of the same order as the supersolid lattice spacing λ. As I will discuss more in detail in the next sections, what we measure is instead the population difference between the left and right halves of the system. The phase difference ϕ_{34} is instead measured from the interference pattern obtained after expanding the supersolid cloud (see Sec. 3.6.3). Thus, we define the experimental variables as $Z = (N_1 + N_2 + N_3 - N_4 - N_5 - N_6)/N$ and $\Delta\phi = \phi_{34}$. Noting that, from Eq. 3.21 with $\alpha = 2$, we have $\Delta N = 2NZ$, we can rewrite the Josephson equations 3.22 with the experimental variables

$$\begin{aligned} \dot{Z} &= -2K\frac{N_{34}}{N}\sin(\Delta\phi)\,. \\ \dot{\Delta\phi} &= 2NUZ\,, \end{aligned} \tag{3.23}$$

Studying the equations of motion of the system, we recover

$$\omega_J = \sqrt{4KN_{34}U}\,, \tag{3.24}$$

which is identical to the prediction for the Josephson junctions array.

3.3 Observation of Josephson oscillations

To experimentally study Josephson oscillations in the dipolar supersolid, we need to carefully prepare the supersolid as close as possible to its ground state, selectively excite the Josephson mode, and then, be able to detect both the phase difference and the population imbalance between neighboring lattice sites, following their time evolution. The system is prepared in a harmonic trap very similar to V_C (Eq. 2.13), used previously in the superfluid-supersolid transition experiment. With trap frequencies $(\nu_x, \nu_y, \nu_z) = 2\pi\,(18, 97, 102)\,\mathrm{Hz}$, the confinement along the transverse direction is sufficiently strong to suppress the 2D response of the system (as discussed Sec. 2.1.3) and allow an adiabatic crossing of a continuous quantum phase transition towards the supersolid phase [15, 10, 3]. This is done by reducing the scattering length a_s of the system, increasing the relative strength $\epsilon_{dd} = a_{dd}/a_s$ of dipole-dipole interactions triggering the supersolid formation. Further details on the preparation of the supersolid are reported in Chapter 4. The transition point for our experimental system, which typically has $N = 3 \times 10^4$ atoms, is $\epsilon_{dd} = 1.38$ and the supersolid range extends up to $\epsilon_{dd} = 1.45$ above which another quantum phase transition leads to the so-called droplet crystal [181], which is characterized by a vanishing Josephson coupling between the clusters. Changing the interactions doesn't affect only such coupling, but also changes the interaction energy U in each cluster. As shown in Fig. 3.5a, our trapped supersolid is inhomogeneous and features two central clusters with coupling K and interaction energy U, plus four other smaller clusters spaced by $\lambda \simeq 4\,\mu\mathrm{m}$.

To trigger the Josephson oscillations we use a phase imprinting technique [26, 117] to tailor the supersolid phase profile in a shape similar to the one presented in Fig. 3.2. To imprint a phase difference between adjacent clusters, that changes sign every lattice cell, we employ a long-spaced optical lattice with period $\approx 2\lambda$, as sketched in Fig. 3.5a. The lattice is aligned such that the position of one of the central clusters matches a maximum of the light intensity, while the other lies in a minimum. The lattice depth is about $V_{lat} \sim k_B 100\,\mathrm{nK}$. By shining the lattice light for a brief pulse of about $\tau = 100\,\mu\mathrm{s}$, we imprint a phase difference $\phi_0 \propto U_{lat}\tau$ of about $\pi/2$ between two clusters. At this point we let the Josephson dynamics run freely, by keeping the harmonic confinement and removing the optical lattice.

At a given time t of the system dynamics, we evaluate the population imbalance Z between the left and right halves of the supersolid and the phase difference $\Delta\phi$ between adjacent clusters, by either in-situ phase-contrast imaging (see Sec. 4.3) or standard absorption imaging

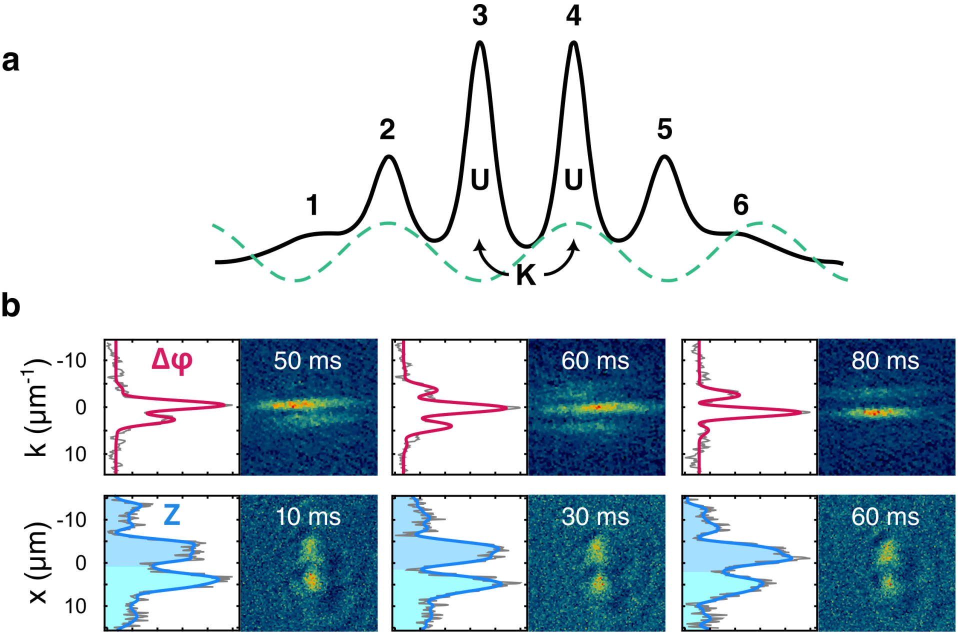

Figure 3.5: Exciting and detecting the Josephson dynamics. (a) Sketch of the experimental system, showing the supersolid density profile obtained by eGPE numerical simulation at the equilibrium (black line) and the optical lattice used for the phase imprinting is (dashed green line). (b) Single shots of the experimental realizations and corresponding signals obtained by integrating along the horizontal direction. Top row: interference pattern after a free expansion. Red curves are fit functions used to extract the phase difference $\Delta\phi$. Bottom row: in-situ images. Colored areas indicate the populations of the left and right halves of the supersolid used to extract the population imbalance Z.

performed after a free expansion of the cloud. Single shots of the dynamics (Fig. 3.5b) show the interference pattern expected from the expansion of the supersolid and the typical double peaks signal associated with its density, for different evolution times t. Since the spatial resolution of the in-situ imaging used for the experiment, is slightly lower than the supersolid spacing λ, we employ an optical manipulation of the density, in order to increase the separation of the central clusters. A few ms before the imaging we use the same optical lattice used for the phase imprinting, but with a much shallower depth, to smoothly separate the central clusters: the one sitting on the minima remains practically untouched, while the other is pushed away by the lattice potential and the dipolar repulsion. The resulting density (lower panel in Fig. 3.5b) conserves the information about the imbalance Z. More details about the so-called *optical separation* and the detection of the phase difference are given in Sec. 3.6. Moreover, the design of a new imaging scheme with increased resolution, able to address the supersolid clusters directly, is discussed in Chapter 4.

The results for the Josephson oscillations are reported in Fig. 3.6. We detect oscillations with single-frequency both in Z and $\Delta\phi$, with a mutual phase shift of $\pi/2$ as expected for standard bosonic [173, 30, 5, 108] or fermionic [187] Josephson junctions. This characteristic phase relation between Z and $\Delta\phi$, is indeed a smoking gun of the Josephson effect [80], since demonstrates that the phase and population imbalance follow the Eqs. 3.23. As shown in Fig. 3.6, the observation time is limited in the experiment by the lifetime[5] of the system, which is about 100 ms. Since the observed frequency decreases for increasing ϵ_{dd} (i.e. for larger contrasts of the supersolid density modulation), this poses a limit to the lower frequencies detectable in the experiment, which are of the order of 10 Hz.

We extract the Josephson frequencies by fitting the experimental data with sinusoidal functions with frequency, amplitude, phase shift, and vertical offset as free parameters. Our experimental data agree with numerical simulations of the Josephson dynamics carried out by

---

[5] This is defined by the coherence time of the supersolid which is limited by the losses. Indeed, even if the number of atoms is still enough to detect a density modulation in-situ, the unavoidable losses at the density peaks scramble the phase of the supersolid, washing away the interference fringes in time-of-flight.

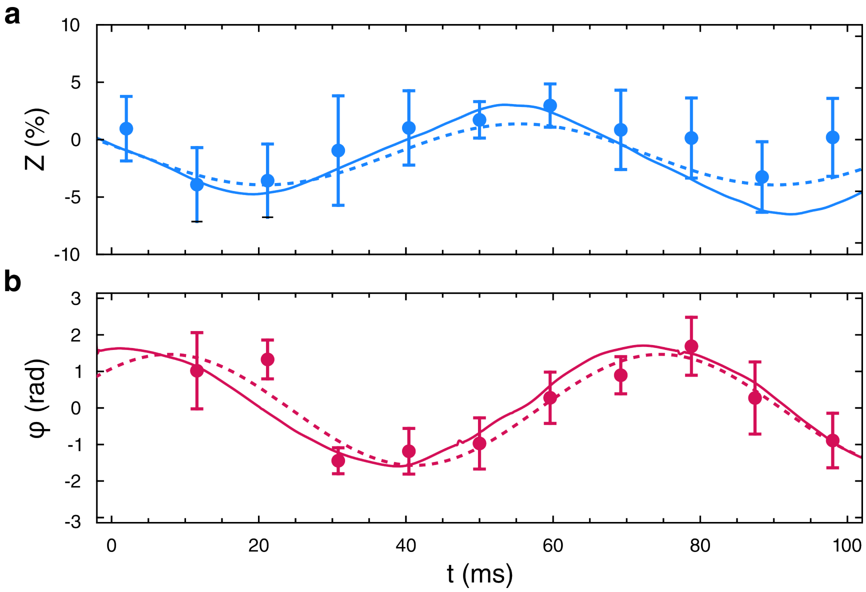

Figure 3.6: Josephson oscillations of Z (a) and $\Delta\phi$ (b) as a function of time at $\epsilon_{dd} = 1.428$. Dots are experimental points. Solid lines are numerical simulations for the same parameters. The dotted lines are sinusoidal fits to the experimental data.

integrating numerically the time-dependent extended Gross-Pitaevskii equation (eGPE) with the same parameters of the experiment. To further validate our observations, we also applied the same excitation scheme discussed here to standard BEC, tuning ϵ_{dd} in the superfluid side of the quantum phase transition, without detecting any oscillation. This demonstrates that the concept of supersolidity is very much associated with the possibility of sustaining Josephson oscillations, without employing external potential to shape the system density creating weak links.

We repeat the measurement by varying the interaction parameter ϵ_{dd}, corresponding to different depths of the supersolid density modulation, hence lower Josephson couplings. The associated decrease of the measured Josephson frequency ω_J as a function of ϵ_{dd} is presented in Fig. 3.7. The experimental data (red and blue markers) are compared with the numerical simulations (black dots), showing an overall agreement with minor deviations for large ϵ_{dd}. The decrease on ω_J for increasing ϵ_{dd}, supports the idea that by weakening the link between the superfluid clusters of the supersolid, the current decreases and the systems get more and more localized. This led to a drastic reduction

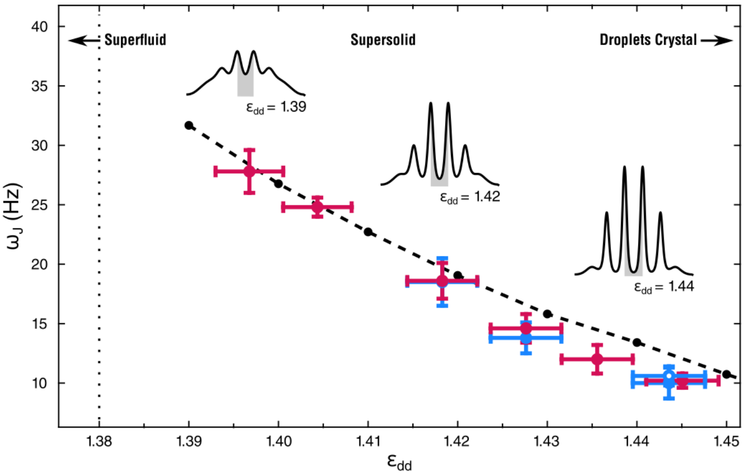

Figure 3.7: Josephson frequencies as a function of the interaction parameter ϵ_{dd}. Red dots are the experimental frequencies for $\Delta\phi$. Filled and open blue dots are the frequencies for Z measured by in situ imaging with and without optical separation, respectively. Black points are the results of numerical simulations. The dashed line is a guide for the eye. The insets show the modulated ground state density profiles obtained from numerical simulations for different values of ϵ_{dd}. The vertical dotted line marks the critical point of the superfluid-supersolid quantum phase transition.

of the coupling energy K, witnessed by the reduction of ω_J, while modifying only slightly the interaction energy U, which changes of 15% roughly within the whole investigated region (based on numerical grounds).

In Fig. 3.7 are reported different types of experimental data, associated with different experiments. Indeed, the measurement of Z and $\Delta\phi$ are not simultaneous, and we need to run the experiment twice[6] with identical preparation and excitation, to measure both observables. In principle, an experimental sequence allowing the measurement of both in-situ densities and time-of-flight momentum distributions may be realized by exploiting non-destructive measurements of the supersolid density. The phase-contrast imaging employed already in our experiment is indeed non-destructive since works with non-resonant light. However, to optimize the signal-to-noise ratio in our measurement, we

---

[6] In each run we scan the evolution time t, with typically 20 realizations per temporal point in order to have enough statistics.

use light not too far from resonance, resulting in a sensible perturbation of the wavefunction caused by the imaging light. Further details on the phase-contrast imaging technique are discussed in Chapter 4. The red dots in Fig. 3.7 are the results for ω_J extracted by the phase difference oscillations. The blued dots are instead the Josephson frequencies extracted from the population imbalance Z employing the optical separation introduced above and discussed in Sec. 3.6. Only for high enough contrasts in the density modulation, namely at $\epsilon_{dd} = 1.444$, we are able to distinguish clearly the supersolid clusters and extract Z directly without any optical manipulation of the density distribution. For this interaction parameter, we performed the oscillation measurement with and without the optical separation. The latter, marked with the open blue circle in Fig. 3.7, agrees with both the data point obtained with the separation and with the associated data point extracted from the $\Delta\phi$ oscillations, demonstrating the validity of our method. When the density contrast is too small, for $\epsilon_{dd} < 1.41$, the signal-to-noise ratio in Z is too high (even with the optical separation) to detect clear oscillations. In this regime, we rely only on the Josephson frequencies based on $\Delta\phi$.

Here I want to stress that, even if the Josephson model of the supersolid holds only up to a certain K, where the multi-mode description is valid, and breaks when the supersolid modulation is too shallow, the results of numerical simulations show that the model holds for the whole range of ϵ_{dd} investigated. Indeed, the numerical simulations, not affected by technical problems such as the finite resolution, show for both Z and $\Delta\phi$ clear oscillations with the characteristic Josephson phase shift, up to $\epsilon_{dd} = 1.39$. Another interesting point of discussion concerns the small deviations of experimental data from the numerical simulations at large ϵ_{dd}. This effect may be related to the different excitation regimes employed in the experiment. Indeed, while in numerical simulations the Josephson dynamics is studied in the small amplitude regime (where a perturbative approach is valid), the initial imprinted phase is large in the experiment, around 1 rad. This *high amplitudes* regime is discussed in Sec. 3.6.1. Even if the deviations from the small amplitude regime can be sensible (at large ϵ_{dd} we have deviations of about 25%), the experimental data has been validated by simulating the high amplitude oscillations using larger initial phase imprints. In Fig. 3.6, solid lines, showing the results of such simulations, are in good agreement with our observations. Nevertheless, the *unperturbed* Josephson frequencies (predicted also by the model in Sec. 3.2) plotted in Fig. 3.7 are the ones extracted in the small amplitude regime.

3.4 Measurement of the superfluid fraction

To translate the measured Josephson frequencies in the superfluid fraction we use the definition in Eq. 3.11, where K is evaluated as

$$K = \frac{\omega_J^2}{4N_{34}U}\,, \tag{3.25}$$

obtained simply by reversing the Eq. 3.24 derived for ω_J with the 6-mode model. This relation remains valid in the regime of high amplitudes. To calculate K, we use the quantity $N_{34}U$ provided by numerical simulations. Here N_{34} is simply the number of atoms in the central clusters at the equilibrium, that can be extracted from the simulated ground states, and U is their interaction energy. To evaluate U, we study the linear dependence between $\Delta\dot{\phi}$ and Z (see Eq. 3.23) on numerical data of the Josephson dynamics. The other parameter entering the superfluid fraction is the spacing of the supersolid structure λ (d in Eq. 3.11), which we obtain from in-situ images to be $\lambda = 3.7(2)\,\mu\mathrm{m}$ at large ϵ_{dd}, where we are able to resolve the two central clusters. Even if the density peaks associated with the two clusters are overlapped due to our finite resolution their center of mass is well defined, meaning that the uncertainty over the average λ could be smaller than the resolution if we consider enough statistics. However, we don't have direct access to the details of the supersolid density. From the numerical simulations, we have evidence that the spacing λ weakly depends on ϵ_{dd}, but in our configuration, the deviations from the average value are smaller than the experimental uncertainty considered in our calculation.

Our results are reported in Fig. 3.8a. The black points represent the calculated superfluid fractions, based on the Josephson frequencies extracted by the phase difference oscillations, using the procedure explained above. The systematic underestimation of the Josephson frequencies in the high amplitude regime (see Fig. 3.12), is taken into account by applying a systematic uncertainty to f_s which increases

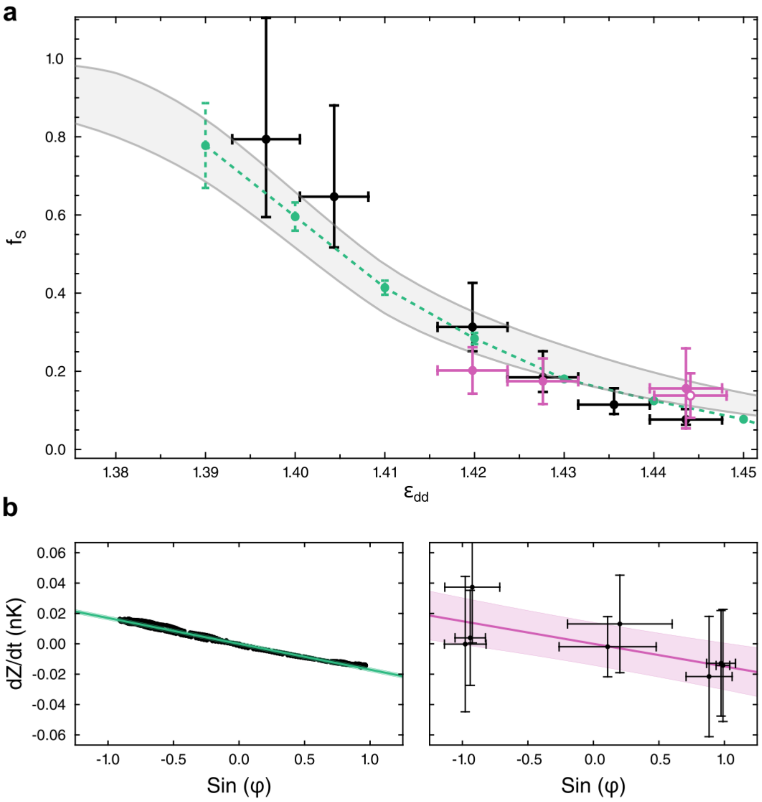

Figure 3.8: Measurement of the superfluid fraction from the Josephson dynamics. (a) Behavior of the superfluid fraction as a function of the interaction parameter ϵ_{dd}. The experimental points (black and pink) are compared to the numerical results (green dots) and the prediction of Leggett's bounds (gray lines). Black points are the experimental f_s extracted from the Josephson frequencies ω_J. The errorbars take into account the experimental uncertainties propagated in Eq. 3.11 and Eq. 3.25, plus a systematic underestimation of ω_J of 15% due to the high amplitude regime of the oscillations (see Sec. 3.6.1). Pink points are the experimental f_s extracted from the current-phase relations (see Eq. 3.23), assuming the fraction of atoms in the central clusters N_{34}/N and NU from the numerical simulations. The pink circle is the same quantity, for the data point where the optical separation was not employed in the detection of the imbalance Z. The green points are the results of the same analysis for numerical data. The errorbars are calculated from the uncertainties in the linear regressions used to extract the numerical values of NU and K. An example of the analysis of the current-phase relation is reported in (b) for numerical (left) and experimental data (right). The shaded regions in each plot are the confidence bands for one standard deviation. The Legget's bounds in (a) are calculated from the ground state density distributions obtained by static simulations.

the upper error bars of 15%. The superfluid fraction shows a smooth reduction for increasing ϵ_{dd}, changing of a factor of ten between unity, near the transition point at $\epsilon_{dd} = 1.38$, towards the lower point experimentally accessible, with $f_s \sim 0.1$ at $\epsilon_{dd} = 1.444$. Our data are in good agreement with the numerical ones, marked as green dots. The latter are derived by using Eq. 3.11, but evaluating K directly from the so-called *phase-current relation*. Similarly to the analysis carried out to extra U, the coupling energy K can be derived from the linear dependence of the current $\dot{Z}$ on the phase $\sin(\Delta\phi)$. An example of such analysis is reported in Fig. 3.8b, where the phase-current relation is plotted for numerical data simulated in the high amplitude regime[7]. For the experimental configurations where we have the paired measurements of Z and $\Delta\phi$, we carried out the same analysis, presented in Fig. 3.8c for the same parameters of the numerical simulation. We calculated numerically $\dot{Z}$ and $\sin(\Delta\phi)$ starting from the respective time evolution of imbalance and phase difference, and we then extracted the slopes $-4K(N_{34}/N)$. To determine K, we inserted the fraction of atoms in the central clusters N_{34}/N evaluated from numerical simulations at the equilibrium. Besides the larger error bars, of the single data points in Fig. 3.8c, the associated f_s calculated with this technique are in good agreement with both the experimental data extracted from the other analysis and numerical data. It's important to note, that this alternative analysis doesn't rely on numerical input besides the fraction N_{34}/N, which is however model independent. In particular, we don't have to rely on the interaction energy U, which is based on the validity of the 6-mode model. Nevertheless, we checked that in the experiment the interaction energy is of the same order as the predicted U, by looking at the linear regression between Z and $\dot{\Delta\phi}$. This analysis is much noisier than the one used to extract K, but we derive an experimental value $(NU)_{epx} \sim 4\,\mathrm{nK}$

3.4.1 Comparison with Leggett's model

Both experimental and numerical results are compared to the superfluid fraction predicted by Leggett's model. This is evaluated by calculating numerically the integral in Eq. 3.9 for the ground state density profiles

---

[7] Typically the linear dependence is between $\dot{Z}$ and $\Delta\phi$. In the regime of high amplitudes, we substitute $\Delta\phi \rightarrow \sin(\Delta\phi)$.

of our system. We calculate bother the upper and lower bounds of the theory [104], plotted in Fig. 3.8a as gray solid lines at the boundary of the shaded region. Note that the two bounds would coincide if the ground state density dependence on the transverse variables y and z is such that $n(x, y, z) = n(x)n(y, z)$. This *separability* condition is not perfectly met in our system, but the two bounds are close enough to be able to compare our results with Leggett's theory. This is due mainly to the fact that the supersolid structure, for this trapping configuration, develops in 1D (see Sec. 2.1). The nice agreement between predicted and observed values demonstrates that Leggett's model applies to our system and that our experimental method is a valid alternative to global measurements for assessing the superfluid fraction of a dipolar supersolid. Indeed, our local measure quantifies the superfluid fraction of the central cell of our confined system, but I argue this quantity would be the same for an ideal infinite system with the same density modulation as ours. In other words, our method allows for local probing of the superfluid fraction without the effects produced by the system inhomogeneity, which instead afflicts global measurements, such as the rotations.

Another approach for the measure of f_s which I did not discuss here, but has been recently applied to condensates loaded in optical lattices [184, 36], is based on the anisotropy in sound velocities measured along different directions, which is introduced by the density modulation. This effect can be linked to a reduced superfluid fraction due to the broken translational symmetry. In the case of a standard superfluid loaded in an external potential, such as an optical lattice, the reduction of superfluidity is not surprising, since the presence of one, or many weak links reduces the transport within the system affecting the sound velocity [191]. The remarkable result of these recent experiments is that the measured superfluid fraction agrees once again with Leggett's predictions. Indeed, in [36] the density modulation in the condensate is created by employing a large-spaced optical lattice, that allows for the experimental measure of Leggett's f_s directly from the atomic density. This result agrees with the superfluid fraction data based on the sound velocities measurements and shows a slow reduction of f_s for increasing depth of the optical lattice. This is due mainly to its large spacing, allowing for a large number of atoms per lattice site, a characteristic in common with our dipolar supersolid.

Previous measurements of the superfluid fraction have been carried out, once again in superfluids in optical lattices, by studying the effective mass [30, 89] of the bosons, which is modified by the periodic external potential [88]. However, both these approaches share the same global nature as rotations. Moreover, in these studies, the presence of an external potential deeply modifies the properties of the system, virtually canceling many new phenomena which may arise from the spontaneously reduced superfluid fraction peculiar to supersolids. Besides partially quantized supercurrents [185] and vortices [56, 7], for which there is still no experimental observation, an interesting property of our system is the presence of a low-energy Goldstone mode. In the next section, I will discuss the impact of such a mode on the Josephson dynamics observed in our trapped system.

3.5 Beyond the Josephson model

Probably the most important difference between a supersolid and a standard bosonic Josephson junctions array is the fact that, in supersolids, the spontaneous breaking of the continuous translational symmetry leads to a low-energy Goldstone mode associated with the position of the lattice sites. Indeed, when the supersolid forms the system has a certain degree of arbitrariness in choosing where to put the weak links. Moreover, since there isn't any external potential to fix the position of the weak links, they can move during the dynamics. In an infinite system, where any spatial shift of the supersolid lattice structure (maintaining the density periodicity) doesn't change the free energy, the energy cost of such motion is zero. This means that an arbitrary small perturbation of the lattice position would trigger a shape-preserving global motion of the supersolid. In a trapped system, the scenario is different because the energy cost of shifting the supersolid structure is finite due to the harmonic confinement. Here I consider only harmonic traps since the phenomenon would be totally different for a box-like potential, where the energy cost for any perturbation is nominally infinite and the supersolid structure tends to form only at the edges [157].

The trapped Goldstone mode has been observed and characterized

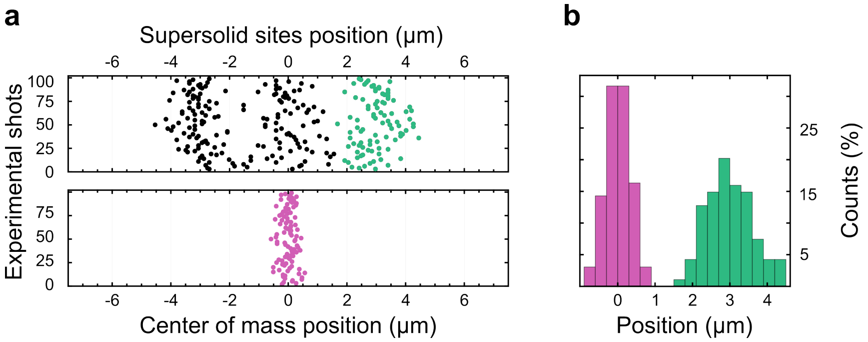

Figure 3.9: Experimental evidence of the Goldstone mode. (a) Fluctuations of the cluster positions (upper panel) and center of mass (lower panel) of the supersolid for about 100 experimental shots. (b) Distributions of the positions of the right cluster (green) and of the center of mass (pink).

for dipolar supersolids in [63]. It consists of a slow oscillation of the position of density maxima (and minima) with a coupled oscillation of the population imbalance, in order to keep the position of the center of mass of the supersolid unchanged. To understand why these oscillations are coupled, we must consider the finite superfluidity of the supersolid. Without the possibility of having currents between the supersolid clusters, the oscillatory motion of the supersolid in the trap would be described by the dipole mode, i.e. an oscillation of the center of mass position with at the trap frequency ω_x. However, the finite couplings between the supersolid clusters, allow to minimize the energy cost of the oscillation, by moving mass in the direction opposite to the motion of the lattice. The result is an oscillation of the the imbalance, which counters the one of the center of mass. The energy associated with this motion is lower than the trap energy $\hbar\omega_G < \hbar\omega_x$, and tends to zero for vanishing harmonic potentials, recovering the same condition of the infinite case.

Given its low frequency, the Goldstone mode cannot be followed experimentally because its time scale exceeds the system's lifetime. However, it can be detected from correlations between the measured imbalance and the position of the clusters in many experimental shots [63]. A similar analysis is shown in Fig. 3.9, where we report the positions of the supersolid clusters for many realizations of the supersolid, without any further manipulation or excitations. In order to extract a good signal we employ a supersolid with a larger number of atoms with respect to the one used for the Josephson experiment, showing three main clusters instead of two. We obtain these data for large ϵ_{dd}, where the position of the clusters can be extracted from the density profiles without using the optical separation. The presence of a Goldstone mode is revealed by the broad distribution of the positions of the cluster, which appear to strongly fluctuate from shot to shot, while the center of mass of the system remains much more stable. The detected fluctuations in the cluster positions have a standard deviation of $\sigma_{clusters} \sim 1\,\mu\text{m}$, which needs to be compared with the center of mass fluctuations, which shows $\sigma_{com} \sim 0.5\,\mu\text{m}$.

From theoretical predictions based on numerical solutions of the Bogoliubov-de-Gennes equations [68], the Goldstone mode has been interpreted as the odd parity mode associated with the softening of the roton accompanying the phase transition towards the supersolid. Its energy is predicted to be about a few Hz, therefore the Goldstone mode is spontaneously excited by thermal fluctuations in experiments. This translates as noise introduced both in Z and $\Delta\phi$. Indeed, a random displacement of the supersolid will produce a non-zero initial imbalance (due to the Goldstone mechanism) and an error in the imprinted phase (due to the wrong alignment with the optical lattice). We estimate the additional noise on our observables, due to the presence of the Goldstone excitations, to be about 20% of the measured Josephson amplitudes.

In the numerical simulations, not affected by thermal fluctuations, it is possible to study the coupling between the Goldstone and Josephson dynamics, which is analyzed in Fig. 3.10. Here we excite the Josephson dynamics inducing an initial imbalance Z_0, instead of imprinting a phase difference. When the new equilibrium density is initialized with $Z_0 > 0$, we also produce a finite displacement of the weak link position x_0 (Fig. 3.10a), which triggers the Goldstone mode. Evaluating Z and $\Delta\phi$ as a function of time, we see the standard Josephson oscillations at the expected frequency ω_J, on top of a slower oscillation associated with the motion of the barrier. For example, for Z we find $\omega_J = 2Pi \times 23.85(3)$ Hz and $\omega_G = 2Pi \times 3.56(8)$ Hz, the latter matching the oscillation frequency of x_0. We checked that exciting the Josephson dynamics with the phase imprinting technique drastically reduces these slow oscillations since it doesn't excite the motion of the barrier.

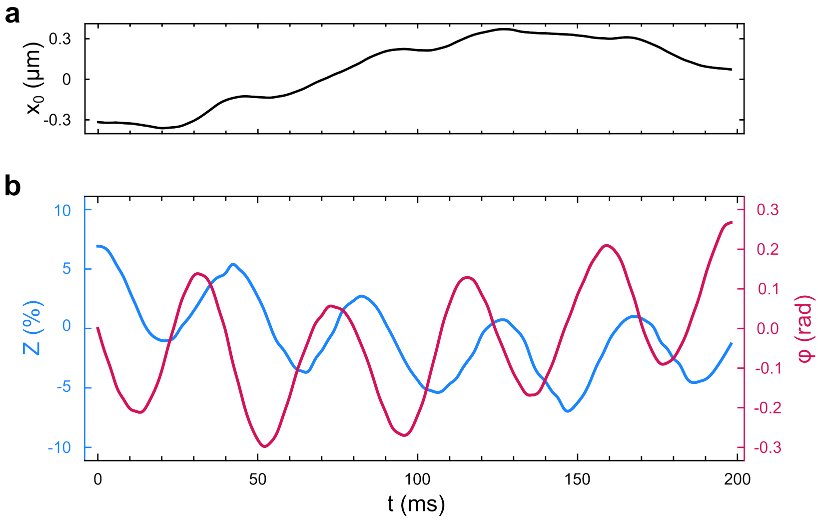

Figure 3.10: Coupling of the Goldstone mode to the Josephson dynamics in numerical simulation. The position of the weak link x_0 (a) shows a clear oscillation at the Goldstone frequency $\omega_G \ll \omega_J$. (b) The oscillations of both Z (blue) and $\Delta\phi$ red, show a double frequency character given by the mixing of ω_G and ω_J.

Even if it's clear that the Goldstone doesn't affect the oscillations of the mean values of Josephson observables during the dynamics, it's not straightforward to understand the connection of the Goldstone mechanism with the fluctuations of Z and $\Delta\phi$. Indeed, it's intuitive to link the nature of the fluctuations to the lowest energy mode of the system, but in the case of supersolids the coupling between Goldstone and Josephson leads to the need for specific theoretical models. In standard bosonic Josephson junctions, the phase fluctuations are linked only to the energy scales of the Josephson mode [141, 57] by

$$\langle \Delta\phi^2 \rangle = \frac{T}{E_J} \,, \tag{3.26}$$

where $E_J \sim 2NK$ is the Josephson energy. Based on this prediction, we can try to estimate the temperature of our system, using the measured Josephson frequencies and the phase fluctuations reported in Fig. 2.14 which gave $\langle \Delta\phi^2 \rangle = 0.035$. We then find

$$k_B T = \frac{h\omega_J}{(NU)_{exp}} N \langle \Delta\phi^2 \rangle \approx 80 nK \,, \tag{3.27}$$

where we used $(NU)_{exp} \sim 4\,\mathrm{nK}$ introduced at the end of Sec. 3.4, $\omega_J \sim 20\,\mathrm{Hz}$, and $N \sim 10^4$ for simplicity. We note that the derived temperature is too high to be correct since exceeds by far the critical temperature for the condensation. Moreover, a careful analysis of the thermal fraction on the superfluid side reveals a temperature around 10 nK for our system. One possibility to get a lower temperature, which would agree with our observation, is to substitute in the model the energy scale of the Goldstone mode, thus obtaining

$$k_B T = \frac{h\omega_G}{(NU)_{exp}} N \langle \Delta\phi^2 \rangle \approx 8nK\,, \tag{3.28}$$

where ω_G is now 2 nK. Although this is just a rough estimation, based on the one theoretical model describing the thermal fluctuations of bosonic Josephson junctions, the fact that using the Goldstone frequency we get the right order of magnitude for our system is quite remarkable. Indeed, the fluctuation properties of supersolids both of thermal and quantum nature, would be an interesting topic for further research.

3.6 Experimental tools

In this section, I will briefly discuss the experimental techniques involved in the selective excitation and detection of the Josephson oscillations discussed in this Chapter. Further details about the preparation of the supersolid, and the imaging techniques can be found in Chapter 4.

3.6.1 Excitation of the Josephson dynamics

As already explained, we employ an optical lattice to imprint an initial phase difference between the central cluster of our supersolid. The optical potential of the lattice, with respect to the position of the clusters, is depicted in Fig. 3.5. The lattice is realized with 1064 nm laser beams, intersecting at a small angle, such that the resulting spacing is $d_{lat} = 7.9(3)\,\mu\text{m}$. The technical details about the optical scheme to realize the lattice potential are given in [14]. In order to imprint the same phase difference in each experimental shot, both the intensity and the alignment of the lattice need to be stable. Moreover, the intensity and pulse duration of the imprint must be calibrated, to estimate the values of the imprinted phase. In Fig. 3.11a, we show the stability of the lattice over a typical experimental run. We first prepare a standard BEC, which is then loaded in a deep lattice potential, in order to distinguish clearly the position of the lattice peaks by looking at the

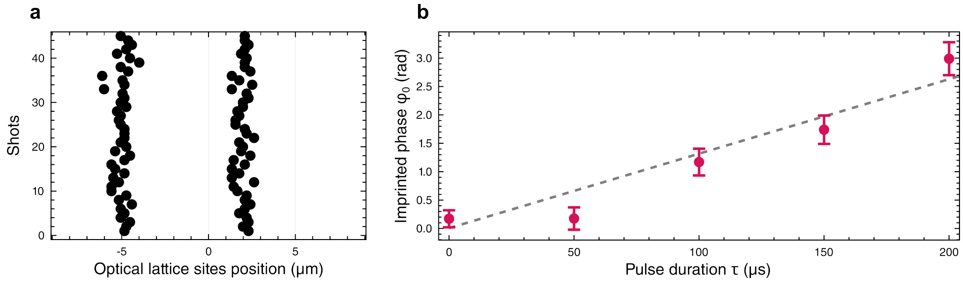

Figure 3.11: Characterization of the optical lattice used for the phase imprinting. (a) Density peaks of a BEC loaded into the optical lattice. The positions of each lattice site (black dots) relative to the center of mass of the system give a standard deviation of $\sigma_{lat} \sim 0.35\,\mu\text{m}$, over 45 experimental shots. (b) Calibration of the imprinted phase difference, measured on the supersolid after expansion, as a function of the imprinting pulse duration. The lattice depth is $U_{lat} \sim 100\,\text{nK}$ (estimated by oscillation frequencies of single site dipole oscillations). The dashed line is the expected imprinted phase $(U_{lat}\tau/\hbar)$.

in-situ density. Such positions are then referenced to the center of mass of the system which is practically the same for the standard BEC (free or loaded into the optical lattice) and the supersolid. The stability in the position of the lattice peaks is better than 10% of its period, and much smaller than the shaking of the supersolid due to the Goldstone fluctuations (see Fig. 3.9). Indeed, we associate the latter with most of the noise in the excitation protocol. The asymmetry in the lattice position is due to the alignment with the supersolid clusters (spaced by $\lambda = 3.7(2)\,\mu\text{m}$), which is optimized for the ratio d_{lat}/λ.

The calibration of the phase difference imprinted by the optical lattice, reported in Fig. 3.11b, is done by varying the duration of the imprinting pulse τ at fixed intensity, corresponding to a lattice depth of about $U_{lat} = k_B 100\,\text{nK}$. After the imprint, we immediately release the supersolid from the trap and we evaluate the phase difference $\Delta\phi$ between the central clusters (see Sec. 3.6.3) which corresponds to the imprinted phase ϕ_0. We compare our results with the prediction $\phi_0 = \tau U_{lat}/\hbar$, finding a good agreement with the observed data. Note that for too short pulses, with $\tau = 50\,\text{ms}$ for example, the imprinted phase could be too small if compared to the noise coming from the Goldstone. Thus, in the experiment, we employ longer pulses of the order of $\tau = 100\,\text{ms}$, which are compatible with imprinted phase differences of at least 1 rad.

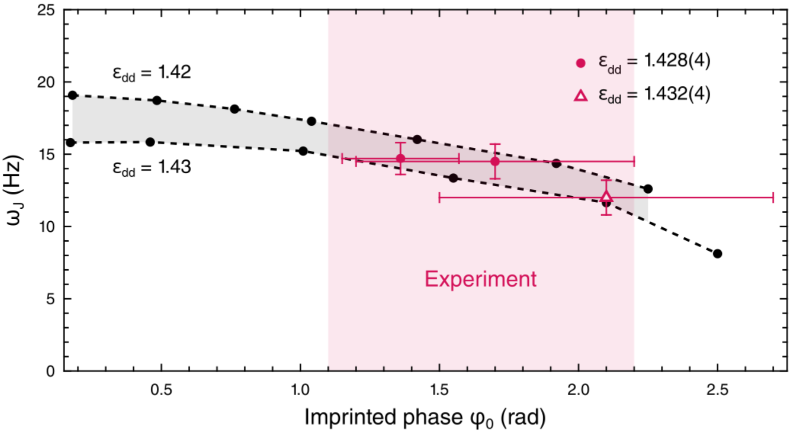

Figure 3.12: Comparison between the numerical and experimental results for the Josephson frequencies as a function of the amplitude of the oscillations. Numerical simulations (black dots) and experimental data (red dots and open red triangles) show a reduction from the small amplitude regime of about 15% around at 1.5 rad. The measures reported in Fig. 3.7 are in the amplitude regime marked by the shaded area.

In this excitations regime the amplitudes of both $\Delta\phi$ and Z are not small enough to be treated perturbatively, then we expect deviations from the measured Josephson oscillations and the ones predicted by the theory and verified by numerical simulations carried out in the regime of small excitations. Indeed, if we compare numerical and experimental results in the same conditions, we find that a small reduction of the Josephson frequencies for increasing oscillation amplitudes may occur. Our results are presented in Fig. 3.12, confirming a reduction of ω_J of about 15%, with respect to the small amplitudes regime. This discrepancy is taken into account when we extract the superfluid fraction in Fig. 3.8, which is based on the Eq. 3.24, obtained in the small amplitude regime.

3.6.2 Detection of the imbalance

The population imbalance is extracted from in-situ density images we acquire in the x-y plane, through an imaging system with a spatial resolution of about 3 µm, slightly smaller than the supersolid spacing 4 µm. The in-situ density is captured using dispersive phase-contrast imaging [82] using the same light employed for absorption imaging, at 421 nm, but with a large detuning. This is fixed at $\delta = 5\Gamma_{421}$, as a compromise to reduce the effects connected with the light absorption, while keeping a large enough dispersive signal which is proportional to the ratio I/δ, with I being the light intensity. Further details about the imaging technique can be found in Sec. 4.3.

We transform each in-situ image into a one-dimensional profile, integrating along the transverse direction y. Then we detect numerically the positions of the supersolid clusters by looking at the peaks in the signal, and the populations $N_1 + N_2 + N_3$, $N_4 + N_5 + N_6$ integrating the signal to the left and to the right of the minimum between the peaks, respectively. From the left and right populations, we compute the experimental observable $Z = (N_1 + N_2 + N_3 - N_4 - N_5 - N_6)/N$.

As explained in Sec. 3.3, we are only able to resolve clearly the two main clusters for high contrasts (large ϵ_{dd} values), where the density modulation leads to a very weak link between the two main clusters. In other cases, the supersolid is still distinguishable from a standard superfluid, but the clusters are not resolved and, in particular, the minimum between the peaks in the extracted 1D profile described above, is not well defined. To increase the signal-to-noise ratio of our detection we need to further manipulate the atomic cloud exploiting the symmetry of the system and dipolar interactions. Our technique employs the same optical lattice used for the selective excitation of the Josephson mode, to separate the two main clusters of the supersolid at a larger distance, which is now accessible by our limited optical setup.

The optical separation is done by shining a shallow lattice potential on the cloud about 5 ms before the imaging pulse. The lattice potential traps the position of the cluster sitting at its minimum, while the dipolar repulsion between the two clusters makes the other one move in the opposite direction, falling into the next minima. The result is an overall increase in the cluster distance, which we studied numerically in Fig. 3.13. However, also the lateral clusters are modified by the lattice potential, thus also the detected imbalance changes during the separation. As reported in Fig. 3.13a, the change in Z is simply an additional offset, which doesn't depend on the starting value (before the optical separation). For this reason the observed Josephson frequencies remain valid, even if the baseline of the oscillations is modified by our manipulation. In Fig. 3.13b, we reported the change of the distance

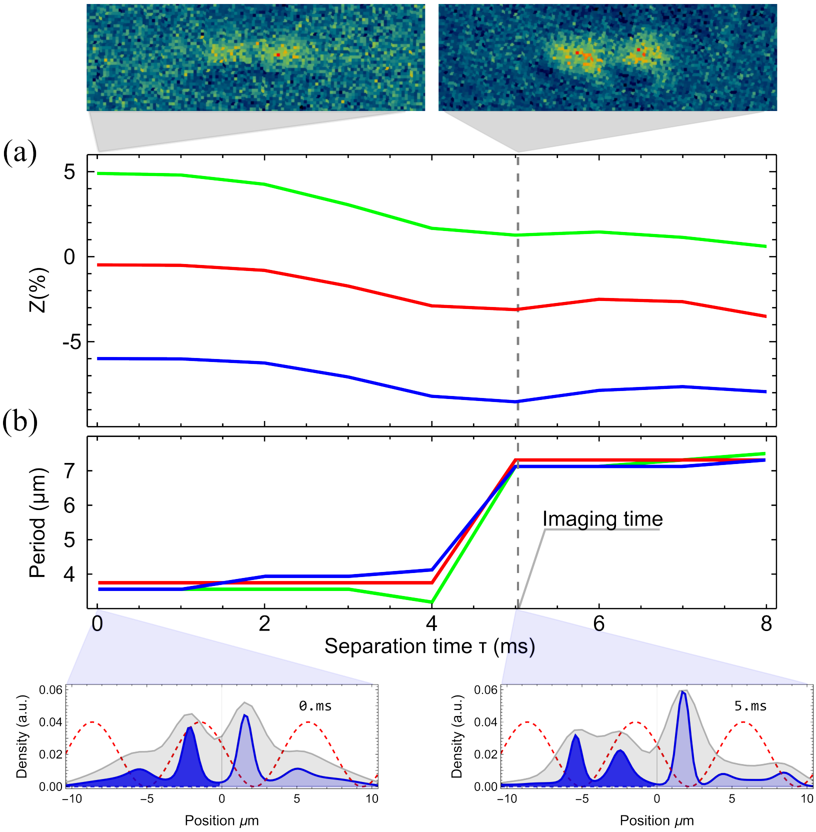

Figure 3.13: Numerical simulations of the dynamics of the system during the optical separation. (a) Evolution of Z for three different supersolids with initial population imbalance $Z_0 = 5\%$ (green), $Z_0 = 0\%$ (red) and $Z_0 = -5\%$ (blue), when the shallow optical lattice is applied. (b) Separation of the clusters during the same dynamics. The upper insets show two experimental in-situ images of supersolids with $Z = 0$ before (left) and after the optical separation (right). The lower insets are snapshots of the separation dynamics: the blue solid line is the supersolid density, the red dashed line is the lattice potential (not to scale), and the gray shaded curve is the supersolid density convoluted with a Gaussian accounting for the finite resolution.

between the clusters, which reaches the lattice spacing right after 5 ms of dynamics. From the snapshots of the numerical simulation, we see the tendency of the clusters to repel one another, keeping the system from rearranging the left clusters together and leading to a structure with three main density maxima. This however must be then convolved with a larger Gaussian envelope to take into account the finite resolution of our system. The resulting signal is something more similar to a two-peak structure, which corresponds with the typical experimental images (see snapshots in Fig. 3.13).

Experimentally, we checked that in the same conditions of atom number and ϵ_{dd}, the Josephson frequencies measured with and without the optical separation are consistent with one another (see the discussion on Fig. 3.7). Moreover, the separation technique alone, without the phase imprinting, don't trigger oscillations in the imbalance. This last check was done both on the supersolid and on the superfluid since the separation allows us to measure a finite Z even without a spontaneous density modulation. We conclude that, although our lattice is not aligned symmetrically to the supersolid (a configuration that would favor the separation) the optical separation employed in our measures produces the desired effect on the supersolid density, without drastically perturbing the imbalance.

3.6.3 Detection of the phase difference

The detection of $\Delta\phi$ is based on time of flight absorption imaging, which gives us the density distribution in momentum space. Such distributions, as already shown in the snapshots of Fig. 3.5, show an interference pattern due to the superposition of the expanding coherent matter waves originating from each supersolid cluster. We analyze this complex interference figure via a simple *double-slit* model, and we extract the phase difference between the two main clusters $\phi_3 - \phi_4$. I will now discuss the details of the procedure, to get an intuition of why the interference from our multi-cluster supersolid can be described as a double-slit interference.

We employ a standard absorption imaging after a time of flight $\tau_{fly} = 61\,\mathrm{ms}$, which is enough to have a complete overlap of the supersolid clusters and enough *magnification* from the expansion to resolve the interference fringes. To reduce the effect of dipole-dipole interactions within the first ms of the expansion (where the density is still high and the clusters close to one another), we boost the scattering length a_s almost to the background values (hence reducing ϵ_{dd} below 1), about 200 µs before releasing the atoms from the optical trap. Since the imaging beam comes from below the atoms, the density distribution is recorded in the horizontal plane, integrating over the depth of focus of the objective (which is comparable to the size of the system along the z direction), obtaining $\rho(k_x, k_y)$. Note that to keep the atom in focus during the expansion, we apply a magnetic gradient along z, which cancels the gravity. From the momentum distribution, we infer the phase difference from the position of the interference fringes relative to the center of the Gaussian envelope of the distribution.

The recorded signal $\rho(k_x, k_y)$ is then integrated over k_y to obtain a one-dimensional distribution $\rho(k_x)$, which is then fitted with the function

$$\rho(k_x) = \mathrm{G}\left(k_x, k_0.\sigma\right)\left[1 + A_1\cos^2\left(\pi\left(k_x - k_0\right)/k_r + \theta\right)\right] , \tag{3.29}$$

which is basically the same[8] as the one in Eq. 2.14 described in the previous Chapter. Note that, since the fringes are described as a $\cos^2(x)$, the actual phase difference is given by $\Delta\phi = 2\theta$. This analysis is repeated for typically 20-30 realizations for each observation time t of the supersolid dynamics. The results are then combined using the circular mean

$$\bar{\Delta\phi} = \arg\left(\sum_{j=1}^{n} e^{i\Delta\phi_j}\right) , \tag{3.30}$$

which is the appropriate way to average together periodic quantities[9]. The corresponding error is given by the circular standard deviation [54].

The outlined procedure would be rigorous for studying the phase difference between two clusters, only when there are only two of them in the supersolid. However, although in our case we have six overlapping

---

[8] The only difference is the choice to use either a $\sin^2$ or $\cos^2$ modulations.

[9] Note that $\arg(x)$ indicates the argument of the complex number x and i is the imaginary unit.

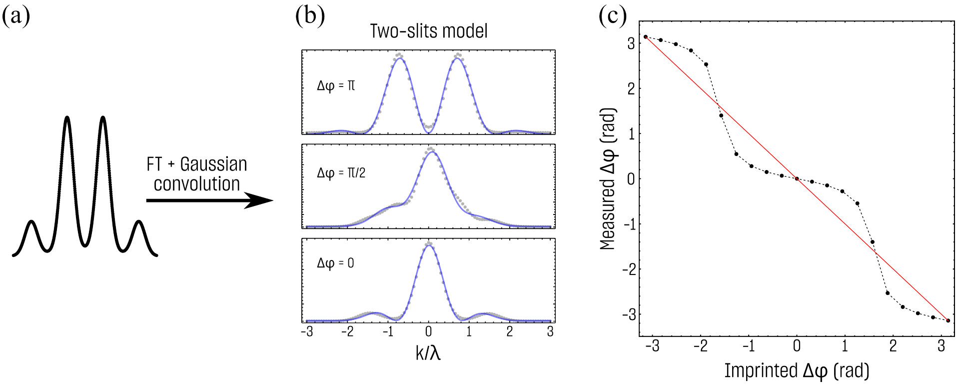

Figure 3.14: Analysis of the double-slit model for the phase difference detection. (a) Sketch of the real part of the test wavefunction, built with 4 Gaussian clusters and alternating phase factors. (b) Results of the Fourier transformed and convoluted wavefunctions for different phase differences. Dots are the results of the calculations. Solid blue lines are non-linear fit curves using the model in Eq. 3.29. (c) Results of the analysis for $\Delta\phi$ ranging from $-\pi$ to π (black dots). The red and the black dotted lines are a guide to the eye.

clusters contributing to the interference pattern, the double-slit model gives still a good approximation of $\Delta\phi$, provided we take into account two main effects. The first one is the finite resolution of the imaging system used for the time of flight measurements. This settles a cutoff to the lowest k which is possible to detect in the momentum distribution, making our observations only sensible to the supersolid k, associated with the distance between neighboring clusters λ. Indeed, for infinite resolutions, one should be able to also detect smaller k, given by the interference between overlapping clusters lying multiples of λ apart from one another. Thus, the measured distribution only shows the effects of the neighboring cluster interference.

The second thing to account for is the inhomogeneity of the system. To analyze this effect we conducted a numerical analysis, starting on a simple distribution with 4 inhomogeneous clusters. The results of the analysis are shown in Fig. 3.14. We start considering a real space wavefunction of 4 Gaussian clusters separated by λ. The side modes amplitudes are 1/3 of the main ones (see Fig. 3.14a). Then we build our test wavefunction by multiplying each Gaussian mode for a phase factor with an alternate sign, as in the experiment. As sketched in Fig. 3.14b, we simulate the expansion of the wavefunction by calculating its Fourier transform and convolving it with a large

Gaussian envelope to take account for the finite resolution ($0.2\,\mu\mathrm{m}^{-}1$). The obtained distribution is then fitted with the model in Eq. 3.29, and the detected phase difference is plotted as a function of the imprinted one. In Fig. 3.14b, we see that the double-slit model gives precise results only around $\Delta\phi = 0\,\mathrm{rad}$ and $\Delta\phi \sim \pm 1.6\,\mathrm{rad}$, while in the other regions there are deviations from the expected values up to 0.5 rad, which are taken into account in the errorbars of Fig. 3.6. Note that such deviations, for the particular configuration of our experiment, don't affect the measured Josephson frequencies, since the crests, nodes, and troughs of the oscillations lay in the vicinity of the points where the double-slit is more precise. Finally, we note that the obtained value of $\Delta\phi$ has the opposite sign with respect to the imprinted phase. This is due to the fact that the imprinted phase difference between lateral and central clusters is $-\Delta\phi$. The measured phase difference is then the sum of two negative contributions from the lateral clusters and a positive one coming from the central clusters, which is of the order of $-\Delta\phi$.

Chapter 4

Probing and manipulating a dipolar supersolid

In this chapter, I will discuss the experimental techniques employed for the study of the superfluid-supersolid quantum phase transition and the Josephson dynamics in the supersolid phase, presented in the previous chapters. Before delving into the details, I will give a very concise overview of the experiment focusing on the main steps needed to produce a dipolar Bose-Einstein condensate of dipolar atoms. The details concerning the experimental sequence together with a more technical description of our apparatus are reported in [115, 116].

The atomic species used in our experiment is dysprosium, the rare-earth metal with the largest magnetic dipole ever cooled down to the quantum degeneracy. This extraordinary property stems from its electronic structure, $[\mathrm{Xe}]4f^{10}6s^2$, which brings dysprosium atoms in the ground state $^5I_8$ to have a total angular momentum $J = 8$[1]. The complexity of this electronic structure results in a rich landscape of electronic transitions.For the laser cooling, we employ two transitions at 421 nm and 626 nm connecting the ground with two excited states obtained by promoting one of the $6s^2$ inner electrons to the $6p$ orbital, either in the $^1P_1$ or $^3P_1$ states. Given its large linewidth, $\Gamma_{421} = 2\pi \times 32.3$ MHz allowing to scatter lots of photons, the blue light is used for the first stages of cooling and for the absorption imaging of the atomic cloud. The red light is used in the 3D Magneto-Optical Trap (MOT), where the atoms are trapped and further cooled, before being able to get trapped in a purely optical dipole trap. Our setup and the geometry of the cooling and trapping beams are shown in Fig. 4.1.

We produce a vapor of ^{162}Dy in an oven operating at $T \sim 1200$°C,

---

[1] Having zero nuclear spin, our bosonic isotope don't have a hyperfine structure.

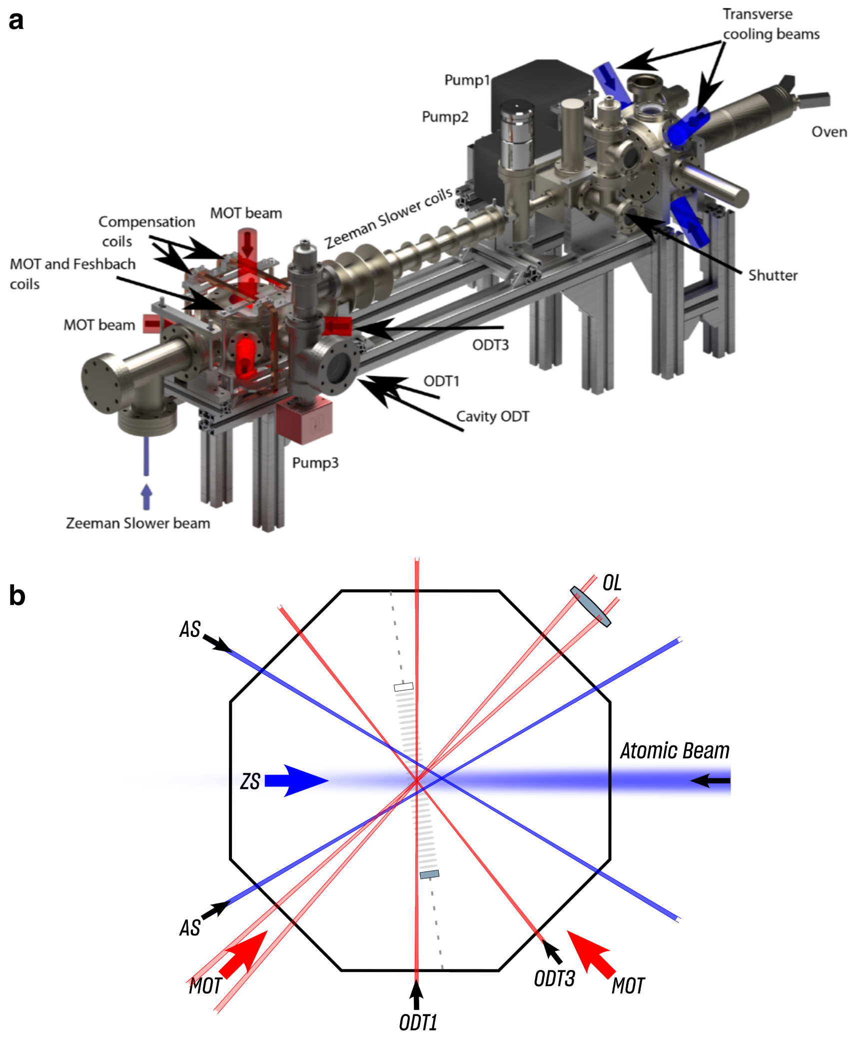

Figure 4.1: Scheme of the experimental setup and geometry of the laser beams involved in the cooling and trapping of dysprosium. (a) Model of the experimental setup. Blue beams mark the 421 nm laser lights used for collimating and slowing down the atomic beam. Red beams mark the 626 nm lights used for the MOT. Two pairs of coils, namely the MOT coils (regulating the quadrupole field and the magnetic field gradient) and the Feshbach coils (used to tune a_s), sit near the vertical upper and lower window of the science cell. Another pair of transverse coils is used to compensate for the Zeeman slower field and adjust the atom's position. (b) Top view of the octagonal science chamber. The big arrows mark respectively the Zeeman slower ZS (blue) and MOT (red) directions. The two thin blue beams show the directions of the angled slowing. The infrared cavity field is sketched in gray. The two cavity mirrors, sitting along the gray dashed line, are held vertically by two *in vacuum* supports. Thin red beams represent infrared laser beams employed to trap the condensate: ODT1 and ODT3 realize the crossed dipole trap, while the two OL beams form the long-spaced optical lattice used to manipulate the supersolid in the Josephson experiment.

which is then turned into an atomic beam after being collimated by a transverse cooling stage, where a pair of back-reflected elliptical blue beams cross just after the oven nozzle. The atomic beam is then slowed down with a Zeeman slower operating with blue light, and loaded into the MOT. To maximize the number of atoms trapped we use also a pair of angled slowing beams that cross just before the MOT location [118]. Moreover the 626 nm light is frequency-modulated to enhance the the capture velocity of the MOT by widening the laser linewidth, which is naturally pretty narrow, with $\Gamma_{626} = 2\pi \times 136$ KHz. During the MOT loading the atomic magnetic dipoles are polarized along the vertical direction $\hat{z}$ via a low magnetic field[2] of about 1.5 G generated by a pair of coils, called *Feshbach coils*, since they are used during the experiment to control the scattering length via Feshbach resonances. After its loading, the MOT is compressed by ramping down the frequency modulation and modifying the magnetic gradient, in order to obtain a denser, but colder sample. At this point we have typically 5×10^7 ($n \sim 10^{11}\,\mathrm{cm}^{-3}$) atoms at $T \sim 20\,\mu\mathrm{K}$. To further reduce the system temperature towards the condensation threshold, which is $T_C \sim 60\,\mathrm{nK}$, we load the atoms in fully optical potentials, realized with infrared light at 1064 nm, to do evaporative cooling.

For the first stage of evaporation, we employ an *in vacuum* optical cavity with finesse $\mathcal{F} \approx 1500$ which allows to amplify the injected infrared light obtaining very intense cavity fields. As a result, all the atoms in the portion of the atomic cloud overlapping the deep cavity potential, are captured in a series of *disks* lying 532 nm from one another along the cavity axis. At this point, the cavity field is ramped down by controlling the injected power. During the cavity evaporation, the scattering length a_s is increased by increasing the Feshbach magnetic field and approaching the resonances at 5.3 G, to enhance the effect of elastic collisions crucial to thermalize the cloud at lower temperatures. Before turning off the cavity field completely the atoms are loaded in a crossed dipole trap and the scattering length is suddenly decreased, while we still have a thermal gas, to approach the critical value for the supersolid phase transition. This abrupt change cannot be done on a BEC, since it will produce excitations ultimately leading to heating the cloud. At the end of the evaporation, we end up with approximately 4×10^4 atoms at $T \sim 10\,\mathrm{nK}$, trapped in an elongated

---

[2] The exact value changes with the optimization of the MOT loading

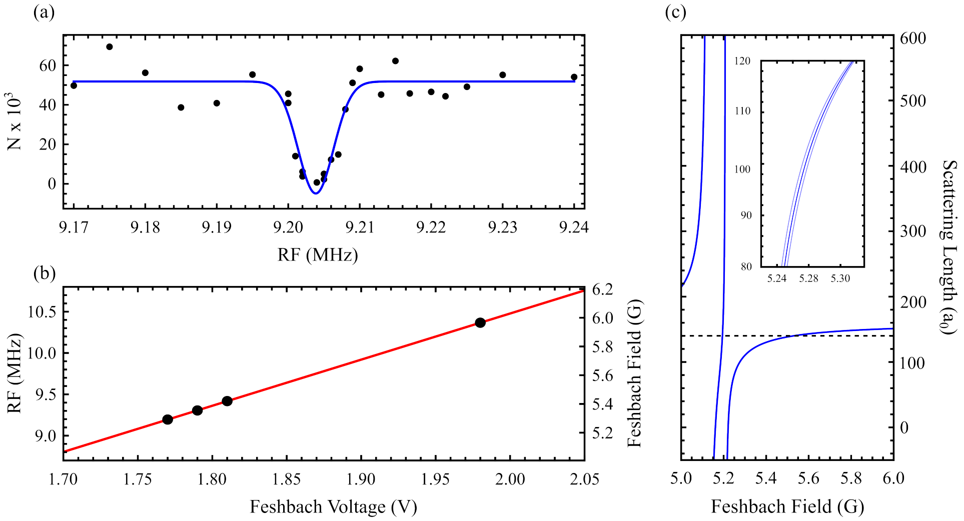

Figure 4.2: Magnetic field calibration. (a) Radio-frequency spectroscopy signal. The loss feature in the atom number is fitted with a Gaussian function (blue line) peaked at resonance. (b) The resonance RF values (translated in B fields) are probed for different values of the voltage controlling the Feshbach coils. The red line is a linear fit. (c) Model of the dependence of the scattering length on the magnetic field (blue line). The dashed black line marks the background scattering length a_{bg}. A detail of the model is presented as inset, where the light blue lines are calculated assuming the uncertainties on the positions and width of the Feshbach resonances considered.

optical dipole trap (ODT) with a vertical frequency, resulting from the competition of optical confinement and gravitational sag, of the order of 100 Hz. The trap frequencies in the $\hat{x}$-$\hat{y}$ plane are fixed by tuning the powers in the two infrared beams ODT1 and ODT3, which allow us minimal control over the trap aspect ratio. The typical trap employed in the experiment, as discussed in the previous chapters, is elongated along $\hat{x}$, which is also the direction where the supersolid develops its density modulation once the quantum phase transition is crossed.

4.1 Magnetic fields

Already at the MOT stage, dysprosium atoms are naturally pumped into the lowest Zeeman sublevel $|\mathrm{J} = 8, m_{\mathrm{J}=-8}$ [50], becoming strong magnetic dipoles that are kept aligned to the vertical direction by the constant Feshbach field. For too low fields (of the order of the Earth's magnetic field) the dipoles *depolarize*, resulting in a sub-optimal loading of the MOT. As discussed in the beginning of this chapter, the magnetic field is controlled during the evaporation sequence to enhance the thermalization and, once the BEC is obtained, to control the role of dipolar interactions. To cross the superfluid-supersolid quantum phase transition, the ratio between dipolar and contact interactions ϵ_{dd} must be controlled accurately, thus requiring a precise calibration of the Feshbach field. In Fig. 4.2 the typical results for the field calibration are presented. The first step is to translate the current flowing in the Feshbach coils into a value for the magnetic field. Since the current is stabilized by an external PID loop controlled with a voltage signal, we need to convert the control voltage into the actual field generated by the coils. This is done by coupling the ground state with the higher Zeeman sub-level $m_\mathrm{J} = -7$ with radio-frequency pulses at about 9.2 MHz, and analyzing the induced losses in the atom number. Indeed, when atoms are pumped to the higher magnetic sub-levels and then decay to the ground state due to dipolar relaxation [43], the excess of kinetic energy is enough to kick them out of the trap. This loss mechanism depends on the detuning, thus from the loss spectroscopy signal we can accurately establish the position of the RF transition. The RF pulses are generated by a self-built antenna with 10 windings of copper wire arranged on a circular coil of about 3 cm diameter. These reduced dimensions allow the antenna to sit just below the lower window of the science chamber, without affecting the laser light shining through, and minimizing the screening of the RF field by the vacuum apparatus. The RF coil is then driven by a function generator (Stanford DS345) producing pulses of 50 ms, triggered by the software controlling the experimental sequence, without the need for further amplification. The relation between the resonant radio-frequency and the magnetic field is given by

$$\nu_{RF}\,[\mathrm{MHz}] = \frac{\mu_\mathrm{B}\, g_\mathrm{J}}{h}\, B\,[\mathrm{G}] = \frac{\mu}{8h}\, B\,[\mathrm{G}]\,, \tag{4.1}$$

where μ is the magnetic moment of dysprosium and $g_\mathrm{J} = \mu/(8\mu_\mathrm{B})$ is the Landé g-factor[3] for J = 8. As it's shown in Fig. 4.2a, we extract ν_{RF} fitting the loss spectroscopy signal with a Gaussian function, where the typical width is 2 KHz, which gives the uncertainty on the calibration. The width can be reduced by decreasing either the amplitude or the duration of the RF pulse, which however reduce also

---

[3] With $\mu = 9.93\mu_\mathrm{B}$, we obtain $g_\mathrm{J} = 1.24$ which agrees with the measurement reported in [134].

the signal-to-noise ratio of the measurement. This procedure is repeated for different magnetic field values, by changing the Feshbach voltage, obtaining the calibration line reported in Fig. 4.2b, which reads $-0.391384\,[\mathrm{G}] + 3.21047\,[\mathrm{G/V}]\,x\,[\mathrm{V}]$. Before each experimental session, we run a single RF spectroscopy scan, comparing the expected B field from the calibration to the measured value (extracted from Eq. 4.1). We observe no changes in the slope and only a slight modification of the offset, mainly due to thermal deviations affecting the electronics, which have to be corrected on a daily basis. The magnetic field stability, within a single experimental session, lasting typically 4 hours, is about 0.5 mG.

To translate the magnetic field into a value of scattering length, we modify the model described in [23] (plotted in Fig. 4.2c). The model takes into account three Feshbach resonances lying at 5.126(1) G, 5.209(1) G, 21.95(5) G and characterized by widths of 35(1) mG, 12(1) mG, and 2.4(8) G respectively. The resonance at highest field has been characterized in [116]. Considering a background scattering length of $a_{bg} = 139(4)\,\mathrm{a}_0$, a_s is given by

$$a_s(B) = a_{bg}\left(1 - \frac{\delta B_1}{B - B_1}\right)\left(1 - \frac{\delta B_2}{B - B_2}\right)\left(1 - \frac{\delta B_3}{B - B_3}\right), \qquad (4.2)$$

where B_i and δB_i are the positions and widths of the Feshbach resonances. The scattering length stability derived from the model is about $0.25\,\mathrm{a}_0$, which is much smaller than the uncertainty associated with its absolute value, of about $4\,\mathrm{a}_0$, translating to a relative uncertainty in ϵ_{dd} of about 4%. This is mainly due to the large error affecting the background scattering length [179, 180][4]. To assess the overall systematic uncertainty on the absolute value of a_s, we can compare the experimental critical value of the scattering length for the superfluid-supersolid quantum phase transition, with its numerical counterpart. Indeed, by looking at the sharp features in the contrast of the modulation (see Fig. 2.8) or the atom number (see Fig. 2.2.2) proper to discontinuous phase transitions, we can measure the shift between observed and expected critical a_s. Using the harmonic potential V_D in Eq. 2.13, we establish a shift of about $6.7\,\mathrm{a}_0$ shift a_s, which is used to correct all the experimental data in the previous chapters.

---

[4] The contribution of the finite width in the RF signal only amounts to $0.5\,\mathrm{a}_0$.

4.1.1 Adiabaticity

The magnetic field is decreased during the experiment, walking down the branch of scattering length plotted in the inset of Fig. 4.2c, in order to cross the transition in the region around $90\,\mathrm{a}_0$. In principle, this must be done as slowly as possible, in order to prevent effects of non-adiabaticity such as spurious excitations of the system or heating, that can be disruptive, especially because they can scramble the global phase of the supersolid. On the other hand, the finite lifetime of the supersolid, dominated by the losses enhanced by the vicinity of Feshbach resonances together with the increase of the peak density, pushes us to be as fast as possible. Moreover, approaching the supersolid region we cross many narrow Feshbach transitions, peculiar to the dense resonance spectrum of dysprosium [122], requiring to spend the least amount of time at a given magnetic field, in order to avoid drastic losses. As a compromise, we employ two different ramps: the first one is fast, and it's used to bring us near the supersolid region avoiding the narrow resonances; the second one is slower and it's used to cross the transition almost adiabatically. To understand the effect of the last ramp speed, on the experimental observables, we performed a detailed study of the adiabaticity we can achieve in our system. In particular, we have to make sure of two things. First, the different characters of the quantum phase transition, investigated in the harmonic potentials V_D and V_C (see Eq. 2.13) discussed in Chapter 2, must not depend on the ramp speed. In particular, the discontinuous behavior of the phase transition in trap V_D should not be an artifact due to a non-adiabatic crossing. Second, we have to check that the quasi-adiabatic ramp used in the experiment, is slow enough to keep the system the least excited possible. This is crucial for the experimental observation of collective modes selectively excited after crossing the transition, such as the Josephson dynamics discussed in Chapter 3.

We first performed a similar experiment as the main one discussed in Sec. 2.2, but varying the ramp speed used to cross the phase transition and come back to the superfluid side. This is done for both V_C and V_D, using the ramp speed employed for the main experiment (see Fig. 2.8) which is $0.5\,\mathrm{a}_0/\mathrm{ms}$, a slow ramp at half this speed, and another one, twice as fast. For the tests, we start from the superfluid side and we cross the transition, then we hold a_s fixed in the supersolid phase (at about $-2\,\mathrm{a}_0$ from the transition point) for a holding time of $t_h = 15\,\mathrm{ms}$.

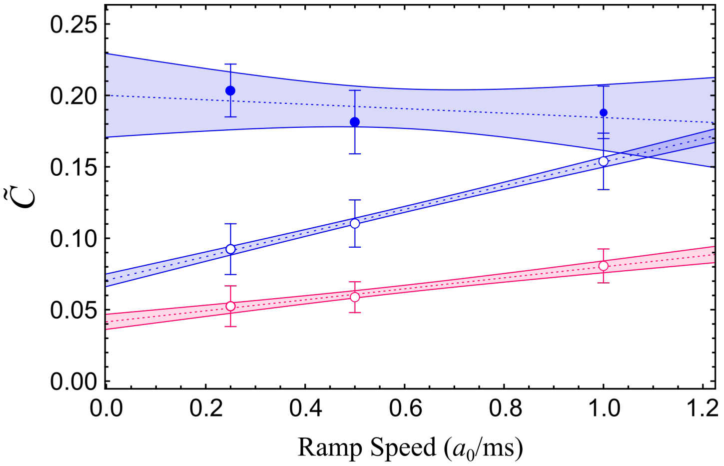

Figure 4.3: Effect of the scattering length ramp speed on the experimental observable $\tilde{C}$. Blue and magenta points and lines refer to experimental data and fit for V_D and V_C respectively. Circles mark the residual contrast after crossing twice (towards the supersolid and back) the quantum phase transition. Dots are instead the measured $\tilde{C}$ after the in-going ramp only. Dotted lines are linear regressions demonstrating the linear dependence between the residual contrast and the ramp speed. Solid lines mark the confidence bands for 1 σ.

At last, we ramp the scattering length back to the superfluid side (at about $+4\,\mathrm{a}_0$ above the transition), we wait a variable time t_w, and we release the system from the trap in order to measure the contrast $\tilde{C}$ from the momentum distribution imaged after the system expansion. The results of this double crossing in the potential V_D and V_C, presented in Fig. 4.3, show that the residual $\tilde{C}$ in the superfluid side increases for both potential for faster ramp speeds. As discussed in Sec. 2.2, this is a measure of the non-adiabaticity of the scattering length ramps, which is reflected in the amplitude of the contrast oscillations in the superfluid. To average out the effects of other collective modes triggered by the ramp, we average together data sets corresponding to different waiting times $t_w = 10, 20, 30\,\mathrm{ms}$. The contrast observed for V_D consistently exceeds that of V_C, and, although both show an almost linear increase with the ramp speed, the slope is higher for V_D. This demonstrates that crossing the transition point twice has a speed-dependent contribution for both continuous and discontinuous transitions to $\tilde{C}$. This behavior can be attributed to the finite formation time of the supersolid, which is around 15 ms, comparable with the oscillation period of the contrast (see Fig. 2.8d-e and Fig. 2.9). Since the in-going ramp is not significantly longer than the formation time, the supersolid doesn't form at the lowest available energy. In this sense, the formation time of the supersolid marks the key time scale to compare with, when choosing the correct ramp duration. The formation time of the dipolar supersolid has been studied numerically in [3, 4], where the dynamics after the scattering length ramp is slowed down due to the absence of dissipation (given mainly by atom losses in the experiment). In particular, in [4] it is shown that the formation time depends on the growth ratio of the most unstable mode of the superfluid, which is the roton mode, thus depending mainly on the *initial* state before starting the ramp. This suggests that different trapping potentials lead to different time scales in the growth of the roton at the instability point and so different formation times for the resulting supersolid. It's important to note that even when extrapolating to zero ramp speed using a linear fit (dashed lines in Fig. 4.3), the residual contrast for V_D continues to be larger than the one for V_C. This reaffirms the discontinuous nature of transition in V_D. The nonzero intercepts at zero speed for V_C, it's instead given by atom losses, which lead to a loss of adiabaticity at long times.

A second type of analysis is focused only on potential V_D. The idea is to study the contrast after the on-going ramp, just after the transition as a function of the ramp speed, to see if the finite jump of $\tilde{C}$ at the transition is produced by the non-adiabaticity of the ramp. To do so, we ramp the scattering length to $92.5a_0$, just before the nominal value for the transition point, and we post-select the realization consistent with a supersolid, by neglecting all the images where $\tilde{C} = 0$. As before, we wait a time $t_h + t_w$ before releasing the system from the trap, with $t_h = 15\,\mathrm{ms}$ and $t_w = 10$, 20, $30\,\mathrm{ms}$. Data sets corresponding to different waiting times are averaged together to minimize the impact of other collective modes. The average $\tilde{C}$ as a function of the ramp speed, shown in Fig. 4.3, is almost constant over the whole speed range. This demonstrates that, indeed, the jump is independent of the ramp speed and it's only given from the discontinuous nature of the phase transition. Note that the same analysis cannot be done for potential V_C since the transition point is not marked by a sharp increase of $\tilde{C}$. An alternative analysis could be performed instead on the variance of the supersolid phase, determining the coherence of the system. However, from the results already presented in Fig. 2.14, we conclude that the speed chosen for the experiment is slow enough to keep the phase coherence of the system intact, even when we go deep in the supersolid phase, where decoherence is enhanced by atom losses.

4.2 Trap geometries

The geometry of the optical dipole trap employed in the experiment can be minimally tuned controlling the power in the infrared beams at the end of the evaporation. Indeed, the beam profile of the two dipole beams have different aspect ratios: 1:1 for the ODT1 and 1:3 for the ODT3. Thus, controlling the relative intensities of the beams, we can control the aspect ratio of the crossed trap. All the harmonic traps used in the experiment have the same vertical confinement, around 100 Hz, since the natural length of the harmonic oscillator in the vertical direction fixes the spacing of the supersolid structure. With this vertical confinement, we produce supersolid with a lattice spacing of about $\lambda \sim 4\,\mu\mathrm{m}$, which results, given our number of atoms, in an inhomogeneous supersolid with 4 main clusters. As shown in the previous chapters, the number of clusters can be reduced by adjusting the atom number (basically waiting for a fraction of the BEC lifetime, in order to lose atoms), and the structural properties of the emerging supersolid can be controlled by manipulating the x-y aspect ratio of the trap. This can be done by controlling the power of the crossed dipole trap beams, keeping fixed the vertical frequency, and changing the transverse ones. Our standard optical trap gives the harmonic potential V_D (defined in Eq. 2.13), which is elongated in the x direction and with a $1:3$ aspect ratio in the x-y plane, resulting in a discontinuous phase superfluid-supersolid quantum phase transition. To manipulate the character of such transition, we need a more confining trap along the transverse direction. We first evaporate in V_D then, when the scattering length is still high above the critical point, we compress the atoms by slightly increasing the power of the ODT1 and ODT3 beams, to reach the configuration of trap V_C (see Eq. 2.13). In the compression process, we don't observe any heating, but the higher density in V_C increases the atom losses, so the standard atom number in the so-called *continuous trap* is about 4×10^4. A similar procedure to reach trap V_C, is used for the Josephson experiment described in Chapter 3.

Trap frequencies are measured by looking at the dipole mode of the condensate in time of flight measurements. To excite the dipole oscillation, after preparing the standard condensate in the harmonic potential of interest, we perturb it imprinting a force using either a pulse of Zeeman slower compensating coils or a pulse of quadrupole magnetic field gradient generated by the MOT coils. The former excites the dipole mode mainly in the transverse direction, triggering oscillations of the center of mass of the atomic cloud in the x-y plane, which is then imaged with our standard vertical imaging. The magnetic gradient, instead, is used to produce dipole oscillations along the vertical direction. To better address these oscillations, we use an alternative scheme employing a blue imaging beam coming from the side (namely it is directed in the same path of the long-spaced optical lattice sketched in Fig. 4.1b) and a secondary camera. Although this lateral imaging has a lower spatial resolution, it is enough to measure dipole oscillations.

4.3 Dispersive phase-contrast imaging

To image the supersolid in-situ without the disruptive effects produced by diffraction in standard absorption images at such high densities, we employ a different technique, where atoms act instead as a dispersive medium. The idea is to use linearly polarized light detuned by δ from the 421 nm transitions to suppress the absorption from the atom cloud. When the light passes through the atoms it acquires a dispersive phase shift proportional to n/δ (where n is the integrated 3D density), and by analyzing the phase shift, after separating the light perturbed by atoms from the rest, we can reconstruct the density directly. Since the atoms do not absorb photons, but just scatter detuned light, this technique is used for non-destructive imaging of ultracold gases in various experiments. Here I just report the first realization of this imaging scheme [25], employed on ^{7}Li to precisely measure the atom number in the condensate, and the many experimental works on dipolar quantum gases [167, 194, 69, 174, 16].

Our imaging scheme is sketched in Fig. 4.4. We use linearly polarized light with $\delta = 5\Gamma_{421}$ coming from below the vacuum cell and collimated to a large beam diameter such that the atoms feel an almost constant light intensity I. The atomic cloud rotates the polarization of the incoming light by an angle β, proportional to the cloud density. The scattered light is then collected by a single objective lens with $f = 75$ mm and then reflected by a dichroic mirror, used to separate the blue light from the 626 nm MOT light, towards a tube lens with $f = 500\,\mathrm{mm}$. At this point, the light passes through a $\lambda/2$ waveplate which adds constant angle θ to the polarization. At the focal plane of the second lens, we use a polarizing beam-splitter to mix the scattered and unperturbed light with polarization angles $\beta + \theta$ and θ respectively. Changing θ we can choose the so-called *dark field* configuration, where all the unperturbed light is filtered out by the polarizing beam-splitter, or the *bright field* configuration, where the measure has a finite background, but a better sensitivity. We can reconstruct the two-dimensional in-situ density as [193]

$$n_{2D} \propto \frac{\delta}{\Gamma_{421}} \left[\theta - \arccos\left(\sqrt{\frac{I_A - I_D}{I_B - I_D}} \cos\theta \right) \right] , \tag{4.3}$$

where I_A and I_B, are the recorded light intensities with and without the atomic cloud, while I_D is the dark configuration with no imaging light.

To collect these images, we use a third lens with $f = 75\,\mathrm{mm}$ at a distance p from the focal plane of the second lens, refocusing the image of the atoms on the sensor of an EMCCD camera (Andor iXon), in order to increase the system magnification up to $M \sim 50$. To acquire I_A and I_B in the same conditions, we use the Fast Kinetic acquisition mode of the camera. This allows us to register the image I_A with a first pulse of imaging light on a reduced portion of the camera sensor, move the information to another sector of the chip, and use a second light pulse to register I_B (reusing the first sector of the chip). In between the two imaging pulses, we use a resonant cleaning pulse of 421 nm light, coming from the horizontal direction, which destroys the atomic cloud. The third image, I_D is recorded instead at the beginning of each experimental run. The column density is then calculated via software in real-time, combining the recorded images and the imaging parameters.

4.4 Design of a new quantum gas microscope

From the discussion in Chapter 3 about the detection of the cluster populations from the supersolid in-situ density, it is clear that the major limiting factor is the optical resolution of our imaging scheme. This has

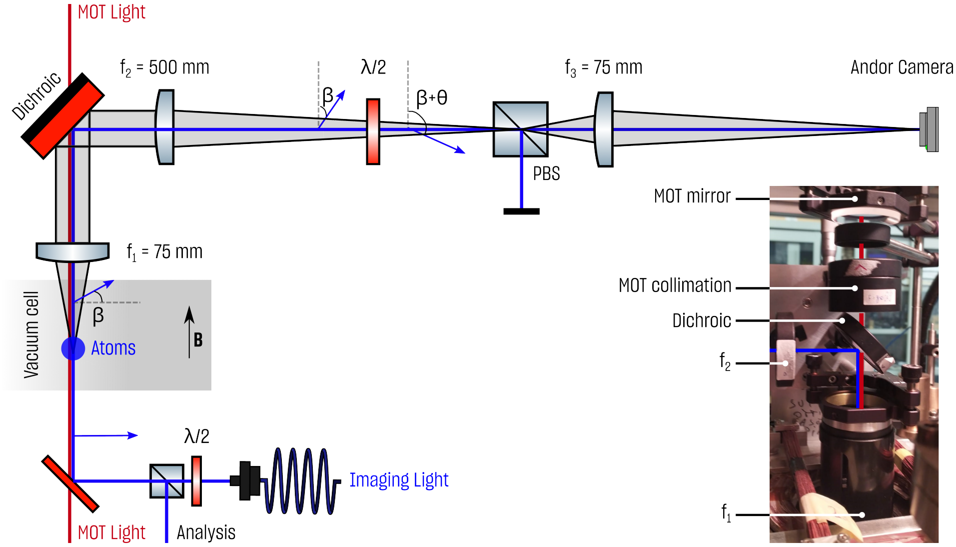

Figure 4.4: Sketch of the optical scheme for the dispersive phase-contrast imaging. The path of the imaging light is marked in blue. The light scattered by the atomic cloud is represented in gray. The red line is the path of the vertical mot beam. The picture shows the detail of the mechanical support holding f_1, f_2, the dichroic separating the MOT from the imaging light after the atoms, and the lens used to collimate the MOT beam which is then back-reflected by the upper mirror.

been designed specifically for the Josephson experiment since it was crucial to measure both phase differences and population imbalance oscillations. The key requirement of the design is the long working distance, of about 66.5 mm, needed to focus the atomic cloud inside the science cell, which is not equipped with re-entrant viewports typically used in combination with high-resolution objectives. In our design, sketched in Fig. 4.4, the light scattered by the atoms is collected by a single lens, held near the glass window of the cell by a mechanical support which can be adjusted in the three spatial directions by a micrometric translational x,y,z stage. We mounted on the same support the dichroic mirror, the tube lens, and the MOT re-collimation lens, so the overall alignment is preserved if we need to adjust the position of the objective lens. This design also allows testing and minimizing the relative tilts of the optical elements, in order to achieve the the best configuration.

4.4.1 Current scheme

The main problem of the current scheme comes from the achromatic doublet (AC508-075A) with $f = 75\,\mathrm{mm}$ used as objective lens, which has in fact very poor optical performances if compared to commercial high-resolution microscopes, typically reaching the diffraction limit. This is typically expressed by the resolution R_{DL}, given by the Rayleigh criterion [21]

$$R_{DL} = 0.61\frac{\lambda_L}{NA}\,, \tag{4.4}$$

which corresponds to the *Airy disk* radius, typically calculated by ray-tracing software. Here $\lambda_L = 421\,\mathrm{nm}$ is the wavelength of the light used for the imaging. Using the full lens aperture (the semi-diameter is 25.4 mm) we have a relatively high numerical aperture $NA = 0.3$, which gives at our wavelength a sub-micron diffraction-limited resolution, of about 0.85 µm. However, the real case is much worse since the doublet is subjected to all kinds of optical aberrations. The single parameter used to describe the impact of such aberrations is the Strehl Ratio, SR which is defined as the height of the point spread function[5] (PSF) in the real case, relative to the diffraction-limited one. With full aperture, we obtained from ray-tracing simulations $SR < 0.1$, meaning that aberrations completely scramble the PSF drastically reducing the light in the central peak. This reduction can be countered by reducing the numerical aperture. Indeed, by positioning an iris on the second lens of our scheme (see f_2 in Fig. 4.4) and reducing the objective lens aperture by 1/3, we achieve a resolution[6] $R_{PSF} \sim 3\,\mathrm{\mu m}$, with $SR \sim 0.7$. In this configuration we have $NA = 0.09$ and $R_{DL} = 2.74\,\mathrm{\mu m}$. In the ray-tracing simulation, we've also considered the fused silica window of the glass cell between the atoms and the objective, with a thickness 7.5 mm.

The system has been then simulated as a whole, including the other two lenses $f_2 = 500\,\mathrm{mm}$ (LA1380A) and $f_3 = 75\,\mathrm{mm}$ (LA1145A), optimizing their positions to have a total magnification $M = 50$ between the plane of the atoms (which is now the object plane) and the image plane placed at the position of the camera. These additional lenses are not critical for the overall performances, and we achieve a $SR \sim 0.6$ on the camera plane for on-axis fields. The off-axis performances (simulated by adding point-like sources at a finite distance from the optical axis)

---

[5] This is just the image of a point-like light source, produced by optical setup

[6] We estimate the resolution R_{PSF}, from the size of the PSF on the image plane

stay the same up to a decenter of 0.1 mm on the object plane. This defines also the Field of View (FOV) of our microscope. These features have been also measured experimentally on a test setup, using a 1951 USAF target (R1DS1P), extracting a resolution of about 3 µm.

4.4.2 New design

To improve the spatial resolution of our system, we plan to substitute the first lens by employing a commercial diffraction-limited N-BK7 aspheric lens (AL50100GA), keeping the current scheme which needs only to be slightly modified since the focal length of the new lens is $f_A = 100\,\text{mm}$. By itself, the aspheric achieves $SR \sim 0.99$, with an aperture of 36 mm, and a resolution $R_{PSF} \approx R_{DL} = 1.4\,\mu\text{m}$ for fields on-axis. Off-axis performances are slightly worse. The resolution decreases to $R_{PSF} = 1.6\,\mu\text{m}$ for fields decentered by 250 µm. These simulations are performed with collimated light passing through the objective and focused on the plane of the atoms. To introduce the displacement in the plane of the atoms (image plane), we use tilted incoming fields. The angle where we lose the diffraction limit is $\sim 0.19\,\circ$ corresponding to a FOV of about 600 µm, well above the supersolid dimensions. Simulating the PSF size through the focal point, we also find the Depth of Focus (DOF) of the system, about 10 µm, which is of the same order as the size of the supersolid clusters along the z direction.

Taking into account the fused silica window, we lose the diffraction-limited performances and we have to further reduce the aperture to 33 mm and optimize the distance between the aspheric and the window (keeping fixed the distance between the latter and the atoms) in order to minimize the spherical aberration and optimize the Strehl ratio. In this new configuration, the performances are similar to the ones without glass window, as reported in Fig. 4.5. We achieve $R_{PSF} = 1.5\,\mu\text{m}$, $SR > 0.9$ with $NA = 0.16$. Note that for marginal rays (decentered by 300 µm), the spot size increases to 2.2 µm. The DOF, instead increases to 15 µm as an effect to the reduced aperture. This last step would be not necessary if we use another optical element to counter the spherical aberrations introduced by the glass window, keeping the same NA. In particular, we tested a custom positive meniscus with $R1 = 400\,\text{mm}$ and $R2 = 500mm$ sitting between the objective and the cell. Optimizing

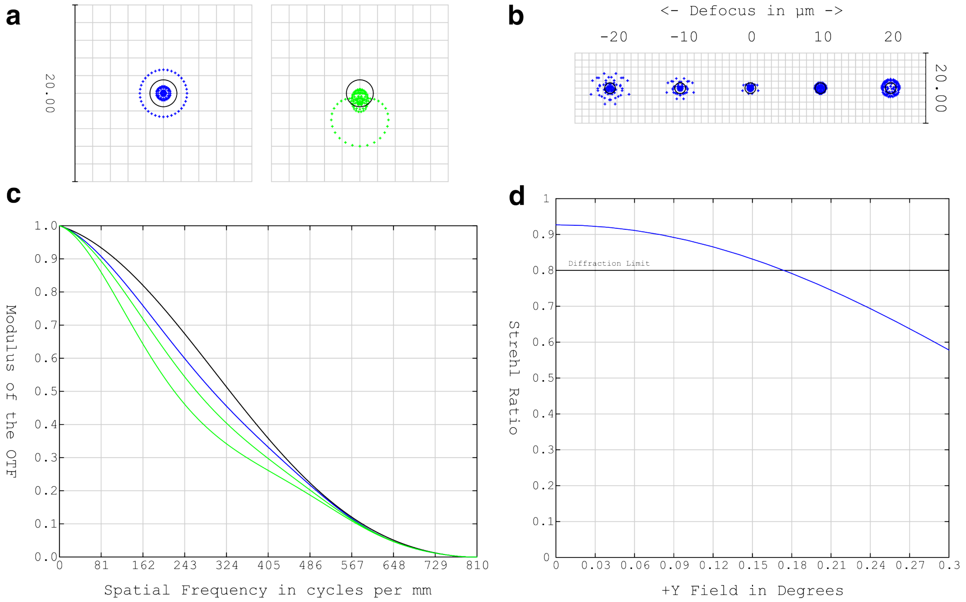

Figure 4.5: Simulated performance of the aspheric lens used in the new design of the imaging scheme. (a) Spot diagram at the image plane for on-axis (blue) and 300 µm off-axis field (green). The calculated PSF radii are respectively 1.5 µm and 2.1 µm. The *Airy disk* (black) radius is 1.56 µm. (b) Spot diagram through focus for the on-axis field. The *Airy disk* is reported in black. (c) Modulation Transfer Function [62] for the optical system for on-axis (blue) and off-axis fields (green). The two green lines refer to the longitudinal and transverse directions with respect to the field decenter. (d) Strehl Ratio as a function of the field tilt in the object plane. The maximum tilt for achieving diffraction-limited performances fixes the FOV. Black lines in (c-d) mark the diffraction limit.

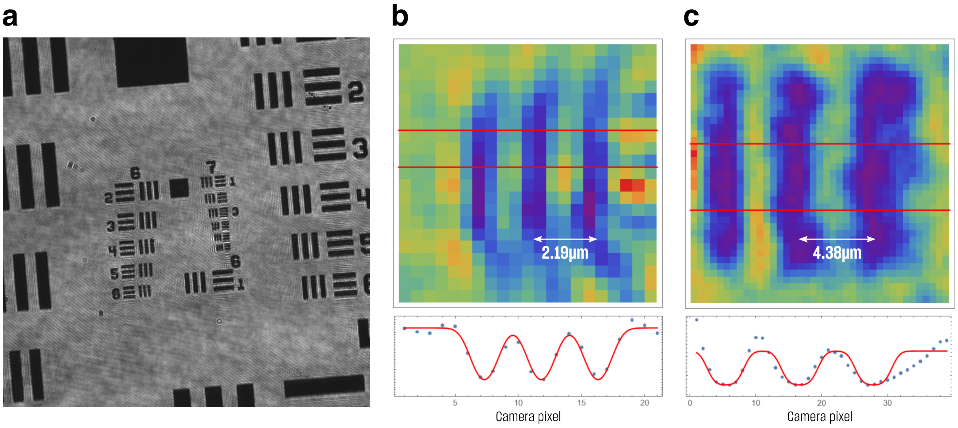

Figure 4.6: Tests of the new imaging system. (a) Full view of the USAF target used for the tests. (b) Image of the smallest resolved element on the target. The spacing is 2.19 μm. (c) Image of a larger element, with spacing similar to that of the supersolid 4.28 μm. The bottom panels in (c-d) show the extracted 1D profiles and the fit function (red line) used to extract the spatial resolution, which is respectively 1.9(3) μm for (c) and 1.7(2) μm for (d).

the relative positions of the two elements we find diffraction-limited performance, with not so small tolerances on the inter-distances (of the order of 1 mm). Since the overall performances are good even without the meniscus, we use the simple trick of reducing the aperture, gaining in depth of focus, thus decreasing the complexity of the objective alignment on the atoms. We simulated the whole system, from the atoms to the camera, reversing the design discussed above and adding the same two commercial lenses as before (LA1380A with $f_2 = 500$ mm and LA1145A with $f_3 = 75$ mm). Being p the distance between f_3 and the image produced by f_2, and q the distance between f_3 and the camera, we fix $p = 80$ mm $> f_3$ and $q = 800$ mm, so the total magnification is $M = 50$ (a first 5 factor coming from the combination of the objective and second lens, multiplied by an additional factor of $10 = p/q$). For point-like sources decentered up to 100 μm in the object plane, we obtain diffraction-limited performances with this design. Note that the tolerance on the position of the third lens is rather small: a shift of about 100 μm is sufficient to drastically reduce the SR.

The final experimental configuration has been tested with a reduced magnification $M \sim 12.7$ and a test camera with pixel size 5.2 μm, employing the USAF target. The results are presented in Fig. 4.6. The intensity profile coming from a single element on the target, is fitted with a series of step functions (which mimic the shape of the USAF element) properly spaced with a Gaussian which takes into account the finite resolution. The measured resolution is then $R = \sigma/0.35$, where σ is the Gaussian width. We obtain $R = 1.7(2)\,\mu\mathrm{m}$ for an element with similar spacing to the one of the supersolid. Remarkably, we are also able to resolve the smallest element on the target, with a spacing $d = 2.19\,\mu\mathrm{m}$, which is below the resolution of the current imaging system.

4.5 Towards arbitrary tailored optical potentials

The higher resolution of the new imaging scheme would also allow projecting light onto the atomic cloud with micrometric precision. This opens up the possibility of exploiting spatial light modulators to build tailored optical potentials to trap and manipulate the dipolar supersolid. Since the supersolid breaks the translational symmetry in the directions orthogonal to the dipoles, the natural choice is to project such potentials in the x-y plane, on top of the standard harmonic confinement. The latter has to be modified from the usual elongated shape (used for the experiments discussed in this thesis) to a more cylindrically symmetric one, allowing the realization of different geometries in 2D. Among all the possible configurations, the most straightforward is the homogeneous box-like potential, which is typically employed for the study of other quantum phases in order to get rid of the inhomogeneities arising from the harmonic confinement. Curiously, the presence of strong walls has quite the opposite outcome in the case of dipolar gases, where the un-screened long-range repulsion leads to the accumulation of most part of the atoms toward the edges [157, 81]. The other paradigmatic configuration for the study of supersolidity, without the effect of an inhomogeneous density, is the annular geometry.

Starting from the connection with the seminal work by Leggett [103], the annulus is indeed the most interesting configuration to study the dipolar supersolid since it realizes a simple one-dimensional system with periodic boundary conditions, approaching the configuration of an infinite system at the thermodynamic limit. The annulus is also the natural platform to benchmark the superfluid properties of supersolids, such as partially quantized supercurrents [56, 185, 7, 130] and non-classical rotational inertia [168, 183, 156]. Moreover, it would be extremely fascinating to study in the annulus the collective modes peculiar to the supersolid, such as the Josephson oscillation between neighboring clusters (discussed in Chapter 3) or zero-energy Goldstone mode [201], with no influence of the external confinement.

4.5.1 DMD setup

In order to shape the projected light intensity and tailor the potential for the supersolid, we use a Digital Micromirror Device (DMD) which is basically a two-dimensional array of tiltable mirrors which can be used to locally control the reflectivity on the device surface. By controlling each pixel of the DMD we can create complex intensity patterns, which then are focused onto the atoms. Indeed, the light reflected by the DMD, after a first demagnification stage, will be then collected by the same objective described in the previous section. To do so we plan to integrate the optical scheme for the DMD light with the one reported in Fig. 4.4, exploiting the polarizing beam splitter which serves as a filter for the dispersive phase-contrast imaging. Since we choose to work with repulsive light at about 404 nm, which is not far from the imaging wavelength, we can use this scheme without optimizations of the objective to support different wavelengths. Our setup employs a Texas Instruments DLP9000X DMD chip, driven by a Vialux V-9001 module, which is controlled by dedicated software. Besides the possibility of projecting static patterns, the high switching rate of this model allows the manipulation of light intensity in real-time, to produce time-dependent potentials which can be employed in the experimental sequence.

To design the DMD optical scheme we started by estimating the total demagnification needed to image the DMD pattern on the atoms. Given the size of the DMD chip, the number of intensity shades employed for the feedback[7], and the dimension of the desired potential we

---

[7] To be able to control the intensity on a single point in the plane of the atoms, more than one pixel is used on the DMD, effectively reducing its available surface.

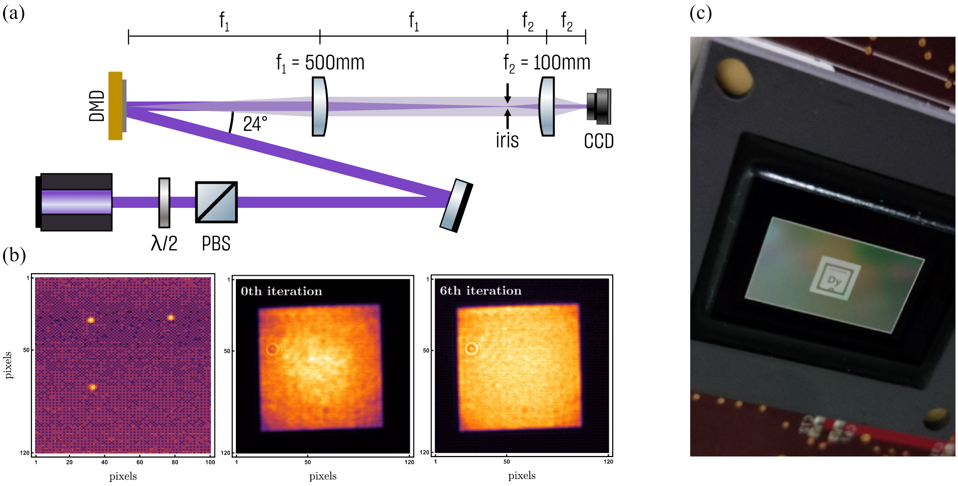

Figure 4.7: Scheme of the DMD test setup and results of the feedback algorithm used for the image correction. (a) Optical scheme for the test of the DMD. The violet light is used for the DMD illumination. The light reflected from each DMD pixel is represented in a gray shade. (b) From left to right: image used to calibrate the mapping between the DMD screen and the camera sensor; square pattern without image correction; the same pattern corrected after 6 iterations of the feedback algorithm. (c) Picture of the DMD surface with micromirrors displaying the symbol of dysprosium element. Adapted from [146].

want to project on the atomic cloud, we set the total demagnification to be $M_{DMD} = 1/25$. The test setup used for the DMD tests is sketched in Fig. 4.7a. Since the combination of tube lens and objective in the imaging scheme gives a magnification $M_{obj} = 1/5$, we use the same lenses in $4f$ configuration for the first stage of the DMD, achieving the required total magnification M_{DMD}. With this scheme, the light from each DMD pixel is collected by $f_1 = 500\,\mathrm{mm}$, passes through an iris sitting in the Fourier plane of the system, and is then focused onto the camera by the lens $f_2 = 100\,\mathrm{mm}$. The iris aperture is adjusted to filter out high spatial frequencies in the final image [49].

From the optical point of view, the DMD behaves as a blazed optical grating, thus its efficiency in reflecting light depends on the illumination angle. Since the lens f_1 is far from the DMD we only use the zero diffractive order. The efficiency, measured as the intensity of the light in the zero-order divided by the total incident intensity, has a maximum for incident light at the blazing angle $\alpha_B = 12\,°$, which is the tilt of the micromirrors set in the *ON* position[8]. Nevertheless, we use an illumination angle of $\alpha = 2\alpha_B$, which has the advantage of having the reflected light orthogonal to the DMD surface. In this configuration, the efficiency is around 20%.

In order to correct for the Gaussian profile of the laser beam used for the DMD illumination, we employ a feedback algorithm that compares the light intensity measured on the camera with a target and computes an optimized pattern for the DMD pixels [49, 146]. In Fig. 4.7b, are shown the images used to calibrate the algorithm and the results, before and after the feedback iterations, for a square pattern. Note that the flatness of the image increases drastically after just 6 iterations. Note that, although the correction of the image is crucial for projecting bright potentials, it is not a strict requirement when the DMD is used with repulsive light, since the atoms are lying in dark spots. Moreover, the feedback acts by switching off the DMD pixels where the Gaussian beam intensity is maximum, thus decreasing the total light intensity. Therefore, a compromise must be found between optimizing the flatness of the image without losing too much light.

4.5.2 Dipolar supersolid on a ring

The first application of our new DMD system would be the creation of a ring potential to study the dipolar supersolid. Using repulsive light, we plan to create a dark annulus and load the atoms initially confined in a cylindrical optical trap. In Fig. 4.8, is reported an example of ring potential, together with numerical simulations of its effect on our system. The first step consists in having the ring potential smooth and homogeneous enough, to host a standard superfluid with constant density along the annulus. Any defect in the potential would produce unwanted localization effects in both the superfluid and the supersolid, making the study of superfluid phenomena impossible. Another problem is the unavoidable presence of diffraction fringes in the dark area of the annulus, given by the very small sizes of the desired potential. Indeed, we estimate the optimal ring dimensions to be $R = 5\,\mu\mathrm{m}$ and $\delta_R = 2\,\mu\mathrm{m}$, with R and δ_R being respectively the radius and thickness of the annulus on the plane of the atoms. With our current atom number and vertical trapping frequency, we expect the supersolid to host 6-8

---

[8] The micromirrors in the *OFF* position are tilted by $-12\,^\circ$.

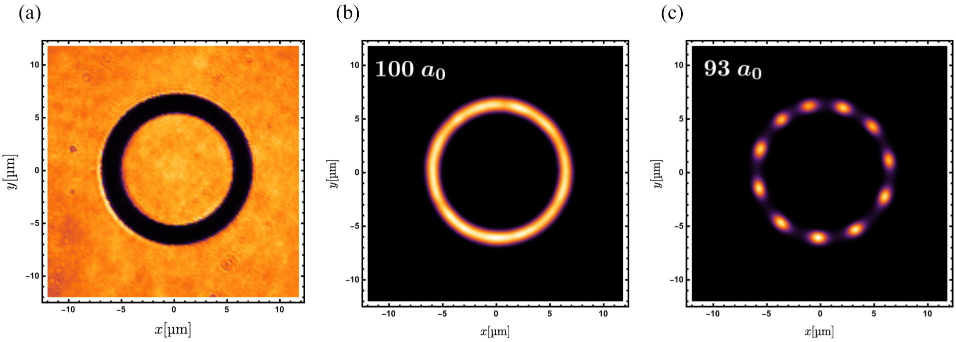

Figure 4.8: Dipolar superfluid and supersolid phases on a ring. (a) Image of the dark annulus produced by the DMD, scaled to realize a ring potential employed to simulate numerically the behavior of the superfluid-supersolid phase transition. (b-c) Ground state densities of a superfluid and a supersolid respectively. Adapted from [146].

clusters. While the maximum R is basically limited by the maximum atom number, we chose δ_R to be small enough[9] to ensure the system features a continuous phase transition towards the supersolid.

The lack of homogeneity of the ring walls and the stray light in the dark area due to diffraction, have been studied with our test setup. We find that filtering out the Fourier components at high spatial frequencies by reducing the aperture of the iris helps in smoothing out the diffraction fringes in the vicinity of the ring walls. Moreover, the overall homogeneity can be improved using the feedback algorithm described in [146]. We also found that our illumination configuration with $\alpha = 2\alpha_B$ strongly reduces the image distortions since the DMD pixels are lying at the same distance from the first lens. An alternative scheme typically used with gratings is the Littrow configuration (or autocollimation), where the DMD surface is tilted by α_B, so incoming and outgoing light are in the same direction and must be separated by polarizing filters [49]. Although this configuration is more compact, the tilt of the DMD surface with respect to the other optical elements introduces distortions, that turned out to be quite important for our application.

To test the overall quality of the ring potential we used the acquired

---

[9] With this choice δ_R is slightly above the spatial resolution of our objective, and we expect the actual thickness to be reduced further by the finite resolution.

images on the camera, properly rescaled, to calculate the ground state and first excited states solutions for a free particle, looking for the configuration that gives the maximum delocalization of the wavefunction along the annulus. We find that, together with the tilt of the DMD surface, the performances of f_2 are pretty critical. In order to minimize the spurious effects introduced by this lens, we use an aspheric, identical to the objective lens, mounted on an x-y-z translational stage that allows a precise alignment.

Circular harmonic trap

As I already mentioned, in order to create the ring potential with our spatial light modulator we first need to modify the current infrared crossed dipole trap to achieve a circular shape instead of an elongated one. Since the geometry and beam waists of the infrared beams do not allow us to reach such a configuration, we built a new crossed dipole trap based on a horizontal light sheet and a vertical beam, both at a wavelength of 532 nm, which is attractive for dysprosium. The light sheet beam has waists $(w_x\,, w_z) = (190\,, 20)$ µm, tightly confining the atoms in the vertical direction and producing a weak confinement along the x direction. To add a confinement potential along the y direction, we use a vertical beam with the same aspect ratio of the horizontal sheet, but at lower power, such that the weak axis is x and the tight axis is y. This way, we can compensate for the anisotropy of the confinement in the plane given by the light sheet alone. The sketch of the beams arrangement is reported in Fig. 4.9a, together with the spatial profile of the sheet beam mode.

The resulting harmonic confinement is almost cylindrical, with trap frequencies $(\nu_x\,, \nu_y\,, \nu_z) = (30\,, 32\,, 140)$ Hz. To obtain the BEC in the circular trap we start the evaporation with our standard infrared crossed dipole trap and we turn on the green beams when the gas is still thermal. Instead of keeping the infrared beams on at the end of the evaporation ramp, we smoothly turn them off letting the system settle in the green potential. With this sequence, we achieve a BEC of about 85% of the atoms in the circular trap, with respect to the infrared alone. In Fig. 4.9b we show the time-of-fligt density distribution of a sample of condensed atoms with $N = 2.5 \times 10^4$, held in the circular trap. Note that the small thermal fraction present could be further reduced by

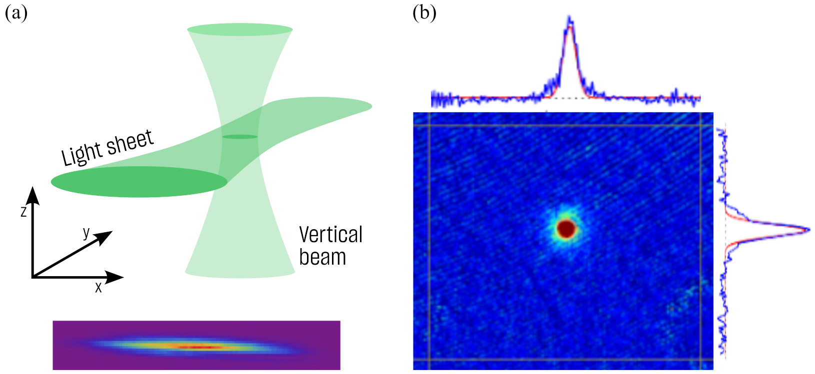

Figure 4.9: Production of a BEC in the new circular trap. (a) Sketch of the 532 nm beams employed to build the circular harmonic potential. The lower panel shows the profile of the beam used for the horizontal light sheet, imaged in the x-z plane with a magnification $M = 1$. From gaussian fits of the beam mode, we measure the waists to be $(w_x\,,w_z) = (190\,,20)$ µm. (b) Bose-Einstein condensate of about 2.5×10^4 atoms in the circular harmonic trap, imaged after an expansion of about 20 ms.

stabilizing the power of the green beams (to avoid parametric heating [164]), and optimizing the evaporation ramp.

4.6 Repulsive light at 404 nm

As discussed in the previous sections, we want to confine ^{162}Dy atoms in a trap resulting from the combination of the attractive 532 nm beams and a repulsive ring-shaped potential projected by the DMD. To produce repulsive light for dysprosium we choose to work slightly blue-detuned from a strong transition coupling the ground state with the excited $[\mathrm{Xe}]4f^{10}\,(^5I_8)\,6s6p\,(^1P_0)\,(8,1)_7$ state at 404.7 nm with $\Gamma/\,(2\pi) \approx$ 30 MHz [195]. This choice is motivated by the possibility of employing commercial laser diodes in this spectral region and the vicinity of the imaging wavelength which makes it possible to use the same objective to project the repulsive light on atoms. Moreover, we expect the atomic polarizability to be strongly enhanced (with respect to other spectral regions [83, 152, 90]) by the presence of the transition, allowing the use of low-power laser sources.

The important disadvantage of working so close to a strong transition is that the spectral profile of the laser source employed for the DMD illumination has to be filtered precisely to prevent resonant light from hitting the atoms, thus reducing drastically the lifetime of the system. We find that, curiously, an external cavity diode laser (ECDL) in single-mode operation provides a good start for building such a source, but the spectral tails due to spontaneous emission are still strong enough to significantly shorten the lifetime, even when the central wavelength is 1 nm away from resonance. Moreover, the maximum power output of ECDLs in this spectral region is typically around 50 mW, so the margin to achieve strong enough potentials for the atoms becomes thin.

The goal is then to demonstrate the possibility of creating potentials of the order of 100 nK, which is enough to manipulate an already condensed sample, without reducing the system lifetime or heating the system. I will discuss this possibility by showing the details of a suitable laser system built for DMD illumination and, equally importantly, the measurement of atomic polarizability carried out with a new technique developed by our group.

4.6.1 Blue laser

We employ a Nichia NDV4313 diode laser which, without any external cavity, runs multimode at a central wavelength of about 405 nm and a maximum power of 120 mW. We realized the external cavity with an optical grating with 3600 grooves/mm in the Littrow configuration positioned after an aspheric collimation lens attached to the laser mount. In single-mode operation, the light wavelength can be tuned by changing the tilt of the grating over a 1 nm range, but the output power is reduced to 20 mW due to the losses in the feedback process. As anticipated in the introduction to this section, the spectrum in this configuration is not sufficiently clean to make the source usable to trap atoms.

We develop a filtering scheme, sketched in Fig. 4.10 together with the results for the system lifetime, employing an additional optical grating and a single-mode fiber. The working principle is the same as a spectrum analyzer, where the incident light on the grating is spatially separated in its spectral component, which then is selected by a slit, which in our case is a fiber. This way we can select precisely a tiny region of the laser spectrum, that coincides with the peak emission of

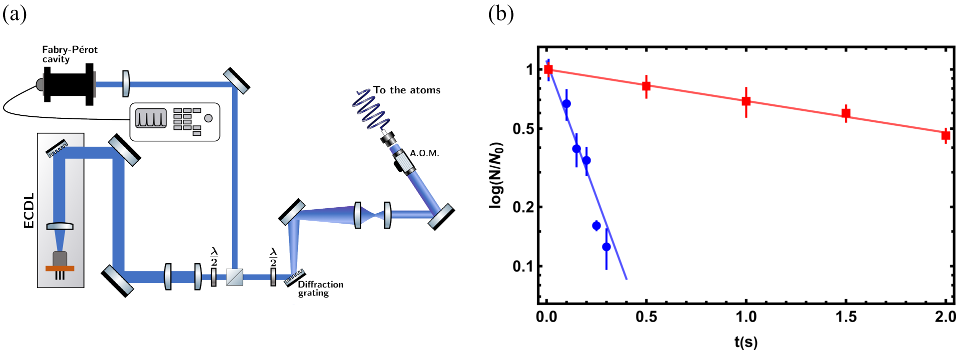

Figure 4.10: Effect of the spectral filter on the atomic lifetime. (a) Sketch of the optical setup for the spectral filtering of the laser light. (b) Measured lifetime on the condensate held in the standard infrared harmonic trap, when we shine 2 mW of blue light at 403.6 nm single-mode. Blue points represent the atom losses for unfiltered light, while for red points we employ the spectral filter.

the ECDL mode, and send it to the atoms. Besides working as an exit slit of our filter, the fiber cleans also the spatial mode of the diode laser, which is then resized and focused onto the atoms. In Fig. 4.10b, we see that the lifetime of the system is $> 2\,$s using filtered light, while is of the order of hundreds of milliseconds without the filter. This last measure can be done by simply coupling the zero-th diffractive order on the filtering grating into the same fiber. Using either the zero-th or the first order we can choose between unfiltered or filtered light.

Although this measure demonstrates the long lifetime of the system, given we take care of the spectral tails of the ECDL, the setup is strongly limited by the power output. To increase the total amount of light available, we developed a master-slave scheme where a first ECDL running in single-mode, is used to feedback a second diode (identical to the first one). In this case, the power of the slave is larger, of about 40 mW, maintaining the characteristics of the master laser. In order to reduce the losses from the filtering method, we also use a tilted spectral filter (Semrock LL01-405) to cut the high wavelengths from the spectrum, instead of the grating. Note that the filter simply suppresses the intensity of light in the excluded spectral region, without eliminating it completely, thus we have slightly more losses with respect to the data in Fig. 4.10, but the lifetime is still above 2 s.

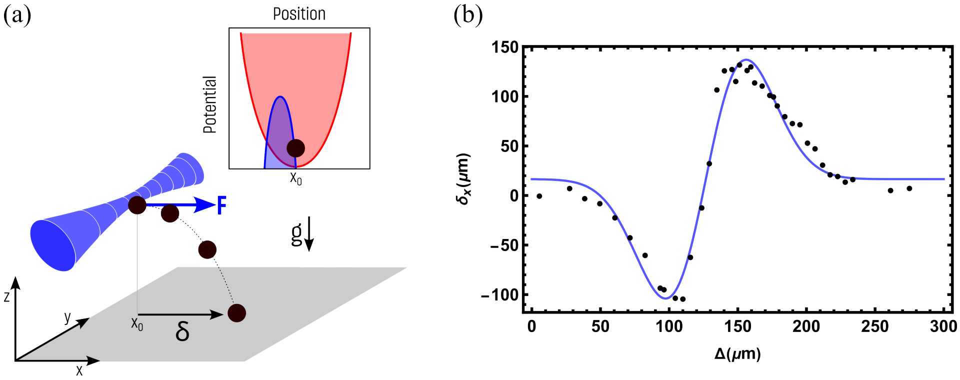

Figure 4.11: Measurement of the total polarizability from the momentum imprinted by blue light onto the atomic cloud. (a) Sketch of the measurement procedure. The atoms, held in x_0 by the standard infrared potential, are pushed by a pulse of light with a force F which depends on the alignment. After releasing the atoms from the trap, the cloud falls and expands. We measure the displacement δ with respect to x_0 of the center of mass of the cloud (black dot) in time-of-flight images. (b) Typical behavior of the measured displacement δ_x as a function of the alignment of the beam. Here Δ is the distance of the atoms to the beam center. Black dots are experimental results, fitted with the derivative of a Gaussian (blue line).

4.6.2 Measure of the atomic polarizability

To be sure that the dipole potential exerted by the blue light onto the atoms is enough to realize repulsive confinements with the DMD, we also need to know the polarizability of dysprosium atoms at this wavelength. Since there is no such data available in the literature, we developed a new method to experimentally extract the polarizability α by measuring the dipole force in time-of-flight. This is conceptually different from the standard methods to measure α for attractive wavelengths, which usually rely on the measurement of trap frequencies [83, 152, 90], not possible in the case of repulsive potentials.

The working principle of our method is sketched in Fig. 4.11. We start with the condensate in our standard infrared trap and we use a pulse of tightly focused linearly polarized blue light to push the atoms imprinting momentum to the cloud. Just after the blue pulse the infrared trap is turned off and the atoms fall under the action of gravity. After the expansion we image the momentum distribution, detecting the displacement δ in the x-y plane which is proportional to the repulsive force. The latter depends clearly on the alignment of the blue beam with the atomic cloud. Assuming a point-like density distribution (for simplicity) and Gaussian beam profile, we expect the force to behave like the derivative of a Gaussian with a maximum

$$F_{max}(\omega) = \frac{2\alpha(\omega)Pe^{-1/2}}{\pi\epsilon_0 c w_z w_x^2}\,, \tag{4.5}$$

when the atomic cloud sits at half the beam waist from the beam center. Here we assumed the beam to be perfectly aligned along z and pushing only along x (since y is the direction of propagation). In the equation, α is the total polarizability, P is the light power, and w_z, w_x are the beam waists along z and x. Controlling the position of the beam Δ we measure the displacement reported in Fig. 4.11b. From the distance between the two maximum values, we infer the waist of the blue beam at the position of the atoms. This is quite remarkable since represents a direct measure of the waist, without the use of any further propagation. The uncertainty of the measure is mainly due to the finite precision in controlling Δ, which is modified using two motorized screws acting on the mirror directing the blue light to the lens which focuses it onto the atoms. The beam tilt induced by the mirror is translated in a displacement of the beam into the focal plane by the lens. We calibrated the single step of the motor to induce a displacement of 4 µm in the plane of the atoms. From the data in Fig. 4.11b, the obtained waists are $w_x = 58(7)\,\mu\text{m}$ and $w_z = 38(3)\,\mu\text{m}$.

To extract the total polarizability we first align the blue beam to have the maximum force described by Eq. 4.5, then we vary the incident power P, and from the slope of a linear regression, we derive α. To extract the contribution of the scalar, vectorial and tensorial polarizabilities, we employ the polarization of the blue light. For linearly polarized light the vectorial component vanishes and, for the ground state of dysprosium we can derive [125]

$$\alpha(\omega) = \alpha_s(\omega) + \frac{3\cos^2\theta - 1}{2}\alpha_t(\omega)\,, \tag{4.6}$$

where α_s and α_t are respectively the scalar and tensorial component of the polarizability and θ is the angle between the quantization axis (defined by the external magnetic field $\boldsymbol{B} = B\hat{z}$) and the polarization vector of the electric field of incident light. Given the sinusoidal dependence of the total polarizability on the polarization angle, we separate the scalar and tensorial component, by measuring δ as a function of θ.

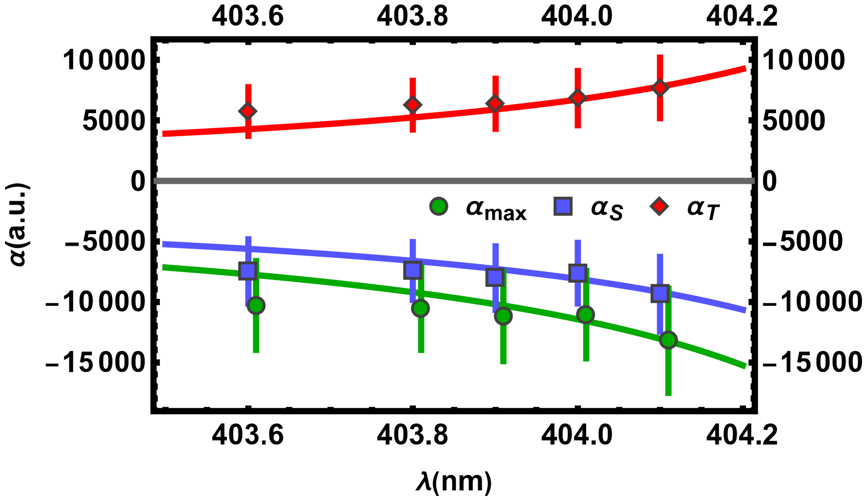

Figure 4.12: Polarizability of ^{162}Dy around 404 nm. The experimental points represents the scalar (blue) and tensorial (red) polarizabilities as a function of the laser wavelength. The maximum of the total polarizability (green) is reported in the same range. Solid lines are theoretical predictions from [51, 109].

From Eq. 4.6, we have the maximum displacement for $\theta = \pi/2 + \ell\pi$ where $\alpha = \alpha_s - \alpha_t/2$, and the minimum displacement for $\theta = \pi + \ell\pi$ where $\alpha = \alpha_s + \alpha_t$. From these relations, we can extract both α_s and α_t.

We performed these kinds of measurements by varying the wavelength of the blue laser. Our results are reported in Fig. 4.12, showing that the maximum total polarizability is indeed very large, of about -13000 a u at 404.1 nm, just 0.6 nm from the transition. With these numbers and the actual optical power available for the DMD scheme, taking also into account its diffraction efficiency and the transmission losses due to the optical fibers, we estimate to reach potential walls even higher than 100 nK, which was our initial goal. Indeed, considering 1.5 mW of blue power, focused on a waist of 60 µm, we calculate the height of the ring walls to be 1.5 µK.

Chapter 5

Towards novel topological excitations in a spinor condensate

In this chapter I will present the work I carried out as a visiting student during my stay at the Kirchhoff Institut für Physik (Heidelberg, DE), where I worked in the group of Prof. Markus K. Oberthaler on a ^{87}Rb spinor Bose-Einstein condensate [84, 176]. The beauty of this quantum system is the richness of accessible internal magnetic states in different energy manifolds that allow for full control over the preparation, the evolution, and the readout of its many-body state. This platform is therefore ideal for exploring many fundamental phenomena such as quantum phase transitions [119, 147], out-of-equilibrium dynamics [166, 148, 149, 150, 102, 100], topological excitations [101, 171, 172], entanglement [128, 129, 92, 93, 94, 91] and entropy transport [31]. For the scope of this chapter, I will just give an overview of the rich physics one can investigate in such a system, focusing only on the details of the experimental work I took part in during my visiting period in the lab.

In general, a spinor condensate can be understood as a mixture of bosonic particles in different spin states, that can interact either by standard collisions or spin-dependent ones, able to change the spin states of particles, which are described collectively by a multi-component wavefunction. Tuning the interactions, the energy landscape of the system can be changed, giving rise to different quantum phases in the ground state, depending on the relative populations of the spin states. Here I will focus on a quasi-one-dimensional spin-1 system, exploring a quantum phase transition from the *polar* phase [169], where the total spin $\mathcal{F}$[1] is zero, towards the so-called *easy-plane* ferromagnetic

---

[1] Here $\mathcal{F}$ is the length of the spin vector defined later in Sec. 5.1.1

phase [150], characterized by a finite transverse spin length $\mathcal{F}_{\perp}$ with respect to the quantization axis. In the experiment, we typically cross this phase transition with a sudden quench of the quadratic Zeeman shift, leading to a non-equilibrium dynamics towards the new ground state. This dynamics have been observed and discussed in [148]. As a preliminary study on the possibility of observing novel topological excitations emerging from the evaluation of the system dynamics, I contributed to characterizing the relaxation dynamics in a new set of observables, confirming previous results, and studying the response of the system to perturbations once in the new ground state. These measurements constitute the first steps toward the experimental validation of an effective theory (under development) governing the system, which is expected to host a variety of topological excitations, such as real-time instantons [172].

During early evolution after the quench, the excitations of the system are understood as Bogoliubov perturbations that grow within the system giving rise to a peculiar spatial dependence of the spin. The emerging structures can be described as the occupation of unstable momentum modes around a specific finite k-vector predicted by the Bogoliubov theory [84]. This spatial structure of the spin is not persistent at later times, since the interactions redistribute the momentum population over a finite range of k-vectors [147]. It's curious to note that the unstable modes of spinor condensates in a quasi-2D confinement, have been proposed to be linked to a possible supersolid phase [37], coming from the interplay of dipolar and spin interactions in the spin-1 system. Indeed, it was observed experimentally that a spatial pattern of magnetization emerges in such systems during slow evaporation [161] Moreover, the system prepared out of equilibrium with a non-homogeneous magnetization texture can spontaneously relax into a spatially modulated structure of spin domains [189]. However, a conclusive connection between these phenomena and the presence of a supersolid has not been traced. Another type of modulated state in the spin condensate is the so-called *spin-wave*, where the modulation of the spin length is not spontaneous, but is the result of the system evolution in the presence of external magnetic field gradients. Spin waves have an important practical utility in the experiment since they are used for calibrating the readout sequence (See Sec. 5.1.2), and they constitute a fascinating initial condition to start the out-of-equilibrium dynamics

[148].

At later evolution times, other non-linear and topological excitations come into play. An interesting phenomenon comes from the possibility of having random excitations of the relative phase between the different spin states. Similarly to what happens with rough waves, phase excitations can build up during the time evolution, as they are *focused* by an effective potential, giving rise to a cusp divergence in the spin length at a given point in space and time. These kinks realize a vortex-like structure in space and time and can be described as real-time instantons, topological excitations predicted to appear randomly after the quench from the polar to the easy-plane phase[172]. However, the out-of-equilibrium dynamics is complicated, and revealing such objects on top of the disordered dynamics of the experimental system is challenging since they appear randomly in the system. This is a major problem for the detection of such excitations since we are not able to measure time series in experiments, which typically rely on absorption images. Another approach to studying this type of excitation would be to prepare a single time-space vortex in a deterministic manner, exploiting the possibility to locally manipulate the spinor condensate in experiments. Driven by this idea, the ongoing project is to study real-time instantons in a quasi-1D system, properly initializing the system in order to have a deterministic formation of instantons in a precise space-time point. Both the right initial condition and the experimental sequence needed to realize it are the subject of ongoing investigations.

Contributions

The results presented in this chapter are preliminary, and they are part of a larger project under the supervision of Prof. Markus K. Oberthaler and coworkers. In particular, I want to acknowledge the contribution of Helmut Strobel, Yannick Deller, Stefan Lannig and Felix Klein for the experimental part, and of Ido Siovitz for the discussion of theoretical aspects and numerical simulations.

5.1 The ^{87}Rb spinor condensate

The experimental platform is a quantum gas of ^{87}Rb confined in an elongated optical trap realizing a quasi-1D system, where all the relevant dynamics happen along only one spatial direction. As the other alkalis, ^{87}Rb has a simple but rather interesting atomic structure, presented in Fig. 5.1. In the ground state, the electronic configuration is [Kr]$5s^1$, with a single electron in a s shell resulting in a $^2S_{1/2}$ state. The electronic spin $\mathrm{J} = 1/2$ couples with the nuclear one $\mathrm{I} = 3/2$, splitting the electronic ground state into two hyperfine levels with total spin $\mathrm{F} = 1, 2$ separated by $\Delta E_{hfs} \approx 6.8\,\mathrm{GHz}$. The rubidium gas is cooled down with standard techniques and condensed in the lowest-lying level, the $\mathrm{F} = 1$, which is the only relevant state for the spin physics we want to discuss in this chapter. However, it's important to note that the possibility of accessing the $\mathrm{F} = 2$ state is crucial, as I will describe in Sec. 5.1.2, for both the readout sequence and the global manipulation of the spinor wavefunction. When external magnetic fields are applied[2], each hyperfine level splits into sub-states labeled by their spin projection $m_\mathrm{F} = -\mathrm{F}, \ldots, \mathrm{F}$ along the quantization axis z, and separated by an energy shift

$$\Delta E_{|\mathrm{F}, m_\mathrm{F}\rangle} = \mu_B \, g_\mathrm{F} \, m_\mathrm{F} \, B_z. \tag{5.1}$$

Let's now focus on the $\mathrm{F} = 1$ manifold, and see how interactions are modeled in a spinor condensate. Since the total magnetic moments of the particles are small, we neglect dipole-dipole interactions and long-range effects, retaining short-range collisions as the only mechanism for two particles to interact in our diluted gas. Being a scattering process, a two-body collision should conserve quantities such as the total energy, momentum, and spin. In particular, when two atoms collide they can either maintain their initial internal state or change Zeeman sub-level across the manifold. I will refer to the first process as *standard* or *density* collisions and to the second one as *spin-changing* collisions (SCC). The latter are of fundamental importance in our spinor condensate since they allow for coherent population transfer between the different spin states, giving rise to the different magnetic phases that we can explore in our system (see discussion in Sec. 5.2).

---

[2] This picture applies to low magnetic fields, where the energy shift is small compared to the hyperfine splitting and we are far from the *Paschen-Back* regime

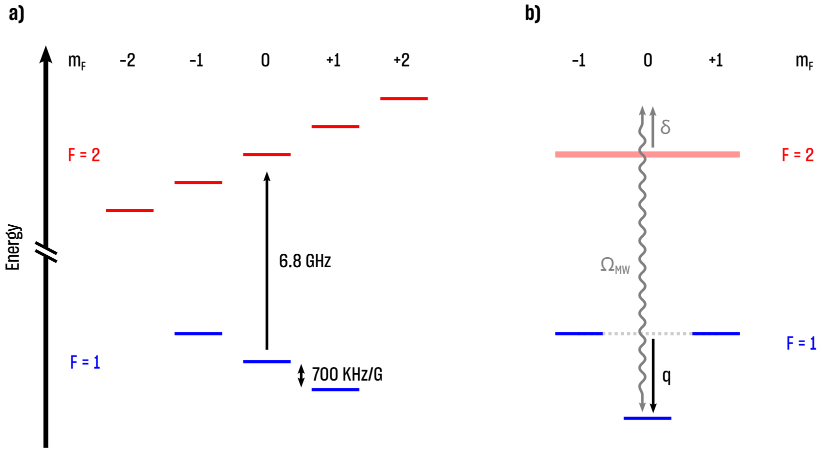

Figure 5.1: Structure of ^{87}Rb $^2S_{1/2}$ hyperfine manifolds. (a) Scheme of the levels in the presence of a weak magnetic field, splitting each F manifold in $-F \cdots +$F sub-states. The hyperfine and linear Zeeman energy shifts are indicated. (b) The same scheme after moving in the frame of reference co-rotating with the spin precession at the Larmor frequency ω_L. The F $=$ 2 manifold is nor resolved. The energy difference from $m_\mathrm{F} = \pm 1$ in the F $=$ 1 manifold is given by the quadratic Zeeman shift q. Coupling the $m_\mathrm{F} = 0$ state with the upper manifold, with a microwave with rabi frequency Ω and detuning δ, q can be tuned experimentally.

Considering two atoms respectively in the m_i and m_j sub-states, the interesting case is the one with $m_i = m_j = 0$, so the only option to conserve $m_i + m_j$, is to transfer the atoms to the $(m_i, m_j) = (1, -1)$ states. Of course, also the opposite process is allowed, where a pair of $(m_i, m_j) = (1, -1)$ atoms are transferred to the $m_\mathrm{F} = 0$ state, making the spin dynamics possible within the system. The strength of pair production and recombination processes depends on the intensity of the SCC, which is not affected by the linear Zeeman shift described in Eq. 5.1, since the spin-changing collisions are symmetric with respect to m_F. From this point of view, it is convenient to describe the system in the rotating frame, sketched in Fig. 5.1(b), canceling the Larmor precession and the energy shifts between the different sub-states. At a given magnetic field, the energy difference between the $m_\mathrm{F} = 0$ and the $m_\mathrm{F} = \pm 1$ sub-states is only given by the quadratic Zeeman shift $\propto q\, m_\mathrm{F}^2$ [165], which ultimately determines the rate of spin-changing collisions.

Tuning q makes then possible to control the spin dynamics: at large q, SCCs are energetically suppressed and only *standard* collisions can happen, while when q is of the order or the interaction strength, which is about 2 Hz for the measurements taken in this thesis, the spin dynamics is enabled. Experimentally, the quadratic Zeeman shift can be tuned by coupling the $m_\mathrm{F} = 0$ state with the F = 2 manifold through a microwave with a given Rabi frequency Ω and detuning δ. This *microwave dressing* introduces a light shift that effectively moves the $m_\mathrm{F} = 0$ level with respect to the side modes $m_\mathrm{F} = \pm 1$, so that $q = q_0 + \Omega^2/(4\delta)$ (q_0 is the bare quadratic Zeeman shift). The stability of the MW power, which fixes Ω, is crucial to keep q constant which is stabilized during the experiment. The performance of this stabilization constitutes the major limit for the overall experimental stability.

5.1.1 Theory of the spin-1 system

The spinor condensate in the F = 1 manifold is usually described in terms of the spinor field $\hat{\boldsymbol{\Psi}}$

$$\hat{\boldsymbol{\Psi}} = \begin{pmatrix} \hat{\psi}_{+1} \\ \hat{\psi}_{0} \\ \hat{\psi}_{-1} \end{pmatrix} \tag{5.2}$$

collecting in a single object the field operators $\hat{\psi}^\dagger_m$, $\hat{\psi}_m$, which describe the creation and annihilation of particles in the $m = 0, \pm 1$ sub-states. The fields $\hat{\psi}_m$ depend on space and satisfy bosonic commutation relations

$$\begin{aligned} \left[\hat{\psi}_m(r), \hat{\psi}^\dagger_{m'}(r)\right] &= \delta_{mm'}\delta(r - r') \\ \left[\hat{\psi}_m(r), \hat{\psi}_{m'}(r)\right] &= \left[\hat{\psi}^\dagger_m(r), \hat{\psi}^\dagger_{m'}(r)\right] = 0. \end{aligned} \tag{5.3}$$

Acting on those fields, we consider the spin operators $\hat{\mathrm{F}}_j = \hat{\boldsymbol{\Psi}}^\dagger \hat{f}_j \hat{\boldsymbol{\Psi}}$ with $j = x, y, z$ and the $\hat{f}_j$ are the spin matrices

$$\hat{f}_x = \frac{1}{\sqrt{2}}\begin{pmatrix} 0 & 1 & 0 \\ 1 & 0 & 1 \\ 0 & 1 & 0 \end{pmatrix}, \quad \hat{f}_y = \frac{i}{\sqrt{2}}\begin{pmatrix} 0 & 1 & 0 \\ -1 & 0 & 1 \\ 0 & -1 & 0 \end{pmatrix}, \quad \hat{f}_z = \begin{pmatrix} 1 & 0 & 0 \\ 0 & 0 & 0 \\ 0 & 0 & -1 \end{pmatrix}. \tag{5.4}$$

It is also useful to gather the spin operators in the vector $\hat{\mathbf{F}} = (\hat{\mathrm{F}}_x, \hat{\mathrm{F}}_y, \hat{\mathrm{F}}_z)$, and define the transverse spin operator

$$\hat{\mathbf{F}}_\perp = \hat{\mathrm{F}}_x + i\hat{\mathrm{F}}_y = \sqrt{2}\left(\hat{\psi}^\dagger_0\hat{\psi}_{+1} + \hat{\psi}^\dagger_{-1}\hat{\psi}_0\right), \tag{5.5}$$

since the real part of its expectation value $\mathcal{F}_\perp$ is the order parameter of the polar to easy-plane phase transition, which evolves during the system dynamics (spin changing collisions conserve $\mathcal{F}_z$, which is typically zero from the initial condition). The total number density of the condensate can be written as $\hat{n} = \hat{n}_{-1} + \hat{n}_0 + \hat{n}_{+1}$, where $\hat{n}_m = \hat{\psi}^\dagger_m\hat{\psi}_m$ is the number density of the $m = 0, \pm 1$ state.

Hamiltonian

With the given definitions, we can now look at the Hamiltonian for the spin-1 system. The *non-interacting* Hamiltonian takes into account the kinetic energy, the confinement potential V_{trap}, and both the linear and quadratic Zeeman shifts

$$\hat{\mathcal{H}}_0 = \int \mathrm{d}r \sum_{mm'} \hat{\psi}^\dagger_m \left[-\frac{\hbar^2\nabla^2}{2M} + V_{trap} + p(f_z)_{mm'} + q(f_z^2)_{mm'}\right]\hat{\psi}_m \tag{5.6}$$

where $(f_z)_{mm'} = m\,\delta_{mm'}$ is the matrix element of the spin matrix $\hat{f}_z$. As discussed in Sec. 5.1, the linear Zeeman term $\propto p$ does not affect the spin dynamics and can be neglected by moving in the co-rotating frame.

To write down the *interacting* part of the Hamiltonian, we need to take a closer look at how the interactions can be described. Usually, to model a low-energy scattering process we rely on a single parameter: the *s-wave* scattering length. When two atoms with $\mathrm{F} = 1$ collide, the total spin can couple either to $\mathrm{F}' = 0$ or $\mathrm{F}' = 2$, and we can define a scattering length for both processes: we call them respectively a_0 and a_2 [84]. These two interaction channels can be combined together to form two interacting terms in the Hamiltonian

$$\hat{\mathcal{H}}_{int} = \frac{1}{2}\int \mathrm{d}r \left[c_0 : \hat{n}(r) : + c_1 : \hat{\mathbf{F}}^2(r) :\right] \tag{5.7}$$

where the coupling constants c_0 and c_1, respectively for standard and spin-changing collisions, are written as

$$c_0 = \frac{g_0 + 2g_2}{3h} \qquad c_1 = \frac{g_2 - g_0}{3h} \tag{5.8}$$

and $g_\mathrm{F} = (4\pi\hbar^2/M)a_\mathrm{F}$ for $\mathrm{F} = 0, 2$, are the coupling constants for the short-range pseudopotential of the single-channel scattering process $V_\mathrm{F}(r, r') = g_\mathrm{F}\delta(r - r')$ describing the interaction of two atoms in r and r'. In the case of ^{87}Rb, the density interactions are repulsive ($c_0 > 0$), and the coupling between the spins is ferromagnetic ($c_1 < 0$), meaning that the system gains energy whenever two spins point in different directions. This energy can be spent to transfer pairs to the side modes, balancing out the interaction cost. This is why, in a nutshell, a rearrangement of the relative populations of the spin states can lead to a finite transverse magnetization $\mathcal{F}_\perp$.

Mean-field theory

The mean-field description of our spinor condensate can be obtained by replacing the field operators $\hat{\psi}_m$ with their expectation values $\langle\hat{\psi}_m\rangle$. To do so, we must expand $\hat{\psi}_m$ using the creation and annihilation operators $\hat{a}^\dagger$,$\hat{a}$, on a basis $\phi(r)$ describing their spatial behavior:

$$\hat{\psi}_m(r) = \sum_k \hat{a}_{mk}\varphi_{mk}(r). \tag{5.9}$$

Here the sum is running on all the possible momentum states k, but for simplicity, we can assume that only the $k = 0$ is populated in the condensate and drop the k index. To describe N atoms in the condensate, we must apply an operator of this kind to the vacuum

$$|N\rangle = \frac{1}{\sqrt{N!}} \left(\sum_m \varsigma_m \hat{a}^\dagger_m \right)^N |vac\rangle \tag{5.10}$$

with coefficients ς_m satisfying $\sum_m |\varsigma_m|^2 = 1$. The expectation value of $\hat{\psi}_m$ on such a state is

$$\psi_m(r) = \sqrt{N} \varsigma_m \varphi_m(r). \tag{5.11}$$

The full state defined in 5.2 can be therefore replaced by $\boldsymbol{\Psi}(r) = (\psi_{-1}, \psi_0, \psi_{+1})$ and, if we are not interested in the spatial features of our spinor gas, we can just specify the complex coefficients $(|\varsigma_{-1}|^2 \mathrm{e}^{i\phi_L/2}$, $|\varsigma_0|^2 \mathrm{e}^{i\phi_S}$, $|\varsigma_{+1}|^2 \mathrm{e}^{-i\phi_L/2})$, where

$$\begin{aligned} \phi_L &= \phi_{+1} - \phi_{-1} \\ \phi_S &= \phi_0 - (\phi_{+1} + \phi_{-1})/2, \end{aligned} \tag{5.12}$$

are called *Larmor phase* and *spinor phase* respectively. From their definition, it's clear that the Larmor phase is the relative phase between the side modes $m_\mathrm{F} = \pm 1$, while the spinor phase is the phase difference between the central mode $m_\mathrm{F} = 0$ and the side modes.

Spin-1 observables

Differently from a spin-1/2 system, which can be easily mapped into a two-level system recovering the *Bloch sphere* as a helpful visualization tool, spin-1 systems are more complex, since their symmetry group has a larger dimension, and require more effort to be represented graphically. Indeed, the dynamics of a spin-1 state cannot be understood only in terms of the rotations in the three-dimensional spin space defined in Eqs. 5.4. During the dynamics, the spin vector's length can also be modified (without loss of coherence) thanks to the additional degrees of freedom of the SU(3) symmetry group describing spin-1 systems. A modification of the spin length can be understood, considering *quadrupole* operators of the form

$$\hat{Q}_{ij} = \hat{f}_i \hat{f}_j + \hat{f}_j \hat{f}_i - \frac{2}{3} \delta_{ij} 1, \tag{5.13}$$

as a rotation of the spin vector in the $\hat{Q}_{ij}$-$\hat{f}_k$ plane, which decreases the spin length, for example, decreasing the projection along $\hat{f}_x$ in favor of the one along $\hat{Q}_{yz}$. These rotations are also connected to the fluctuations of the spin length in spin-1 systems, as the definition of quadrupole operators in Eq. 5.13 is linked to the covariance matrix of the spin operators [91].

Being mainly interested in the length and orientation of the spin, it's clear that we need at least two different *spaces* to describe our system: the *spin space* f_x-f_y-f_z and the so-called *spin-nematic space* f_x-Q_{yz}-Q_0, where $\hat{Q}_0 = -1/31 - \hat{Q}_{zz}$[3] Typically, we can change the readout sequence in the experiment to simultaneously measure either the pair f_x-f_y or f_x-Q_{yz}. In the first case, we can extract the transverse magnetization $\mathcal{F}_\perp$ as the projection of the spin vector in the f_x-f_y plane, and the Larmor phase as the angle of the spin vector with respect to the f_x axis. Whit f_x-Q_{yz}, we have instead only partial information about the spin length, but we can extract the spinor phase ϕ_S. The details of the readout sequence are presented in the next section.

5.1.2 Experimental tools

To present the experimental techniques involved in this project, I will start with the setup depicted in Fig. 5.2, giving an overview of the main ingredients needed to study the spin physics outlined at the beginning of this chapter. The details about ^{87}Rb cooling, trapping, and condensation are given in [147]. Here I will focus on three fundamental aspects of the experiment: the high-fidelity preparation of the sample in a given state $\mathbf{\Psi}(r)$, the manipulation of the spinor phase via global rotations, and the readout of the system after long evolution times.

As sketched in Fig. 5.2, our spinor condensate of about $N \approx 10^5$ atoms, is kept at a typical temperature of about 20 nK in a glass cell at a constant magnetic field $\mathbf{B} = 0.884\hat{z}\,$G, confined by a combination of optical potentials shaping an elongated cloud along the $\hat{x}$ direction. The condensation is achieved by evaporating in a crossed dipole trap (XDT), which is then gradually turned off while ramping up the power of an optical beam forming a wave-guide (WG) along the $\hat{x}$ with

---

[3] The expectation value of $\hat{Q}_0$ is connected to the population imbalance between the $m_\mathrm{F} = \pm 1$ side-modes and the central mode $m_\mathrm{F} = \pm 0$.

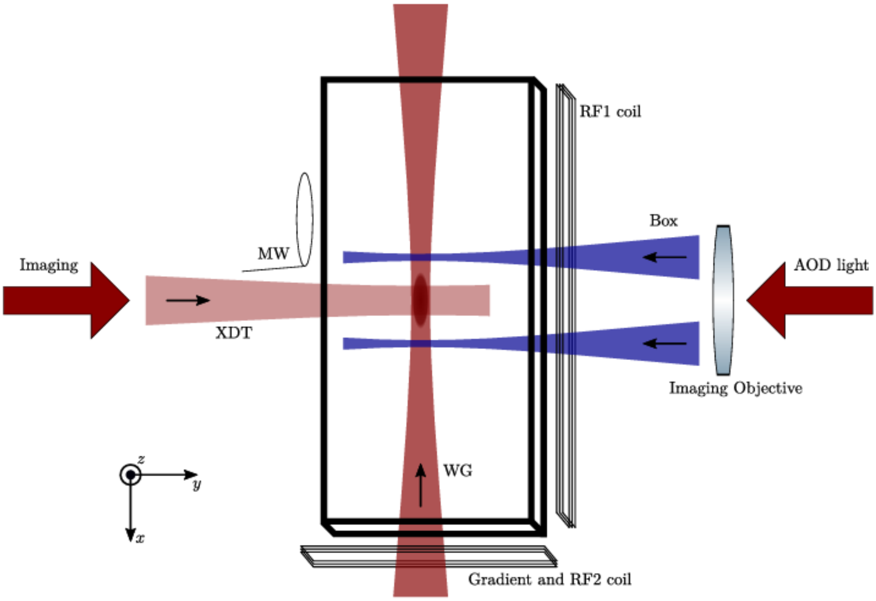

Figure 5.2: Sketch of the experimental setup from [100]. The condensate is held at the center of the vacuum glass cell, trapped by the XDT and WG red-detuned laser beams. The two radio frequency coils RF1 and RF2, face respectively $\hat{y}$ and $\hat{x}$ directions such that it is possible to control the polarization of the RF pulse that couples the sub-states of the hyperfine manifolds. A single-loop microwave antenna is placed just outside the glass cell to selectively control the couplings between the F = 1 and F = 2 sub-states and the microwave dressing used to control q.

$(\omega_x, \omega_\perp) = 2\pi \times (1.6, 170)$ Hz. At this point, the gas reaches in practice a quasi-1D regime, with a linear density of about $n = 400\,\mu\mathrm{m}^{-1}$ in the central region of the wave-guide. Shining a pair of blue-detuned laser beams in the transverse direction, we can also reach an almost constant density, turning the harmonic confinement given by the wave-guide alone into a one-dimensional box-like potential. These blue-detuned beams come from a series of two crossed AODs[4] which control the position of the beam focus in the x-z plane. Besides the optical confinement, the other key element of the system is a set of radio frequency (RF) and microwave (MW) coils used to control the spin state. By precisely tuning the frequency of such coils and the experiment timing, we can use the coil to build very complex sequences of pulses for the state preparation and readout of our system. In simple words, the RF coils are used to couple together all the m_F sub-states in a given manifold[5], while the MW coil is used for the microwave dressing that controls the effective quadratic Zeeman shift q, and, ultimately, the spin-changing collisions.

Let's now have a closer look at the experimental sequence. In the following, I will use the notation $|\mathrm{F}, m_\mathrm{F}\rangle$ to address a certain sub-state of the system.

Preparation

When the gas is condensed all the atoms are in $|1, -1\rangle$, which is the *trapped* state in the magnetic trap used for the cooling stage. Usually, we want the spin dynamics to start either in the *polar* state, where all the atoms are in $|1, 0\rangle$ and the spin is not defined or with an elongated spin $\mathcal{F}_\perp$. The first configuration can be prepared with the pulse sequence sketched in Fig. 5.3(a): first we do a π-pulse from $|1, -1\rangle$ to $|2, -1\rangle$ and shortly after another π-pulse towards $|1, 0\rangle$. Even for optimized transfers, minor imperfections in the timing and detuning of these pulses may lead to spurious populations in the $|1, \pm 1\rangle$ states or in the $\mathrm{F} = 2$ manifold. These can be eliminated by a short pulse of magnetic gradient (produced by the MOT coils) which pushes atoms in $|1, \pm 1\rangle$ out of the trap.

---

[4] Acousto-Optic Deflector

[5] even if the hyperfine spacing is nearly the same for both $\mathrm{F} = 1$ and $\mathrm{F} = 2$, we can selectively enable the coupling in each of them by controlling the relative phase of the coils.

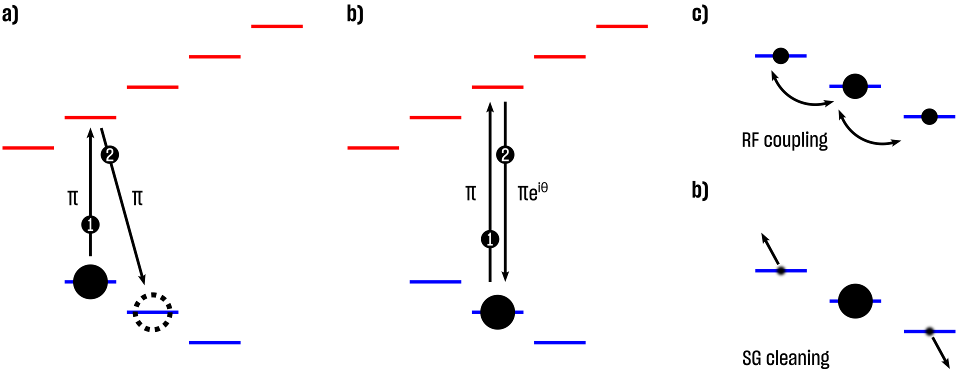

Figure 5.3: Different pulse schemes for the preparation and manipulation of the spin vector. (a) Preparation of a polar state. Atoms are transferred by a first MW π-pulse from the initial state $|1,-1\rangle$ to $|2,-1\rangle$, and from there to $|1,0\rangle$ with another MW π-pulse. The spurious population left in the $|1,\pm 1\rangle$ states are then cleaned using a Stern-Gerlach cleaning pulse (c). (b) Global rotation of the spinor phase ϕ_S. Whatever the population is in the side-modes, atoms are transferred from $|1,0\rangle$ to $|2,0\rangle$ and back, applying a couple of MW π-pulse with a phase difference θ. This affects just the phase factor of the ψ_0, changing in practice ϕ_S by θ. (d) Sketch of the RF coupling used to transfer populations among the F = 1 manifold. Tuning the frequency of the RF we can address selectively the F = 2 manifold, or both of them.

Manipulation

At any point during the system's evolution, we can perform global rotations of the spin vector, once again by applying a sequence of pulses coupling the different sub-states. For the scope of this chapter, I will describe in particular how such rotations can be used to control the spinor phase ϕ_S defined in Eq. 5.12. To imprint a spinor phase rotation of an angle θ to the whole system, we just need to modify $\psi_0(r)$ with a phase factor $e^{i\theta}$. This is done by the two microwave pulses sketched in Fig. 5.3(b), coupling $|1,0\rangle$ to $|2,0\rangle$, having the phase of the second π-pulse shifted by θ. This procedure obviously requires precise calibration of the $\theta = 0$ phase value set for the Arbitrary Waveform Generator that drives the microwave antenna. The calibration can be done by optimizing the amplitude of a *spin wave*. To create such perturbation, the system is prepared with an elongated spin and then it evolves in the presence of a magnetic field gradient along $\hat{x}$, such that the Larmor frequency becomes space-dependent. At a generic time t during the dynamics, the effect of this space-dependent dephasing results in a spatial modulation of the spin length. The amplitude of this modulation is maximum for $\phi_S = 0$, so repeating this measure for

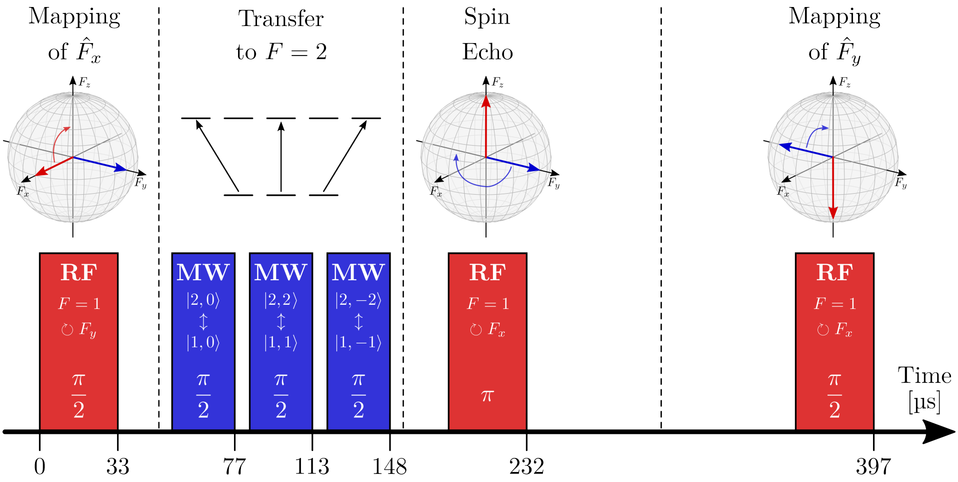

Figure 5.4: Sketch of the f_x-f_y readout sequence from [100]. The different nature of pulses, their time duration, and their effect on the spin vector are presented as a function of the experimental time. The first RF rotation (coupling only the states in F = 1) maps the f_x observable onto f_z of the F = 1 manifold. Then, three MW pulses transfer half of the population of $|1, \pm 1\rangle$ and $|1, 0\rangle$ states to $|2, \pm 2\rangle$ and $|2, 0\rangle$ respectively, transferring the information about f_x in the F = 2 manifold. To correct for the dephasing of the spin accumulated during the pulse sequence we now use a *spin echo* pulse (an RF π-pulse rotating around f_x. Then, the second RF rotation is performed, mapping the f_y observable in the f_z of the F = 1.

different θ, we can calibrate the optimal phase value.

Readout

As anticipated in the previous section, our goal is to extract information about the transverse spin length $\mathcal{F}_\perp$ and both the Larmor and spinor phases by measuring either f_x-f_y or f_x-Q_{yz}. Let's consider first the simple case of the f_z readout, where we have to measure the population imbalance between $|1, -1\rangle$ and $|1, 1\rangle$ which gives directly the expectation value of the $\hat{f}_z$ operator. To do so, we resolve the different sub-states with standard absorption imaging after a short time of flight in the presence of a magnetic gradient along $\hat{z}$. This realizes the so-called *Stern-Gerlach* imaging, where sub-states with opposite magnetic moments (such $|1, \pm 1\rangle$) are pushed in opposite directions and can be then resolved by a high-resolution objective [91]. After having recorded the populations N_m, f_z is simply given by

$$f_z = \frac{N_{+1} - N_{-1}}{N_{+1} + N_0 + N_{-1}}. \tag{5.14}$$

This quantity clearly depends on the $\hat{x}$ spatial direction but in our case tends to be constant for homogeneous densities.

Let's now come to the more complex sequence, needed for the f_x-f_y readout. The sequence is presented in Fig. 5.4. Indeed, we can use the F = 2 manifold to efficiently *store* part of the population in each sub-state, using it as an ancillary spin-1 system, and address it separately from the true spin-1 system left in the lower manifold. Since we measure always f_z-like observables, we start by mapping f_x into f_z by rotating the spin vector around the F$_y$ axis using an RF $\pi/2$-pulse. At this point, repeating the measure 5.14 on the $F = 1$ manifold, would give us f_x, but we will lose the information about f_y. Before the imaging, we need then to transfer half of the population from the $F = 1$ manifold to the F = 2 one, by applying MW $\pi/2$-pulses coupling each sub-state with its respective one above. At this point, we copied the information about f_x in F = 2, and we can now rotate in the F = 1 to map f_y into f_z, again using an RF $\pi/2$ rotation, but this time around F$_x$. Note that this second RF pulse doesn't rotate the state stored in F = 2. At the end of the sequence, we have f_x mapped into f_z in F = 2 and f_y mapped into f_z in F = 1. Our observables are then given by

$$\begin{aligned} f_x &= \frac{N_{2,+2} - N_{2,-2}}{N_{2,+2} + N_{2,0} + N_{2,-2}} \\ f_y &= \frac{N_{1,+1} - N_{1,-1}}{N_{1,+1} + N_{1,0} + N_{1,-1}}. \end{aligned} \tag{5.15}$$

For each experimental shot, these two quantities are calculated at each position in the atomic cloud and can be plotted in the f_x-f_y plane. The distance of the data distribution from the origin gives an experimental measure of $\mathcal{F}_\perp$.

To extract the spinor phase, we must use a different readout sequence which gives us f_x-q_{yz}, sketched in Fig. 5.5. The sequence starts, as before, with the mapping of f_x into f_z in the F = 1 manifold. This information is stored in the F = 2 manifold by transferring half of the population from the $|1, \pm 1\rangle$ and $|1, 0\rangle$ states to $|2, \pm 1\rangle$ and $|2, 0\rangle$

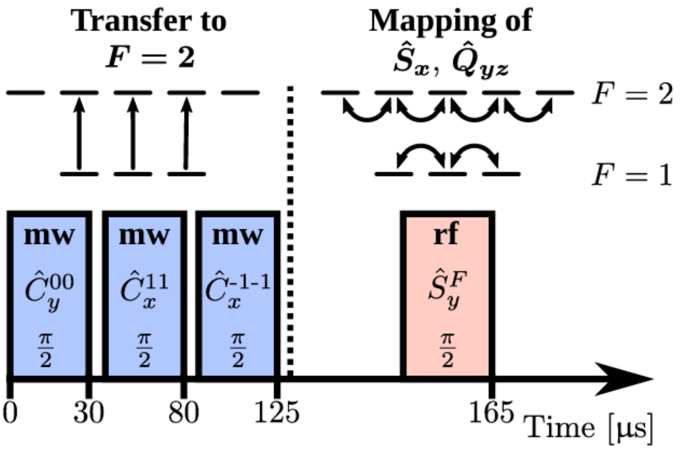

Figure 5.5: Sketch of the f_x-q_{yz} readout sequence from [94]. The different nature of pulses and their time duration are presented as a function of the experimental time. First, half of the population in the F = 1 manifold is transferred to $|2,\pm1\rangle$ and $|2,0\rangle$ respectively, which is then used as an auxiliary spin-1 manifold. Then, we use an RF pulse to do a $\pi/2$ rotation in both F = 1 and F = 2. The RF frequency is in fact chosen such that the detuning is the same for both manifolds. In F = 1, the $\pi/2$ rotation maps f_x into f_z. The phase of the pulse is chosen such that in F = 2 the same rotation maps q_{yz} into the $|2,\pm1\rangle$ states.

respectively. Then we have to map q_{yz} into f_z in F = 1. To do so, we first reverse the initial mapping rotation, and then we apply a spinor phase global imprint of $\pi/2$ using the same procedure sketched in Fig. 5.3(b). This rotates the quadrupole q_{yz} into f_x that can be mapped with another RF rotation (identical to the initial one) into f_z. In the end, the observables are extracted from the relative populations in the side modes, as

$$\begin{aligned} f_x &= \frac{N_{2,+1} - N_{2,-1}}{N_{2,+2} + N_{2,+1} + N_{2,0} + N_{2,-1} + N_{2,-2}} \\ q_{yz} &= \frac{N_{1,+1} - N_{1,-1}}{N_{1,+1} + N_{1,0} + N_{1,-1}}. \end{aligned} \tag{5.16}$$

Similarly to the f_x-f_y case, these observables are calculated at each position in the atomic cloud for each experimental realization and plotted, this time, in the f_x-q_{yz} plane. As I will show in the next sections, when the system develops an elongated spin the energy minima in the f_x-q_{yz} are two points. By studying the slope of the line connecting the minima we can extract the spinor phase from the experimental data.

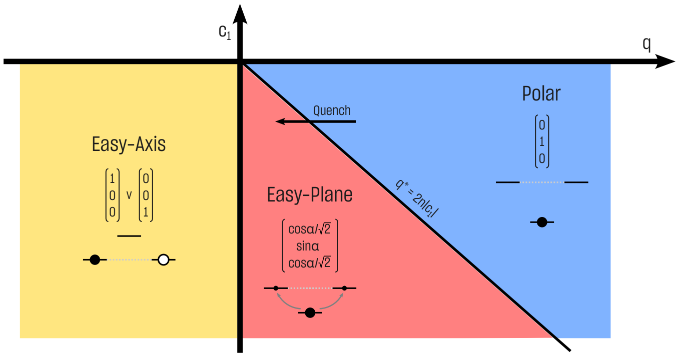

Figure 5.6: Mean-field phase diagram of the F = 1 manifold of a ^{87}Rb spinor condensate in a single spatial mode. Three different magnetic phases emerge as a function of the quadratic Zeeman shift q, acting as the energy separation between $|1,0\rangle$ and $|1,\pm1\rangle$, and the spin-changing interactions strength c_1. Polar phase: all the atoms are in the lowest energy level $|1,0\rangle$. Easy-plane ferromagnetic phase: the competition between q and the spin-changing collisions allows population transfer in the $|1,\pm1\rangle$. This mechanism is triggered at a critical value $q^* = 2n|c_1|$. Easy-axis ferromagnetic phase: at negative q the atoms occupy either $|1,1\rangle$ or $|1,-1\rangle$.

5.2 The polar to easy-plane ferromagnet quantum phase transition

In Sec. 5.1 I briefly discussed the role of the quadratic Zeeman shift q and the importance of the spin-changing collisions for the emergent quantum phases of a spinor condensate. Indeed, we can have an intuitive description of such phases just by looking at the behavior of the energy levels in Fig. 5.1(b) when we change q. For q larger than the critical value q^*, we saw that the spin-changing collisions are turned off and the ground state is the so-called polar (P) phase, where all the atoms collectively occupy the lowest energy level $m_{\mathrm{F}} = 0$. In this phase, the spin direction is not defined because the expectation values $f_x = f_y = f_x = 0$ however, the spin fluctuations vanish only in the f_z direction and are finite in the f_x-f_y plane. Since we are not interested in the fluctuation properties, we can represent the polar phase as a point in the origin of the spin sphere. When q approaches the critical value, a quantum phase transition is crossed and the system develops a finite transverse spin $\mathcal{F}_\perp$. Indeed, spin-changing collisions bring pairs of $m_{\mathrm{F}} = 0$ atoms to the side-modes, giving rise to a spin vector with finite length with random Larmor phase ϕ_L. This phase is called easy-plane (EP) ferromagnet and can be represented as a circle of radius $\mathcal{F}_\perp$ in the f_x-f_y plane of the spin sphere. At $q = 0$ the transverse magnetization takes the maximum value $\mathcal{F}_\perp = 1$, then for negative values of the quadratic Zeeman shift, we cross another quantum phase transition where the lowest energy states are the $m_\mathrm{F} = \pm 1$. This phase is the so-called *easy-axis* (EA) ferromagnet, which minimizes the ferromagnetic interaction energy by having a full occupation of either $m_\mathrm{F} = 1$ or $m_\mathrm{F} = -1$. This phase is not important for the scope of this chapter, since it can be reached during the system dynamics only by preparing the initial condition with a finite magnetization f_z, which is conserved during the system evolution. On the contrary, in the experiment, we want to start in the polar phase and drive the quantum phase transition toward the easy-plane phase. However, the easy-axis phase could be extremely interesting to explore since driving the system through the two phase transitions separating it from the polar state, one can generate entanglement within the system [120]. The emerging phase diagram is sketched in Fig. 5.6 as a function of q and c_1. Note that, while q can be tuned in the experiment, $c_1 < 0$ is fixed with $c_0/|c_1| \approx 200$ in the case of ^{87}Rb.

5.2.1 Mean-field phase diagram

The different phases introduced so far, can be understood by looking at the mean-field picture. Considering the Hamiltonian $\hat{\mathcal{H}}_0 + \hat{\mathcal{H}}_{int}$, obtained by putting together Eq. 5.6 and Eq. 5.7, we can write the total energy per particle as

$$\epsilon = V_{trap} + p\left(|\varsigma_{+1}|^2 - |\varsigma_{-1}|^2\right) + q\left(|\varsigma_{+1}|^2 + |\varsigma_{-1}|^2\right) + \frac{1}{2}nc_0 + \frac{1}{2}nc_1\mathbf{F}^2. \tag{5.17}$$

As already mentioned, we are interested in the experimental configurations where $\mathrm{F}_z = 0$ and is fixed during the dynamics, therefore the linear Zeeman shift term can be neglected since $|\varsigma_{+1}| - |\varsigma_{-1}| = 0$. Moreover, for homogeneous densities the V_{trap} and the first interaction term nc_0, accounting for the density interactions, are simple constants. The only two terms we retain are the quadratic Zeeman shift and the spin-changing collision terms. These can be rewritten as

$$\epsilon = \frac{q}{2}\left(1 - \sqrt{1 - \left(\mathrm{F}_x^2 + \mathrm{F}_y^2\right)}\right) + \frac{1}{2}nc_1\left(\mathrm{F}_x^2 + \mathrm{F}_y^2\right), \tag{5.18}$$

which, as a function of F_x and F_y is plotted in Fig. 5.7. This energy landscape can show either a single minimum in the origin in the po-

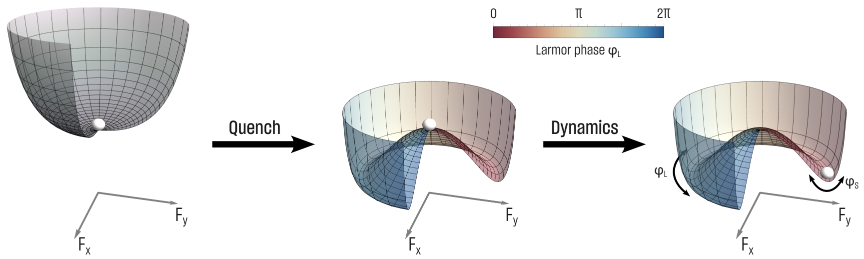

Figure 5.7: Mean field energy of Eq. 5.18 as a function of F_x and F_y. At high values of q we have a single minimum sitting in the origin. Quenching to $q < 2n|c_1|$ the free energy develops a minimum at a finite distance, and the old ground state is now an unstable state. Since the energy depends only on $\left(\mathsf{F}_x^2 + \mathsf{F}_y^2\right)$ the system is free to explore all the the values of the Larmor phase ϕ_L. Once in the new energy minimum, the perturbations of the spin length $\mathcal{F}_\perp$ can be described by oscillations of the spinor phase ϕ_S.

lar phase, for $q > 2n|c_1|$ or, below this critical value, a *bottle-bottom* shape with a minimum at a distance $\mathcal{F}_\perp$ describing the easy-plane ferromagnet. Since the energy only depends on the spin length, the system is free to explore all the possible values of the Larmor phase ϕ_L without paying an energy cost. Modifications of the transverse spin length can be described by modifications of the spinor phase ψ_S. Changing adiabatically q, we can pass from the polar phase to the easy-plane phase continuously, developing a non-zero $\mathcal{F}_\perp$ accordingly to the position of the energy minimum, therefore slow changes in q can be described as slow rotations in the spin-quadrupole space which modifies the spinor phase, from $\psi_S \approx \pi$ (where the spin vector is basically along the quadrupole) towards an elongated spin state $\psi_S \approx 0$.

The intuitive picture presented above is strictly valid only for a single spatial mode condensate, indeed for extended systems, we must take all the possible k modes in Eq. 5.9 into account. This results in the presence of stable and unstable modes in the condensate for a given q, giving rise to perturbations with a specific k vector, that can grow in the system. The unstable k modes at a given q predicted by the Bogoliubov theory have been calculated in [84]. For the scope of this chapter, we are not interested in the spatial behavior of the perturbations, since they are only relevant at short times during the dynamics of the system, where the perturbative approach applies and Bogoliubov theory holds.

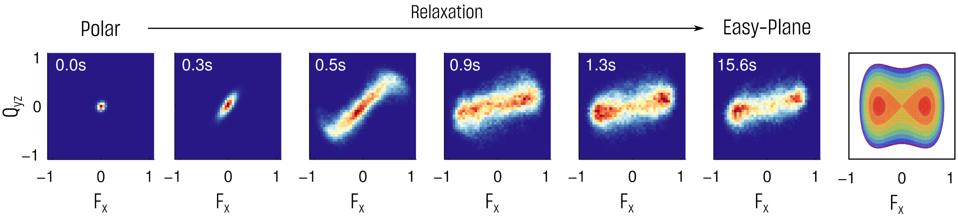

Figure 5.8: Dynamics of a the system in the nematic subspace F_x-Q_{yz} after a quench from a polar phase. The quadratic Zeeman shift is fixed to q, just below the critical value. Each distribution is extracted from a sample of 100-150 experimental realizations. In single realizations, the observables are extracted from the spin modes populations calculating the quantities in Eqs. 5.16, pixel-by-pixel. The last panel to the right is a sketch of the free energy expected in the easy-plane phase.

5.2.2 Quench dynamics

Experimentally, we explore the relaxation dynamics after the quench sketched in Fig. 5.7, by suddenly enabling the microwave dressing after the preparation of the system in the polar phase, and tuning q below the critical value $2n|c_1|$. In this experiment the spinor gas is confined in a box-like potential, thus the density is almost constant along the longitudinal direction of the cloud. This is crucial to have a global value of the critical q, such that the energy landscape does not depend on spatial coordinates. After the quench we wait a variable time, ranging from a few milliseconds up to 20 s, and then we image the spin and density distributions.

In Fig. 5.8, the F_x-Q_{yz} distributions extracted from experimental data are presented as a function of the evolution time, for a fixed value of q corresponding to the easy-plane phase. At $t = 0$ the nematic distribution is concentrated in the origin since the spin length is zero and the spinor phase ϕ_S is not well defined. In the first second, of the dynamics, the distribution spreads along the diagonal direction, following the energy contours typical of the easy-plane phase. Indeed, the energy landscape in the F_x-Q_{yz} plane (as sketched in the last panel on the right of Fig. 5.8) has a typical *eight shape*, coming from the interplay between the quadratic Zeeman shift (last term in the free hamiltonian 5.6) and the spin changing collisions (the term proportional to c_1 in the interaction hamiltonian 5.7). After 1 s of evolution, the system begins to relax in the two minima, lying on the F_x axis at a finite distance from the origin, reflecting the establishment of a finite transverse spin length $\mathcal{F}_\perp$. The same dynamics in the F_x-F_y plane would be an evolution from a point in the origin (polar) towards a ring, as expected for the *bottle-bottom* potential in Fig. 5.7. At late times (see the panel at 15.6 s) the histogram shows a nice double-peak structure, slightly tilted from the horizontal direction. This tilt is due to a probable imperfection in the readout sequence, which shifts the spinor phase of the system, thus rotating the measured distribution along Q_0. To test this hypothesis, we performed similar measures on the other basis, measuring F_x-F_y, to exclude a possible error in the system preparation. The data are consistent with the previous one, reported in [102], confirming that the origin of the tilt is linked to the other detection sequence.

Most of the dynamics seem to happen in the first 16 s or so, curiously revealing a faster relaxation with respect to previous experiments [102]. At later times the double peak structure remains unchanged on top of a small fraction of excitations, which persists up to 20 s. Note that, the dynamics affecting the spin length $\mathcal{F}_\perp$, can also be understood as the spinor phase changing during the system evolution. Indeed, the spinor phase follows an effective mean field potential even far from equilibrium in the extended system. As I'll discuss in the next section, it is reasonable to assume that the spinor phase is settling in the minima of periodic potential energy derived by low energy effective field theory calculations[6].

5.3 Spinor phase detection and manipulation

To understand better the behavior of the spinor phase, we analyzed its distributions in a similar experiment where we instead fixed the observation time and varied the value of q. The idea is to exploit the system dynamics to explore the *effective potential* experienced by the spinor phase, and map it on the fluctuations of ϕ_S. Similarly to the technique explained in Chapter 2 to extract the shape of the free energy from the fluctuations of the supersolid order parameter, we want the system to be enough *energetic* so that the fluctuations can probe better

---

[6] Such calculations are currently under analytical and numerical investigations by Ido Siovitz (*Kirchhoff Institut für Physik - Heidelberg, DE*).

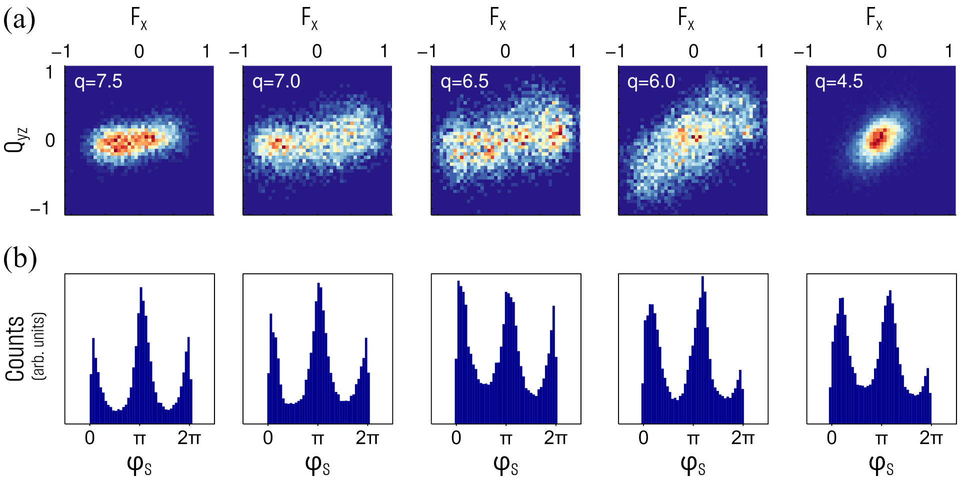

Figure 5.9: Behavior of the spinor phase for different q. (a) Distributions in the F_x-Q_{yz} plane extracted after $t = 1\,\mathrm{s}$ from the quench, starting from the polar phase. Note that the second panel from the right is equivalent to the one in Fig. 5.8 for $t = 0.9$, however, the lower statistics affect the quality of the F_x-Q_{yz} histograms. (b) Distribution of the spinor phase ϕ_S extracted from the histograms in panel (a).

the shape of the potential. We thus fix the evolution time to 1 s.

In Fig. 5.9 are shown the results for q ranging from 7.5 Hz to 4.5 Hz. Note that this is the experimental value of q, which has a frequency offset from the nominal case. Thus the second phase transition from the easy-plane to the easy-axis ferromagnet shouldn't occur at $q = 0$ in the experimental reference. Indeed, already around 4.5 Hz, we see important deviations from the expected elongated distribution in the F_x-Q_{yz} plane[7]. For larger values of q we see instead the expected behavior for the easy-plane phase: the separation between the two lobes of the distribution starts to grow around 7.5 Hz and the spin projection along $\hat{x}$ become maximal around 6.5 Hz.

The spinor phase shows interesting behavior. Basically in the whole investigated range, ϕ_S shows a periodic structure at multiples of π, which shifts only at low q, retaining its periodicity. This periodic structure is perfectly symmetric around π for large q, where the separation

---

[7] If we quench into the easy-axis phase, we expect the distribution to look more similar to the polar phase, which is our initial condition. In fact, the free evolution from the polar phase towards the easy-axis ferromagnet is not allowed in our system, where the F_z must be conserved.

between the lobes of the F_x-Q_{yz} is still small. At smaller q, in fact, such distribution spreads more along F_x and ϕ_S start to show slight asymmetries, connected with the tilt already discussed in the previous section. The interesting result is the presence of a periodic structure, that can be mapped in a periodic effective potential, which regulates the evolution of ϕ_S over time.

5.3.1 Global spinor phase rotations

To get more quantitative results on the effective potential that governs the spinor phase during the evolution, we carried out another type of experiment, where the system is prepared closer to the easy-plane ground state and then perturbed. The perturbation consists of a global rotation of the spinor phase, which is described by a rotation along Q_0 in the nematic sphere. To do so, we employ the technique discussed in Sec. 5.1.2, which allows us to imprint a finite spinor phase to the system just after the preparation. We start as before from the polar phase, we quench q, we wait about 16 s for the system to relax, and then we imprint a global phase rotation. This way the system starts very near the ground state, and we can study its dynamics dominated by the spinor phase perturbation.

In Fig. 5.10 are shown the results for the oscillations of the spinor phase caused by the global imprint. The spinor phase is perturbed by $\delta\phi_S \sim 0.08\pi$, leading to damped oscillation with a frequency of 13(1) Hz. To extract the spinor phases from the two-dimensional histograms in Fig. 5.10a, we rotate counter-clockwise each distribution for an angle θ, we calculate the horizontal projection and we look for its maximum value $A(\theta)$. This is now a 1D distribution showing, as a function of θ, a peak for the optimal angle $\theta = \pi - \phi_S$ with a width, which depends on the shape of the initial distribution, that can be associated with the spinor phase uncertainty. Both the optimal angles and the width are extracted from the Gaussian fits of $A(\theta)$ and then rescaled to obtain ϕ_S. We repeated the experiment for larger imprints, with $\delta\phi_S \sim 0.15\pi$, obtaining oscillations at the same frequency and similar damping. The comparison between our experimental results and numerical simulations of our system focused on the spinor phase, is part of the ongoing investigations. It will be also interesting to check the behavior of the spinor phase when the waiting time between the quench and the global

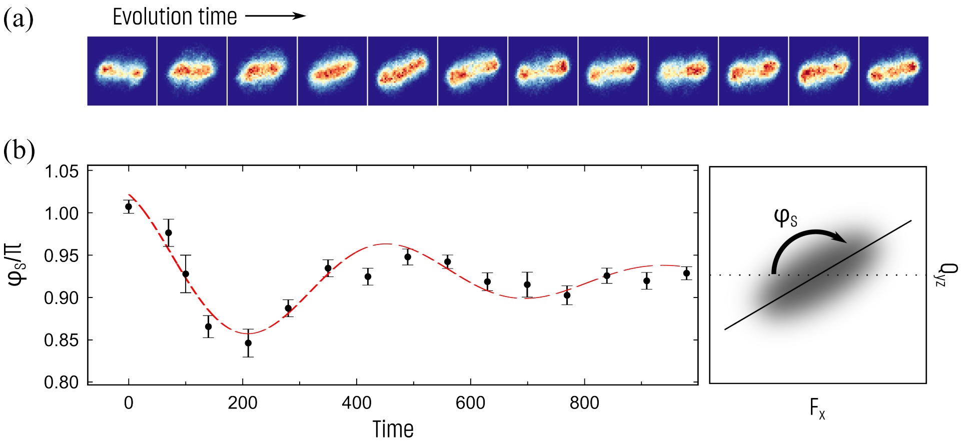

Figure 5.10: Linear response measurements with global rotations of ϕ_S. (a) Typical evolution of the system prepared in an elongated spin with $\mathcal{F}_\perp \sim 0.8$, after a global rotation of the spinor phase. The time steps between the different histograms is the same of the analysis in panel (b). The histogram shows the F_x-Q_{yz} plane in the same scale of previous figures. (b) Extracted spinor phase and analysis of the damped oscillations. The left panel shows experimental data (black dots) and the best-fit curve corresponding to a characteristic frequency of 13(1) Hz (dashed red curve). The right panel shows the reference for the values of ϕ_S.

imprint is longer. In that scenario, ϕ_S would be completely settled in the minima of the effective potential and the system would be closer to a single spatial mode setting, where no spatial excitations are present.

Our data proves that the spinor phase can be manipulated precisely in experiments, opening the way to the more fascinating scenario of local perturbation of ϕ_S. Indeed, the evolution of such perturbations in an effective periodic potential as the one we started to characterize experimentally, may lead to interesting phenomena connected to caustics [172].

Chapter 6

Conclusions and outlook

In this thesis I discussed the results of my experimental work in the context of dipolar supersolids and spinor condensates, tied together by the common language of quantum phase transitions. While dipolar supersolids are a new fundamental state of matter still requiring the exploration of their defining properties, in the case of ferromagnetic phases in spin-1 systems, which have been extensively studied in the last decades, an interesting direction is the study of their topological excitations. Although the two systems are quite different, there are multiple points of contact both from the fundamental and technical point of view. Both dipolar gases and spin-1 systems feature instabilities leading to either density or spin spatial modulations, where the latter has been proposed in the past as a candidate for supersolidity [161]. Moreover, the concept of superfluid fraction, which has a fundamental relevance for supersolids, can be extended to spin systems [84]. Connecting these two topics, it would be interesting to understand the relation between the spin stiffness [64] and the properties of the easy-plane ferromagnetic phases that can be realized in spin-1 condensates. Another interesting aspect would be to probe the density or momentum correlations in dipolar supersolids, with the same tools used to probe spin correlations in spinor condensates [94].

Crystalline and superfluid properties of dipolar supersolids

In this work, I focused mainly on the superfluid-supersolid quantum phase transition showing the results of two experiments, in which we studied the behavior of the phase transition across a dimensional crossover [15, 10], and we measure for the first time the superfluid fraction of a dipolar supersolid [16]. With the first experiment we reconciled a rather large variety of previous theoretical, numerical and experimental results, tracing a connection between the character of the quantum phase transition and the supersolid dimensionality. We used Landau theory of quantum phase transitions [97] to build a model suitable for trapped supersolids, comparing numerical simulations and experimental data with the model predictions and demonstrating that both continuous and discontinuous transitions can happen in single-row supersolids. In the second experiment we shifted our focus from the crystalline structure of dipolar supersolids towards their superfluid response, establishing a new method to measure Leggett's superfluid fraction [103] from Josephson oscillations [80]. Our main idea is the mapping of Leggett's model, developed for rotations, into a Josephson description of the supersolid, where the superfluid fraction is directly linked to the Josephson coupling energy [173], which can be measured experimentally from the Josephson frequencies or the phase-current relations.

Remarkably, the superfluid-supersolid quantum phase transition can be studied experimentally in finite-sized systems, as the one described in this thesis, where the effect of the external confinement on the supersolid structure give an additional knob to change the physics at play. Indeed, we find a crossover from 1D-like systems exhibiting continuous phase transitions and 2D-like system featuring discontinuous phase transitions, by changing the transverse confinement or the atom number. This crossover is linked to the soft nature of the supersolid structure which can be deformed and compressed by the external potential. When the natural two-dimensional structure in the plane transverse to the dipoles orientation is suppressed along one direction, the supersolid lattice forms in only one dimension. In this configuration, the transition is similar to the one of true one-dimensional systems showing a continuous behavior. In an intermediate regime, where the 2D structure is suppressed, but still present in the superfluid background of the system, single-row supersolids still feature a discontinuous phase transition, reminiscent of the true two-dimensional case. Increasing the atom number has the same effect of increasing the transverse confinement, up to the point where density is so high that the effect of quantum fluctuations become dominant, resulting in a second crossover towards a discontinuous region [18, 197], which however we explored only numerically.

We demonstrated that the continuous or discontinuous character of the supersolid transition can be controlled in experiments, by changing the transverse harmonic confinement. Indeed, we studied the behavior of the quantum phase transition in two different harmonic potentials associated to a continuous and a discontinuous character respectively, finding a variety of experimental evidences of the two different transitions. The most striking difference is the behavior of the order parameter $\tilde{C}$ once the transition is crossed back to reach the superfluid side, revealing an excess of energy gained in the discontinuous case as excitations of the system. The comparison with the continuous configuration, shows that this effect can arise only from the lacking of adiabaticity typical of discontinuous transition, where for any finite speed of the crossing we can't follow adiabatically the system ground state. The energy excess measured in the experiment is of the same order of the height of the free energy barrier calculated with our model for the trapped system. The different character of the continuous and discontinuous phase transitions is also evident from the shape of the distributions of the order parameter in different region of scattering length, showing one or two maxima respectively, associated to a single or double-minima structure in the Landau free energy.

Intuitively, the possibility to use continuous transitions to produce excitations free supersolids is the key to study this fascinating phase of matter without the presence of spurious effects. This is particularly important for the measurement of low energy collective excitations which can be washed out in highly excited systems, or in revealing fragile effects such as quantum correlations. The first use of the continuous phase transition has been the measurement of the superfluid fraction from the Josephson oscillations. The Josephson dynamics, namely a coherent oscillation of both the population imbalance and the phase difference between two adjacent superfluids connected by a weak link, is a natural effect in the dipolar supersolid, which realizes an array of coupled Josephson junctions in absence of an external potential to form the barriers between neighboring clusters. Indeed, we find that the Josephson oscillations are a normal mode of the system, which can be excited selectively in experiments. In our experiment we initialize the Josephson oscillations by imprinting a phase difference between adjacent supersolid clusters and then we follow the system dynamics. We found that starting with a supersolid too far from its ground state (such as in the case of discontinuous transition) make it impossible to observe Josephson oscillations, probably because the initial phase profile is scrambled by the excitations. The high coherence of the supersolid produced by continuous transitions is then a crucial aspect for the superfluid fraction measurement.

We showed that the original model by Leggett [103] for supersolids on a ring under rotations, can be mapped in linear supersolids with a phase twist, allowing to shift from a global measurement of the superfluid fraction, as the one provided by the nonclassical rotational inertia, to a local one, which in our case is based on the Josephson coupling between the central clusters of our supersolid. We find, by using the general definition of superfluid fraction, a direct connection between f_s and the coupling energy K of a single junction, and we build a 6-modes model to describe the trapped supersolids as a Josephson junctions array in order to compare experimental and numerical results with theoretical predictions. From the experimental data, we extract the coupling energy K from the Josephson frequencies, using the results from the model, or from the phase-current relations, which are model independent. Once K is translated into f_s, we find a remarkable agreement with Leggett's bounds, demonstrating the reduced superfluid fraction of the dipolar supersolid, arising only from the breaking of the translational symmetry. Given its generality, our method may be applied in many other supersolid-like phases, especially in superconducting systems [1] where the Josephson coupling has been already used to probe other properties of the system. Moreover, the supersolid realizes a new type of Josephson junction array, since the weak links, relying only on the interactions, are not fixed by an external potential and can move during the dynamics.

New directions

The impact of the additional degree of freedom associated to the Goldstone mode of the supersolid lattice, to the fluctuations of the Josephson observables is still to be investigated. This direction would be interesting for linear systems, where a model of the fluctuations in the number and phase difference may lead to the estimation of the system temperature, like in standard bosonic Josephson junctions [57], as well as for supersolids confined in a ring potential, where the Goldstone fluctuations costs no energy. The next experimental step is indeed the realization of a dipolar supersolid in a ring potential, employing the techniques I discussed in this work. Choosing the right thickness of the ring potential, we can achieve a one-dimensional system with boundary conditions, approaching the ideal case of an infinite supersolid, and realize the ideal setup to study superfluidity. Exploiting the continuous phase transition, we would be able to form the supersolid near its ground state, and manipulate it using light shaped by our spatial light modulator. For example we can imprint a global phase gradient to put the system under rotation and study the moment of inertia as in the original theory by Leggett [103] or partially quantized supercurrents [185]. Moreover, we can study collective modes of the system, like the Josephson oscillations and the Goldstone mode [201] without the effects of the density inhomogeneity.

Another interesting direction, which instead involve the linear geometry, is the study of quantum correlations and entanglement in the dipolar supersolids. Although our system is currently dominated by technical noise (mainly fluctuations in the atom number), it would be interesting to understand if phenomena like entanglement in momentum space can be detected in the supersolid. Indeed, there are evidences that quantum correlations increase crossing a quantum phase transitions [120], leading to entanglement creation. In the case of dipolar supersolids, it would be intuitive to think about correlations arising from pair production in two opposite momentum states $\pm k_{SS}$, that globally form the density modulation. Since the phase of the system is preserved during the breaking of the translational symmetry, the process must be coherent. Quantum correlations can also be measured looking at the Josephson observables, measuring again the fluctuations of both number and phase [140].

Ongoing research on topological excitations in spinor condensates

My work about spinor condensates, which has been the topic of my visiting period in Heidelberg, is part of a preliminary investigation on the possible detection of novel topological excitations resulting from quenching across a quantum phase transition [172]. The main idea is that the chaotic dynamics of the spinor phase after the quench from the polar to the easy-plane phase could produce an exotic kind of vortex excitation, the so-called real time instanton, characterized by a cusp divergence of the spin length which vanish at a precise point in space and time. To describe the emergence of such topological excitation, a preliminary model of an effective periodic potential governing the spinor phase is under investigation, motivated by analytical calculations based on a low energy effective theory carried out by the theory group in Heidelberg. In this thesis I discussed a preliminary set of experimental measures aimed to characterize such effective potential. The next experimental step would be to establish a procedure to deterministically prepare the system in order to create real-time instantons in a precise spatio-temporal point of the dynamics, making it possible to detect this fascinating object for the first time.

Bibliography

[1] D. F. Agterberg, J. S. Davis, S. D. Edkins, E. Fradkin, D. J. Van Harlingen, S. A. Kivelson, P. A. Lee, L. Radzihovsky, J. M. Tranquada, and Y. Wang. The physics of pair-density waves: Cuprate superconductors and beyond. *Annual Review of Condensed Matter Physics*, 11(1):231–270, 2020. doi: 10.1146/annurev-conmatphys-031119-050711. URL `https://doi.org/10.1146/annurev-conmatphys-031119-050711`.

[2] A. Alaña. Supersolid-formation-time shortcut and excitation reduction by manipulating the dynamical instability. *Phys. Rev. A*, 109:023308, Feb 2024. doi: 10.1103/PhysRevA.109.023308. URL `https://link.aps.org/doi/10.1103/PhysRevA.109.023308`.

[3] A. Alaña, N. Antolini, G. Biagioni, I. L. Egusquiza, and M. Modugno. Crossing the superfluid-supersolid transition of an elongated dipolar condensate. *Phys. Rev. A*, 106:043313, Oct 2022. doi: 10.1103/PhysRevA.106.043313. URL `https://link.aps.org/doi/10.1103/PhysRevA.106.043313`.

[4] A. Alaña, I. L. Egusquiza, and M. Modugno. Supersolid formation in a dipolar condensate by roton instability. *Phys. Rev. A*, 108: 033316, Sep 2023. doi: 10.1103/PhysRevA.108.033316. URL `https://link.aps.org/doi/10.1103/PhysRevA.108.033316`.

[5] M. Albiez, R. Gati, J. Fölling, S. Hunsmann, M. Cristiani, and M. K. Oberthaler. Direct observation of tunneling and nonlinear self-trapping in a single bosonic josephson junction. *Phys. Rev. Lett.*, 95:010402, Jun 2005. doi: 10.1103/PhysRevLett.95.010402. URL `https://link.aps.org/doi/10.1103/PhysRevLett.95.010402`.

[6] L. Amico, G. Falci, R. Fazio, and G. Giaquinta. Supersolid phase in fully frustrated josephson-junction arrays. *Phys. Rev. B*, 55:

1100–1109, Jan 1997. doi: 10.1103/PhysRevB.55.1100. URL https://link.aps.org/doi/10.1103/PhysRevB.55.1100.

[7] F. Ancilotto, M. Barranco, M. Pi, and L. Reatto. Vortex properties in the extended supersolid phase of dipolar bose-einstein condensates. *Phys. Rev. A*, 103:033314, Mar 2021. doi: 10.1103/PhysRevA.103.033314. URL https://link.aps.org/doi/10.1103/PhysRevA.103.033314.

[8] W. Anderson. *Basic Notions Of Condensed Matter Physics*. Basic Notions of Condensed Matter Physics Series. Basic Books, 1984. ISBN 9780805302202. URL https://books.google.it/books?id=-QRBAQAAIAAJ.

[9] A. F. Andreev and I. M. Lifshitz. Quantum theory of defects in crystals. *Soviet Physics Uspekhi*, 13(5):670–670, 1971. doi: 10.1070/pu1971v013n05abeh004235. URL https://doi.org/10.1070%2Fpu1971v013n05abeh004235.

[10] N. Antolini. Controlling the character of the superfluid-supersolid quantum phase transition. *Il nuovo cimento C*, 45 (6):1–4, 2022. doi: http://dx.doi.org/10.1393/ncc/i2022-22159-7. URL https://www.sif.it/riviste/sif/ncc/econtents/2022/045/06/article/2.

[11] D. P. Arovas, E. Berg, S. A. Kivelson, and S. Raghu. The hubbard model. *Annual Review of Condensed Matter Physics*, 13(1):239–274, 2022. doi: 10.1146/annurev-conmatphys-031620-102024. URL https://doi.org/10.1146/annurev-conmatphys-031620-102024.

[12] M. A. Baranov, M. Dalmonte, G. Pupillo, and P. Zoller. Condensed matter theory of dipolar quantum gases. *Chemical Reviews*, 112(9):5012–5061, 2012. doi: 10.1021/cr2003568. URL https://doi.org/10.1021/cr2003568. PMID: 22877362.

[13] J. Beugnon and N. Navon. Exploring the kibble–zurek mechanism with homogeneous bose gases. *Journal of Physics B: Atomic, Molecular and Optical Physics*, 50(2):022002, jan 2017. doi: 10.1088/1361-6455/50/2/022002. URL https://dx.doi.org/10.1088/1361-6455/50/2/022002.

[14] G. Biagioni. Evidence of superfluidity in a dipolar supersolid through non-classical rotational inertia. *Master Thesis - Università degli Studi di Firenze*, 2020. URL `https://quantumgases.lens.unifi.it/theses/thesis_biagioni_master.pdf`.

[15] G. Biagioni, N. Antolini, A. Alaña, M. Modugno, A. Fioretti, C. Gabbanini, L. Tanzi, and G. Modugno. Dimensional crossover in the superfluid-supersolid quantum phase transition. *Phys. Rev. X*, 12:021019, Apr 2022. doi: 10.1103/PhysRevX.12.021019. URL `https://link.aps.org/doi/10.1103/PhysRevX.12.021019`.

[16] G. Biagioni, N. Antolini, B. Donelli, L. Pezzè, A. Smerzi, M. Fattori, A. Fioretti, C. Gabbanini, M. Inguscio, L. Tanzi, and G. Modugno. Sub-unity superfluid fraction of a supersolid from self-induced josephson effect, 2023. URL `https://doi.org/10.48550/arXiv.2311.04757`.

[17] R. N. Bisset, P. B. Blakie, and S. Stringari. Static-response theory and the roton-maxon spectrum of a flattened dipolar bose-einstein condensate. *Phys. Rev. A*, 100:013620, Jul 2019. doi: 10.1103/PhysRevA.100.013620. URL `https://link.aps.org/doi/10.1103/PhysRevA.100.013620`.

[18] P. B. Blakie, D. Baillie, L. Chomaz, and F. Ferlaino. Supersolidity in an elongated dipolar condensate. *Phys. Rev. Research*, 2:043318, Dec 2020. doi: 10.1103/PhysRevResearch.2.043318. URL `https://link.aps.org/doi/10.1103/PhysRevResearch.2.043318`.

[19] T. Bland, E. Poli, C. Politi, L. Klaus, M. A. Norcia, F. Ferlaino, L. Santos, and R. N. Bisset. Two-dimensional supersolid formation in dipolar condensates. *Phys. Rev. Lett.*, 128:195302, May 2022. doi: 10.1103/PhysRevLett.128.195302. URL `https://link.aps.org/doi/10.1103/PhysRevLett.128.195302`.

[20] L. Bonnes and S. Wessel. Generic first-order versus continuous quantum nucleation of supersolidity. *Phys. Rev. B*, 84:054510, Aug 2011. doi: 10.1103/PhysRevB.84.054510. URL `https://link.aps.org/doi/10.1103/PhysRevB.84.054510`.

[21] M. Born, E. Wolf, A. B. Bhatia, P. C. Clemmow, D. Gabor, A. R. Stokes, A. M. Taylor, P. A. Wayman, and W. L. Wilcock. *Principles of Optics: Electromagnetic Theory of Propagation,*

Interference and Diffraction of Light. Cambridge University Press, 7 edition, 1999. doi: 10.1017/CBO9781139644181.

[22] F. Böttcher, J.-N. Schmidt, M. Wenzel, J. Hertkorn, M. Guo, T. Langen, and T. Pfau. Transient supersolid properties in an array of dipolar quantum droplets. *Phys. Rev. X*, 9:011051, Mar 2019. doi: 10.1103/PhysRevX.9.011051. URL https://link.aps.org/doi/10.1103/PhysRevX.9.011051.

[23] F. Böttcher, M. Wenzel, J.-N. Schmidt, M. Guo, T. Langen, I. Ferrier-Barbut, T. Pfau, R. Bombín, J. Sánchez-Baena, J. Boronat, and F. Mazzanti. Dilute dipolar quantum droplets beyond the extended Gross-Pitaevskii equation. *Phys. Rev. Research*, 1:033088, Nov 2019. doi: 10.1103/PhysRevResearch.1.033088. URL https://link.aps.org/doi/10.1103/PhysRevResearch.1.033088.

[24] I. Božović, X. He, J. Wu, and A. T. Bollinger. Dependence of the critical temperature in overdoped copper oxides on superfluid density. *Nature*, 536(7616):309–311, Aug 2016. ISSN 1476-4687. doi: 10.1038/nature19061. URL https://doi.org/10.1038/nature19061.

[25] C. C. Bradley, C. A. Sackett, and R. G. Hulet. Bose-einstein condensation of lithium: Observation of limited condensate number. *Phys. Rev. Lett.*, 78:985–989, Feb 1997. doi: 10.1103/PhysRevLett.78.985. URL https://link.aps.org/doi/10.1103/PhysRevLett.78.985.

[26] S. Burger, K. Bongs, S. Dettmer, W. Ertmer, K. Sengstock, A. Sanpera, G. V. Shlyapnikov, and M. Lewenstein. Dark solitons in bose-einstein condensates. *Phys. Rev. Lett.*, 83:5198–5201, Dec 1999. doi: 10.1103/PhysRevLett.83.5198. URL https://link.aps.org/doi/10.1103/PhysRevLett.83.5198.

[27] F. Böttcher, J.-N. Schmidt, J. Hertkorn, K. S. H. Ng, S. D. Graham, M. Guo, T. Langen, and T. Pfau. New states of matter with fine-tuned interactions: quantum droplets and dipolar supersolids. *Reports on Progress in Physics*, 84(1): 012403, dec 2020. doi: 10.1088/1361-6633/abc9ab. URL https://dx.doi.org/10.1088/1361-6633/abc9ab.

[28] C. R. Cabrera, L. Tanzi, J. Sanz, B. Naylor, P. Thomas, P. Cheiney, and L. Tarruell. Quantum liquid droplets in a mixture of bose-einstein condensates. *Science*, 359(6373):301–304, 2018. doi: 10.1126/science.aao5686. URL `https://www.science.org/doi/abs/10.1126/science.aao5686`.

[29] B. Capogrosso-Sansone, C. Trefzger, M. Lewenstein, P. Zoller, and G. Pupillo. Quantum phases of cold polar molecules in 2d optical lattices. *Phys. Rev. Lett.*, 104:125301, Mar 2010. doi: 10.1103/PhysRevLett.104.125301. URL `https://link.aps.org/doi/10.1103/PhysRevLett.104.125301`.

[30] F. S. Cataliotti, S. Burger, C. Fort, P. Maddaloni, F. Minardi, A. Trombettoni, A. Smerzi, and M. Inguscio. Josephson junction arrays with bose-einstein condensates. *Science*, 293(5531):843–846, Aug 2001. doi: 10.1126/science.1062612. URL `https://doi.org/10.1126/science.1062612`.

[31] F. Cattani, C. Gross, M. K. Oberthaler, and J. Ruostekoski. Measuring and engineering entropy and spin squeezing in weakly linked bose–einstein condensates. *New Journal of Physics*, 15(6):063035, jun 2013. doi: 10.1088/1367-2630/15/6/063035. URL `https://dx.doi.org/10.1088/1367-2630/15/6/063035`.

[32] P. M. Chaikin and T. C. Lubensky. *Principles of Condensed Matter Physics*. Cambridge University Press, 1995. doi: 10.1017/CBO9780511813467.

[33] T. Chalopin, T. Satoor, A. Evrard, V. Makhalov, J. Dalibard, R. Lopes, and S. Nascimbene. Probing chiral edge dynamics and bulk topology of a synthetic hall system. *Nature Physics*, 16(10):1017–1021, Oct 2020. ISSN 1745-2481. doi: 10.1038/s41567-020-0942-5. URL `https://doi.org/10.1038/s41567-020-0942-5`.

[34] M. H. W. Chan, R. B. Hallock, and L. Reatto. Overview on solid ^{4}He and the issue of supersolidity. *Journal of Low Temperature Physics*, 172(5):317–363, 2013. ISSN 1573-7357. doi: 10.1007/s10909-013-0882-x. URL `https://doi.org/10.1007/s10909-013-0882-x`.

[35] M.-S. Chang, C. D. Hamley, M. D. Barrett, J. A. Sauer, K. M. Fortier, W. Zhang, L. You, and M. S. Chapman. Observa-

tion of spinor dynamics in optically trapped ^{87}Rb bose-einstein condensates. *Phys. Rev. Lett.*, 92:140403, Apr 2004. doi: 10.1103/PhysRevLett.92.140403. URL https://link.aps.org/doi/10.1103/PhysRevLett.92.140403.

[36] G. Chauveau, C. Maury, F. Rabec, C. Heintze, G. Brochier, S. Nascimbene, J. Dalibard, J. Beugnon, S. M. Roccuzzo, and S. Stringari. Superfluid fraction in an interacting spatially modulated bose-einstein condensate. *Phys. Rev. Lett.*, 130:226003, Jun 2023. doi: 10.1103/PhysRevLett.130.226003. URL https://link.aps.org/doi/10.1103/PhysRevLett.130.226003.

[37] R. W. Cherng and E. Demler. Roton softening and supersolidity in rb spinor condensates. 2008. URL https://arxiv.org/abs/0806.1991.

[38] G. V. Chester. Speculations on Bose-Einstein Condensation and Quantum Crystals. *Phys. Rev. A*, 2:256–258, Jul 1970. doi: 10.1103/PhysRevA.2.256. URL https://link.aps.org/doi/10.1103/PhysRevA.2.256.

[39] C. Chin, R. Grimm, P. Julienne, and E. Tiesinga. Feshbach resonances in ultracold gases. *Rev. Mod. Phys.*, 82:1225–1286, Apr 2010. doi: 10.1103/RevModPhys.82.1225. URL https://link.aps.org/doi/10.1103/RevModPhys.82.1225.

[40] J. Choi, A. A. Zadorozhko, J. Choi, and E. Kim. Spatially modulated superfluid state in two-dimensional ^{4}He films. *Phys. Rev. Lett.*, 127:135301, Sep 2021. doi: 10.1103/PhysRevLett.127.135301. URL https://link.aps.org/doi/10.1103/PhysRevLett.127.135301.

[41] L. Chomaz, R. M. W. van Bijnen, D. Petter, G. Faraoni, S. Baier, J. H. Becher, M. J. Mark, F. Wächtler, L. Santos, and F. Ferlaino. Observation of roton mode population in a dipolar quantum gas. *Nature Physics*, 14(5):442–446, May 2018. ISSN 1745-2481. doi: 10.1038/s41567-018-0054-7. URL https://doi.org/10.1038/s41567-018-0054-7.

[42] L. Chomaz, D. Petter, P. Ilzhöfer, G. Natale, A. Trautmann, C. Politi, G. Durastante, R. M. W. van Bijnen, A. Patscheider, M. Sohmen, M. J. Mark, and F. Ferlaino. Long-lived and transient

supersolid behaviors in dipolar quantum gases. *Phys. Rev. X*, 9:021012, Apr 2019. doi: 10.1103/PhysRevX.9.021012. URL https://link.aps.org/doi/10.1103/PhysRevX.9.021012.

[43] L. Chomaz, I. Ferrier-Barbut, F. Ferlaino, B. Laburthe-Tolra, B. L. Lev, and T. Pfau. Dipolar physics: a review of experiments with magnetic quantum gases. *Reports on Progress in Physics*, 86(2):026401, dec 2022. doi: 10.1088/1361-6633/aca814. URL https://dx.doi.org/10.1088/1361-6633/aca814.

[44] F. Cinti, P. Jain, M. Boninsegni, A. Micheli, P. Zoller, and G. Pupillo. Supersolid droplet crystal in a dipole-blockaded gas. *Phys. Rev. Lett.*, 105:135301, Sep 2010. doi: 10.1103/PhysRevLett.105.135301. URL https://link.aps.org/doi/10.1103/PhysRevLett.105.135301.

[45] S. Conti, A. Perali, A. R. Hamilton, M. V. Milošević, F. m. c. M. Peeters, and D. Neilson. Chester supersolid of spatially indirect excitons in double-layer semiconductor heterostructures. *Phys. Rev. Lett.*, 130:057001, Feb 2023. doi: 10.1103/PhysRevLett.130.057001. URL https://link.aps.org/doi/10.1103/PhysRevLett.130.057001.

[46] L. Corman, L. Chomaz, T. Bienaimé, R. Desbuquois, C. Weitenberg, S. Nascimbène, J. Dalibard, and J. Beugnon. Quench-induced supercurrents in an annular bose gas. *Phys. Rev. Lett.*, 113:135302, Sep 2014. doi: 10.1103/PhysRevLett.113.135302. URL https://link.aps.org/doi/10.1103/PhysRevLett.113.135302.

[47] F. Dalfovo, S. Giorgini, L. P. Pitaevskii, and S. Stringari. Theory of bose-einstein condensation in trapped gases. *Rev. Mod. Phys.*, 71:463–512, Apr 1999. doi: 10.1103/RevModPhys.71.463. URL https://link.aps.org/doi/10.1103/RevModPhys.71.463.

[48] J. Day and J. Beamish. Low-temperature shear modulus changes in solid 4he and connection to supersolidity. *Nature*, 450(7171): 853–856, Dec 2007. ISSN 1476-4687. doi: 10.1038/nature06383. URL https://doi.org/10.1038/nature06383.

[49] G. del Pace. Tunneling transport in strongly-interacting atomic fermi gases. *Ph.D. Thesis - Università degli Studi di Firenze*,

2020. URL https://quantumgases.lens.unifi.it/theses/thesis_delpace_phd.pdf.

[50] D. Dreon, L. A. Sidorenkov, C. Bouazza, W. Maineult, J. Dalibard, and S. Nascimbene. Optical cooling and trapping of highly magnetic atoms: the benefits of a spontaneous spin polarization. *Journal of Physics B: Atomic, Molecular and Optical Physics*, 50(6):065005, mar 2017. doi: 10.1088/1361-6455/aa5db5. URL https://dx.doi.org/10.1088/1361-6455/aa5db5.

[51] V. A. Dzuba, V. V. Flambaum, and B. L. Lev. Dynamic polarizabilities and magic wavelengths for dysprosium. *Phys. Rev. A*, 83:032502, Mar 2011. doi: 10.1103/PhysRevA.83.032502. URL https://link.aps.org/doi/10.1103/PhysRevA.83.032502.

[52] T. Esslinger. Fermi-hubbard physics with atoms in an optical lattice. *Annual Review of Condensed Matter Physics*, 1(1):129–152, 2010. doi: 10.1146/annurev-conmatphys-070909-104059. URL https://doi.org/10.1146/annurev-conmatphys-070909-104059.

[53] M. E. Fisher, M. N. Barber, and D. Jasnow. Helicity modulus, superfluidity, and scaling in isotropic systems. *Phys. Rev. A*, 8:1111–1124, Aug 1973. doi: 10.1103/PhysRevA.8.1111. URL https://link.aps.org/doi/10.1103/PhysRevA.8.1111.

[54] N. Fisher. *Statistical Analysis of Circular Data*. Statistical Analysis of Circular Data. Cambridge University Press, 1995. ISBN 9780521568906. URL https://books.google.it/books?id=wGPj3EoFdJwC.

[55] A. Frölian, C. S. Chisholm, E. Neri, C. R. Cabrera, R. Ramos, A. Celi, and L. Tarruell. Realizing a 1d topological gauge theory in an optically dressed bec. *Nature*, 608(7922):293–297, Aug 2022. ISSN 1476-4687. doi: 10.1038/s41586-022-04943-3. URL https://doi.org/10.1038/s41586-022-04943-3.

[56] A. Gallemí, S. M. Roccuzzo, S. Stringari, and A. Recati. Quantized vortices in dipolar supersolid bose-einstein-condensed gases. *Phys. Rev. A*, 102:023322, Aug 2020. doi: 10.1103/PhysRevA.102.023322. URL https://link.aps.org/doi/10.1103/PhysRevA.102.023322.

[57] R. Gati, B. Hemmerling, J. Fölling, M. Albiez, and M. K. Oberthaler. Noise thermometry with two weakly coupled bose-einstein condensates. *Phys. Rev. Lett.*, 96:130404, Apr 2006. doi: 10.1103/PhysRevLett.96.130404. URL `https://link.aps.org/doi/10.1103/PhysRevLett.96.130404`.

[58] V. L. Ginzburg and L. D. Landau. On the Theory of superconductivity. *Zh. Eksp. Teor. Fiz.*, 20:1064–1082, 1950. doi: 10.1016/B978-0-08-010586-4.50035-3. URL `https://doi.org/10.1016/B978-0-08-010586-4.50035-3`.

[59] M. Greiner, O. Mandel, T. Esslinger, T. W. Hänsch, and I. Bloch. Quantum phase transition from a superfluid to a mott insulator in a gas of ultracold atoms. *Nature*, 415(6867):39–44, Jan 2002. ISSN 1476-4687. doi: 10.1038/415039a. URL `https://doi.org/10.1038/415039a`.

[60] R. Grimm, M. Weidemüller, and Y. B. Ovchinnikov. Optical dipole traps for neutral atoms. volume 42 of *Advances In Atomic, Molecular, and Optical Physics*, pages 95–170. Academic Press, 2000. doi: https://doi.org/10.1016/S1049-250X(08)60186-X. URL `https://www.sciencedirect.com/science/article/pii/S1049250X0860186X`.

[61] E. P. Gross. Unified theory of interacting bosons. *Phys. Rev.*, 106:161–162, Apr 1957. doi: 10.1103/PhysRev.106.161. URL `https://link.aps.org/doi/10.1103/PhysRev.106.161`.

[62] H. Gross. *Handbook of Optical Systems: Volume 1: Fundamentals of Technical Optics*. John Wiley & Sons, Ltd, 2005. ISBN 9783527699223. doi: https://doi.org/10.1002/9783527699223. URL `https://onlinelibrary.wiley.com/doi/abs/10.1002/9783527699223`.

[63] M. Guo, F. Böttcher, J. Hertkorn, J.-N. Schmidt, M. Wenzel, H. P. Büchler, T. Langen, and T. Pfau. The low-energy goldstone mode in a trapped dipolar supersolid. *Nature*, 574(7778):386–389, Oct 2019. ISSN 1476-4687. doi: 10.1038/s41586-019-1569-5. URL `https://doi.org/10.1038/s41586-019-1569-5`.

[64] B. I. Halperin and P. C. Hoenberg. Hydrodynamic theory of spin waves. *Phys. Rev.*, 188:898–918, Dec 1969. doi: 10.1103/PhysRev.

188.898. URL https://link.aps.org/doi/10.1103/PhysRev.188.898.

[65] B. I. Halperin, T. C. Lubensky, and S.-k. Ma. First-order phase transitions in superconductors and smectic-a liquid crystals. *Phys. Rev. Lett.*, 32:292–295, Feb 1974. doi: 10.1103/PhysRevLett.32.292. URL https://link.aps.org/doi/10.1103/PhysRevLett.32.292.

[66] M. H. Hamidian, S. D. Edkins, S. H. Joo, A. Kostin, H. Eisaki, S. Uchida, M. J. Lawler, E.-A. Kim, A. P. Mackenzie, K. Fujita, J. Lee, and J. C. S. Davis. Detection of a cooper-pair density wave in bi2sr2cacu2o8+x. *Nature*, 532(7599):343–347, Apr 2016. ISSN 1476-4687. doi: 10.1038/nature17411. URL https://doi.org/10.1038/nature17411.

[67] N. Henkel, R. Nath, and T. Pohl. Three-dimensional roton excitations and supersolid formation in rydberg-excited bose-einstein condensates. *Phys. Rev. Lett.*, 104:195302, May 2010. doi: 10.1103/PhysRevLett.104.195302. URL https://link.aps.org/doi/10.1103/PhysRevLett.104.195302.

[68] J. Hertkorn, F. Böttcher, M. Guo, J. N. Schmidt, T. Langen, H. P. Büchler, and T. Pfau. Fate of the amplitude mode in a trapped dipolar supersolid. *Phys. Rev. Lett.*, 123:193002, Nov 2019. doi: 10.1103/PhysRevLett.123.193002. URL https://link.aps.org/doi/10.1103/PhysRevLett.123.193002.

[69] J. Hertkorn, J.-N. Schmidt, F. Böttcher, M. Guo, M. Schmidt, K. S. H. Ng, S. D. Graham, H. P. Büchler, T. Langen, M. Zwierlein, and T. Pfau. Density fluctuations across the superfluid-supersolid phase transition in a dipolar quantum gas. *Phys. Rev. X*, 11: 011037, Feb 2021. doi: 10.1103/PhysRevX.11.011037. URL https://link.aps.org/doi/10.1103/PhysRevX.11.011037.

[70] J. Hertkorn, J.-N. Schmidt, M. Guo, F. Böttcher, K. S. H. Ng, S. D. Graham, P. Uerlings, H. P. Büchler, T. Langen, M. Zwierlein, and T. Pfau. Supersolidity in two-dimensional trapped dipolar droplet arrays. *Phys. Rev. Lett.*, 127:155301, Oct 2021. doi: 10.1103/PhysRevLett.127.155301. URL https://link.aps.org/doi/10.1103/PhysRevLett.127.155301.

[71] J. Hertkorn, J.-N. Schmidt, M. Guo, F. Böttcher, K. S. H. Ng, S. D. Graham, P. Uerlings, T. Langen, M. Zwierlein, and T. Pfau. Pattern formation in quantum ferrofluids: From supersolids to superglasses. *Phys. Rev. Research*, 3:033125, Aug 2021. doi: 10.1103/PhysRevResearch.3.033125. URL `https://link.aps.org/doi/10.1103/PhysRevResearch.3.033125`.

[72] G. B. Hess and W. M. Fairbank. Measurements of angular momentum in superfluid helium. *Phys. Rev. Lett.*, 19:216–218, Jul 1967. doi: 10.1103/PhysRevLett.19.216. URL `https://link.aps.org/doi/10.1103/PhysRevLett.19.216`.

[73] C. C. Homes, S. V. Dordevic, M. Strongin, D. A. Bonn, R. Liang, W. N. Hardy, S. Komiya, Y. Ando, G. Yu, N. Kaneko, X. Zhao, M. Greven, D. N. Basov, and T. Timusk. A universal scaling relation in high-temperature superconductors. *Nature*, 430(6999): 539–541, Jul 2004. ISSN 1476-4687. doi: 10.1038/nature02673. URL `https://doi.org/10.1038/nature02673`.

[74] K. Huang. *Introduction to Statistical Physics*. Taylor & Francis, 2001. ISBN 9780748409419. URL `https://books.google.it/books?id=JOU9IxcmuJ8C`.

[75] K. Huang and C. N. Yang. Quantum-mechanical many-body problem with hard-sphere interaction. *Phys. Rev.*, 105:767–775, Feb 1957. doi: 10.1103/PhysRev.105.767. URL `https://link.aps.org/doi/10.1103/PhysRev.105.767`.

[76] P. Ilzhöfer, M. Sohmen, G. Durastante, C. Politi, A. Trautmann, G. Natale, G. Morpurgo, T. Giamarchi, L. Chomaz, M. J. Mark, and F. Ferlaino. Phase coherence in out-of-equilibrium supersolid states of ultracold dipolar atoms. *Nature Physics*, 17(3):356–361, Mar 2021. ISSN 1745-2481. doi: 10.1038/s41567-020-01100-3. URL `https://doi.org/10.1038/s41567-020-01100-3`.

[77] E. Inönü and E. P. Wigner. Representations of the galilei group. *Il Nuovo Cimento (1943-1954)*, 9(8):705–718, Aug 1952. ISSN 1827-6121. doi: 10.1007/BF02782239. URL `https://doi.org/10.1007/BF02782239`.

[78] B. Jackson, J. F. McCann, and C. S. Adams. Output coupling and flow of a dilute Bose-Einstein condensate. *J. Phys. B: At.*

Mol. Opt. Phys., 31(20):4489–4499, 1998. ISSN 0953-4075. URL https://doi.org/10.1088/0953-4075/31/20/008.

[79] D. Jaksch, C. Bruder, J. I. Cirac, C. W. Gardiner, and P. Zoller. Cold bosonic atoms in optical lattices. *Phys. Rev. Lett.*, 81: 3108–3111, Oct 1998. doi: 10.1103/PhysRevLett.81.3108. URL https://link.aps.org/doi/10.1103/PhysRevLett.81.3108.

[80] B. Josephson. Possible new effects in superconductive tunnelling. *Physics Letters*, 1(7):251–253, 1962. ISSN 0031-9163. doi: https://doi.org/10.1016/0031-9163(62)91369-0. URL https://www.sciencedirect.com/science/article/pii/0031916362913690.

[81] P. Juhász, M. Krstajić, D. Strachan, E. Gandar, and R. P. Smith. How to realize a homogeneous dipolar bose gas in the roton regime. *Phys. Rev. A*, 105:L061301, Jun 2022. doi: 10.1103/PhysRevA.105.L061301. URL https://link.aps.org/doi/10.1103/PhysRevA.105.L061301.

[82] H. Kadau, M. Schmitt, M. Wenzel, C. Wink, T. Maier, I. Ferrier-Barbut, and T. Pfau. Observing the rosensweig instability of a quantum ferrofluid. *Nature*, 530(7589):194–197, Feb 2016. ISSN 1476-4687. doi: 10.1038/nature16485. URL https://doi.org/10.1038/nature16485.

[83] W. Kao, Y. Tang, N. Burdick, and B. Lev. Anisotropic dependence of tune-out wavelength near dy 741-nm transition. *Optics Express*, 25(4):3411–3419, Feb 2017. doi: 10.1364/OE.25.003411. URL https://opg.optica.org/oe/fulltext.cfm?uri=oe-25-4-3411&id=359890.

[84] Y. Kawaguchi and M. Ueda. Spinor bose–einstein condensates. *Physics Reports*, 520(5):253–381, 2012. ISSN 0370-1573. doi: https://doi.org/10.1016/j.physrep.2012.07.005. URL https://www.sciencedirect.com/science/article/pii/S0370157312002098.

[85] D. Y. Kim and M. H. W. Chan. Absence of supersolidity in solid helium in porous vycor glass. *Phys. Rev. Lett.*, 109:155301, Oct 2012. doi: 10.1103/PhysRevLett.109.155301. URL https://link.aps.org/doi/10.1103/PhysRevLett.109.155301.

[86] E. Kim and M. H. W. Chan. Probable observation of a supersolid helium phase. *Nature*, 427(6971):225–227, Jan 2004. ISSN 1476-4687. doi: 10.1038/nature02220. URL `https://doi.org/10.1038/nature02220`.

[87] E. Kim and M. H. W. Chan. Observation of superflow in solid helium. *Science*, 305(5692):1941–1944, 2004. doi: 10.1126/science.1101501. URL `https://www.science.org/doi/abs/10.1126/science.1101501`.

[88] C. Kittel. *Introduction to Solid State Physics.* Wiley, 2004. ISBN 9780471415268. URL `https://books.google.it/books?id=kym4QgAACAAJ`.

[89] M. Krämer, L. Pitaevskii, and S. Stringari. Macroscopic dynamics of a trapped bose-einstein condensate in the presence of 1d and 2d optical lattices. *Phys. Rev. Lett.*, 88:180404, Apr 2002. doi: 10.1103/PhysRevLett.88.180404. URL `https://link.aps.org/doi/10.1103/PhysRevLett.88.180404`.

[90] M. Kreyer, J. Han, C. Ravensbergen, V. Corre, E. Soave, E. Kirilov, and R. Grimm. Measurement of the dynamic polarizability of dy atoms near the 626-nm intercombination line. *Phys.Rev.A*, 104:033106, 2021. doi: 10.1103/PhysRevA.104.033106. URL `https://link.aps.org/doi/10.1103/PhysRevA.104.033106`.

[91] P. Kunkel. *Splitting a Bose Einstein condensate enables EPR steering and simultaneous readout of noncommuting observables.* PhD thesis, Universität Heidelberg, 2019. URL `http://www.kip.uni-heidelberg.de/Veroeffentlichungen/download.php/6440/temp/3991.pdf`.

[92] P. Kunkel, M. Prüfer, H. Strobel, D. Linnemann, A. Frölian, T. Gasenzer, M. Gärttner, and M. K. Oberthaler. Spatially distributed multipartite entanglement enables epr steering of atomic clouds. *Science*, 360(6387):413–416, 2018. doi: 10.1126/science.aao2254. URL `https://www.science.org/doi/abs/10.1126/science.aao2254`.

[93] P. Kunkel, M. Prüfer, S. Lannig, R. Rosa-Medina, A. Bonnin, M. Gärttner, H. Strobel, and M. K. Oberthaler. Simultaneous readout of noncommuting collective spin observables beyond the

standard quantum limit. *Phys. Rev. Lett.*, 123:063603, Aug 2019. doi: 10.1103/PhysRevLett.123.063603. URL `https://link.aps.org/doi/10.1103/PhysRevLett.123.063603`.

[94] P. Kunkel, M. Prüfer, S. Lannig, R. Strohmaier, M. Gärttner, H. Strobel, and M. K. Oberthaler. Detecting entanglement structure in continuous many-body quantum systems. *Phys. Rev. Lett.*, 128:020402, Jan 2022. doi: 10.1103/PhysRevLett.128.020402. URL `https://link.aps.org/doi/10.1103/PhysRevLett.128.020402`.

[95] T. Lahaye, J. Metz, B. Fröhlich, T. Koch, M. Meister, A. Griesmaier, T. Pfau, H. Saito, Y. Kawaguchi, and M. Ueda. *d*-wave collapse and explosion of a dipolar bose-einstein condensate. *Phys. Rev. Lett.*, 101:080401, Aug 2008. doi: 10.1103/PhysRevLett.101.080401. URL `https://link.aps.org/doi/10.1103/PhysRevLett.101.080401`.

[96] T. Lahaye, C. Menotti, L. Santos, M. Lewenstein, and T. Pfau. The physics of dipolar bosonic quantum gases. *Reports on Progress in Physics*, 72(12):126401, nov 2009. doi: 10.1088/0034-4885/72/12/126401. URL `https://dx.doi.org/10.1088/0034-4885/72/12/126401`.

[97] L. Landau. The theory of phase transitions. *Nature*, 138(3498): 840–841, Nov 1936. ISSN 1476-4687. doi: 10.1038/138840a0. URL `https://doi.org/10.1038/138840a0`.

[98] R. Landig, L. Hruby, N. Dogra, M. Landini, R. Mottl, T. Donner, and T. Esslinger. Quantum phases from competing short- and long-range interactions in an optical lattice. *Nature*, 532(7600): 476–479, Apr 2016. ISSN 1476-4687. doi: 10.1038/nature17409. URL `https://doi.org/10.1038/nature17409`.

[99] T. Langen, G. Valtolina, D. Wang, and J. Ye. Quantum state manipulation and science of ultracold molecules, 2023. URL `https://doi.org/10.48550/arXiv.2305.13445`.

[100] S. Lannig. *Vector Solitons and Different Scenarios of Universal Dynamics in a Spin-1 Bose-Einstein Condensate.* PhD thesis, Universität Heidelberg, 2022. URL `https://archiv.ub.uni-heidelberg.de/volltextserver/32047/1/phd_sl.pdf`.

[101] S. Lannig, C.-M. Schmied, M. Prüfer, P. Kunkel, R. Strohmaier, H. Strobel, T. Gasenzer, P. G. Kevrekidis, and M. K. Oberthaler. Collisions of three-component vector solitons in bose-einstein condensates. *Phys. Rev. Lett.*, 125:170401, Oct 2020. doi: 10.1103/PhysRevLett.125.170401. URL `https://link.aps.org/doi/10.1103/PhysRevLett.125.170401`.

[102] S. Lannig, M. Prüfer, Y. Deller, I. Siovitz, J. Dreher, T. Gasenzer, H. Strobel, and M. K. Oberthaler. Observation of two non-thermal fixed points for the same microscopic symmetry, 2023. URL `https://arxiv.org/abs/2306.16497`.

[103] A. J. Leggett. Can a solid be "superfluid"? *Phys. Rev. Lett.*, 25:1543–1546, Nov 1970. doi: 10.1103/PhysRevLett.25.1543. URL `https://link.aps.org/doi/10.1103/PhysRevLett.25.1543`.

[104] A. J. Leggett. On the superfluid fraction of an arbitrary many-body system at t=0. *Journal of Statistical Physics*, 93 (3):927–941, Nov 1998. ISSN 1572-9613. doi: 10.1023/B:JOSS.0000033170.38619.6c. URL `https://doi.org/10.1023/B:JOSS.0000033170.38619.6c`.

[105] A. J. Leggett. Superfluidity. *Rev. Mod. Phys.*, 71:S318–S323, Mar 1999. doi: 10.1103/RevModPhys.71.S318. URL `https://link.aps.org/doi/10.1103/RevModPhys.71.S318`.

[106] J. Léonard, A. Morales, P. Zupancic, T. Esslinger, and T. Donner. Supersolid formation in a quantum gas breaking a continuous translational symmetry. *Nature*, 543(7643):87–90, Mar 2017. ISSN 1476-4687. doi: 10.1038/nature21067. URL `https://doi.org/10.1038/nature21067`.

[107] L. V. Levitin, B. Yager, L. Sumner, B. Cowan, A. J. Casey, J. Saunders, N. Zhelev, R. G. Bennett, and J. M. Parpia. Evidence for a spatially modulated superfluid phase of ^{3}He under confinement. *Phys. Rev. Lett.*, 122:085301, Feb 2019. doi: 10.1103/PhysRevLett.122.085301. URL `https://link.aps.org/doi/10.1103/PhysRevLett.122.085301`.

[108] S. Levy, E. Lahoud, I. Shomroni, and J. Steinhauer. The a.c. and d.c. josephson effects in a bose–einstein condensate. *Nature*,

449(7162):579–583, Oct 2007. ISSN 1476-4687. doi: 10.1038/nature06186. URL https://doi.org/10.1038/nature06186.

[109] H. Li, J.-F. Wyart, O. Dulieu, S. Nascimbène, and M. Lepers. Optical trapping of ultracold dysprosium atoms: transition probabilities, dynamic dipole polarizabilities and van der waals c6 coefficients. *Journal of Physics B: Atomic, Molecular and Optical Physics*, 50(1):014005, dec 2016. doi: 10.1088/1361-6455/50/1/014005. URL https://dx.doi.org/10.1088/1361-6455/50/1/014005.

[110] J.-R. Li, J. Lee, W. Huang, S. Burchesky, B. Shteynas, F. Top, A. O. Jamison, and W. Ketterle. A stripe phase with supersolid properties in spin–orbit-coupled bose–einstein condensates. *Nature*, 543(7643):91–94, Mar 2017. ISSN 1476-4687. doi: 10.1038/nature21431. URL https://doi.org/10.1038/nature21431.

[111] C. N. Likos, A. Lang, M. Watzlawek, and H. Löwen. Criterion for determining clustering versus reentrant melting behavior for bounded interaction potentials. *Phys. Rev. E*, 63:031206, Feb 2001. doi: 10.1103/PhysRevE.63.031206. URL https://link.aps.org/doi/10.1103/PhysRevE.63.031206.

[112] A. R. P. Lima and A. Pelster. Beyond mean-field low-lying excitations of dipolar Bose gases. *Phys. Rev. A*, 86:063609, Dec 2012. doi: 10.1103/PhysRevA.86.063609. URL https://link.aps.org/doi/10.1103/PhysRevA.86.063609.

[113] Y. Liu, T. Wei, G. He, Y. Zhang, Z. Wang, and J. Wang. Pair density wave state in a monolayer high-tc iron-based superconductor. *Nature*, 618(7967):934–939, Jun 2023. ISSN 1476-4687. doi: 10.1038/s41586-023-06072-x. URL https://doi.org/10.1038/s41586-023-06072-x.

[114] M. Lu, N. Q. Burdick, S. H. Youn, and B. L. Lev. Strongly dipolar bose-einstein condensate of dysprosium. *Phys. Rev. Lett.*, 107:190401, Oct 2011. doi: 10.1103/PhysRevLett.107.190401. URL https://link.aps.org/doi/10.1103/PhysRevLett.107.190401.

[115] E. Lucioni, G. Masella, A. Fregosi, C. Gabbanini, S. Gozzini, A. Fioretti, L. Del Bino, J. Catani, G. Modugno, and M. Inguscio.

A new setup for experiments with ultracold dysprosium atoms. *The European Physical Journal Special Topics*, 226(12):2775–2780, Jul 2017. ISSN 1951-6401. doi: 10.1140/epjst/e2016-60387-6. URL `https://doi.org/10.1140/epjst/e2016-60387-6`.

[116] E. Lucioni, L. Tanzi, A. Fregosi, J. Catani, S. Gozzini, M. Inguscio, A. Fioretti, C. Gabbanini, and G. Modugno. Dysprosium dipolar bose-einstein condensate with broad feshbach resonances. *Phys. Rev. A*, 97:060701, Jun 2018. doi: 10.1103/PhysRevA.97.060701. URL `https://link.aps.org/doi/10.1103/PhysRevA.97.060701`.

[117] N. Luick, L. Sobirey, M. Bohlen, V. P. Singh, L. Mathey, T. Lompe, and H. Moritz. An ideal josephson junction in an ultracold two-dimensional fermi gas. *Science*, 369(6499):89–91, 2020. doi: 10.1126/science.aaz2342. URL `https://www.science.org/doi/abs/10.1126/science.aaz2342`.

[118] W. Lunden, L. Du, M. Cantara, P. Barral, A. O. Jamison, and W. Ketterle. Enhancing the capture velocity of a dy magneto-optical trap with two-stage slowing. *Phys. Rev. A*, 101:063403, Jun 2020. doi: 10.1103/PhysRevA.101.063403. URL `https://link.aps.org/doi/10.1103/PhysRevA.101.063403`.

[119] X.-Y. Luo, Y.-Q. Zou, L.-N. Wu, Q. Liu, M.-F. Han, M. K. Tey, and L. You. Deterministic entanglement generation from driving through quantum phase transitions. *Science*, 355(6325):620–623, 2017. doi: 10.1126/science.aag1106. URL `https://www.science.org/doi/abs/10.1126/science.aag1106`.

[120] X.-Y. Luo, Y.-Q. Zou, L.-N. Wu, Q. Liu, M.-F. Han, M. K. Tey, and L. You. Deterministic entanglement generation from driving through quantum phase transitions. *Science*, 355(6325):620–623, 2017. doi: 10.1126/science.aag1106. URL `https://www.science.org/doi/abs/10.1126/science.aag1106`.

[121] T. Macrì, F. Maucher, F. Cinti, and T. Pohl. Elementary excitations of ultracold soft-core bosons across the superfluid-supersolid phase transition. *Phys. Rev. A*, 87:061602, Jun 2013. doi: 10.1103/PhysRevA.87.061602. URL `https://link.aps.org/doi/10.1103/PhysRevA.87.061602`.

[122] T. Maier, H. Kadau, M. Schmitt, M. Wenzel, I. Ferrier-Barbut, T. Pfau, A. Frisch, S. Baier, K. Aikawa, L. Chomaz, M. J. Mark, F. Ferlaino, C. Makrides, E. Tiesinga, A. Petrov, and S. Kotochigova. Emergence of chaotic scattering in ultracold er and dy. *Phys. Rev. X*, 5:041029, Nov 2015. doi: 10.1103/PhysRevX.5.041029. URL https://link.aps.org/doi/10.1103/PhysRevX.5.041029.

[123] O. M. Maragò, S. A. Hopkins, J. Arlt, E. Hodby, G. Hechenblaikner, and C. J. Foot. Observation of the scissors mode and evidence for superfluidity of a trapped bose-einstein condensed gas. *Phys. Rev. Lett.*, 84:2056–2059, Mar 2000. doi: 10.1103/PhysRevLett.84.2056. URL https://link.aps.org/doi/10.1103/PhysRevLett.84.2056.

[124] O. M. Maragò, G. Hechenblaikner, E. Hodby, S. A. Hopkins, and C. J. Foot. The moment of inertia and the scissors mode of a bose-condensed gas. *Journal of Physics: Condensed Matter*, 14(3):343, dec 2001. doi: 10.1088/0953-8984/14/3/305. URL https://dx.doi.org/10.1088/0953-8984/14/3/305.

[125] J. Mitroy, M. S. Safronova, and C. W. Clark. Theory and applications of atomic and ionic polarizabilities. *Journal of Physics B: Atomic, Molecular and Optical Physics*, 43(20):202001, oct 2010. doi: 10.1088/0953-4075/43/20/202001. URL https://dx.doi.org/10.1088/0953-4075/43/20/202001.

[126] M. Modugno, L. Pricoupenko, and Y. Castin. Bose-Einstein condensates with a bent vortex in rotating traps. *Eur. Phys. J. D*, 22(2):235–257, 2003. doi: 10.1140/epjd/e2003-00015-y. URL https://doi.org/10.1140/epjd/e2003-00015-y.

[127] O. Morsch and M. Oberthaler. Dynamics of bose-einstein condensates in optical lattices. *Rev. Mod. Phys.*, 78:179–215, Feb 2006. doi: 10.1103/RevModPhys.78.179. URL https://link.aps.org/doi/10.1103/RevModPhys.78.179.

[128] W. Muessel, H. Strobel, D. Linnemann, D. B. Hume, and M. K. Oberthaler. Scalable spin squeezing for quantum-enhanced magnetometry with bose-einstein condensates. *Phys. Rev. Lett.*, 113:103004, Sep 2014. doi: 10.1103/PhysRevLett.113.103004.

URL https://link.aps.org/doi/10.1103/PhysRevLett.113.103004.

[129] W. Muessel, H. Strobel, D. Linnemann, T. Zibold, B. Juliá-Díaz, and M. K. Oberthaler. Twist-and-turn spin squeezing in bose-einstein condensates. *Phys. Rev. A*, 92:023603, Aug 2015. doi: 10.1103/PhysRevA.92.023603. URL https://link.aps.org/doi/10.1103/PhysRevA.92.023603.

[130] M. Nilsson Tengstrand, P. Stürmer, J. Ribbing, and S. M. Reimann. Toroidal dipolar supersolid with a rotating weak link. *Phys. Rev. A*, 107:063316, Jun 2023. doi: 10.1103/PhysRevA.107.063316. URL https://link.aps.org/doi/10.1103/PhysRevA.107.063316.

[131] M. A. Norcia, C. Politi, L. Klaus, E. Poli, M. Sohmen, M. J. Mark, R. N. Bisset, L. Santos, and F. Ferlaino. Two-dimensional supersolidity in a dipolar quantum gas. *Nature*, 596(7872):357–361, Aug 2021. ISSN 1476-4687. doi: 10.1038/s41586-021-03725-7. URL https://doi.org/10.1038/s41586-021-03725-7.

[132] M. A. Norcia, E. Poli, C. Politi, L. Klaus, T. Bland, M. J. Mark, L. Santos, R. N. Bisset, and F. Ferlaino. Can angular oscillations probe superfluidity in dipolar supersolids? *Phys. Rev. Lett.*, 129:040403, Jul 2022. doi: 10.1103/PhysRevLett.129.040403. URL https://link.aps.org/doi/10.1103/PhysRevLett.129.040403.

[133] J. Nyéki, A. Phillis, A. Ho, D. Lee, P. Coleman, J. Parpia, B. Cowan, and J. Saunders. Intertwined superfluid and density wave order in two-dimensional 4he. *Nature Physics*, 13(5):455–459, May 2017. ISSN 1745-2481. doi: 10.1038/nphys4023. URL https://doi.org/10.1038/nphys4023.

[134] Y. Ogata, H. Chudo, M. Ono, K. Harii, M. Matsuo, S. Maekawa, and E. Saitoh. Gyroscopic g factor of rare earth metals. *Applied Physics Letters*, 110(7):072409, 02 2017. ISSN 0003-6951. doi: 10.1063/1.4976998. URL https://doi.org/10.1063/1.4976998.

[135] B. Pasquiou, E. Maréchal, G. Bismut, P. Pedri, L. Vernac, O. Gorceix, and B. Laburthe-Tolra. Spontaneous demagnetization of a dipolar spinor bose gas in an ultralow magnetic

field. *Phys. Rev. Lett.*, 106:255303, Jun 2011. doi: 10.1103/PhysRevLett.106.255303. URL https://link.aps.org/doi/10.1103/PhysRevLett.106.255303.

[136] C. J. Pethick, N. Chamel, and S. Reddy. Superfluid Dynamics in Neutron Star Crusts. *Progress of Theoretical Physics Supplement*, 186:9–16, 10 2010. ISSN 0375-9687. doi: 10.1143/PTPS.186.9. URL https://doi.org/10.1143/PTPS.186.9.

[137] D. S. Petrov. Quantum mechanical stabilization of a collapsing bose-bose mixture. *Phys. Rev. Lett.*, 115:155302, Oct 2015. doi: 10.1103/PhysRevLett.115.155302. URL https://link.aps.org/doi/10.1103/PhysRevLett.115.155302.

[138] D. Petter, G. Natale, R. M. W. van Bijnen, A. Patscheider, M. J. Mark, L. Chomaz, and F. Ferlaino. Probing the roton excitation spectrum of a stable dipolar Bose gas. *Phys. Rev. Lett.*, 122:183401, May 2019. doi: 10.1103/PhysRevLett.122.183401. URL https://link.aps.org/doi/10.1103/PhysRevLett.122.183401.

[139] D. Petter, A. Patscheider, G. Natale, M. J. Mark, M. A. Baranov, R. van Bijnen, S. M. Roccuzzo, A. Recati, B. Blakie, D. Baillie, L. Chomaz, and F. Ferlaino. Bragg scattering of an ultracold dipolar gas across the phase transition from bose-einstein condensate to supersolid in the free-particle regime. *Phys. Rev. A*, 104:L011302, Jul 2021. doi: 10.1103/PhysRevA.104.L011302. URL https://link.aps.org/doi/10.1103/PhysRevA.104.L011302.

[140] L. Pezzè, A. Smerzi, M. K. Oberthaler, R. Schmied, and P. Treutlein. Quantum metrology with nonclassical states of atomic ensembles. *Rev. Mod. Phys.*, 90:035005, Sep 2018. doi: 10.1103/RevModPhys.90.035005. URL https://link.aps.org/doi/10.1103/RevModPhys.90.035005.

[141] L. Pitaevskii and S. Stringari. Thermal vs quantum decoherence in double well trapped bose-einstein condensates. *Phys. Rev. Lett.*, 87:180402, Oct 2001. doi: 10.1103/PhysRevLett.87.180402. URL https://link.aps.org/doi/10.1103/PhysRevLett.87.180402.

[142] L. Pitaevskii and S. Stringari. *Bose-Einstein Condensation and Superfluidity*. Oxford University Press, 01 2016. ISBN 9780198758884. doi: 10.1093/acprof:oso/9780198758884.001.0001. URL https://doi.org/10.1093/acprof:oso/9780198758884.001.0001.

[143] E. Poli, T. Bland, C. Politi, L. Klaus, M. A. Norcia, F. Ferlaino, R. N. Bisset, and L. Santos. Maintaining supersolidity in one and two dimensions. *Phys. Rev. A*, 104:063307, Dec 2021. doi: 10.1103/PhysRevA.104.063307. URL https://link.aps.org/doi/10.1103/PhysRevA.104.063307.

[144] Y. Pomeau and S. Rica. Dynamics of a model of supersolid. *Phys. Rev. Lett.*, 72:2426–2429, Apr 1994. doi: 10.1103/PhysRevLett.72.2426. URL https://link.aps.org/doi/10.1103/PhysRevLett.72.2426.

[145] W. H. Press, S. A. Teukolsky, W. T. Vetterling, and B. P. Flannery. *Numerical Recipes: The Art of Scientific Computing*. Cambridge University Press, USA, 3 edition, 2007. ISBN 0521880688. URL https://dl.acm.org/doi/10.5555/1403886.

[146] N. Preti. Towards dipolar quantum gases in a ring. *Master Thesis - Università degli Studi di Firenze*, 2020. URL https://quantumgases.lens.unifi.it/theses/thesis_preti_master.pdf.

[147] M. Prüfer. *Experimentally testing quantum field theory concepts with spinor Bose gases far from equilibirum*. PhD thesis, Universität Heidelberg, 2020. URL https://www.google.com/url?q=https%3A%2F%2Fwww.kip.uni-heidelberg.de%2FVeroeffentlichungen%2Fdownload%2F6456%2Fpdf-6456.pdf&sa=D&sntz=1&usg=AOvVaw1FE-rlrgum0_VmkfwkPzJ7.

[148] M. Prüfer, P. Kunkel, H. Strobel, S. Lannig, D. Linnemann, C.-M. Schmied, J. Berges, T. Gasenzer, and M. K. Oberthaler. Observation of universal dynamics in a spinor bose gas far from equilibrium. *Nature*, 563(7730):217–220, Nov 2018. ISSN 1476-4687. doi: 10.1038/s41586-018-0659-0. URL https://doi.org/10.1038/s41586-018-0659-0.

[149] M. Prüfer, T. V. Zache, P. Kunkel, S. Lannig, A. Bonnin, H. Strobel, J. Berges, and M. K. Oberthaler. Experimental extraction of the quantum effective action for a non-equilibrium many-body system. *Nature Physics*, 16(10):1012–1016, Oct 2020. ISSN 1745-2481. doi: 10.1038/s41567-020-0933-6. URL `https://doi.org/10.1038/s41567-020-0933-6`.

[150] M. Prüfer, D. Spitz, S. Lannig, H. Strobel, J. Berges, and M. K. Oberthaler. Condensation and thermalization of an easy-plane ferromagnet in a spinor bose gas. *Nature Physics*, 18(12):1459–1463, Dec 2022. ISSN 1745-2481. doi: 10.1038/s41567-022-01779-6. URL `https://doi.org/10.1038/s41567-022-01779-6`.

[151] A. Putra, F. Salces-Cárcoba, Y. Yue, S. Sugawa, and I. B. Spielman. Spatial coherence of spin-orbit-coupled bose gases. *Phys. Rev. Lett.*, 124:053605, Feb 2020. doi: 10.1103/PhysRevLett.124.053605. URL `https://link.aps.org/doi/10.1103/PhysRevLett.124.053605`.

[152] C. Ravensbergen, V. Corre, E. Soave, M. Kreyer, S. Tzanova, E. Kirilov, and R. Grimm. Accurate determination of the dynamical polarizability of dysprosium. *Phys. Rev. Lett.*, 120:223001, May 2018. doi: 10.1103/PhysRevLett.120.223001. URL `https://link.aps.org/doi/10.1103/PhysRevLett.120.223001`.

[153] A. Recati and S. Stringari. Supersolidity in ultracold dipolar gases. *Nature Reviews Physics*, Oct 2023. ISSN 2522-5820. doi: 10.1038/s42254-023-00648-2. URL `https://doi.org/10.1038/s42254-023-00648-2`.

[154] G. Roati, C. D'Errico, L. Fallani, M. Fattori, C. Fort, M. Zaccanti, G. Modugno, M. Modugno, and M. Inguscio. Anderson localization of a non-interacting bose–einstein condensate. *Nature*, 453(7197):895–898, Jun 2008. ISSN 1476-4687. doi: 10.1038/nature07071. URL `https://doi.org/10.1038/nature07071`.

[155] S. M. Roccuzzo and F. Ancilotto. Supersolid behavior of a dipolar Bose-Einstein condensate confined in a tube. *Phys. Rev. A*, 99:041601, Apr 2019. doi: 10.1103/PhysRevA.99.041601. URL `https://link.aps.org/doi/10.1103/PhysRevA.99.041601`.

[156] S. M. Roccuzzo, A. Recati, and S. Stringari. Moment of inertia and dynamical rotational response of a supersolid dipolar gas. *Phys. Rev. A*, 105:023316, Feb 2022. doi: 10.1103/PhysRevA.105.023316. URL `https://link.aps.org/doi/10.1103/PhysRevA.105.023316`.

[157] S. M. Roccuzzo, S. Stringari, and A. Recati. Supersolid edge and bulk phases of a dipolar quantum gas in a box. *Phys. Rev. Res.*, 4:013086, Feb 2022. doi: 10.1103/PhysRevResearch.4.013086. URL `https://link.aps.org/doi/10.1103/PhysRevResearch.4.013086`.

[158] S. Ronen, D. C. E. Bortolotti, and J. L. Bohn. Bogoliubov modes of a dipolar condensate in a cylindrical trap. *Phys. Rev. A*, 74:013623, Jul 2006. doi: 10.1103/PhysRevA.74.013623. URL `https://doi.org/10.1103/PhysRevA.74.013623`.

[159] R. E. Rosensweig. *Ferrohydrodynamics.* Cambridge monographs on mechanics and applied mathematics. Cambridge University Press Cambridge, Cambridge, 1985. ISBN 0521256240; 9780521256247.

[160] S. Sachdev. Quantum phase transitions. *Physics World*, 12(4): 33, apr 1999. doi: 10.1088/2058-7058/12/4/23. URL `https://dx.doi.org/10.1088/2058-7058/12/4/23`.

[161] L. E. Sadler, J. M. Higbie, S. R. Leslie, M. Vengalattore, and D. M. Stamper-Kurn. Spontaneous symmetry breaking in a quenched ferromagnetic spinor bose–einstein condensate. *Nature*, 443(7109): 312–315, Sep 2006. ISSN 1476-4687. doi: 10.1038/nature05094. URL `https://doi.org/10.1038/nature05094`.

[162] L. Santos, G. V. Shlyapnikov, and M. Lewenstein. Roton-maxon spectrum and stability of trapped dipolar Bose-Einstein condensates. *Phys. Rev. Lett.*, 90:250403, Jun 2003. doi: 10.1103/PhysRevLett.90.250403. URL `https://link.aps.org/doi/10.1103/PhysRevLett.90.250403`.

[163] T. Satoor, A. Fabre, J.-B. Bouhiron, A. Evrard, R. Lopes, and S. Nascimbene. Partitioning dysprosium's electronic spin to reveal entanglement in nonclassical states. *Phys. Rev. Res.*, 3:043001,

Oct 2021. doi: 10.1103/PhysRevResearch.3.043001. URL https://link.aps.org/doi/10.1103/PhysRevResearch.3.043001.

[164] T. A. Savard, K. M. O'Hara, and J. E. Thomas. Laser-noise-induced heating in far-off resonance optical traps. *Phys. Rev. A*, 56:R1095–R1098, Aug 1997. doi: 10.1103/PhysRevA.56.R1095. URL https://link.aps.org/doi/10.1103/PhysRevA.56.R1095.

[165] L. I. Schiff and H. Snyder. Theory of the quadratic zeeman effect. *Phys. Rev.*, 55:59–63, Jan 1939. doi: 10.1103/PhysRev.55.59. URL https://link.aps.org/doi/10.1103/PhysRev.55.59.

[166] C.-M. Schmied, M. Prüfer, M. K. Oberthaler, and T. Gasenzer. Bidirectional universal dynamics in a spinor bose gas close to a nonthermal fixed point. *Phys. Rev. A*, 99:033611, Mar 2019. doi: 10.1103/PhysRevA.99.033611. URL https://link.aps.org/doi/10.1103/PhysRevA.99.033611.

[167] M. Schmitt, M. Wenzel, F. Böttcher, I. Ferrier-Barbut, and T. Pfau. Self-bound droplets of a dilute magnetic quantum liquid. *Nature*, 539(7628):259–262, Nov 2016. ISSN 1476-4687. doi: 10.1038/nature20126. URL https://doi.org/10.1038/nature20126.

[168] N. Sepúlveda, C. Josserand, and S. Rica. Nonclassical rotational inertia fraction in a one-dimensional model of a supersolid. *Phys. Rev. B*, 77:054513, Feb 2008. doi: 10.1103/PhysRevB.77.054513. URL https://link.aps.org/doi/10.1103/PhysRevB.77.054513.

[169] G. V. Shlyapnikov and A. M. Tsvelik. Polar phase of one-dimensional bosons with large spin. *New Journal of Physics*, 13(6):065012, jun 2011. doi: 10.1088/1367-2630/13/6/065012. URL https://dx.doi.org/10.1088/1367-2630/13/6/065012.

[170] A. J. Shook, V. Vadakkumbatt, P. Senarath Yapa, C. Doolin, R. Boyack, P. H. Kim, G. G. Popowich, F. Souris, H. Christani, J. Maciejko, and J. P. Davis. Stabilized pair density wave via nanoscale confinement of superfluid ^{3}He. *Phys. Rev. Lett.*, 124:015301, Jan 2020. doi: 10.1103/PhysRevLett.124.015301.

URL https://link.aps.org/doi/10.1103/PhysRevLett.124.015301.

[171] I. Siovitz. Topological excitations and universal scaling of the one-dimensional spin-1 bose-einstein condensate far from equilibrium. Masterarbeit, Universität Heidelberg, Feb 2022.

[172] I. Siovitz, S. Lannig, Y. Deller, H. Strobel, M. K. Oberthaler, and T. Gasenzer. Universal dynamics of rogue waves in a quenched spinor bose condensate. *Phys. Rev. Lett.*, 131:183402, Nov 2023. doi: 10.1103/PhysRevLett.131.183402. URL https://link.aps.org/doi/10.1103/PhysRevLett.131.183402.

[173] A. Smerzi, S. Fantoni, S. Giovanazzi, and S. R. Shenoy. Quantum coherent atomic tunneling between two trapped bose-einstein condensates. *Phys. Rev. Lett.*, 79:4950–4953, Dec 1997. doi: 10.1103/PhysRevLett.79.4950. URL https://link.aps.org/doi/10.1103/PhysRevLett.79.4950.

[174] M. Sohmen, C. Politi, L. Klaus, L. Chomaz, M. J. Mark, M. A. Norcia, and F. Ferlaino. Birth, life, and death of a dipolar supersolid. *Phys. Rev. Lett.*, 126:233401, Jun 2021. doi: 10.1103/PhysRevLett.126.233401. URL https://link.aps.org/doi/10.1103/PhysRevLett.126.233401.

[175] G. Spagnolli, G. Semeghini, L. Masi, G. Ferioli, A. Trenkwalder, S. Coop, M. Landini, L. Pezzè, G. Modugno, M. Inguscio, A. Smerzi, and M. Fattori. Crossing over from attractive to repulsive interactions in a tunneling bosonic josephson junction. *Phys. Rev. Lett.*, 118:230403, Jun 2017. doi: 10.1103/PhysRevLett.118.230403. URL https://link.aps.org/doi/10.1103/PhysRevLett.118.230403.

[176] D. M. Stamper-Kurn and M. Ueda. Spinor bose gases: Symmetries, magnetism, and quantum dynamics. *Rev. Mod. Phys.*, 85: 1191–1244, Jul 2013. doi: 10.1103/RevModPhys.85.1191. URL https://link.aps.org/doi/10.1103/RevModPhys.85.1191.

[177] J. Stenger, S. Inouye, D. M. Stamper-Kurn, H.-J. Miesner, A. P. Chikkatur, and W. Ketterle. Spin domains in ground-state bose–einstein condensates. *Nature*, 396(6709):345–348,

Nov 1998. ISSN 1476-4687. doi: 10.1038/24567. URL https://doi.org/10.1038/24567.

[178] J. Stuhler, A. Griesmaier, T. Koch, M. Fattori, and T. Pfau. Magnetostriction in a degenerate quantum gas. *Journal of Magnetism and Magnetic Materials*, 316(2):429–432, 2007. ISSN 0304-8853. doi: https://doi.org/10.1016/j.jmmm.2007.03.097. URL https://www.sciencedirect.com/science/article/pii/S0304885307004295. Proceedings of the Joint European Magnetic Symposia.

[179] Y. Tang, A. Sykes, N. Q. Burdick, J. L. Bohn, and B. L. Lev. s-wave scattering lengths of the strongly dipolar bosons ^{162}Dy and ^{164}Dy. *Phys. Rev. A*, 92:022703, Aug 2015. doi: 10.1103/PhysRevA.92.022703. URL https://link.aps.org/doi/10.1103/PhysRevA.92.022703.

[180] Y. Tang, A. G. Sykes, N. Q. Burdick, J. M. DiSciacca, D. S. Petrov, and B. L. Lev. Anisotropic expansion of a thermal dipolar bose gas. *Phys. Rev. Lett.*, 117:155301, Oct 2016. doi: 10.1103/PhysRevLett.117.155301. URL https://link.aps.org/doi/10.1103/PhysRevLett.117.155301.

[181] L. Tanzi, E. Lucioni, F. Famà, J. Catani, A. Fioretti, C. Gabbanini, R. N. Bisset, L. Santos, and G. Modugno. Observation of a dipolar quantum gas with metastable supersolid properties. *Phys. Rev. Lett.*, 122:130405, Apr 2019. doi: 10.1103/PhysRevLett.122.130405. URL https://link.aps.org/doi/10.1103/PhysRevLett.122.130405.

[182] L. Tanzi, S. M. Roccuzzo, E. Lucioni, F. Famà, A. Fioretti, C. Gabbanini, G. Modugno, A. Recati, and S. Stringari. Supersolid symmetry breaking from compressional oscillations in a dipolar quantum gas. *Nature*, 574(7778):382–385, 2019. ISSN 1476-4687. doi: 10.1038/s41586-019-1568-6. URL https://doi.org/10.1038/s41586-019-1568-6.

[183] L. Tanzi, J. G. Maloberti, G. Biagioni, A. Fioretti, C. Gabbanini, and G. Modugno. Evidence of superfluidity in a dipolar supersolid from nonclassical rotational inertia. *Science*, 371(6534):1162–1165, 2021. ISSN 0036-8075. doi: 10.1126/science.aba4309. URL https://science.sciencemag.org/content/371/6534/1162.

[184] J. Tao, M. Zhao, and I. B. Spielman. Observation of anisotropic superfluid density in an artificial crystal. *Phys. Rev. Lett.*, 131:163401, Oct 2023. doi: 10.1103/PhysRevLett.131.163401. URL `https://link.aps.org/doi/10.1103/PhysRevLett.131.163401`.

[185] M. N. Tengstrand, D. Boholm, R. Sachdeva, J. Bengtsson, and S. M. Reimann. Persistent currents in toroidal dipolar supersolids. *Phys. Rev. A*, 103:013313, Jan 2021. doi: 10.1103/PhysRevA.103.013313. URL `https://link.aps.org/doi/10.1103/PhysRevA.103.013313`.

[186] Y. J. Uemura, L. P. Le, G. M. Luke, B. J. Sternlieb, W. D. Wu, J. H. Brewer, T. M. Riseman, C. L. Seaman, M. B. Maple, M. Ishikawa, D. G. Hinks, J. D. Jorgensen, G. Saito, and H. Yamochi. Basic similarities among cuprate, bismuthate, organic, chevrel-phase, and heavy-fermion superconductors shown by penetration-depth measurements. *Phys. Rev. Lett.*, 66:2665–2668, May 1991. doi: 10.1103/PhysRevLett.66.2665. URL `https://link.aps.org/doi/10.1103/PhysRevLett.66.2665`.

[187] G. Valtolina, A. Burchianti, A. Amico, E. Neri, K. Xhani, J. A. Seman, A. Trombettoni, A. Smerzi, M. Zaccanti, M. Inguscio, and G. Roati. Josephson effect in fermionic superfluids across the bec-bcs crossover. *Science*, 350(6267):1505–1508, 2015. doi: 10.1126/science.aac9725. URL `https://www.science.org/doi/abs/10.1126/science.aac9725`.

[188] G. Valtolina, K. Matsuda, W. G. Tobias, J.-R. Li, L. De Marco, and J. Ye. Dipolar evaporation of reactive molecules to below the fermi temperature. *Nature*, 588(7837):239–243, Dec 2020. ISSN 1476-4687. doi: 10.1038/s41586-020-2980-7. URL `https://doi.org/10.1038/s41586-020-2980-7`.

[189] M. Vengalattore, S. R. Leslie, J. Guzman, and D. M. Stamper-Kurn. Spontaneously modulated spin textures in a dipolar spinor bose-einstein condensate. *Phys. Rev. Lett.*, 100:170403, May 2008. doi: 10.1103/PhysRevLett.100.170403. URL `https://link.aps.org/doi/10.1103/PhysRevLett.100.170403`.

[190] F. Wächtler and L. Santos. Ground-state properties and elementary excitations of quantum droplets in dipolar bose-

einstein condensates. *Phys. Rev. A*, 94:043618, Oct 2016. doi: 10.1103/PhysRevA.94.043618. URL https://link.aps.org/doi/10.1103/PhysRevA.94.043618.

[191] G. Watanabe, F. Dalfovo, F. Piazza, L. P. Pitaevskii, and S. Stringari. Critical velocity of superfluid flow through single-barrier and periodic potentials. *Phys. Rev. A*, 80:053602, Nov 2009. doi: 10.1103/PhysRevA.80.053602. URL https://link.aps.org/doi/10.1103/PhysRevA.80.053602.

[192] H. Watanabe and T. c. v. Brauner. Spontaneous breaking of continuous translational invariance. *Phys. Rev. D*, 85:085010, Apr 2012. doi: 10.1103/PhysRevD.85.085010. URL https://link.aps.org/doi/10.1103/PhysRevD.85.085010.

[193] M. Wenzel. A dysprosium quantum gas in highly controllable optical traps. 2015. URL https://www.pi5.uni-stuttgart.de/documents/abgeschlossene-arbeiten/2015-Wenzel-Matthias-A-dysprosium-quantum-gas-in-highly-controllable-optical-traps-MSC.pdf.

[194] M. Wenzel, F. Böttcher, J.-N. Schmidt, M. Eisenmann, T. Langen, T. Pfau, and I. Ferrier-Barbut. Anisotropic superfluid behavior of a dipolar bose-einstein condensate. *Phys. Rev. Lett.*, 121:030401, Jul 2018. doi: 10.1103/PhysRevLett.121.030401. URL https://link.aps.org/doi/10.1103/PhysRevLett.121.030401.

[195] M. Wickliffe, J. Lawler, and G. Nave. Atomic transition probabilities for dy i and dy ii. *Journal of Quantitative Spectroscopy and Radiative Transfer*, 66(4):363–404, 2000. ISSN 0022-4073. doi: https://doi.org/10.1016/S0022-4073(99)00173-9. URL https://www.sciencedirect.com/science/article/pii/S0022407399001739.

[196] I. Zapata, F. Sols, and A. J. Leggett. Josephson effect between trapped bose-einstein condensates. *Phys. Rev. A*, 57:R28–R31, Jan 1998. doi: 10.1103/PhysRevA.57.R28. URL https://link.aps.org/doi/10.1103/PhysRevA.57.R28.

[197] Y.-C. Zhang, F. Maucher, and T. Pohl. Supersolidity around a critical point in dipolar Bose-Einstein Condensates. *Phys. Rev. Lett.*, 123:015301, Jul 2019. doi: 10.1103/PhysRevLett.123.015301.

URL https://link.aps.org/doi/10.1103/PhysRevLett.123.015301.

[198] Y.-C. Zhang, T. Pohl, and F. Maucher. Phases of supersolids in confined dipolar Bose-Einstein condensates. *Phys. Rev. A*, 104:013310, Jul 2021. doi: 10.1103/PhysRevA.104.013310. URL https://link.aps.org/doi/10.1103/PhysRevA.104.013310.

[199] T.-W. Zhou, G. Cappellini, D. Tusi, L. Franchi, J. Parravicini, C. Repellin, S. Greschner, M. Inguscio, T. Giamarchi, M. Filippone, J. Catani, and L. Fallani. Observation of universal hall response in strongly interacting fermions. *Science*, 381(6656): 427–430, 2023. doi: 10.1126/science.add1969. URL https://www.science.org/doi/abs/10.1126/science.add1969.

[200] W. H. Zurek. Cosmological experiments in superfluid helium? *Nature*, 317(6037):505–508, Oct 1985. ISSN 1476-4687. doi: 10.1038/317505a0. URL https://doi.org/10.1038/317505a0.

[201] M. Šindik, T. Zawiślak, A. Recati, and S. Stringari. Sound, superfluidity and layer compressibility in a ring dipolar supersolid. 2023. URL https://arxiv.org/abs/2308.05981.